A New Computer Aided LNA Design Approach Targeting Constant Noise-figure and Maximum Gain

N. Roy and V. K. Devabhaktuni
Department of ECE, Concordia University, 1455 de Maisonneuve W, Montreal, H3G 1M8, Canada

Abstract— Low-noise amplifiers (LNAs) are critical to a wide variety of electronic circuits such as those used in aerospace and Bluetooth applications. Because of the way noise propagates through a system, LNAs are desired to have a low noise-figure and a high gain. In this paper, we propose an RF/microwave-oriented LNA design approach based on constrained line search optimization, which targets a maximum gain for a specified noise-figure. The proposed approach is automated and hence requires minimal user-intervention. Simulation results show that the approach is extremely effective in terms of meeting the user-defined specifications.

1. INTRODUCTION

Amplifiers are an integral part of modern communication circuits and systems. Specifically, low-noise amplifiers occupy an important subset of amplifier applications in which noise reduction is paramount. In high-frequency high-speed circuits/systems, noise can be highly destructive to signal integrity [1]. It is therefore important to understand the way in which noise propagates through an electronic system.

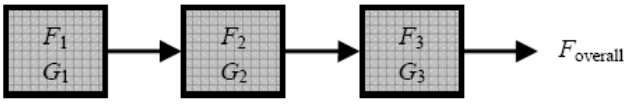

Figure 1: Block diagram of a cascaded electronic system.

Consider the cascaded electronic system shown in Fig. 1, in which each block represents a particular electronic device (*i.e.*, amplifier, filter *etc*). Let F_1, F_2, F_3, G_1, G_2, and G_3 represent the noise-figures and gains of each block respectively. The overall noise-figure of the system F_{overall} is given by

$$F_{\text{overall}} = F_1 + \frac{F_2 - 1}{G_1} + \frac{F_3 - 1}{G_1 G_2}. \tag{1}$$

From (1), it is clear that the first block is the most critical in terms of overall noise-figure. For this reason, a good LNA should have a high gain (G_1) and a low noise-figure (F_1). By placing the LNA at the front-end of the electronic system, we can substantially reduce the overall noise-figure. Unfortunately, noise-figure and gain are not independent parameters. In general, increasing the gain of an LNA will increase its noise-figure and vice-versa. As such, engineers typically design an LNA for a specific/desired noise-figure and the maximum possible gain for such a noise level. One approach for solving this problem [2] involves designing multiple LNAs to have the same noise-figure, and then finding through trial-and-error, the LNA that has the largest gain. This approach is not particularly efficient as it could take many design iterations to find an acceptable solution. Moreover, the approach in [2] relies heavily on manual Smith-chart plots, and hence the accuracy of the final design depends on the designer's expertise. In the proposed approach, we strive to overcome these difficulties.

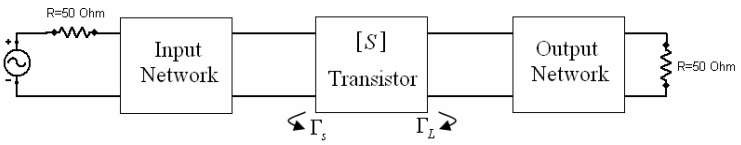

Figure 2: Block diagram of a typical LNA.

2. TRADITONAL RF/MICROWAVE-ORIENTED LNA DESIGN

Referring to Fig. 2, a typical LNA design problem involves the creation of input/output networks such that the input/output reflection coefficients meet the desired user-specifications. Based on the transistor's S-parameters, a reasonable LNA design can be achieved by following the approach suggested in [2] and [3]. The equations for the center (C_{F}) and radius (R_{F}) of a constant noise-figure circle on a Smith-chart can be expressed as

$$C_{\mathrm{F}} = \frac{\Gamma_{\mathrm{opt}}}{N+1} \tag{2}$$

and

$$R_{\mathrm{F}} = \frac{\sqrt{N\left(N+1-|\Gamma_{\mathrm{opt}}|^2\right)}}{N+1}, \tag{3}$$

where C_{F} is a complex quantity, R_{F} is a scalar, Γ_{opt} is the optimum source admittance that results in the minimum noise-figure, and N is the noise-figure parameter given by

$$N = \frac{F - F_{\mathrm{min}}}{4R_{\mathrm{N}}/Z_0}\left|1+\Gamma_{\mathrm{opt}}\right|^2. \tag{4}$$

In (4), F is the desired noise-figure, F_{min} is the minimum noise-figure for the transistor, R_{N} is the equivalent noise resistance of the transistor, and Z_0 is the characteristic impedance of the source (typically $50\,\Omega$). Any point on the radius of the constant noise-figure circle represents a reflection coefficient that will result in a noise-figure F, while the center of the circle represents a reflection coefficient that will yield the minimum noise-figure F_{min}. Any point, *i.e.*, reflection coefficient, within the circle results in a noise-figure between F_{min} and F. Similarly, the equations for the center (C_{S}) and radius (R_{S}) of a constant gain circle on a Smith-chart can be expressed as

$$C_{\mathrm{S}} = \frac{g_{\mathrm{S}} S_{11}^*}{1-(1-g_{\mathrm{S}})|S_{11}|^2} \tag{5}$$

and

$$R_{\mathrm{S}} = \frac{\sqrt{1-g_{\mathrm{S}}}(1-|S_{11}|^2)}{1-(1-g_{\mathrm{S}})|S_{11}|^2}. \tag{6}$$

In Equations (5) and (6), g_{S} is the normalized gain factor at the source given by

$$g_{\mathrm{S}} = \frac{1-|\Gamma_{\mathrm{S}}|^2}{|1-S_{11}\Gamma_{\mathrm{S}}|^2}(1-|S_{11}|^2), \tag{7}$$

where S_{11} for the transistor under consideration is available/given.

In the traditional approach to LNA design, a noise-figure is specified by the user, and the associated constant noise-figure circle is plotted on a Smith-chart. The goal is to find a Γ_{S} (*i.e.*, source reflection coefficient), which will result in a constant gain circle that touches the constant noise-figure circle at a single point. This task is achieved by a trial-and-error plotting of multiple constant gain circles until a satisfactory circle (not necessarily "the" best circle) is found. The point at which both circles meet represents the reflection coefficient that has both the desired noise-figure and the maximum possible gain at that noise level. Finally, the output reflection coefficient (*i.e.*, Γ_{L}) is set to the conjugate of the transistor's S_{22} value.

3. PROPOSED APPROACH

In the traditional approach to LNA design, we use trial-and-error to find the best possible gain circle to meet the user-specifications. Because this approach relies on manually plotting circles on a Smith-chart and visually checking to see if the two circles meet, the accuracy of the final solution depends on how well these circles were drawn. Moreover, it may take several tedious manual iterations to find an acceptable gain circle. The proposed approach strives to solve these issues through the use of constrained line search optimization.

For simplicity, we assume that the transistor is unilateral (*i.e.*, $S_{12} = 0$). In practice, S_{12} can be ignored since the reverse signal path is due solely to the gate-drain capacitance, which tends to be

very small [2]. In fact, near-unilateral transistors are now available. Nevertheless, the assumption results in an error that is bounded *i.e.*,

$$\frac{1}{(1+U)^2} < \frac{G_{\mathrm{T}}}{G_{\mathrm{TU}}} < \frac{1}{(1-U)^2}, \tag{8}$$

where G_{T} and G_{TU} are the transducer and unilateral transducer gains respectively, and U is the unilateral figure of merit given by

$$U = \frac{|S_{12}||S_{21}||S_{11}||S_{22}|}{(1-|S_{11}|^2)(1-|S_{22}|^2)}. \tag{9}$$

Considering the Smith-chart to be the complex reflection coefficient plane, it is possible to write the equation for a constant noise-figure circle as

$$(x - real\{C_{\mathrm{F}}\})^2 + (y - imag\{C_{\mathrm{F}}\})^2 = R_{\mathrm{F}}^2, \tag{10}$$

where x and y represent the real and imaginary axes respectively. Similarly, it is possible to write the equation for a constant gain circle as

$$(x - real\{C_{\mathrm{S}}\})^2 + (y - imag\{C_{\mathrm{S}}\})^2 = R_{\mathrm{S}}^2. \tag{11}$$

In the proposed approach, we make use of .S2P files from the transistor vendor, to minimize the need for user-inputs and to automate the approach. This file type is an industry standard that is recognized by most simulation programs. Within a .S2P file is the noise and S-parameter information for a given device/transistor at several frequencies. In fact, the .S2P file associated with a transistor contains all the information needed to solve for the constant noise-figure circle (Equation (10)) with the exception of desired noise-figure F. Since F is a user-specification, all parameters in Equation (10) are known. Hence, the LNA design problem is to find a $\Gamma_{\mathrm{S}} = x + jy$, which will make Equations (10) and (11) intersect. Re-arranging (10) to solve for y gives

$$y = \sqrt{R_{\mathrm{F}}^2 - (x - real\{C_{\mathrm{F}}\})^2} + imag\{C_{\mathrm{F}}\}. \tag{12}$$

Substituting (12) into (11) leads to

$$(x - real\{C_{\mathrm{S}}\})^2 + \left[\left(\sqrt{R_{\mathrm{F}}^2 - (x - real\{C_{\mathrm{F}}\})^2} + imag\{C_{\mathrm{F}}\}\right) - imag\{C_{\mathrm{S}}\}\right]^2 = R_{\mathrm{S}}^2 \tag{13}$$

Equation (13) has only one unknown *i.e.*, x representing the real part of Γ_{S}. Upon close inspection of (13), it may be seen that x may have two possible solutions. Geometrically, this makes sense since two overlapping circles could intersect at two points. To ensure that the two circles meet/touch at one and only one point, a constraint (the distance between the centers of the two circles must be equal to the sum of their radii) *i.e.*,

$$\sqrt{(real\{C_{\mathrm{S}}\} - real\{C_{\mathrm{F}}\})^2 + (imag\{C_{\mathrm{S}}\} - imag\{C_{\mathrm{F}}\})^2} = (R_{\mathrm{F}} + R_{\mathrm{S}}). \tag{14}$$

is added. Equation (14) can be re-arranged as

$$F(x) = \sqrt{(real\{C_{\mathrm{S}}\} - real\{C_{\mathrm{F}}\})^2 + (imag\{C_{\mathrm{S}}\} - imag\{C_{\mathrm{F}}\})^2} - (R_{\mathrm{F}} + R_{\mathrm{S}}), \tag{15}$$

where $F(x)$ represents the equation to be minimized. The smaller the value of $|F(x)|$, the closer the two circles will be. When $|F(x)| = 0$, the two circles intersect at exactly one point. In the proposed approach, a line search based optimization technique is used to find a value of x that satisfies (13) and minimizes (15). Once x is found, y can be solved for using (12) and hence Γ_{S} becomes known. Our line search optimization sub-routine allows the user to specify a resolution parameter, which determines the degree of accuracy of the final design.

4. EXAMPLE

At 4 GHz, the .S2P file for a GaAs FET transistor gives the following S-parameters and noise parameters ($Z_0 = 50\,\Omega$): $S_{11} = 0.6\angle -60°$, $S_{21} = 1.9\angle 81°$, $S_{12} = 0.05\angle 26°$, $S_{22} = 0.5\angle -60°$, $F_{\min} = 1.6$ dB, $\Gamma_{\text{opt}} = 0.62\angle 100°$, and $R_{\text{N}} = 20\,\Omega$. Making use of this transistor, the objective is to design an LNA that has a noise-figure of 2 dB and an associated maximum gain. The proposed CAD approach is employed.

From Equations (8) and (9), $U = 0.059$ and the error in gain will be less than $+/-0.5$ dB. The parameters in Equations (2) through (4) are calculated and the equation for the constant noise-figure circle is found to be

$$(x + 0.097996)^2 + (y - 0.55576)^2 = (0.2416)^2. \tag{16}$$

Given the user-desired resolution of 0.0001, the constrained optimization routine is executed. After 14 iterations, it is observed that $x = 0.1436$ minimizes (15), and correspondingly $y = 0.5567$ and $\Gamma_{\text{S}} = 0.14136 + 0.5567j = 0.574\angle 75.752°$. Using stub-matching techniques and the calculated value of Γ_{S}, the circuit shown in Fig. 3 is simulated. A summary of the numerical results is shown in Table 1.

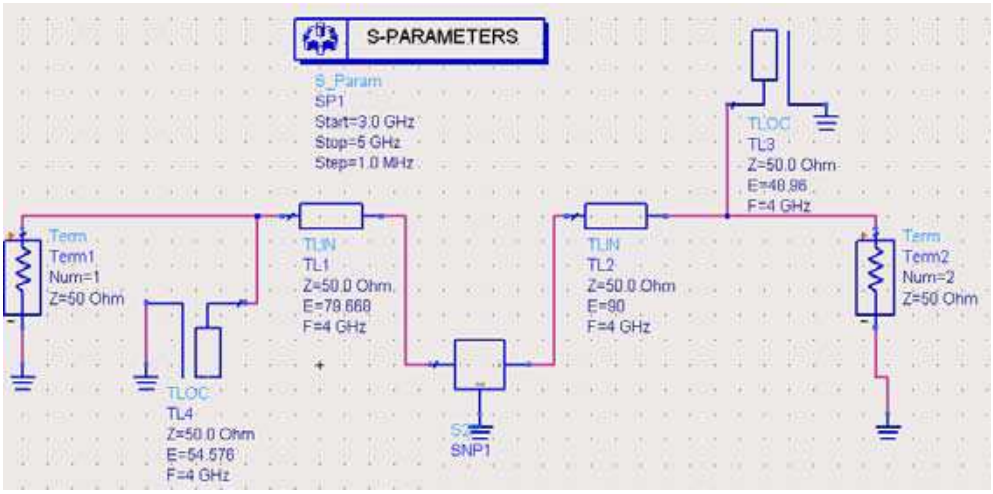

Figure 3: LNA design using the proposed CAD approach.

Table 1: Comparison of the traditional and the proposed approaches.

Metric	Simulation Results at 4 GHz	
	Traditional Approach [2]	Proposed Approach
C_{S}	$0.58\angle 60.0$	$0.57767\angle 60.00$
R_{S}	0.150	0.156
Number of gain circles solved	> 3	1
Number of optimization iterations	Not Applicable	14
$\lvert F(x)\rvert$	0.2376	0.0066
Gain	8.36 dB	8.47 dB
Noise-figure	1.47 dB	1.99 dB

Comparing the values of $|F(x)|$ resulting from the traditional and the proposed approaches (see Table 1), it is obvious that error measure $|F(x)|$ is much smaller in the latter case. As such, the proposed approach results in an LNA design that meets the given user-specifications to a relatively closer degree. In addition, as a consequence of obtaining a relatively closer value of noise-figure w.r.t. the user-specification, the LNA design from the proposed approach is able to achieve a higher gain.

5. CONCLUSIONS

This work presents a new RF/microwave-oriented LNA design approach, which targets maximum gain for a desired noise-figure. The automated approach avoids the need for both trial-and-error and manual Smith-chart plots to find the largest possible constant gain circle that will meet/touch the desired constant noise-figure circle. The problem has been formulated mathematically and solved employing constrained line search optimization. The proposed approach is shown to be highly accurate and is of practical use to RF/microwave engineers.

REFERENCES

1. Lee, T., *The Design of CMOS Radio Frequency Integrated Circuits*, Cambridge University Press, Cambridge, UK, 1998.
2. Pozar, D. M., *Microwave and RF Design of Wireless Systems*, John Wiley & Sons, New York, NY, 2000.
3. Pozar, D. M., *Microwave Engineering*, John Wiley & Sons, New York, NY, 2005.

EDA Designs of RFIC Inductors

Tianquan Deng

School of Computer Science & Engineering
University of Electronic Science & Technology of China
Chengdu 610054, China

Abstract— **Inductor Design Tool (IDT)** is an interactive software package that has been fitted and approved by the results based full-wave analysis method and experimental approach to realize Electronic Design Automation (EDA) of RFIC inductors. Its functionality may include analysis, synthesis, optimization, interpolation, and modeling of spiral inductors with any shape on any material substrate for microwave and wireless applications.

1. BACKGROUND

As dramatically increasing IC demand of computer and wireless communication industries, especially when CPU goes to high speed, thus its high frequency up to a few GHz processor ICs will be going to the market, inductor designs will pay more important role in such high frequency IC designs, for example, in RFIC and MMIC designs. It is noted that any kinds of ICs are basically constructed by four components: resistor (R), capacitor (C), inductor (L), and transistor (T). Among them, resistors and capacitors are easily analyzed and designed by simple formulas. Transistors are mainly modeled by measurement ways due to their process dependency and not easy scalability. So far, it really lacks an effective tool for inductor design. Here, only IDT fills in this blank with full functionality.

2. METHODOLOGY OF IDT

The Inductor Design Tool (IDT) is an Electronic-Design-Automation (EDA) tool used for RFIC/MMIC designs. It basically employs curve-fitting methods to interpolate and extrapolate either available full-wave EM simulation results or measurement results to fulfill design equation extractions. Then the unique calibration techniques are applied to improve accuracy of such design equations basing on any specified foundry processing technologies. Among this procedure, a real design flow is used, i.e., from initial design, fabrication and calibration, re-design, till the specified accuracy obtained. Therefore the design accuracy is guaranteed when the foundry processing technologies constantly change; the accuracy even becomes better and better when the design library fills in more and more components.

3. DESCRIPTION OF IDT

As shown in Fig. 1, IDT has a user-friendly interface.

3.1. Unique Features:

When playing with the IDT platform, it has the following unique features:

- For PCs running Microsoft Windows
- Fast enough, even able to run via the Internet
- Interactive graphical user interface
- Functions of analyzer, calculator, synthesizer, optimizer, and interpolator
- Easy to use, basing on the real design flow, i.e., from initial design, fabrication and calibration, re-design, till the specified accuracy obtained
- Layout demonstration and output
- List for a single point result of the inductor analysis or synthesis
- 2D curve versus a sweep variable for analysis or synthesis
- 3D graph versus two sweep variables for analysis or synthesis
- Output of the equivalent circuit model extracted
- Feasible to transfer the designs into the design environment of available commercial software

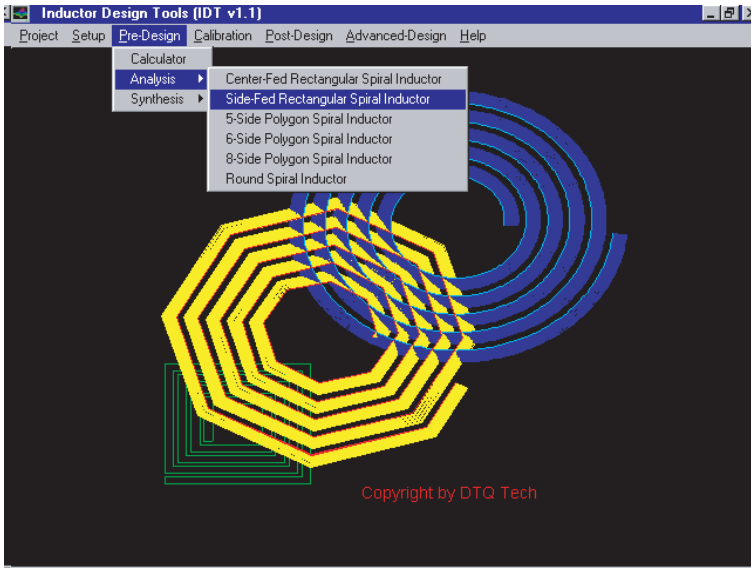

Figure 1: The main window of IDT.

3.2. Simulation Code:

IDT has stable and reliable simulation code because almost effects of either in the design or foundry processing are taken into account:

- Dependent process design is more practical by the unique calibration technique
- The design accuracy is guaranteed when the foundry processing technologies constantly change
- The accuracy even becomes better and better when the design library fills in more and more components
- Fast simulation within seconds for a typical inductor, while in minutes for optimization and sweeping
- Analysis to predict inductance, resistance, capacitance, Q factor, self resonance frequency for a given dimension and process parameters of an inductor
- Synthesis to obtain the physical dimension of the inductor for a specified inductance
- Optimization to get the physical dimension of the inductor for a specified inductance with maximum Q value
- Interpolation to approach higher accuracy while to save at least one-order of working time to interpolate and extrapolate either available EM simulation result or measurement result
- Extractions of the equivalent circuit models

3.3. Metal Geometry:

IDT is suitable for any kind of geometrical shapes of inductors:

- Rectangular, any polygon shape, and round spiral inductors
- No need to manually draw the layout, just to key in the dimension numbers
- Multiple-layer metals
- Considering ohmic loss, skin effect, and metal thickness of any kind of metals

3.4. Substrate Material:

Use of any kind of substrate materials in any foundry processing to fabricate inductors have been verified in IDT:

- Hybrid fabrication materials such as alumina, ceramic, duroid, etc., and on any other PCB
- Semiconductor materials such as GaAs, CMOS, BiCmos, Bipolar, etc.
- MEMS, SOI, and any other advanced-foundry technologies
- And user-defined, as well as, multiple-layer substrates

4. RESULTS AND ANALYSIS

Figure 2 shows a typical example by using synthesis function of IDT to design an RFIC inductor fabricated on a standard CMOS process. For a given center frequency of 1.9 GHz, the metal width(W) of 10 μm, the spacing(S) of 4 μm, number of turns $N = 5$, for the design target of inductance $L = 4$ nH, running within one second's time, the result comes out, the outer diameter $D = 200.27$ μm, other results (including resistance and capacitance values in the inductor equivalent circuit, resonant frequency, and Q value) are listed at the right side. It is shown that the design error $= (4.01679 - 4.003)/4.003^{*}100\% = 0.3\%$, its accuracy is quit high.

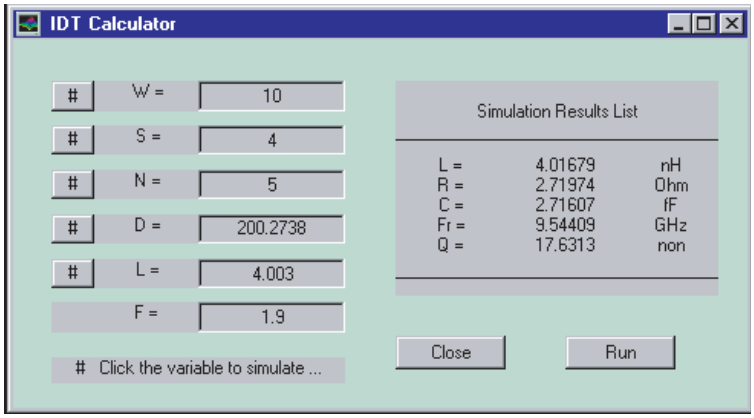

Figure 2: A typical example by using synthesis function of IDT.

Figure 3 shows how changes of the metal width (W) affect the inductance L, the resistance R, Q value, and the resonant frequency of RFIC inductors, by using of IDT codes.

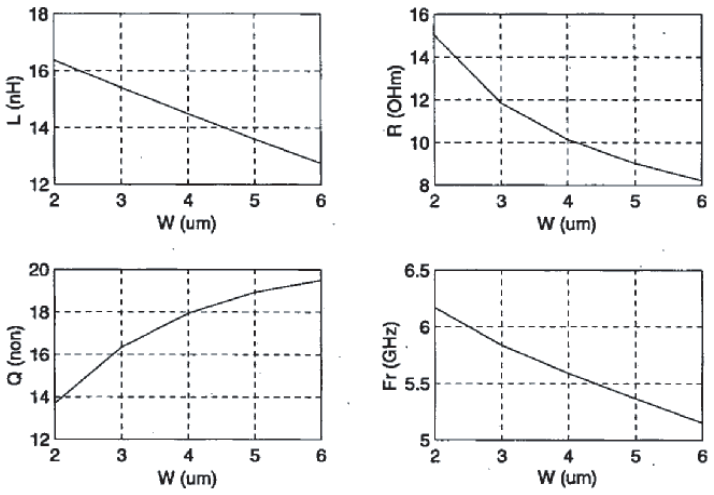

Figure 3: The inductance L, the resistance R, Q value, and the resonant frequency Fr of RFIC inductors varying with the metal width (W).

Figure 4 shows how changes of the metal spacing (S) affect the inductance L, the resistance R, Q value, and the resonant frequency of RFIC inductors, by using of IDT codes.

Own to the fast simulation speed of IDT, within a few minutes it is possible to sweep variables of W or S versus the inductor parameters such as the inductance L, the resistance R, Q value, and the resonant frequency, as shown in Fig. 3 and Fig. 4. From Fig. 5, it is showing two sets of results with comparison between the IDT results and the measurement results designed for several different inductance values. It is observed that the accuracy is better than 0.5%. And the accuracy even becomes better and better through the unique calibration techniques. And the IDT results can be applied to much wider ranges by IDT features of interpolations and extrapolations.

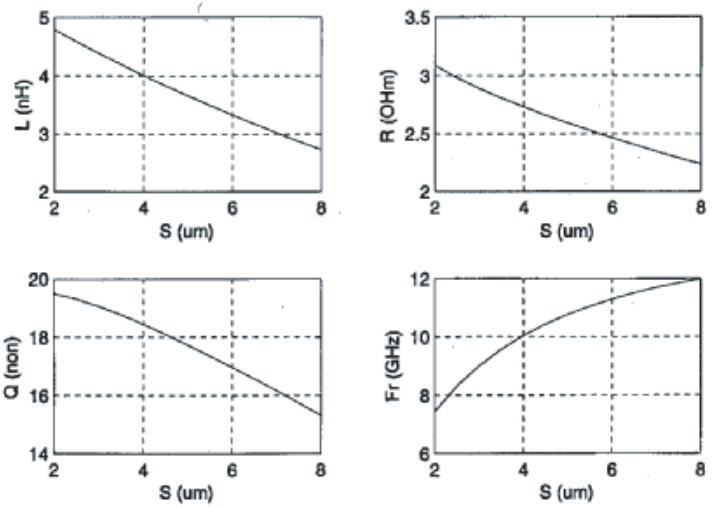

Figure 4: The inductance L, the resistance R, Q value, and the resonant frequency Fr of RFIC inductors varying with the metal spacing (S).

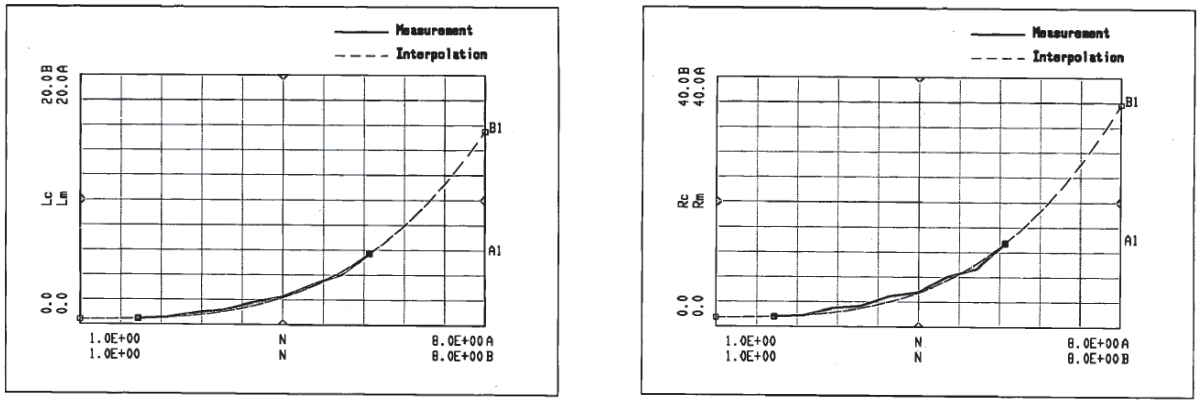

Figure 5: Two sets of results with comparison between the IDT results and the measurement results designed for several different inductance values.

5. CONCLUSIONS

Unique calibration technique has been used for RFIC inductor designs having advantages of high accuracy with independent process technologies. Comparisons with experimental results show that IDT is a practical EDA tool with one more choice for RFIC designers.

REFERENCES

1. Deng, T. Q., "CAD model for coplanar waveguide synthesis," *IEEE Trans. Microwave Theory Tech.*, Vol. 44, No. 10, 1733–1738, 1996.
2. Deng, T. Q., M. S. Leong, P. S. Kooi, and T. S. Yeo, "Synthesis formulas for coplanar lines in hybrid and monolithic MICs," *Electron. Lett.*, Vol. 32, No. 24, 2253–2254, 1996.
3. Deng, T. Q., M. S. Leong, P. S. Kooi, and T. S. Yeo, "Synthesis formulas simplify coplanar-waveguide design," *Microwaves & RF, Wireless Technology Issue*, Vol. 36, No. 3, 84–98, March 1997.
4. Long, J. R. and M. A Copeland, "The modeling, characterization, and design of monolithic inductors for silicon RF IC's," *IEEE J Solid-State Circuits*, Vol. 32, 1997.
5. Zhao, J. X. and M. J. Fa, "Parameters extraction and modeling for planar spiral inductor on Si substrates by DDM for conformal modules," *IEEE Trans. Microwave Theory Tech.*, 2003.

CAD Models for Estimating the Capacitance of a Microstrip Interconnect: Comparison and Improvisation

S. R. Nelatury[1], **M. N. O. Sadiku**[2], **and V. K. Devabhaktuni**[3]

[1]School of Engineering, Pennsylvania State University, Erie, PA 16563, USA
[2]College of Engineering, Prairie View A&M University, Prairie View, TX 77446, USA
[3]Department of ECE, Concordia University, Montreal, QC, H3G 1M8, Canada

Abstract— Although the field of numerical electromagnetics (EM) has come to a relatively high level of maturity, RF/microwave engineers seem to prefer simple yet accurate closed-form expressions for design parameters of interest. For instance, a common practice is to use empirical formulae for the estimation of capacitance per unit length of microstrip interconnects. Literature survey reveals that several formulae have been proposed in the past 40 years or so. Each of these works involves the building of a CAD model (or formulae) based on certain assumptions. It is these assumptions that differentiate one work from another (e.g., in terms of model accuracy, valid frequency range etc). Comparison of these formulae against measurements indicates, to an RF/microwave engineer, which of these formulae best-suits a given CAD scenario. In this paper, we compare 12 such formulae, all of which estimate the same quantity, i.e., capacitance. Cross-fertilization of certain intermediate steps of the above works could potentially lead to composite models that offer relatively better accuracies. The work is of practical relevance to RF/microwave designers.

1. INTRODUCTION

In the coming years, integrated circuits using printed microstrip transmission lines are expected to operate at higher and higher clock frequencies. The analysis of these lines was originally carried out using heavy-duty analytical and numerical techniques. Periodically, RF/microwave engineers look for simple formulae for quantities such as capacitance per unit length. Since the interconnect capacitance between junctions on a chip plays a key role in digital circuit performance, having a handy formula for this quantity is vital. At frequencies above a few MHz, the characteristic impedance of the traces relies heavily on the interconnect capacitance.

Most digital gates are edge-triggered and prone to timing errors unless rise/fall times are less than 10% of the clock period. Assuming R_{gate} to be the output driving resistance and $C_{interconnect}$ to be the interconnect capacitance, the time constant τ_{RC} is their product. The rise time can be considered as 5 times the time constant. These times are depicted graphically in Fig. 1.

Several attempts have been made to calculate the capacitance of a microstrip line through rigorous numerical analysis. Such computation is time-consuming when integrated into computer-aided design (CAD) programs. To overcome this situation, simple formulae that are accurate enough for engineering analysis have been proposed. Some of these formulas were compared by Bogatin [1] in 1988. Since then other models have been proposed. The purpose of this paper is to extend the work in [1].

In this paper, we compare a variety of existing models for calculating the capacitance per unit length of a microstrip geometry in Fig. 2. For each model, we define the effective relative permittivity

$$\varepsilon_{eff} = \frac{C}{C_o} \tag{1}$$

and the line impedance

$$Z_o = \frac{\sqrt{\varepsilon_{eff}}}{u_o C}, \tag{2}$$

where C_o is the capacitance per unit length when $\varepsilon_r = 1$, C is the capacitance per unit length when filled with material, and $u_o = 3 \times 10^8$ m/s is the speed of light in free space. In what follows, several model equations are presented in chronological order. Comparison is made with the bench mark of measurements reported in [1].

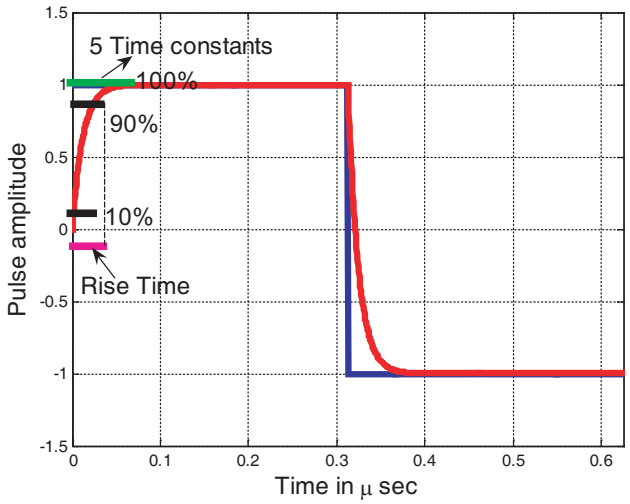

Figure 1: Distortion in the pulse response due to interconnect capacitance. Approximate non-zero rise time is shown.

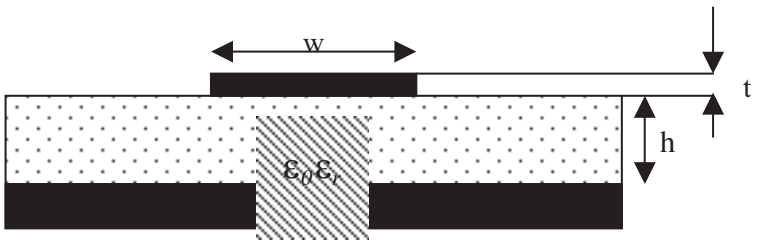

Figure 2: Geometry of the microstrip.

2. MODELS

We now present twelve models for calculating the capacitance per unit length of the microstrip. The models presented here may readily be handled using a pocket calculator. They can be easily incorporated into CAD routines.

Model 1: Parallel plate [2]

$$C = \varepsilon_o \varepsilon_r \frac{w}{h} \tag{3}$$

Model 2: Kaupp [3]

$$C = \frac{\varepsilon_{eff}}{60 u_o \ln\left(5.98 \frac{h}{w_{eff}}\right)} \tag{4}$$

where

$$\left.\begin{array}{rcl} \varepsilon_{eff} & = & 0.475\varepsilon_r + 0.67 \\ w_{eff} & = & 0.8w + t \end{array}\right\} \tag{5}$$

Model 3: Schneider [2, 4]

$$C = \begin{cases} \frac{\varepsilon_{eff}}{60 u_o \ln\left(\frac{8h}{w} + \frac{w}{4h}\right)}, & w/h \le 1 \\ \varepsilon_o \varepsilon_{eff} \left[\frac{w}{h} + 2.42 - 0.44\frac{h}{w} + \left(1 - \frac{h}{w}\right)^6\right], & w/h \ge 1 \end{cases} \tag{6}$$

where

$$\varepsilon_{eff} = \frac{\varepsilon_r + 1}{2} + \frac{\varepsilon_r - 1}{2}\left(1 + \frac{10h}{w}\right)^{-0.5} \tag{7}$$

Model 4: Kumar et al. [5]

$$C = \varepsilon_o \varepsilon_{eff} \left[\frac{w}{h} + \frac{2\pi}{\ln\left(\frac{4h}{t}\right)}\right] \tag{8}$$

where

$$\varepsilon_{eff} = \frac{\varepsilon_r + 1}{2} + \frac{\varepsilon_r - 1}{2}\left(1 + \frac{w}{10t}\right)^{-1} \tag{9}$$

Model 5: Wheeler [6, 7]

$$C = \frac{4\varepsilon_o \varepsilon_{eff}}{\ln\left\{1 + \frac{1}{2}\left(\frac{8h}{w_{eff}}\right)\left[\left(\frac{8h}{w_{eff}}\right) + \sqrt{\left(\frac{8h}{w_{eff}}\right)^2 + \pi^2}\right]\right\}} \tag{10}$$

where

$$w_{eff} = w + \frac{t}{\pi}\ln\left\{\frac{4e}{\sqrt{\left(\frac{t}{h}\right)^2 + \left[\frac{1}{\pi\left(\frac{w}{t}+1.10\right)}\right]^2}}\right\} \tag{11}$$

$$\varepsilon_{eff} = \frac{\varepsilon_r + 1}{2} + \frac{\varepsilon_r - 1}{2}\left(1 + \frac{10h}{w_{eff}}\right)^{-0.5} \tag{12}$$

Model 6: Poh et al. [8]
For $w/h \leq 0.6$,

$$C = \frac{\varepsilon_o(1+\varepsilon_r)\pi h}{\varepsilon_r w\left\{\ln\left(\frac{8h}{w}\right) + \frac{1}{16(1+\varepsilon_r)}\left(\frac{w}{h}\right)^2 + \frac{\varepsilon_r - 1}{\varepsilon_r}\left[0.041\left(\frac{w}{h}\right)^2 - 0.454\right]\right\}} \tag{13}$$

and for $w/h > 0.6$,

$$C = \frac{\varepsilon_o w}{h}\left\{1 - \frac{2h}{\pi\varepsilon_r w}\left[(1+\varepsilon_r)\ln\left(\frac{2h}{w}\right) - 2.230 - 4.554\varepsilon_r - (4.464 + 3.89\varepsilon_r)\frac{h}{w}\right]\right\}^{1/2} \tag{14}$$

Model 7: Sakurai and Tamaru [9]

$$C = \varepsilon_o\varepsilon_r\left(1.15\frac{w}{h} + 2.80\left(\frac{t}{h}\right)^{0.222}\right) \tag{15}$$

Model 8: Edwards [10]
For $w/h < 3.3$

$$C = 2.78\times10^{-11}\varepsilon_o\sqrt{2\left(\varepsilon_r+1\right)}\left[\ln\left\{\frac{4h}{w} + \sqrt{\left(\frac{4h}{w}\right)^2 + 2}\right\} - \frac{1}{2}\left(\frac{\varepsilon_r - 1}{\varepsilon_r + 1}\right)\left(\ln\frac{\pi}{2} + \frac{1}{\varepsilon_r}\ln\frac{4}{\pi}\right)\right]^{-1} \tag{16}$$

For $w/h > 3.3$

$$C = \frac{5.56\times10^{-11}\varepsilon_o\sqrt{\varepsilon_r}}{\pi}\left[\frac{w}{2h} + \frac{\ln 4}{\pi} + \frac{\ln\left(e\pi^2/16\right)}{2\pi}\left(\frac{\varepsilon_r - 1}{\varepsilon_r^2}\right) + \frac{\varepsilon_r + 1}{2\pi\varepsilon_r}\left\{\ln\frac{\pi e}{2} + \ln\left(\frac{w}{2h} + 0.94\right)\right\}\right] \tag{17}$$

where $e = 2.7182818$.
Model 9: Abuelma'atti [11]

$$C = \frac{\varepsilon w}{h}\left[3.355 + 1.108b - 0.00045b^3 - \frac{2.355}{(1 + 0.54b^{0.765} + 0.0236b^{3.9})}\right] \tag{18}$$

where $b = h/w$.

Model 10: Chow and Tang [12]

$$C = \varepsilon_o \left[\left(\frac{\varepsilon_r W}{h} \right)^n + \left(0.9 \frac{\varepsilon_r + 1}{2} \sqrt{8\pi W} \right)^n \right]^{1/n} \tag{19}$$

with $n = 1.114$.

Model 11: Shapiro [13]

$$C = \frac{\varepsilon_o \varepsilon_{eff}}{\pi} \left[\frac{w}{h} + 1.393 + 0.667 \ln \left(\frac{w}{h} + 1.444 \right) \right]^{-1} \tag{20}$$

where

$$\varepsilon_{eff} = \frac{\varepsilon_r + 1}{2} + \frac{\varepsilon_r - 1}{2} \left[\left(1 + 12 \frac{h}{w} \right)^{-0.5} + 0.04 \left(1 - \frac{w}{h} \right)^2 \right] \tag{21}$$

Model 12: Kwok et al. [14]

$$C = \varepsilon_o \left\{ \left(\frac{\varepsilon_r w}{h} \right)^{1.08} + \left\langle \pi(\varepsilon_r + 1) \left[\frac{1}{\ln \left(\frac{8h}{w} + 1 \right)} - \frac{w}{8h} \right] \right\rangle^{1.08} \right\}^{1/1.08} \tag{22}$$

Bogatin [1] made a comparison of the first six models. The remaining six models that have been proposed following his research work are included here. In the next section, we present a comparison of these models.

3. COMPARISON

In order to compare the models listed in the preceding section, we re-use the measured values in [1] (also reported in [15]). The capacitance values tabulated were used in the comparison process. We have used the norm of the relative error $||E||$ as the error metric defined as

$$|E| = \sqrt{\sum_{i=1}^{N} \left[\frac{C_{Measured}(i) - C_{Calculated}(i)}{C_{Measured}(i)} \right]^2} \tag{23}$$

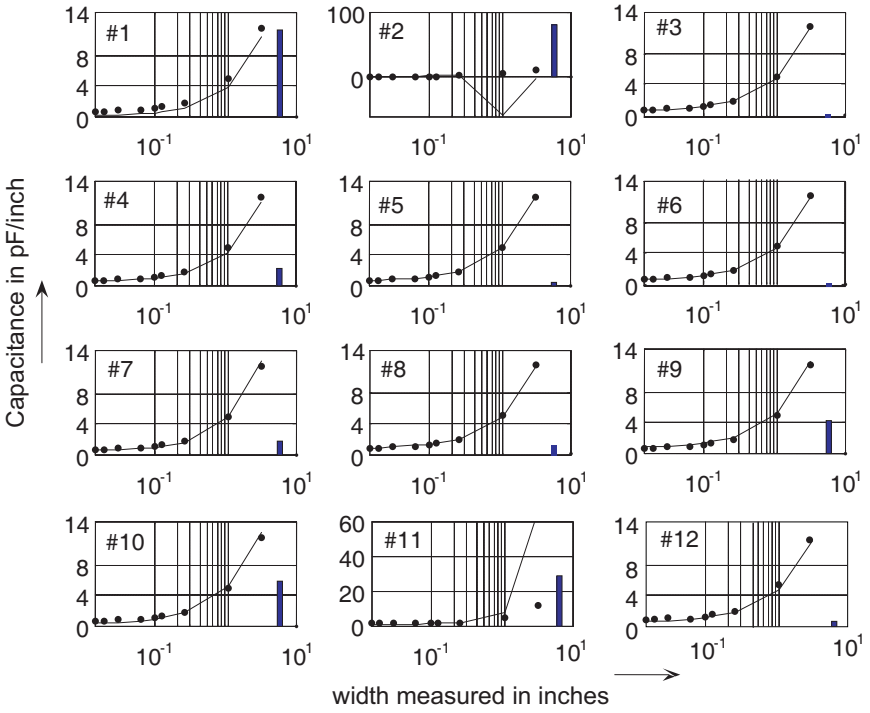

Figure 3: Capacitance per unit length measured in pF/inch for all 12 models.

where N represents the number of measurements available. Fig. 3 depicts the capacitance per unit length measured in pF/inch for all 12 models. The measured values are shown as the dots on each graph. The reader may note that each subplot in Fig. 3 has a vertical bar whose height is proportional to the error. These bars lead to an appreciation of the performance for each model. Note that for model 2, the $y-$axis limit reaches up to 100. Thus the error bar should be interpreted as highest for this model. Table 1 shows the error norm for all models. As can be seen, Schneider's model has the least error, followed by Wheeler's model. Of all, the Kaupp model has the largest error. This is explained through the denominator term. Whenever the ratio w_{eff}/h equals 5.98, a singularity is created since the denominator results in the log of unity. This greatly offsets the values and hence, a higher error is noted. In [1], Bogatin remarks that it is possible to create a composite model by taking the $\varepsilon_{\text{reff}}$ from one model and the capacitance per unit length from another. With this idea in mind, we have tried to use Schneider's expression in several other models (i.e., models 4, 8, 9, and 11). It is interesting to note that the error norm appears to decrease in all cases. This is shown in the third column of Table 1. The error norm is also shown as a histogram plot (Fig. 4), wherein we depict pair-wise comparisons of models 4, 8, 9, and 11 with and without model 3 combined. Model 9 of Abuelma'atti coupled with Schneider's model 3 for $\varepsilon_{\text{reff}}$ has the least error of 0.0267. Even Shapiro's model (refered to as model 11) gained significant accuracy through this composite approach (i.e., the error is reduced from 4.7115 to 0.2707).

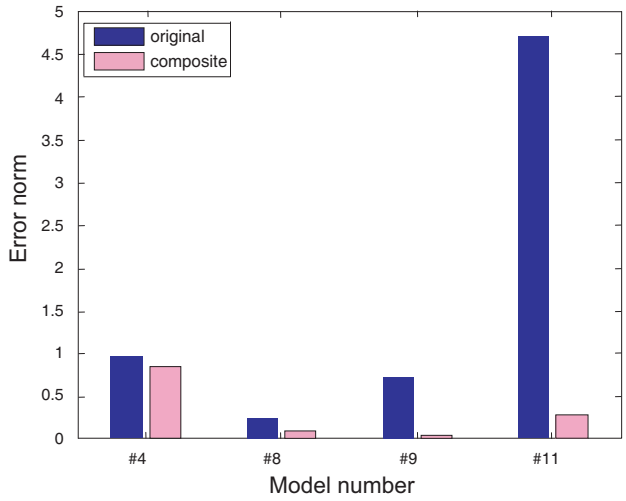

Figure 4: The reduction in $||E||$ resulting from combining model 3 with models 4, 8, 9, and 11.

Table 1: Various models and their error norms.

Model	Error norm $\|\|E\|\|$	Error norm $\|\|E\|\|$ (composite model)
♯ 1 Parallel plate	1.9380	-
♯ 2 Kaupp	13.1240	-
♯ 3 Schneider	0.0480	-
♯ 4 Kumar et al.	0.9632	0.8336
♯ 5 Wheeler	0.0656	-
♯ 6 Poh et al.	0.0724	-
♯ 7 Sakurai and Tamaru	0.2982	-
♯ 8 Edwards	0.2275	0.0760
♯ 9 Abuelma'atti	0.7152	0.0267
♯ 10 Chow & Tang	0.9865	-
♯ 11 Shapiro	4.7115	0.2707
♯ 12 Kwok et al.	0.0851	-

Most of the models presented thus far are inspired by physical and analytical considerations. However, for the data under consideration, we propose the following empirical formula which has

an error of about 0.1 over the entire range of w/h. This model shows improved performance w.r.t. eight of the listed models.

$$C = \varepsilon_r \left[\left(\frac{w}{10h} \right)^3 - \left(\frac{w}{5.423h} \right)^2 + \left(\frac{4w}{3h} \right) + 1.0626 \right] \tag{24}$$

Moreover, if model 3 is used for $w/h < 6$ and the proposed model in (24) for $w/h > 6$, the error in model 3 is reduced from 0.048 to 0.0388. Interestingly, use of model 3 for $w/h < 6$ and the model 5 for $w/h > 6$ also resulted in the error being reduced to 0.0388. It is worth exploring as to which model works better for a given range and to use it accordingly.

4. CONCLUSIONS

Reliable closed-form expressions for the capacitance per unit length of a microstrip line are useful for RF/microwave engineers. In this paper, we compared various models proposed by researchers in the area. Through examples, it has been shown that composite models (e.g., created *via* use of Schneider's model) offer improved accuracies. A further attempt was made to reduce the error in Schneider's model. It was found that the proposed model could be used for $w/h < 6$ and for $w/h > 6$, it is recommended that Wheeler's model or the proposed model in (24) be used. The proposed model has a cubic polynomial in w/h and was found to yield acceptable reduction in overall error. As a future work, we intend to research into the creation of several more reliable composite models.

REFERENCES

1. Bogatin, E., "Design rules for microstrip capacitance," *IEEE Trans. Components Hybrids Manufacturing Tech.*, Vol. 11, No. 3, 253–259, 1988.
2. Sadiku, M. N. O., *Elements of Electromagnetics*, Oxford University Press, New York, 2007.
3. Kaupp, H. R., "Characteristics of microstrip transmission lines," *IEEE Trans. Energy Conversion*, Vol. 16, No. 2, 185, 1967.
4. Schneider, M. V., "Microstrip lines for microwave integrated circuits," *Bell Systems Tech. J.*, Vol. 48, No. 5, 1421, 1969.
5. Kumar, A., et al., "A method for the calculation of the characteristic impedance of microstrips," *Int. J. Electronics*, Vol. 40, No. 1, 45, 1976.
6. Wheeler, H. A., "Transmission line properties of a strip on a dielectric sheet on a plane," *IEEE Trans. Microwave Theory Tech.*, Vol. 25, No. 8, 631, 1977.
7. Bogatin, E., "A closed form analytical model for the electrical properties of microstrip interconnects," *IEEE Trans. Components Hybrids Manufacturing Tech.*, Vol. 13, No. 2, 258–266, 1990.
8. Poh, S. Y., W. C. Chew, and J. A. Kong, "Approximate formulas for line capacitance and characteristic impedance of microstrip line," *IEEE Trans. Microwave Theory Tech.*, Vol. 29, 135–142, 1981; and the erratum in Vol. 29, No. 10, 1119, 1981.
9. Sakurai, T. and K. Tamaru, "Simple formulas for two and three dimensional capacitances," *IEEE Trans. Electron Devices*, Vol. 30, No. 2, 183–185, 1983.
10. Edwards, T. C., *Foundations for Microstrip Circuit Design*, John Wiley & Sons, New York, 1983.
11. Abuelma'atti, M. T., "An improved approximation to the microstrip line capacitance," *Int. J. Infrared Millimeter Waves*, Vol. 13, No. 11, 1795–1800, 1992.
12. Chow, Y. L. and W. C. Tang, "CAD formulas of integrated circuit components by fuzzy electromagnetics — Simplified formulation by rigorous derivation," *Proc. IEEE Antennas Prop. Soc. Int. Symp.*, 1566–1569, Salt Lake City, UT, July 2000.
13. Shapiro, A. A., M. L. Mecartney, and H. P. Lee, "A comparison of microstrip models to low temperature co-fired ceramic-silver microstrip measurements," *Microelectronics Journal*, No. 33, 443–447, 2002.
14. Kwok, S. K., K. F. Tsang, and Y. L. Chow, "A novel capacitance formula of the microstrip line using synthetic asymptote," *Microwave Optical Tech. Lett.*, Vol. 36, No. 5, 327–330, 2003.
15. Sadiku, M. N. O., S. M. Musa, and S. Nelatury, "Comparison of approximate formulas for the capacitance of microstrip line," *Proc. IEEE SoutheastCon*, 427–432, Richmond, VA, March 2007.

Spacecraft Power Systems Design to Minimize Electro Magnetic Interference (EMI) Effects

Krishna Shenai
Electrical and Computer Engineering Department, Utah State University, Logan, UT, USA

Abstract— The electrical power system in a spacecraft more or less determines the payload, spacecraft size, cost, operating life, and mission efficiency [1]. Hence, it represents the most critical part of the overall spacecraft architecture. Typical components in a spacecraft power system include the power source (a solar array), energy storage system (a battery), power distribution and control unit, power conversion and voltage regulation unit, and payloads as illustrated in Fig. 1. The output voltage derived from the power source is generally variable in nature. There is also a battery charging circuitry to ensure adequate energy storage capability to power the spacecraft at times when the power source is not available. Depending on the mission objectives, high DC as well as AC voltages and currents may be generated on-board from the power source. Consequently, electro-magnetic interference (EMI) and signal integrity are important design constraints.

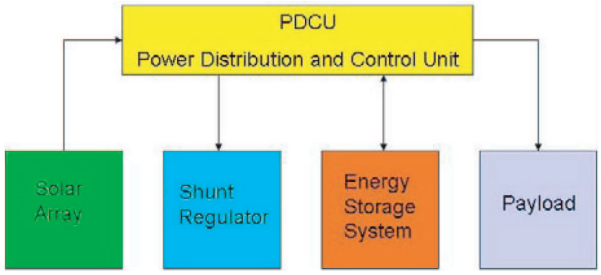

Figure 1: Block diagram of a spacecraft electrical power system.

The main objective in the design of a spacecraft electrical power system is two-fold. The first goal is the reduction of overall power consumption within the spacecraft so that minimum heat is dissipated, which in turn ensures minimal thermal management and cooling requirements, and improved reliability. This will guarantee prolonged operation of the mission and overall reduction of the payload. To reduce the overall power consumption, the spacecraft power system must be designed to obtain the highest power conversion efficiency under all loading conditions. The second consideration pertains to the overall reduction in size and weight of the spacecraft. To achieve this objective, the power system must be designed to operate at the highest power conversion frequency so that power passives and magnetics become small, thereby leading to an increase in power density [2]. The main problem here is that at higher power conversion frequencies, power system components become excessively lossy, and thereby result in increased on-board heating. Hence, a careful tradeoff in power density and power loss is needed to optimize the power system design [3].

The overall power loss in a spacecraft power system may be reduced by ensuring that the power conversion efficiency is at the highest under all loading conditions. Two approaches are used in spacecraft power systems as illustrated in Fig. 2 [4]. In either case, power loss reduction will require increased peak power efficiency and excellent load regulation. The efficiency may be increased by reducing the conduction power loss and the load regulation is improved by ensuring good power switching and control strategies. Further reduction in spacecraft power consumption can result from on-board power management of various loads. Spacecraft power management is in its infancy, and there is a great deal that can be done in this regard. Adaptive intelligent power management (AIPM) is a promising approach where the power system is capable of delivering on-demand efficient point-of-load power [5]. However, AIPM requires the ability to sense local power requirements within finite-state architecture and then delivering the right amount of power at the right time. Such advances are rapidly being accomplished in the commercial applications [6], and hence, tremendous opportunities to adapt AIPM in designing next generation spacecraft power systems exist.

The performance and reliability of the spacecraft power system critically hinges on minimizing application-level electro-thermal stresses [7]. The power system design and layout must be carried

out to minimize interconnect and package parasitic elements, including the parasitic resistances, capacitances and inductances. The circuit models used for various components (power switches, control electronics, resistors, inductors, capacitors, batteries, solar array, packaging, cooling, thermal management, and so on) must be accurate and physics-based. Such models are not generally available for space-qualified applications because they are technology-dependent. The component non-linearity, charge generation and storage within circuit components, and thermal problems further complicate the design of the spacecraft power system.

An increase in the spacecraft power density generally causes on-board EMI to increase. The spacecraft power system design must then account for EMI considerations in addition to conventional reliability issues pertaining to harsh environmental operation in space.

Past attempts to model the spacecraft electrical power system have generally neglected many of the effects described above, and hence, cannot be used to design reliable and compact power systems. These methodologies have been either circuit-oriented [8] or general purpose state-flow or signal-flow simulators [9]. A more recent approach focuses on a more integrative environment in a virtual test bed approach wherein some aspects of both methods have been applied [10]. However, the problem remains intact in that none of these approaches have the ability to design and model a spacecraft electrical power system to obtain the performance and reliability required. As a result, component specifications are severely de-rated to ensure power system reliability, thus causing significant performance penalty.

In the commercial arena, the SABER circuit simulator has become an industry-standard design tool in power system development [11]. It has the ability to perform a wide range of electrical, thermal and mechanical simulations and consists of state-of-the-art component models. The most important feature of SABER is its behavioral modeling and simulation capability using the MAST language. Component models and physical phenomena can be modeled using behavioral descriptions, thus allowing for tremendous flexibility in the design of complex circuits and systems. There is an opportunity to adapt SABER simulator to design and model advanced spacecraft power systems.

We have developed an approach to power management of devices within a power system that holds out the potential for significant reductions in power consumption. We will present a novel methodology for the design and modeling of next generation spacecraft electrical power systems. Our approach is unique and consists of the following essential elements. We have implemented advanced physics-based models for spacecraft power system components in SABER. We have developed an advanced integrated power system computer-aided design (CAD) infrastructure by integrating SABER simulation environment with two-dimensional (2-D) electromagnetic (EM) and semiconductor device simulation tools to facilitate circuit-level analysis and optimization of EMI, non-linear charge storage and parasitic effects. We will demonstrate the utility of the new simulation infrastructure to model and design compact and reliable spacecraft power systems. We will further demonstrate the flexibility and scalability of the new CAD infrastructure for application in large spacecraft power system design.

1. CORRECT-BY-DESIGN CAD ENHANCEMENT FOR EMI AND SIGNAL INTEGRITY

EMI filtering is an important application when it comes to modeling power electronic systems. Accurate EMI filter design based on the designed model will have a great impact of the overall system. Thus, it is necessary to review the status of EMI modeling and filter design of the modeled power device thoroughly. For example, the switching behavior of an IGBT in high-power circuits is the main source of EMI emission. Therefore, modeling of IGBT EMI behavior is a necessity to characterize and model conducted EMI emission. This can be done through time-domain and frequency-domain EMI emission modeling. A time domain modeling method is used to model EMI emission source in power sub-systems such as switches, resistors, inductors and capacitors. The advantage of modeling the EMI emission source in the time domain is the easiness to understand the EMI emission mechanisms of the system. Frequency domain modeling dominates in the Pulse Width Modulation (PWM) system. It turns the waveform into frequency domain by Fourier transformation. This type of modeling is essential for high frequency EMI noise emission, which is caused by the power circuit parasitics. The EMI phenomenon is a very complex concept. Therefore, building an accurate and practical EMI source model to achieve a proficient EMI filtering solution is the basis to attenuate the EMI noise in the power system [12].

With increased power density at high power switching frequencies in harsh-environmental space operating conditions, EMI and signal integrity become important design constraints. In particular,

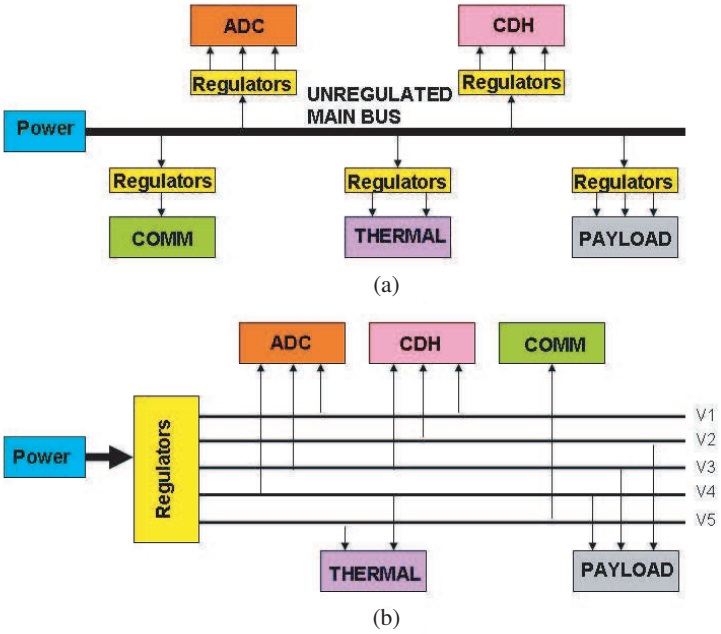

Figure 2: (a) Decentralized voltage regulation approach and (b) centralized voltage regulation approach used in spacecraft power systems.

voltage and current overshoots, charge storage, circuit di/dt and dv/dt, high-frequency impedance mismatch, and circuit and package parasitic pose serious challenges to long-term reliable operation of a power system, especially in harsh-environmental space applications. At present, there are no commercially available design tools that can account for these effects in electrical power system design [13–19].

We have implemented a novel approach to introduce models of these effects into SABER. The goal is to develop a correct-by-design methodology in which constraints on signal cross-talk and EMI are considered along with power switching in performing circuit floor-planning and routing. To perform topdown synthesis of reliable systems, we expand SABER modeling to include two additional parameters: EMI victim status and EMI point-source contributions. Three steps are followed to implement this technique. First, existing MAST language structural definitions are expanded to include an anticipated EMI contribution that can be referred to during architecture synthesis. Second, a component model file is enhanced with compact models of signal integrity and EMI to guarantee that the layout of a component meets its behavioral specifications. In this approach, system optimization proceeds in a top-down manner in which both functional performance and EMI levels are simultaneously considered. Third, our modeling methodologies and algorithms are validated using the Ansoft Maxwell tool suite for combined EMI field solving and interconnect extraction and equivalent circuit construction.

ANSOFT Maxwell is the leading electromagnetic (EM) design software for the simulation and analysis of high performance electromagnetic and electromechanical components that are widely used in the automotive, aerospace, and industrial applications. It can be considered as a virtual lab placed on a computer to study static, time-varying, and frequency-domain EM fields in a complex 3-D structure. It contains the following built-in simulators [20]:

- Transient: used for time-varying electromagnetic field.
- AC magnetic simulation: analyzes systems that have effects due to eddy currents, skin effect, and proximity effects.
- DC Magnetic: computes static magnetic field when the source is a DC source or a permanent magnet.
- Electric Field: computes static electric field due to applied potentials and stationary charge.
- Modeler: users can build libraries of geometric components to be reused in later designs.
- Dynamic Link (HFSS): To evaluate the radiation effects in low-frequency applications.

- Equivalent Circuit Generation: Automatic generation of DC magnetic and electrostatic field circuits.

Guarantees of EMI levels after physical layout are provided by making the software more savvy to signal coupling. A simple scalable interconnect model is introduced with parameters including routing width and spacing, path length and its resulting inductance, source and load impedance, switching frequency, and signal power. These techniques are established for PCBs but have yet to penetrate to power system design [21–25]. Since multi-layer interconnect produces extremely complex net-to-net coupling, part of our research seeks to define a minimal set of 3-D geometries that can be combined and permuted to provide 90% or better coverage of actual interconnect network geometries. The compact models are derived from and verified with 2- and 3-D field solvers from Ansoft Maxwell Eminence. An equivalent RLC network is produced, and a pad-like approximation used to replace a multi-pole response with a reduced-order network that matches the first "n" moments of the response, as shown in Fig. 3. This information presents to design tools a set of additional constraints; currently these tools seek only to optimize layout area, maximum (or matched) path length, a maximum number of jogs, and path width and spacing.

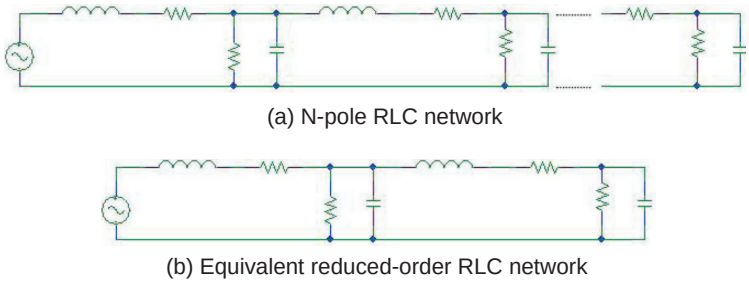

Figure 3: Compact interconnect modeling.

To prevent the placement and routing optimization analysis from becoming intractable, a net criticality factor is used to weight the optimization in favor of major signals or user selection. The factor is either user-specified or calculated from circuit schematic estimates of key critical paths. In this manner the complexity of the RLC networks can be scaled to match the importance of the signal with a significant improvement in memory requirements and analysis time. The EMI modeling task is a one-time effort that can be calibrated by a combination of two- and three-dimensional field solvers and measured data.

The compact models of EMI and signal integrity are combined with model parameters to define for each system component (e.g., in its MAST coding) its nominal EMI contribution and standard deviation. A large deviation accounts for complex components with multiple possible implementations; but simple components with limited implementations are represented with a small deviation. Depending on a component's complexity, its deviation can be reduced by exploring several possible block-level implementations (and their corresponding layouts) to derive more accurate bounds on the EMI. This EMI specification process is similar to that of defining signal delay or power characteristics in a component behavioral code. The EMI intensity is related to signal di/dt, with tolerances for signal inductance also specified and used to further guide the layout tools in ensuring EMI limits are met. Library preparation is a one-time procedure that follows a bottom-up methodology for introducing additional physical characteristics into a component definition.

Power system optimization progresses from a top-down specification of EM1 requirements and a functional definition. An iterative refinement is possible based on the nominal EMI values associated with each block. This process is illustrated in Fig. 4.

Beginning from system-level requirements for EMI, the architectural definitions are synthesized into a block definition (similar to the standard synthesis of hardware behavioral code into a structural format). Blocks are selected, in addition to their functional definition, on their ability to meet EMI limits and their deviation.

An overall system EMI level is obtained from a statistical addition of the contributions from all synthesized blocks, and a system confidence value rates how probably the physical implementation can meet the predicted goals. Potential EM1 violations are reported at this time.

We do not develop CAD GUI code. Instead we exploit, whenever possible, the existing graphical output capabilities of commercial placement and route tools. Since no tool currently provides

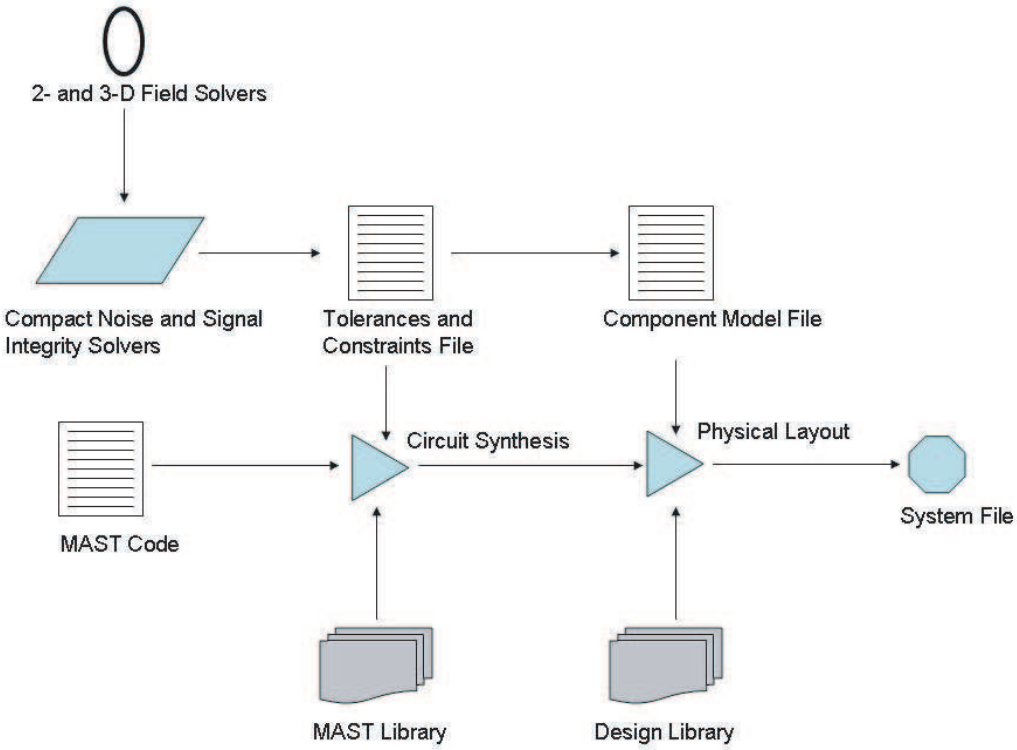

Figure 4: System synthesis flowchart showing modeling and library input to ensure correct-by-design CAD methodology.

detailed optimization techniques for RLC or EMI, we adapt displays of parasitic RC to also include L.

The information is encoded in modified SDF and SPF files. These can be compared offline with standard SDF and SPF tiles to observe the effects of the full RLC/EMI models. We are also developing C-code postprocessor to reduce network dependencies by pruning insignificant coupling as compared to a userspecified threshold value.

Based on system-level requirements, a weight is attached to each block indicating the relative importance of its meeting the target EMI goals. A heavily weighted block is one that is critical to functional performance, at the edge of its deviation, or significantly more complex than other blocks.

System optimization is an iterative and repeatable task in which various block-level or component-level implementations can be investigated to explore the resulting functional performance or EMI levels. Our approach is to enable several sample system syntheses to validate the EMI optimization approach and its accuracy.

Victim blocks are separated from strong aggressors while simultaneously balancing the resulting average signal path lengths. After placement has been completed, automated routing is responsible for meeting the specified EMI ratings.

Beginning with heavily weighted signals, assignments to routing channels are made, and, on a per-net basis, a path width and length (or inductance), and separation are determined. Variable-geometry routing ensures that signal integrity can be met and that signal propagation delay can be tuned.

Final routing is completed by exploding the channels, again favoring the heavily weighted nets, and producing path lengths that minimize signal reflections.

REFERENCES

1. Cassineli, J., et al., "Analytical modeling of spacecraft power system," TRW, Redondo Beach, CA, Final Report to NASA GSFC, 1982.

2. Shenai, K., "Potential impact of emerging semiconductor technologies on advanced power electronic systems," *IEEE Electron Device Lett.*, Vol. 11, No. 11, 520–522, November 1990.
3. Shenai, K., P. G. Neudeck, and G. Schwarze, "Design and technology of compact high-power converters," *IEEE Aerospace and Electronic Systems Magazine*, Vol. 16, Issue 3, 27–31, March 2001 (invited).
4. Yousef, H., "Power management and distribution for future spacecraft," Fountain Valley, California, Available: http://ieeexplore.ieee.org/iel5/852/2490/00074522.pdf?arnumber=74522.
5. Shenai, K., featured in *Semiconductor Innovation Letter*, 1, 17 March, 2002.
6. MAX2291 Power Amplifier with Variable VCC from MAX8506 Switching Regulator, Maxim Integrated Products, Inc., Sunnyvale, CA.
7. Shenai, K., "Made-to-order power electronics," *IEEE Spectrum*, Vol. 37, No. 7, 50–55, July 2000 (invited).
8. Nelms, R. M., B. W. Evans, and L. L. Grigsby, "Simulation of AC spacecraft power systems," *IEEE Trans. Industrial Electronics*, Vol. 36, No. 3, 398–402, Aug. 1989.
9. Cho, B. H. and F. C. Y. Lee, "Modeling and analysis of spacecraft power systems," *IEEE Trans. Power Electronics*, Vol. 3, No. 1, 44–54, Jan. 1988.
10. Jhang, Z., S. Liu, and R. A. Dougal, "Design and testing of spacecraft power systems using VTB," *IEEE Trans. Aerospace and Electronic Systems*, Vol. 39, No. 3, 976–989, July 2003.
11. Synopsys Inc., http://www.synopsys.com/products/mixedsignal/saber/saber.html.
12. Liu, Q., W. Shen, F. Wang, D. Borojevich, and V. Stefanovic, *Power Electronics and Motion Control Conference, IPEMC 2004*, Vol. 3, 1515–1520, 14–16 Aug., 2004.
13. Maksimovic, D., A. M. Stankovic, V. J. Thottuvelil, and G. C. Varghese, "Modeling and simulation of power electronic converters," *Proc. IEEE*, Vol. 89, No. 6, 898–912, June 2001.
14. Anagram, Inc., www.anagraminc.com.
15. Avanti, Inc., www.avanticorp.com.
16. Cadence Design Systems, Inc., www.cadence.com.
17. High Level Design Systems, Inc., www.hlds.com.
18. Mentor Graphics, Inc., www.mentorg.com.
19. Saha, P. K. and J. Dowling, "Reliable prediction of EM radiation from a PCB at the design stage of electronic equipment," *IEEE Trans. EMC*, Vol. 40, No. 2, 166–173, 1998.
20. ANSOFT Corporation: http://www.ansoft.com/products/em/max3d/overview.cfm?&vflash=y.
21. Hjellen, G. A., "Including dielectric loss in printed circuit models for improve EdM I/EMC protection," *IEEE Trans. EMC*, Vol. 39, No. 3, 236–246, 1997.
22. Cerri, G., R. DeLeo, and V. M. Primiani, "A rigorous model for radiated emission prediction in PCB circuits," *IEEE Trans. EMC*, Vol. 35, No. l, 102–108, 1993.
23. Ingels, M. and M. S. J. Steyaert, "Design strategies and decoupling techniques for reducing the effects of electrical interference in mixed-mode," *IEEE J. Solid-state Circuits*, Vol. 32, No. 7, 1136–1141, 1997.
24. Verghese, N. K., D. J. Allstot, and M. A. Wolfe, "Verification techniques for substrate coupling and their application to mixed-signal IC design," *IEEE J. Solid-state Circuits*, Vol. 31, No. 3, 354–365, 1996.
25. Mohan, N., T. M. Undeland, and W. P. Robbins, *Power Electronics: Converters, Applications, and Design*, 2nd ed., John Wiley & Sons, 1995.

Intertwined Two-section Dual-polarized Log Periodic Dipole Antenna

A. Tran and M. C. E. Yagoub
School of Information Technology and Engineering, University of Ottawa
800 King Edward, Ottawa, ON K1N 6N5, Canada

Abstract— In this paper, we investigate the double-section (orthogonally intertwined) printed dual-polarized log periodic dipole antenna (LPDA) within the frequency band from 0.8 GHz to 2 GHz. Dual-polarized wideband antenna is often used in spherical antenna measurement systems where the measurement antennas are desired to transmit and receive alternatively in both vertical and horizontal polarizations. The antenna was designed using Ansoft-HFSS and then fabricated on Rogers RT/Duroid 5880 substrate. Measured results show a very high cross-polarization discrimination (< -35 dB) at boresight ($\theta = 0$).

1. INTRODUCTION

The design for the broadband dual-polarized antenna is motivated by the need for a measurement antenna for spherical antenna-measurement systems. In all spherical measurement systems, the positioning system can often rotate on both axis (φ and θ) to measure and generate spherical data tables and radiation pattern plots in 3D. Often the total radiated power (TRP) and total isotropic sensitivity (TIS) are the required figures of merit. The TRP calculation involves the discrete integration of the measured radiated power due to E_θ and E_φ. To reduce the measurement time inside the anechoic chamber, it is highly desirable to have a measurement antenna that can be electronically switched to transmit and receive both field polarizations. Traditionally, the measurement antenna are mechanically rotated for each polarization, making the test twice as long, and increase the possibility of measurement uncertainty due to variation in the positioning of not only the antennas but also of the mechanical support. Dual polarized dipoles have been used to achieve dual polarization [1]. Cross-polarization isolation of at least 20 dB can be achieved with these dual dipoles. However, as the frequency gets higher (over 5.2 GHz), the dipoles are very short (length less than 2 cm) and become more difficult to construct. Also, dipoles are inherently narrow-band; therefore it is preferable to replace them with a broadband dual-polarized antenna. The dipole array antenna is a well known broadband printed antenna. This paper presents our investigation of an original idea of orthogonally intertwining two sections of two printed log-periodic dipole antenna (LPDA) to achieve dual-polarization.

2. DESIGN AND MODELING

Log-periodic antennas are generally seen as well suited structures for the design of antenna modules with theoretically frequency independent transmission characteristics [2]. The operation of the LPDA antenna itself has been well studied. Interested readers are referred to the books by Kraus [3], and Balanis [4], which provide detail descriptions of the LPDA and its design procedure. LPDA structures consist of a certain elementary geometry that is periodically repeated, scaled by a factor τ. Practical bandwidths have been reported in [5] to be 20 : 1 for log periodic antenna structures. Each arm is a half wave-length dipole. The center conductor is designed to have a 50-Ω-characteristic-impedance.

To achieve the dual polarization, a printed horizontal and a printed vertical LPDA are arranged into an orthogonal set of two antennas. The two orthogonal sections are orthogonally intertwined with each other. When one section of the antenna is transmitting or receiving, the cross-polarized section can be conveniently activated and deactivated using an RF switch. The arrangement of the array is such that it is almost symmetric around its axis. A few advantages can be seen from this arrangement. First, the phase center of the array will practically be on the arrays axis regardless of which polarization is activated. Second, due to symmetry, the effect of the enabled element on the deactivated (cross-polarized) element is expected to be minimal. It is expected that some cross-coupling will occur due to proximity of the two elements. To minimize the cross coupling between the cross-polarized elements, dielectric septum might be inserted between the two sections. This aspect will be investigated in the near feature. In the event the two orthogonal pairs of antenna dipole arms introduce low cross-polarization coupling, the use of this antenna

will permit to save a considerable amount of measurement time without significantly reducing the antenna's gain. Simulation results for impedance and radiation patterns were derived by 3D Finite-Element-Method simulations using the commercial software Ansoft-HFSS.

In order to verify the simulation results, the optimized log periodic antenna was fabricated on Rogers RT/Duroid 5880 substrate ($\varepsilon_r = 2.2$) and thickness 1.57 mm and fed by semi-rigid 50 Ohm braided coax cables. One side of the fabricated antenna was then partially cut-out so that two similar LPDA can be intertwined. To observe the effect of the removed part of the substrate, the return-loss before (pre-cut) and after (post-cut) were measured. The antenna radiation patterns were measured in an anechoic chamber at 2 GHz.

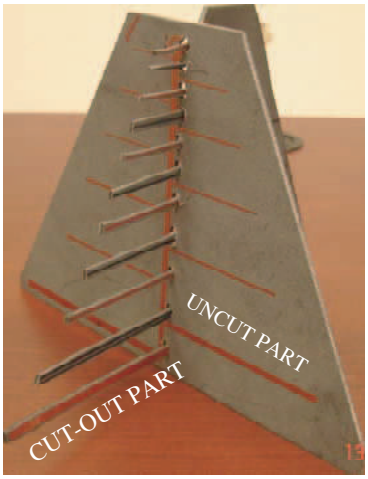

Figure 1: Double-section intertwined LPDA (height: 11 cm, width: 15 cm).

3. SIMULATION AND TEST RESULTS

The input return-losses of the antenna obtained from EM simulation and measurements are given in Figure 2, where the antenna is matched to a 50 Ω input impedance. The figure indicates that after removing part of the substrate, the return-loss remains nearly the same except at frequencies towards the end of the band. The right side of Figure 2 presents both the simulated and measured S11 magnitudes of the optimized antenna. Compared to the simulation, the return-loss of the measured prototype antenna decreases slightly.

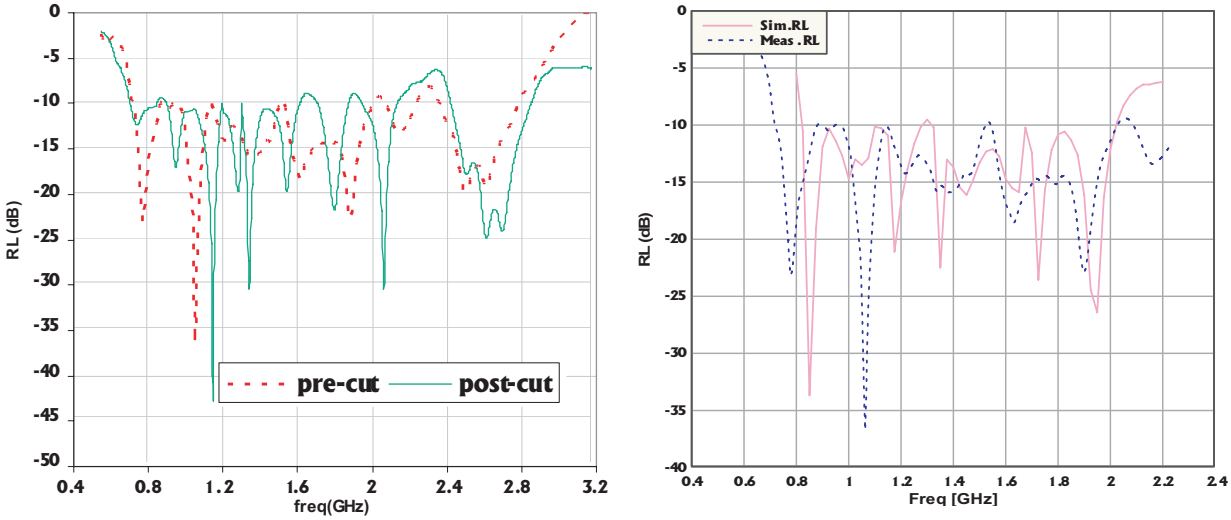

Figure 2: Left: Return loss with substrate-pre-cut vs. post-cut. Right: Simulated vs. measured of the final antenna.

The double-section LPDA radiation patterns in the elevation plane for an excitation at various θ-angles are depicted in Figure 3 at the frequency of 2 GHz. Figure 4 shows the pattern in the

azimuth plane. The antenna gain was about 3.3 dB. Early results show that the double-section LPDA maximum gain is about 3.4 dB lower than the single-section LPDA. This problem is believed to be caused by the coupling with the cross-polarized section of the antenna. Separating the two sections with a dielectric septum might reduce this coupling.

As shown Figure 3, the radiation pattern shows a maximum at boresight (at angular position of $\theta = 0°$) with a half-power beamwidth of 80°. The measured radiation pattern shows the cross-polarization discrimination level is 15 dB at angle less than 45° from boresight. The cross-polarization discrimination level increases to at least 35 dB as one approaches boresight.

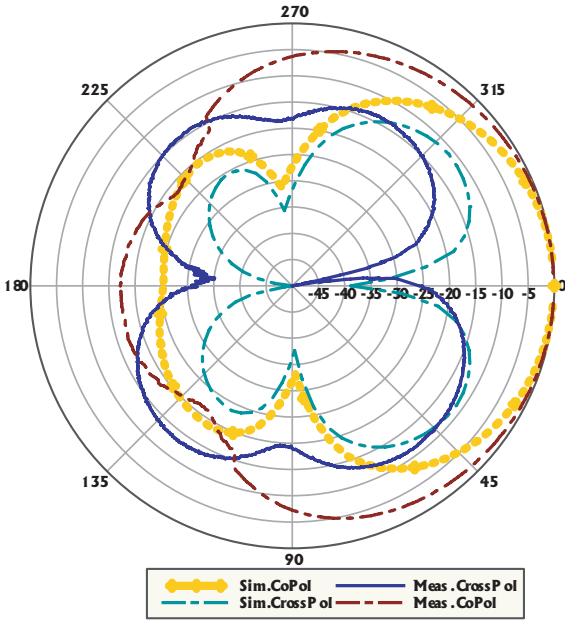

Figure 3: Measured and simulated radiation patterns of the double-section LPDA in the Elevation plane.

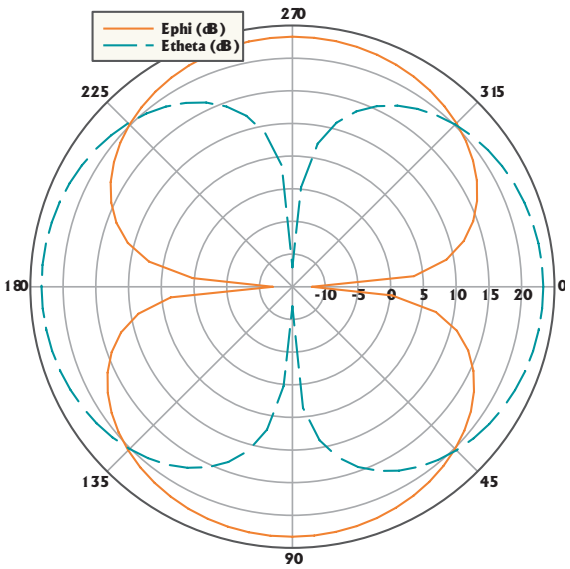

Figure 4: Simulated radiation patterns of the double-section LPDA in the Azimuth plane.

4. CONCLUSIONS

In this article, an orthogonally intertwined dual-polarized log periodic antenna was designed and tested. This antenna is intended to be used in spherical antenna measurement systems where the measurement antennas are desired to transmit and receive alternatively in both vertical and

horizontal polarizations. Input return loss measurements from the fabricated antenna agree well with simulated results. The fabricated antenna shows a cross-polarization discrimination of at least 35 dB at boresight. Further study of the coupling between the two sections and methods to reduce it will be object of another investigation and will be reported in the near future.

ACKNOWLEDGMENT

We would like to thank Mr. A. Lehenaff for his assistant in the fabrication of the antennas.

REFERENCES

1. Liu, Y., A. T. Bu, E. S. Li, D. M. Fu, and L. Y. Xiao, "A new dual polarization dipole antenna," *ICMMT 4th International Conference on Microwave and Millimeter Wave Technology 2004, Proceedings*, 5–7, 18–21 Aug., 2004.
2. DuHamel, R. H. and D. E. Isbell, "Broadband logarithmically periodic antenna structures," *IRE International Convention Record*, Vol. 5, 119–128, 1957.
3. Kraus, J. D., *Antennas*, 703–710, 2nd Ed., McGraw-Hill, New York, 1988.
4. Balanis, C. A, *Antenna Theory Analysis and Design*, 413–444, Harper & Row, New-York, 1982.
5. Mayes, P. E., "Frequency-independent antennas and broadband derivatives thereof," *Proc. IEEE*, Vol. 80, 103–112, Jan. 1992.

A Complete Simulation of a Radiated Emission Test according to IEC 61000-4-20

X. T. I Ngu, **A. Nothofer**, **D. W. P. Thomas**, **and C. Christopoulos**
University of Nottingham, United Kingdom

Abstract— In a radiated emission test according to IEC 61000-4-20 the radiated power of the equipment under test (EUT) is calculated from three measurements. The algorithm used to calculate this power assumes the EUT to be electrically small and have the radiation characteristics of a set of dipoles. Since this assumption is not always valid, the calculated radiated power by this method may be different from the total power radiated by the EUT. This work presents a complete simulation of a radiated emission test according to IEC 61000-4-20 using the TLM method. This is then compared to the total radiated power of the EUT in free space, space above ground plane and in the GTEM cell numerically. The differences in these power values are analyzed to predict a contribution to the uncertainty budget of the radiated emission test.

1. INTRODUCTION

IEC 61000-4-20 [1] describes radiated emission measurements using a Transverse Electromagnetic (TEM) or Gigahertz Transverse Electromagnetic (GTEM) waveguide. To perform this test, the equipment under test (EUT) is placed inside the cell in three orientations and the voltages at the cell port are measured. From these three voltages, the power radiated by the EUT is calculated. To enable comparison to the Open Area Test Site (OATS) or a Fully Anechoic Chamber (FAC), the maximum field strength generated by the calculated power is determined above a ground plane and in free space respectively.

This work is fully a numerical study where Transmission Line (TLM) [2] simulation method is used. A complete GTEM TLM model is created to study the errors and the construction of the TLM model is explained in Section 2. This paper presents a full 3D TLM simulation of three orientations radiated emissions test according to IEC 61000-4-20. The power radiated by the EUT is then calculated from the three voltages. This is described in Section 3. The total radiated power of the EUT in free space and above a ground plane is determined in separate simulations. In addition, the total radiated power of the EUT inside the GTEM cell is simulated. These simulations are described in Section 4. In Section 5, the results are presented and all these values for the radiated power are compared and the electric field strength that this power would produce is included for each scenario. These preliminary results will help EMC engineers establish an uncertainty budget in their measurements, since the difference in the calculated field strength is an indicator for the potential error caused by the correlation method described in IEC 61000-4-20.

2. GTEM TLM MODEL

An important aspect in this work is the GTEM TLM model. A complete detail of the GTEM TLM model is explained in [3]; however some details will be outlined here. The TLM simulation involves the generation of a comprehensive simulation code to represent the geometry of the GTEM model. In this code, the cells in the TLM meshes were arranged as closely as possible to represent the real GTEM cell geometry. Each component in the GTEM model was constructed by joining cell by cell in three-dimensions. Model construction was based on GTEM 5407 manufactured by ETSI Lindgren, USA. An important feature that was included in the modeling of GTEM cell is the inclusive of a realistic sized pyramidal RAM model which has not been reported in other previous numerical models. To increase accuracy, we employ a large mesh in excess of 14 million ($224 \times 156 \times 417$) cells and one round of simulation took 70 hours to complete. We kept well within the $\lambda/10$ limit and also checked that staircasing errors are negligible. This model is fully electrically tested to comply with 50 ohm characteristic impedance.

3. IEC 61000-4-20 GTEM MEASUREMENT

Various GTEM to OATS correlation algorithm [4–8] have been produced over the years. This paper concentrates on the correlation algorithm that is used in the IEC 61000-4-20 standard. Any source of radiation can be replaced by an equivalent multipole expansion which should result in the same radiation pattern and same power outside a volume enclosing the source. Once these multiple

moments are known, the radiation both in free space and over a ground plane can be calculated. The method specified in the standards is the three-measurement method. This three-measurement method requires three major orientations of an EUT inside the GTEM cell shown in Figure 1. In each orientation, the voltage at the cell port is measured. Based on these three voltages, the radiated power of the EUT, and from there the electric field over a ground plane, representing the correlation to OATS, can be calculated. In a similar way, the maximum field at a point in free space can also be calculated, representing the correlation to a fully anechoic chamber.

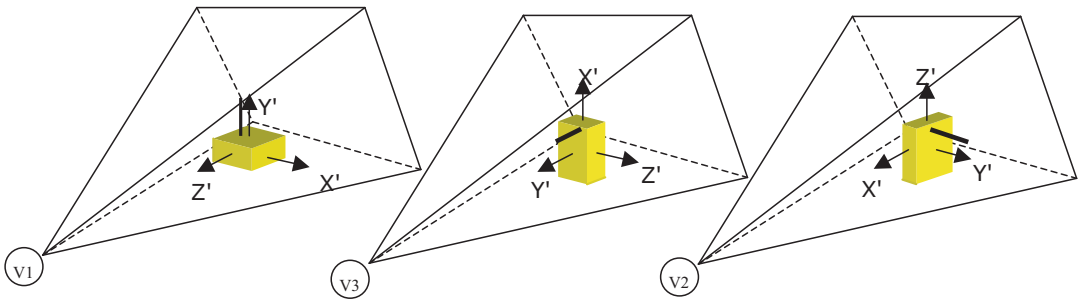

(a) (b) (c)

Figure 1: EUT in the (a) first orientation (b) second orientation and (c) third orientation.

4. TOTAL RADIATED POWER

Three different environments were considered in this work. These are inside the GTEM cell environment, free space and space above a ground plane. In this work, a realistic model of an EUT is represented by a monopole sitting on the top of a metal box shown Figure 2. The metal box itself is a $29 \times 29 \times 11$ cm perfect electric conductor (PEC) with a 19 cm monopole sitting on top of the metal box. The monopole is located 12 cm from the center point of the top of the box. The method used is based on the simulation of the total radiated power [9] where a surface of a rectangular structure can be defined over a certain volume to give the total power passing through the assigned surface with the EUT within the volume shown in Figure 2. The purpose is to examine how this power changes in different environments. The frequency chosen for this work is 200 MHz. The input power for all the simulation setups was equally set to $0.02\,V_{peak}$.

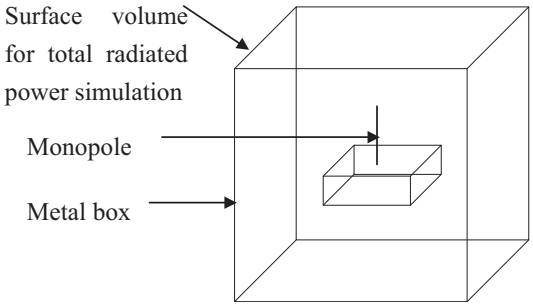

Figure 2: Total radiated power by the EUT in a volume enclosing the EUT.

4.1. Free Space Radiation

The radiation from the EUT is simulated in a free space environment. This result serves as a control to examine the actual total power radiated by the EUT itself without taking reflections into account. The result from this simulation can be used to calculate the maximum electric field E_{max} for later comparison with the other two environments. This method simulates an EMC test performed using full anechoic chamber.

4.2. Space Radiation over the Ground Plane

The EUT is then placed over a ground plane to simulate an EMC test performed using OATS. The total power radiated in this method takes the reflection by the image dipole introduced by the ground plane into account. The maximum electric field E_{max} can also be calculated from the simulated result of this setup and later served as a comparison for results obtained from the GTEM to OATS correlation algorithm stated in IEC 61000-4-20.

4.3. Radiation inside the GTEM Cell

The radiation inside the GTEM cell is the main observation in this paper. For this, the EUT is placed inside the GTEM cell. In contrast to the other two methods mentioned above, the GTEM cell has unique characteristics in that it ideally only couples to the TEM modes. In addition, at the lower frequencies, the structure of the GTEM is within the near field of the EUT and this may alter the characteristics of the EUT. This is different from the simulation in Section 4 Part A and B because the total power radiated by the EUT inside the GTEM cell is not simulated over an enclosing surface, but it is calculated from the three voltages simulated from three orientations according to IEC 61000-4-20 as described in Section 3.

5. SIMULATION RESULTS AND COMPARISON

Table 1 shows the comparison values of the different total radiated power in the different environments at 200 MHz. The EUT in free space has the lowest total radiated power compared to the EUT above a ground plane and also inside the GTEM cell. From Table 1 it can also be seen that the total power calculated from the three voltages from three respective orientations was greater than the total power radiated in the free space by the EUT. The comparison of various values of E_{max} for vertical and horizontal polarizations calculated from the total radiated power in different environments is shown in Table 2 and Table 3. They show the maximum electric field strength at a distance of 3 m between the EUT and the antenna. For Table 2 the field strength was calculated above a ground plane representing OATS, and for Table 3 it was calculated in free space representing FAC. Table 4 shows the value of the total radiated power in the different environments when the above simulations were repeated using higher frequency such as 1 GHz in this case. In such case, the EUT was considered to be electrically large. Interestingly, at higher frequency, the radiated power predicted from the three voltages method seemed to underestimate the total radiated power obtained from other environments.

Table 1: Comparison of total radiated in different environments at 200 MHz.

Environments	**Total radiated power (W)**
Calculated from three simulated voltages	3.324×10^{-7}
In free space	2.902×10^{-7}
In space above a ground plane	3.178×10^{-7}

Table 2: Comparison of maximum electric field E_{max} in OATS calculated from total radiated power in different environments at 200 MHz.

Total radiated power environments	**E_{max} Horizontal (V/m)**	**E_{max} Vertical (V/m)**
Three simulated voltages	2.313×10^{-3}	1.589×10^{-3}
Space above a ground plane	2.261×10^{-3}	1.554×10^{-3}

Table 3: Comparison of maximum electric field E_{max} in FAC calculated from total radiated power in different environments at 200 MHz.

Total radiated power environments	**E_{max} Horizontal (V/m)**	**E_{max} Vertical (V/m)**
Three simulated voltages	1.730×10^{-3}	1.557×10^{-3}
Free space	1.691×10^{-3}	1.522×10^{-3}

Table 4: Comparison of total radiated in different environments at 1 GHz.

Environments	**Total radiated power (W)**
Calculated from three simulated voltages	1.243×10^{-7}
In free space	1.784×10^{-6}
In space above a ground plane	1.787×10^{-6}

6. CONCLUSION

Various references in the literature such as [10] and [11] present examples for uncertainty budgets in measurements done using a GTEM cell. The uncertainties may be due to mismatch to instrument errors and poor repeatability. However, most uncertainties reported are easily distributed to instrument errors, cable loss, EUT orientations, impedance matching and so forth. These uncertainties are well defined with a high level of confidence since they are parameters that can be measured and observed easily. However, the GTEM to OATS correlation is one particular uncertainty which is hard to determine during experiments since it is difficult to isolate the other uncertainties. We have shown here a method to define the contribution to the uncertainty budget due to the GTEM to OATS correlation. Simulation work could omit various parameters in real measurements, thus a particular uncertainty could be examined effectively which is the GTEM to OATS correlation in this case. The results gathered in this work would be useful in future examples of uncertainty budget calculations for the GTEM to OATS correlation.

In this work, we have shown that the algorithm based on IEC 61000-4-20 for correlating three voltages from the three position method seems to agree reasonably well compared to the free space and above ground plane environment but, it over-predicts the total power radiated from EUT. However, at higher a frequency approaching 1 GHz in our case, the total power radiated obtained from the prediction based on the three voltage method seriously underestimated compared to other environments. The algorithm stated in IEC 61000-4-20 is ideal for the case when the EUT consists of a dipole antenna. The EUT chosen in this work is not a dipole on purpose in order to demonstrate the accuracy of the algorithm when the EUT is not a dipole. It appears that the differences cannot be simply due to normal random errors and more likely are due to systematic factors. The preliminary results shown here justify a further investigation to establish the origin of the differences and if possible eliminate them. One possible reason for the observed discrepancies is the omission of the phase information or the propagation of higher order modes, which at higher frequencies are likely to play a greater part. We hope to be able to report in more detail in the future on work in progress to quantify the impact of phase [12] on these measurements.

Another interesting aspect of this work is the importance of using TLM in examining problems in EMC world. The GTEM TLM model in this work was delicately created using 3-D square mesh and has been proven to have high accuracy and useful in the characterization of emission in GTEM cell.

REFERENCES

1. IEC 61000-4-20, Electromagnetic Compatibility (EMC) — Part 4: Testing and measurement techniques, Section 20: Emission and immunity testing in transverse electromagnetic (TEM) waveguides, International Electrotechnical Commission, Geneva, Switzerland, 2003.
2. Christopoulos, C., *The Transmission Line Modeling Method TLM*, IEEE Press, Piscataway, NJ, 1995.
3. Ngu, X. T. I., A. Nothofer, D. W. P. Thomas, and C. Christopoulos, "A complete model for simulating magnitude and phase of emissions from a DUT placed inside a GTEM cell," to appear in *IEEE Transaction on Electromagnetic Compatibility*.
4. Lee, A.-K., "An algorithm for an advanced GTEM to ground plane correlation of radiated emission tests", *IEEE Symposium on Electromagnetic Compatibility*, 58–62, Santa Clara, CA, August 1996.
5. Osburn, J. D. M. and E. L. Bronaugh, "Advances in GTEM to OATS correlation models," *IEEE Symposium on Electromagnetic Compatibility*, 95–98, Dallas, TX, August 1993.
6. Thelberg, M. J., "GTEM to OATS emission correlation 1–5 GHz," Technical report, Chalmers University of Technology, Gothenburg, Sweden, 1993.
7. Thelberg, M. J., E. L. Bronaugh, and J. D. M. Osburn, "GTEM to OATS emission correlation 1–5 GHz," *IEEE International Symposium on Electromagnetic Compatibility*, 387–392, Chicago, IL, August 1994.
8. Wilson, P., "On correlating TEM cell and OATS emission measurements," *IEEE Transaction on Electromagnetic Compatibility*, Vol. EMC-37, 1–16, February 1995.
9. Paul, J., C. Christopoulos, and D. W. P. Thomas, "A 3D time domain TLM electromagnetic field solver regSolve.cc," *Regsolve Manual*, Electromagnetics Research Group, School of Electrical and Electronic Engineering, University of Nottingham.

10. Nothofer, A., D. Bozec, A. Marvin, M. Alexander, and L. McCormack, "The use of GTEM cells for EMC measurements", *Measurement Good Practice Guide*, No. 65, National Physical Laboratory, York EMC Services Ltd, UK, 2003.
11. Harrington, T. E. and E. L. Bronaugh, "EUT directivity and other uncertainty considerations for GHz-range use of TEM waveguides," *IEEE International Symposium on Electromagnetic Compatibility*, 117–122, Vol. 1, Montreal, QUE, August 2001.
12. Ngu, X. T. I., A. Nothofer, D. W. P. Thomas, and C. Christopoulos, "The impact of phase in GTEM and TEM emission measurements," *EMC Europe International Symposium on Electromagnetic Compatibility*, Barcelona, September 2006.

Design and Modeling of Planar Power Switching Inductors for Monolithic and Single Chip DC-DC Power Converters

Mohamad Hamoui and Krishna Shenai
Microsystems Design Laboratory
Department of Electrical and Computer Engineering
Utah State University Logan, UT, 84322, USA

Abstract— Engineers are continuously trying to integrate active circuit components of dc-dc converters on chip, while leaving behind the passive components because of their limited capabilities under small-scale integration. This document describes several key issues and design considerations relating to dc-dc converters under high frequencies. Inductor modeling and design of a buck converter are investigated, and a performance plot of the inductor under high switching frequency is presented.

1. INTRODUCTION

As handheld electronic hardware become smaller in size, higher demands for low voltage operation and high output current are becoming a necessity. The main unit in portable devices responsible for such functionality is the dc-dc converter. This means that the converter should maintain high efficiency in order to achieve a longer battery life, while shrinking it to fit on a smaller silicon die. The key to achieve full integration, which will reduce size and cost, is to operate these converters at high frequencies, typically greater than 5 MHz, while maintaining the required specs.

High switching frequency is becoming essential to achieve designs that are required for next generation handheld electronics. An engineer has to understand the high frequency design constraints and their issues before initiating the step to design a high switch mode converter [1]. The system description, design philosophy, and key issues of operating the buck dc-dc converter under high frequency are presented in section II. Inductor equivalent circuit, modeling, and operation under high switching frequency are included in section III. In Section IV performance plot of the Inductor as the operating frequency increases is reported. Operating at high frequency will allow the engineer to integrate the passive components of the converter along with the active components to achieve a single chip dc-dc converter.

2. CIRCUIT DESCRITON

The circuit schematic of a buck dc-dc converter is shown in Fig. 1. In this converter topology, when M1 turns on, the input voltage will be applied on the left side of the inductor. Thus, the input voltage will induce current through the inductor and will cause the current of the inductor to rise. When M1 turns off and M2 turns on, a closed loop consisting of the transistor M2, the inductor, and the capacitor will be formed and the inductor current will decrease as the off time increases. The main essential parameter in designing dc-dc converters is efficiency. This means that the converter should perform the same along the full load range. Usually the best efficiency is achieved at maximum load, which corresponds to maximum current supplied. However, the engineer faces a huge difficulty in maintaining a high efficiency at low load operation. Different techniques such as PFM, which skips pulses generated by the control circuitry, have been developed to maintain the required efficiency. Nevertheless, this degrades the converter stability and puts it at the risk of failure under extreme conditions. Also, this defeats the purpose of operating the converter at high frequencies. In the end, the ultimate goal is to operate these converters at high frequencies in order to integrate the whole unit on a single chip.

Method and design approaches for a high frequency dc-dc converter operating in the range of 100 MHz have been reported [2]. However, the suggested design approach is not economical, since the bill of materials of the components needed is enormous. Thus, it is not feasible in industrial applications where cost is the main driving element. In general, one needs to operate at high frequency while marinating the same number of components and reducing their respective sizes, which eventually reduces the overall cost. A problem arises, however, by keeping the same number of components and increasing the switching frequency. [3] analyzes the main problems associated with high frequency operation. A high frequency parasitic model of the boost dc-dc converter has been studied. It has been reported that parasitic resistances, inductances, and capacitances

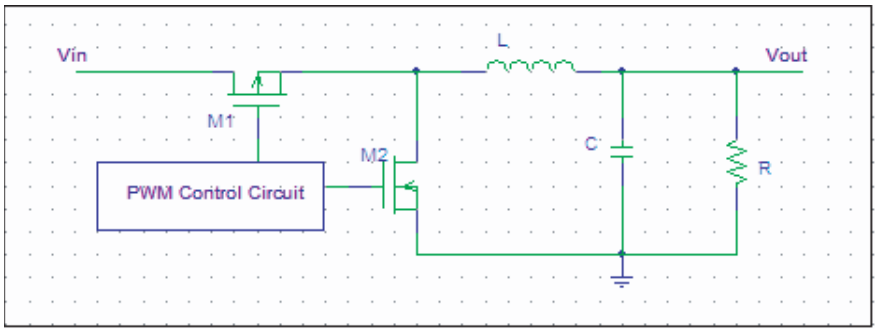

Figure 1: A buck dc-dc converter.

generated from packaging and interconnections of the converter arises at high frequencies. All these components will aid in degrading the converter efficiency. Thus, new packaging techniques should be introduced to overcome this major obstacle.

3. INDUCTOR MODELING

The inductor is the largest component in a dc-dc converter. Thus, innovative ideas of how to integrate the inductor on chip are necessary for achieving a miniaturized dc-dc converter. This is achieved by investigating the consequences of having a small inductor operating at a high frequency, and by modeling the inductor and its behavior under high frequency. Fig. 2 shows the equivalent circuit of an inductor at a frequency above 5 MHz.

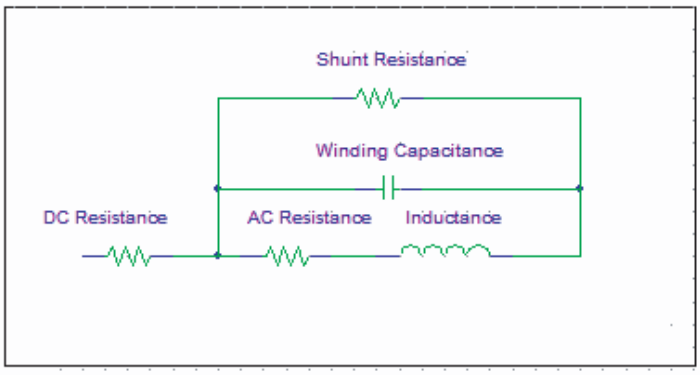

Figure 2: Inductor equivalent circuit.

The inductor in Fig. 2 consists of many frequency dependent elements: the AC resistance, the Inductance, and the shunt resistance. [1] illustrates that for small valued inductors, the resonance frequency occurs in the range of few GHz. This will ease defining the corner frequency of the LC filter in the converter when designing it. However, as shown in Fig. 2 above, the engineer should take into consideration the nonideality of the inductor under high frequency. One advantage of high frequency operation is that it allows reducing the size of the inductor, which will need less turns ratio which reduce resistive losses. Also, this will enable a faster dynamic response due to the wide bandwidth introduced in the control feedback circuit. The main problem with a smaller inductor is that the average rms current of the transistor switch will increase, and this will increase the conduction losses. This is because the peak-current rating of the inductor will increase, and this will force us to keep a large capacitor at the output. The Enpirion, EN5312QI 1A synchronous buck regulator, have achieved an integrated Inductor but on a separate die brought close to the converter's active circuitry die because of interference issues [1]. However, it was necessary to keep the capacitor as large as possible to eliminate voltage ripples at the output. Various methods and techniques on integrating the inductor on chip was studied in [4]. It was found that to minimize the AC resistance of the inductor at a high frequency range up to 10 MHz can be achieved by using "outof- plane" inductors constructed using PDMA. "The PDMA technology would have a smaller footprint and probably higher quality." [4].

4. HIGH FREQUENCY INDUCTOR PERFORMANCE

The power inductor in a commercial semiconductor process is designed using ANSOFT microwave modeling package including all of the electrical and thermal effects. The 3D HFSS model for the inductor designed is shown in Fig. 3. Fig. 4 illustrates a typical performance of the inductor at RF frequency. Inductors with values in excess of 100 nH capable of handling more than 1A current have been designed with a Q value of 40.

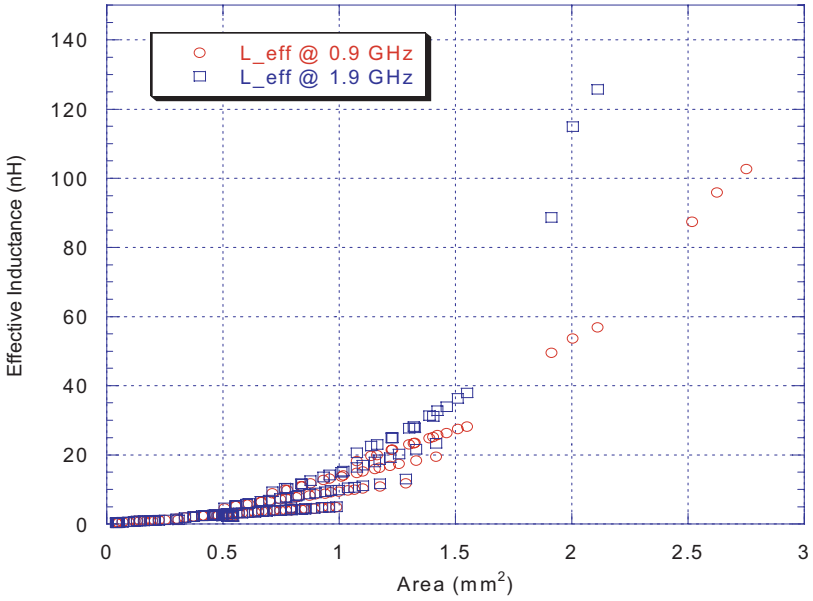

Figure 3: Inductor performance vs. frequency.

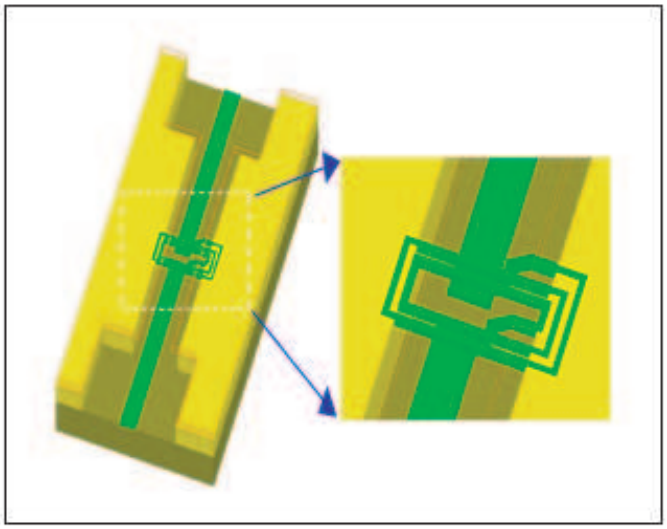

Figure 4: HFSS 3D inductor model.

The inductor is fabricated using a thick film Cu process with air as the dielectric. Experimental results are validated with 3D model calculations.

REFERENCES

1. Enpirion Inc, Power Management Design Line, "High frequency implications for switch-mode DC-DC converters." http://powermanagementdesignline.com/howto/showArtic le.jhtml?articleId=196800936

2. Rivas, J. M., D. Jackson, O. Leitermann, A. D. Sagneri, Y. Han, and D. J. Perreault, "Design considerations for very high frequency dc-dc converters," *Power Electronics Specialists Conference*, 1-11, June 2006.
3. Duan, X. M., H. F. Deng, N. X. Sun, A. Q. Huang, and D. Y. Chen, "A high performance integrated boost DC-DC converter for portable power supply," *Applied Power Electronics Conference and Exposition*, Vol. 2, 1039–1044, 2004
4. Munsunuri, S., P. L. Chapman, J. Zou, and C. Liu, "Inductor design for monolithic DC-DC converters," *Power Electronics Specialist Conference*, Vol. 1, 227–232, 2003.

Study of Magnetic Field Distribution in Infant Incubators

H. Aniolczyk[1] and P. Bieńkowski[2]

[1]Department of Physical Hazards, The Nofer Institute of Occupational Medicine, Lodz, Poland
[2]Institute of Telecommunication, Teleinformatics and Acoustics
Electromagnetic Environment Protection Laboratory
Wroclaw University of Technology, Wroclaw, Poland

Abstract— Preliminary analysis of construction and equipment of incubators for infants shows that energy power lines and devices that use their power are the main source of EMF. In this range of extremely low frequencies (ELF) the magnetic component becomes the most important due to the use of relatively low voltage. The continuous monitoring of the magnetic field induction in a selected area of the incubator's chamber (with the infant inside) was carried out. The study aimed at defining the field's variability in time, during the regular infant caretaking activities. The 24-hour monitoring, with observation of characteristic activities performed by the medical staff and the infant's mother, was carried out. The following values have been established on the basis of the study results: magnetic field induction average value on the level of 0.24 μT with standard deviation 0.07 μT, maximum field induction value on the level of 0.37 μT and minimum field induction value close to the background level (ca. 0.07 μT).

1. INTRODUCTION

Infant incubator (infant warmer) is indispensable equipment of hospitals and maternity wards, ensuring a possibility of effective treatment of premature newborn infants, sensitive as well as frail infants. Incubators provide optimal climatic conditions for the life of these infants, lower the risk of infection, facilitate their treatment and fast physical development. Temperature, air humidity and oxygen concentration in the infant space can be controlled. Electrical data: voltage 230 V, nominal frequency 50–60 Hz. The power of heaters amounts to several hundred watts (W). Temperature control data: nominal working temperature limits: $(20 \div 37)^\circ$C $\pm(2 \div 3)^\circ$C. Ambient temperature should be at least 2°C lower than the regulated lowest temperature of the space in which the infant is placed.

An infant stays in the incubator even up to several months. All electrical and electronic devices and installations are a source of electromagnetic fields (EMF); they can be also a source of interference, or their work may cause interference in the work of other devices.

The sources of magnetic field with the frequency of 50 Hz are: electronic controlling systems, heating system, ventilation system, lighting system, as well as other external devices, such as, for example, a respirator or a phototherapy device for infants.

Preliminary analysis of construction and equipment of incubators shows that power supplies and devices that use their power are the main source of extremely low frequency (ELF) EMF. In this frequency range, the magnetic component is the most significant factor. Due to the use of relatively low voltage, electric field intensity is limited to several dozen-several hundred V/m, which is negligible if compared to the normative value for this frequency range (here: 1 kV/m on housing development areas). Another frequency range which can occur in incubators are "kilohertz"- range fields (VLF). The sources of fields in this range are mostly switching power supplies and AC/DC voltage converters. These devices are a source of both magnetic and electric fields (in this frequency range, admissible electric field levels are considerably lower than in ELF range) [1, 2].

24 different epidemiological studies showed increased incidence of leukemia in children with environmental (residence) exposure to the 50 Hz magnetic field with magnetic induction above 0.3 μT [3]. The 50/60 Hz magnetic field is on the IARC list in the 2B group as a possible carcinogenic agent for humans [4].

Incubators belong to medical products and, as such, have to fulfill specific safety requirements for medical electrical equipment, which are regulated by PN-EN norms, series 60601, Part 2. The structure of the above mentioned norms is standardized and covers, among others, sections: 5 — concerning protection against hazards caused by unwanted or excessive radiation, 8 — concerning the accuracy of work parameters and protection against dangerous values of initial (output) parameters [5].

2. MATERIALS AND METHOD

The objective of studies was the measurement of the 50 Hz magnetic field induction levels and its distribution in incubators used in Polish hospitals.

Measurements were carried out for 17 incubators of different types: AIR-SHIELDS USA — Infant Intensive Care System type BF (half-open), Atom Infant Incubator V-850 ATOM with Intelligent Environment Control, Medicor IK-31 and ISOLETTE VHS 682. Detail measurements of magnetic induction intensity pattern in the incubator have been performed for V-850 (2004 year of production) that is in use at the Pathology and Emergency Ward of one of the Neonatology Clinics.

Magnetic field induction measurements inside incubators were carried out in the conditions that simulating the device's normal work (empty incubator, but with temperature stabilization switched on) and during the device's real work (incubator with an infant). Magnetic induction background level measurements were also carried out in rooms with incubators. The magnetic field meter type DMFM-ELF05 (designed at Wroclaw Univ. of Tech.), equipped with a miniature measuring probe and with the capacity for attaching a registering device, spectrum analyzing device or oscilloscope, was used for 50 Hz magnetic field measurements. The meter allows for measurements of magnetic field with values from 0.04 μT up to 250 μT in the frequency range from 30 Hz up to 1 kHz. Measurement error caused by the properties of the meter in the frequency range 30 Hz–300 Hz is ± 5% and in the frequency range 300 Hz–1 kHz it is ±15%. The meter was calibrated in the Certified Calibrating Laboratory LWiMP at Wroclaw Univ. of. Tech. Estimated entire uncertainty of measurement taking into account also inaccuracies of probe positioning in measured points and the selection of these points was established at 25%. In order to determine spectrum parameters of the measured magnetic field (H), spectrum analysis of the measured field with the use of oscilloscope with the FFT function connected to the meter was carried out.

Methodology of studies of magnetic field induction distribution inside incubator: measurement result of complex (equivalent of RMS value of isotropy probe) magnetic field induction in incubator was determined on the basis of field spatial measurements for 300 points evenly distributed on the incubator up to the 0.15 m above the bedding with a mattress. During the measurements it allowed for covering the whole space in which the infant can stay.

Methodology of measurement of magnetic field induction fluctuations over time: 24-hour field intensity monitoring with the measuring probe placed in a selected point inside the incubator with infant.

3. RESULTS OF THE MEASUREMENTS

The measurements confirmed previous assumptions that the dominating role in the spectrum of the measured field inside the cradle of incubators is played by the field component with the basic supply frequency (of the energy power lines), i.e., 50 Hz. Contribution of a higher harmonic was negligible. Measurements of magnetic field induction distribution inside empty incubator cradle were carried out. Fig. 1 shows measurement results for two different incubator types.

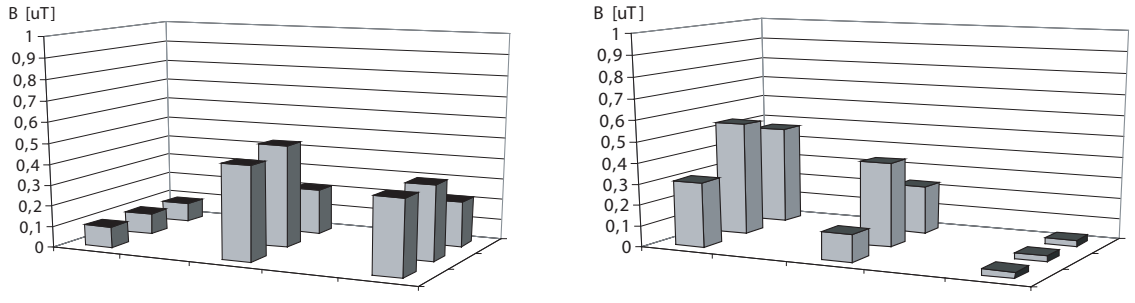

Figure 1: Example of magnetic induction distribution on the mattress surface for two different incubator types.

The charts show that magnetic field distribution inside incubator cradle depends on the type of the heater and its placement inside the incubator's case.

The more detail measurement of magnetic induction distribution was carried out in selected incubator type V-850 (2004 year of the production). Measurements were performed: Fig. 2 presents

measurements results on the level +5 cm above mattress surface. During measurements incubator's heater worked with maximum power.

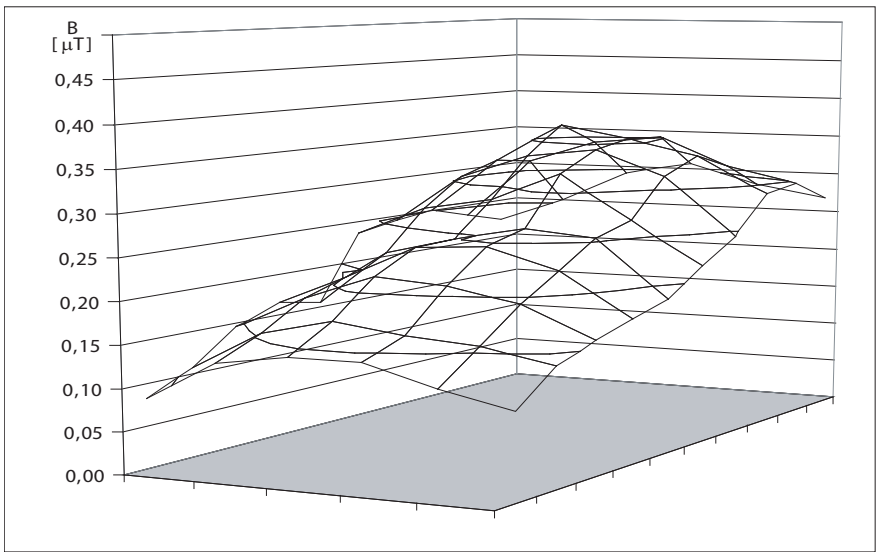

Figure 2: "Map" of distribution magnetic induction on the level +5 cm above mattress surface.

Summarize those results, the following things were established (measurement conditions: heater-maximum power, measurements at the level +5 cm above mattress):

- field induction average value (B) on the level of 0.24 μT with standard deviation 0.07 μT,
- maximum field induction value (B) on the level of 0.37μT
- minimum field induction value (B) close to the background level (ca. 0.07 μT).

Uncertainty of measurements can be estimated as 20%, assuming that the position of the probe did not change. The value close to average is also the value most often registered during measurements. Analysis of obtained results confirms observations of preliminary monitoring of incubators' work.

It was determined that changes of magnetic field induction over time are directly connected with the momentary power of incubator heater, which is illustrated on Fig. 3. Average heater power during stabilized incubator work is around 20–30% of the maximum power. In case of the heater's complete switching off, the induction was falling down to the background level and in measurement points was below 0.1 μT.

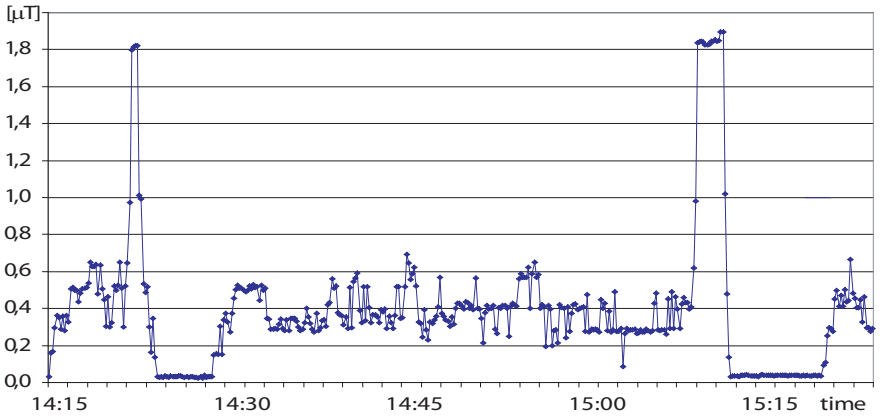

Figure 3: The shape of magnetic field changes inside incubator cradle during its frequent opening (forcing the heater's work with changing power).

For the sake of comparison, background measurements in Room "A" showed: inside the room 0.05 μT, in the window plane 0.14 μT, near distribution board 0.44 μT, whereas background level measurements in Room "B" showed 0.15 μT inside the room.

4. CONCLUSION

1. A measurement method and a measuring probe for infant exposure to 50 Hz magnetic field and its harmonics occurring in incubators were worked out.

2. It was determined that magnetic field induction changes over time are directly connected with momentary power of incubator's heater.

3. Magnetic field induction average value during monitoring was 0.325 μT, which is c. 16% of the maximum value.

REFERENCES

1. Ordinance of the Minister of Environmental Protection of 30 October 2003 on admissible EMF levels in environment and ways of checking how these levels are observed. *Dz. U.* Nr 192, poz. 1883, 2003.
2. Council Recommendation 1999/519/EC of July 1999 on the limitation of exposure of the general public to electromagnetic fields (0 Hz–300 GHz), *Off J Eur Communities*, L199/59–70, 1999.
3. Ahlbom, A. et al., "A pooled analysis of magnetic fields and childhood leukemia," *Br. J. Cancer*, Vol. 83, 692–698, 2000.
4. "Monograph on static and extremely low-frequency (ELF) electric and magnetic fields," *IARC 2001*, Vol. 80, 2002.
5. Medyczne urządzenia elektryczne, Część 2, Szczegółowe wymagania bezpieczeństwa cieplarek dla noworodków, *PN-EN 60601-2-19*, wrzesień, 2001.

Scientific Thematic Network "Electromagnetic Compatibility of Devices, Systems and Installations for IT Community EMC-Net"

S. Lysiak, **T. Reczek**, **and T. W. Więckowski**
Wrocław University of Technology, Poland

Abstract— This article describes in short the history, structure and scope of activities of the scientific thematic Network EMC-net, which unites several academic institutions, laboratories and other organizations involved in electromagnetic compatibility issues. The authors present an overview of the Network's developments so far as well as current joint projects involving it's members and the Network's activities as an opinion-setting authority.

1. BEGINNINGS OF EMC-NET

The idea for uniting EMC related academic and scientific institutions has originated already in April 2003, among a few employees of the Electronics faculty of Wrocław University of Technology. Then, a little over four years ago, as the result of an initiative of the Wrocław University of Technology Prof. Tadeusz Więckowski, a meeting was held at the Wrocław EMC 2003 Workshop to discuss the possibilities of bringing this idea to life. During this meeting as well as further discussions, the idea of the Network was refined, establishing the following key objective:

- Provide know-how and technological support to academic and research institutions involved in EMC research, by initiating, coordinating and carrying out joint research and implementations as well as conducting staff training,
- Provide support and coordinate member institutions' participation in EU Framework Programme integrated projects and Networks of Excellence, based on their experience and consolidated research potential,
- Create an information exchange/sharing forum, which will also allow for presentation of current results and achievements in the field of electromagnetic compatibility research.

The next step consisted of formalizing the earlier stipulations, defining the internal regulations and the official name. This was followed by an application to the Ministry of Science and Information Society Technologies regarding co-financing, which was positively approved (13. 08. 2004), allowing for the launch of our organization: Scientific thematic Network "Electromagnetic Compatibility of Devices, Systems and Installations for IT community EMC-Net".

2. NETWORK STRUCTURE AND MEMBERS

Currently, the Network includes the 17 founding members, which have been with the Network from the day it was established. Also, during the three years of existence, 5 new members have joined the Network, including one from abroad, which we hope is a first step towards converting EMC-net from a local to an international organization.

In order to minimize bureaucracy, EMC-net has a very simple management structure: a (5 person) Steering Committee is elected from among all representatives of the Network members, which comprise the so-called General Network Assembly. The term of office of the Steering Committee is 3 years and it is headed by the Network Coordinator. The responsibilities of the Steering Committee comprise of undertaking regular decisions in regards to Network activities, which do not require formal approval of the General Assembly. Currently the Network is headed by Institute of Telecommunications, Teleinformatics and Acoustics of Wrocław University of Technology, along with it's accredited Electromagnetic Compatibility Laboratory.

The internal regulations clearly define the objectives and goals for the Network and it's members, which besides the earlier mentioned points include:

- Consolidation of scientific institutions to implement and improve EMC research methods and to develop methods and technologies for assurance of electromagnetic compatibility of devices and electronic systems in the era of IT society,
- Support development of new techniques and technologies in view of requirements of EC directive 89/336/EEC,

- Support the Network members in participation in projects carried out under EU Structural or Cohesion Funds,
- Raise the level and rank of Polish research and development achievements in the field of electromagnetic compatibility of devices and systems, within the European Research Area (ERA),
- Develop international cooperation in order to transform the national Network and bring it to an international level.

These stipulations are fairly general, thus allowing the Network members to present and discuss practically any ideas related to EMC research and development or ideas related to popularization of EMC knowledge, some of which eventually can lead to some tangible activities. The next sections describe some of the areas, where EMC-net already had some successful achievements.

3. LEGISLATURE

As an organization uniting renowned academic institutions, EMC-net was quickly recognized as an authoritative body to provide opinions for foreseen legal acts, articles and ordinances as well as other documents pertaining to the area of expertise of the Network. Some of the more important activities in this area include:

a) In January 2004 our Network provided an opinion pertaining to the foreseen EMC Act, which was supposed to introduce to Polish legislature Directive 89/336/EEC, unfortunately this Act was not passed at this time,
b) In December 2004 our Network was invited by the Ministry of Infrastructure to participate in discussions over the new Directive 2004/108/WE, in order to prepare for the informative meeting in Brussels (03. 02. 2005), which was to clarify and explain the new directive. Our Network Members had many remarks regarding the Polish translation of this directive and pointed out that it is necessary to quickly establish the requirements for notified bodies, as implementation of the new directive in Polish legislature will also call for implementation of an appropriate quality assurance system.
c) At the turn of March and April 2006, our Network was providing an opinion for the new EMC Act. After the first series of remarks, a representative of EMC-net also participated in the second stage of establishing this Act — participating in the meetings of the Seym Committee, which was debating various changes to this project. The final version of the EMC Act was settled on 13th April 2007, and was signed shortly after by the Polish President on the 25th of April.
d) In October 2006 EMC-net was invited to review the proposed changes introduced by the EU Regulatory Framework for electronic communications networks and services.

Besides the above mentioned documents, the Network members were also asked to provide opinions to some other minor legal acts, including among others: a project related to the introduction of Digital Video Broadcasting (DVB-T), amendment of Telecommunication Law.

Currently (05. 2007) the network is providing advice in regards to a few ordinances related to the EMC Act.

4. ACTIVITIES FOR INCLUSION OF EMC ISSUES IN THE 7TH FRAMEWORK PROGRAMME: EUROPEAN TECHNOLOGY NETWORK — SUSTAINABLE ELECTROMAGNETIC ENVIRONMENTS (EMC, INCLUDING EMF) ETN-SEE

In March 2005 EMC-net was invited to participate in a pan-European initiative, which was aimed at consolidating EMC research on a pan-European level and to guide and organize the introduction of EMC related matters into the 7th Framework Programme.

These activities began with the idea for creating an EMC Technological Platform and eventually led to the establishing of European Technology Network (ETN-SAA). This group includes such world renowned authorities as: Ir. Marcel van Doorn, Dr. Marco Klinger, Prof. Dr. Frank Leferink, Dr. Marco Leone, Dr. Amaury Soubeyran, Prof. Dr. Christos Christopoulos.

5. RESEARCH

The Network members defined a joint research program, which consolidates some of the consortium members' research works. Discussions about possible research directions allowed for definition of

four major projects, which the Steering Committee decided to develop and present for further discussion. These four proposals were then sent out to the Network members, asking for comments, definition of additional objectives etc. The research subjects are as follows:

1. Electromagnetic hazards from devices, systems and installations in view of the work environment and human health,
2. Electromagnetic compatibility (EMC) of advanced microelectronic components — methods of analysis, modeling and measurements,
3. Methods for assessment of electromagnetic compatibility at frequencies exceeding 1 GHz,
4. Intersystem compatibility — radiocommunication systems (among others 3 G, 4 G)

Considering that currently Ministry of Science and Higher Education is evaluating the first of the above proposals for potential funding, we will present herein the project in more detail:

This project shall evaluate potential electromagnetic hazards at human work and living environments, in order to provide appropriate safety and health protection measures. The next steps should include priority research in the area of:

- Development of methods for definition of electromagnetic field strength using mathematical models for the near field, multipath propagation areas (building interior, urban areas) and open space, as required for assessment of EMF in view of safety and health protection,
- Development of methods for definition of resultant ("replacement") electromagnetic field strength levels at human environments, as required for assessment of required electromagnetic hazard protection measures as well as environmental monitoring requirements,
- Development of methods for assessment of EMF levels occurring at human work environments, in view of modulation parameters (including pulse EM), in order to verify existing measurement methods used by measurement/control and sanitary/epidemiology authorities,
- Development of methods and measurement equipment for assessment of EMF levels at human work and living environments and their implementation at the national research/measurement laboratories responsible for control of safety and health protection in regards to EMF,
- Development of human (including child) models (phantoms) for measurements of the Specific Absorption Rate (SAR) when exposed to EMF,
- Development of methods for testing of technical measures (screening etc.) designed to eliminate or limit undesirable EMF at human work and living environments.

This project is being coordinated by Łódź Institute of Occupational Medicine and Wrocław University of Technology.

6. OTHER INITIATIVES

Another interesting initiative of our Network was to perform comparative measurements of a reference conducted interference source. On 08. 02. 06 a proposal was sent out to the consortium members as well as other centers cooperating with our Network, proposing to perform the comparative measurements. We were greatly surprised by the number of eager participants — as we have received a reply from 10 laboratories:

- Institute of Power Systems Automation (Instytut Automatyki Systemów Energetycznych), Wrocław,
- Electrotechnical Institute (Instytut Elektrotechniki), Warsaw,
- Electrotechnical Institute (Instytut Elektrotechniki), Gdańsk branch,
- National Institute of Telecommunications (Instytut łączności), Warsaw,
- Institute of Telecommunication and Acoustics of Wrocław University of Technology (Instytut Telekomunikacji i Akustyki Politechniki Wrocławskiej),
- R&D Marine Technology Center (OBR Centrum Techniki Morskiej), Gdynia
- Technical University of Łódź, Department of Electrical Engineering and Instrument Transformers K-23 (Politechnika Łódzka, Katedra Elektrotechniki Ogólnej i Przekładników K-23),
- Industrial Research Institute for Automation and Measurements (Przemysłowy Instytut Automatyki i Pomiarów), Warsaw
- Mining Electrification and Automation Center EMAG (Centrum Elektryfikacji i Automatyzacji Górnictwa EMAG), Katowice.

- VOP-026 Sternberk, s.p., divize VTUPV Vyskov.

Currently this research is close to an and the results should be shortly available.

During this project we have checked not only if the measurements are being performed correctly at each of the institutions (obviously highly dependent on the owned equipment), but also the knowledge pertaining to he procedures for such measurements.

This was achieved by instructing each of the laboratories to perform the measurements in a standard way, which they would use when performing measurements for a Client for a similar device. I.e., they did not receive any additional guidelines or instructions about any specific requirements, where our final evaluation will check also for compliance of the measurement procedures with the appropriate regulations.

The reference device was a nonstandard but verified source of interference. It is being handed over from laboratory to laboratory, however being retested each time by the organizer (i.e., evaluation in a star-pattern). As proven by experience, comparative measurements are the best method for discovering any anomalies and inaccuracies in measurement procedures as well as measurements themselves — many a time we have seen measurements performed for the same object differ by few to even a few dozen decibels! Collection of results from so many institutions will also allow for assessment of the way in which the results are presented — it might come as a surprise, but this seemingly easy task often leaves much to be desired.

We hope that this project will also allow for improvement of quality of measurements at all laboratories participating in this initiative.

Another interesting initiative is the response to signals from consortium members, about insufficient education of engineers in the area of EMC. This is becoming a growing problem for employers who nowadays are looking for people with an extended knowledge of different EMC aspects, especially in the area of design as well as co-usage of different devices/systems. To make a wider audience aware of this problem, EMC-net has contacted the organizers of Pozna Telecommunication Workshops, who responded with great interest in including this in their workshop program and agreed to even host an entire session dedicated to compatibility (it should be mentioned that the organizers pay great attention to education in the field of electronics and telecommunications instead of just concentrating on the newest developments in these areas). Of course EMC-net will be responsible for preparing at least a few papers for such workshop sessions, however considering the short time before the last Workshops (held on 7–8. 12. 06) in 2006 only one paper was submitted about EMC education, nevertheless EMC-net plans in this area for future Workshops are much more ambitious.

REFERENCES

1. EMC-net webpage: http://www.emc-net.org/
2. European Technology Netwerk for Sustainable Electromagnetic Environments: http://www.emc-esd.nl/smartsite8305.htm?goto=19017

Implanted Antenna for an Artificial Cardiac Pacemaker System

Tamotsu Houzen[1], **Masaharu Takahashi**[2], **and Koichi Ito**[3]

[1]Graduate school of Science and Technology, Chiba University, Japan
[2]Research Center for Frontier Medical Engineering, Chiba University, Japan
[3]Graduate School of Engineering, Chiba University, Japan

Abstract— A planar inverted-F antenna (PIFA) using an implanted antenna for medical implant telemetry system (MITS) is proposed. The antenna is located on the surface of an artificial cardiac pacemaker in order to monitor medical information such as a cardiac beat. Design of the antenna is applied to the human body which is substituted by a 2/3 muscle-equivalent phantom and the antenna is numerically analyzed by use of the finite-differential time domain (FDTD) method. Moreover, to estimate a communication in the real environment a link budget calculation is presented. As a result, the proposed antenna operating at 402–405 MHz-band is able to create a communication link of the MITS with the external equipment which is located within 6 m distance and 104 degree of altitude.

1. INTRODUCTION

Recently, the medical implant telemetry system (MITS) has been investigated with a great interest. MITS is a tool that transmitting vital signals such as a cardiac beat of a patient from an implanted antenna which embedded into the human body to the external antenna using wireless communication link. This system is able to reduce a number of visits of doctors to diagnose the patients, and to facilitate physical or mental burden of the patients. In addition, it can communicate without a wire piercing of the skin which has an advantage to prevent the infection with a germ in a medical diagnosis. Up to now, many of the implanted antennas have been developed [1–3] to realize the system. In this paper, a planar inverted-F antenna (PIFA) is proposed as the implanted antenna which is located on the surface of the artificial cardiac pacemaker as the implanted medical equipment.

2. DESIGN AND ANALYZING METHOD OF IMPLANTED ANTENNA

The PIFA has some merits i.e., simple, thin, and compact. In order to realize MITS, the PIFA is chosen for the implanted antenna which located on the surface of the artificial cardiac pacemaker. Fig. 1 shows the configuration of the antenna model with the pacemaker. The antenna element whose dimension by $35 \times 20\,\mathrm{mm}^2$ is located between the substrate and superstrate layer ($\varepsilon_r = 10.0$) in order to prevent the effect of the human body by decreasing effects of a high conductive tissue. The PIFA is fed near the center of the element and shorted at the right edge to the pacemaker in order to make the PIFA matched on $50\,\Omega$. Here, the pacemaker whose dimension by $39 \times 30 \times 9\,\mathrm{mm}^3$ serves as the ground of the PIFA. To analyze the numerical calculation model, the pacemaker is imitated in the box of a perfect electric conductor (PEC). Fig. 2 depicts the numerical calculation model when the whole structure of the antenna is embedded into the 2/3 muscle-equivalent phantom ($\varepsilon_r = 38.09$, $\sigma = 0.53\,\mathrm{S/m}$) with the used electrical constants is at 403.5 MHz [4]. In order to evaluate the electric effects of the antenna to the phantom, the distance between the surface of the phantom and the surface of the antenna (d) is changed.

3. PERFORMANCES OF IMPLANTED ANTENNA AND LINK BUDGET CALCULATION

Figure 3 describes the S-parameter performance by numerical calculation using the 2/3 muscle-equivalent phantom. From this figure, the resonant frequency shifts to the higher by increasing the distance between the surface of the phantom and the surface of the PIFA (d). However, it is confirmed that S_{11} performance is lower than $-10\,\mathrm{dB}$ at the target frequency (402–405 MHz) for both of the PIFA models. Fig. 4 represents radiation characteristics of the PIFA in the x-z and y-z plane by numerical calculation using the 2/3 muscle-equivalent phantom. Here, the radiation characteristics are in the main polarization direction. In this case, as the distance d increases, the gain decreases in the both planes because of the loss of human tissue. The direction of maximum radiation in the y-z plane is at $\theta = 0$ degree. However, the one in the x-z plane is about $\theta = 60$

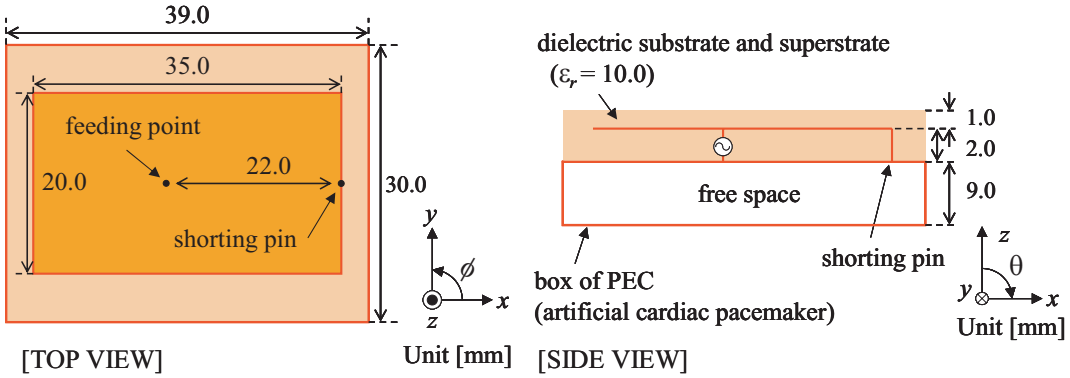

Figure 1: Configuration of PIFA and artificial cardiac pacemaker model.

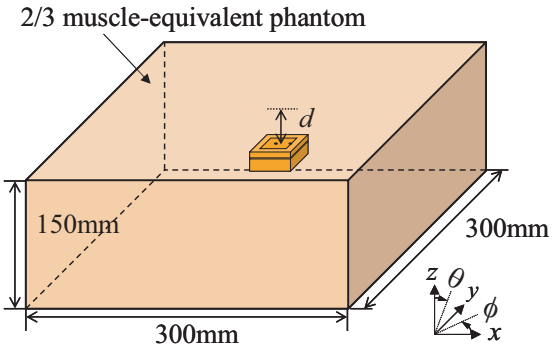

Figure 2: Numerical calculation model.

degree because the dimension of the ground plane is very small. The maximum gain of the model at $d = 5$ mm, $d = 10$ mm and $d = 15$ mm is -28.9 dBi, -30.0 dBi and -30.5 dBi, respectively.

Table 1 shows a link budget between the implantable antenna and the receiver. The distance between the transmitter and the receiver is 6.0 m and the application is supposed to be used in the sickroom. When the bit rate is assumed 7 kbps in consideration of the transmitting vital signal, the needed implanted antenna gain should be more than -35.0 dBi in Table 1. It can be stated that that the wireless communication is possible to be occurred within the range of about 232° centered at 0° in the x-z plane, or 104° centered at 0° in the y-z plane as shown in Fig. 4.

Table 1: Link budget calculation

Frequency	403.5 MHz
Transmission power	-72.6 dBW
Tx antenna gain	-35.0 dBi
EIRP	-108.6 dBW
Distance	6.0 m
Path loss	40.1 dB
Bit rate	7 kbps
Link C/N_0	51.6 dBHz
Require C/N_0	50.6 dBHz
Margin	1.0 dB

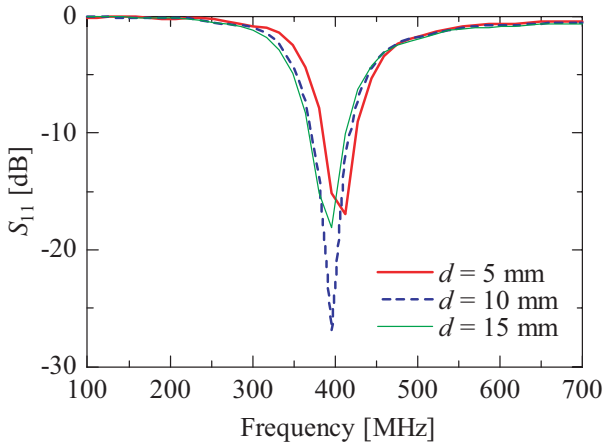

Figure 3: S-parameter.

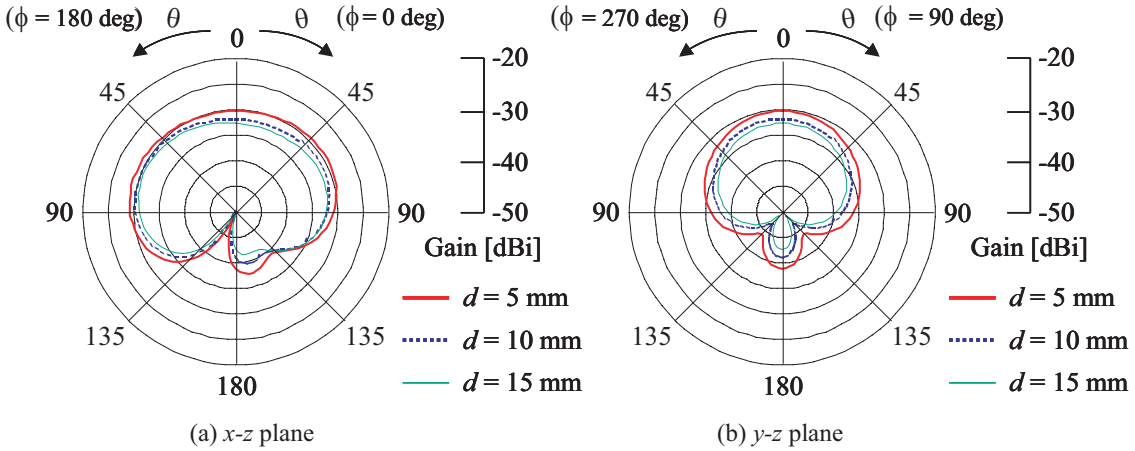

(a) x-z plane (b) y-z plane

Figure 4: Radiation characteristics.

4. CONCLUSION

This paper proposed a PIFA with an artificial cardiac pacemaker for use of MITS. The calculation model is composed of the PIFA and the pacemaker embedded in the 2/3 muscle-equivalent phantom. The distance between the top of the phantom and the antenna (d) is changed and the model is numerically analyzed by use of the FDTD method. Numerical results show that as the distance d increases, the resonant frequency shifts to the higher and the gain decreases because of the loss and the high permittivity of the human tissue. However, the proposed antenna resonates at 402–405 MHz band, and the maximum gain is −30.5 dBi is confirmed. Moreover, according to the link budget calculation, required gain is −35.0 dBi for the wireless communication, when the distance between the transmitter and the receiver is 6.0 m. Here, the wireless communication is possible to be occurred in the range of 104° and, the proposed antenna is able to be used for the MITS.

REFERENCES

1. Kim, J. and Y. Rahmat-Samii, "Implanted antennas inside a human body: simulations, designs, and characterizations," *IEEE Trans. Microwave Theory Tech.*, Vol. 52, No. 8, 1934–1943, August 2004.
2. Soontornpipit, P., C. Y. Furse, and Y. C. Chung, "Design of implantable microstrip antenna for communication with medical implants," *IEEE Trans. Microwave Theory Tech.*, Vol. 52, No. 8, 1944–1951, August 2004.
3. Ito, K., H. Usui, and M. Takahashi, "Performances of an implanted cavity slot antenna embedded in the human upper arm," *Proceedings of 2006 International Symposium on Antennas and Propagation (ISAP 2006)*, 88, Singapore, November 2006.

4. Gabriel, C and S Gabriel, "Compilation of the dielectric properties of body tissues at RF and microwave frequencies," Armstrong Laboratory (AFMC), Radiofrequency Radiation Division, Brooks Air Force Base, USA. Available from http://www.brooks.af.mil/AFRL/HED/hedr/reports/dielectric/Report/Report.html, 1996.

Extension of the Finite Network Method to Magnetic Materials and Its Application to Eddy-current Testing

A. Farschtschi and T. Richter

Chemnitz University of Technology, Germany

Abstract— The finite network method (FNM) is a method for eddy-current and inductance calculation in the low-frequency case. Since FNM discretises only conducting materials it is well-suited for systems with little material expended in space. A detailed derivation of FNM to magnetic materials is made and the applicability to eddy-current testing of magnetic materials is shown.

1. INTRODUCTION

It is well known that conductive non-magnetic media can be calculated by the finite network method (FNM) ([1, 2]) and the similar partial element equivalent circuit (PEEC) technique including inductive coupling ([3, 4]). Homogeneous media are discretised into cuboid volume elements. The midpoints of these elements form a staggered grid of resistor elements. The length of these resistor elements is equal to the distance of neighboured points of the staggered grid whereas the cross section is taken from the interface of the both volume elements belonging to the considered grid points of the staggered grid (see Fig. 1). In the following section we introduce the extension of FNM to magnetic materials with linear magnetic permeability. To preserve homogeneous material properties circuit elements across the interface between materials are divided into two circuit elements by the interface (see Fig. 2). This allows an extension of the FNM and PEEC technique to magnetic materials ([1, 2]). The authors present a more detailed derivation then compared to Long et al. [5] and show the applicability of the derived method to eddy-current testing of magnetic materials.

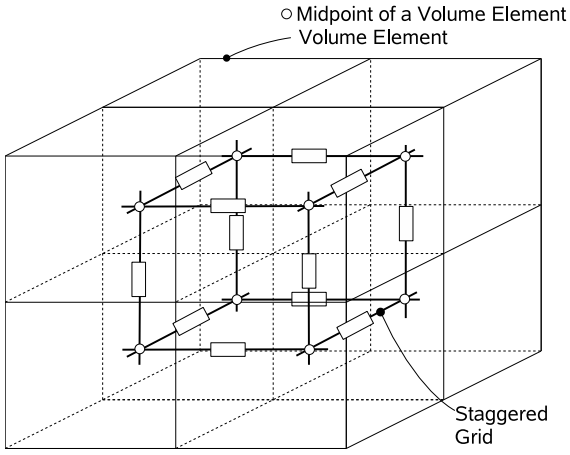

Figure 1: Discretisation of a homogeneous volume into volume elements. The midpoints of the volume elements form a staggered grid with inductive coupled resistor elements.

2. EXTENSION TO MAGNETIC MATERIALS

The starting point of the derivation are the time-dependent Maxwell's equations in the quasi-static limit:

$$\frac{\partial}{\partial \vec{r}} \times \vec{E} = -\frac{\partial \vec{B}}{\partial t} \tag{1}$$

$$\frac{\partial}{\partial \vec{r}} \times \vec{H} = \vec{J} \tag{2}$$

$$\frac{\partial}{\partial \vec{r}} \cdot \vec{B} = 0 \tag{3}$$

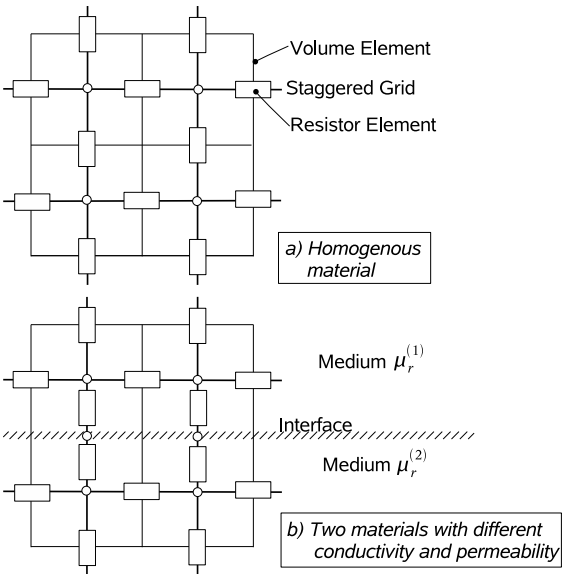

Figure 2: The upper picture shows the staggered grid and its resistor elements in the case of a homogeneous material. In the case of two different materials (lower picture) each resistor element perpendicular to the interface is divided into two elements. This preserves the homogeneity for all equivalent circuit elements.

$$\vec{J} = \gamma \left(\vec{E} + \vec{E}_e \right) \tag{4}$$

$$\vec{B} = \mu_r \mu_0 \vec{H} \tag{5}$$

$$\vec{B} = \frac{\partial}{\partial \vec{r}} \times \vec{A}, \quad \frac{\partial}{\partial \vec{r}} \cdot \vec{A} = 0 \tag{6}$$

The derivation is valid for linear material properties (4) and (5) with electric conductivity γ and the relative magnetic permeability μ_r. In (4) the electric field $\vec{E}_e$ of external voltage sources is introduced. To calculate the flux density $\vec{B}$ the vector potential $\vec{A}$ in Coulomb gauging is introduced in (6).

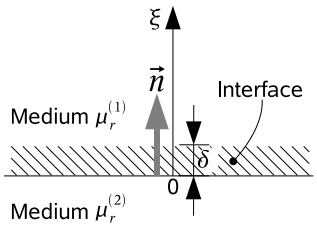

Figure 3: Interface of thickness δ between magnetic materials with linear change of μ_r across the interface.

The interface between different magnetic materials has the small thickness δ (see Fig. 3). We assume a linear change (variable ξ) across the interface in normal direction $\vec{n}$ with constant relative permeabilities $\mu_r^{(1)}$ and $\mu_r^{(2)}$ above and below the interface:

$$\mu(\xi) = \mu_r{}^{(2)} \mu_0 + \frac{\mu_r^{(1)} - \mu_r^{(2)}}{\delta} \mu_0 \xi, \quad \xi \in [0, 1]$$

Thus the gradient of $\mu(\vec{r})$ across the interface is given by:

$$\frac{\partial}{\partial \vec{r}} \mu(\vec{r}) = \vec{n} \frac{\partial \mu(\xi)}{\partial \xi} = -\frac{\mu_r^{(2)} - \mu_r^{(1)}}{\delta} \mu_0 \vec{n} \tag{7}$$

Applying (7) to (6) gives Poisson's equation of the vector potential where the second term is

valid only across the interfaces between magnetic materials:

$$-\Delta\vec{A} = \frac{\partial}{\partial\vec{r}} \times \vec{B}(\vec{r}) = \frac{\partial}{\partial\vec{r}} \times \left[\mu_r(\vec{r})\mu_0\vec{H}(\vec{r})\right] = \mu_r(\vec{r})\mu_0 \frac{\partial}{\partial\vec{r}} \times \vec{H}(\vec{r}) + \frac{(\mu_r^{(2)} - \mu_r^{(1)})\mu_0}{\delta}\vec{H}(\vec{r}) \times \vec{n} \quad (8)$$

The second term of (8) only proves the tangential component of $\vec{H}$. Since we exclude electric surface currents from our theory $\vec{H}(\vec{r}) \times \vec{n}$ is continuous across interfaces. The integration of the second part of (8) yields in the limit $\delta \to 0$:

$$\lim_{\delta\to 0} \int_{\xi=0}^{+1} \frac{(\mu_r^{(2)} - \mu_r^{(1)})\mu_0}{\delta}\vec{H}(\vec{r}) \times \vec{n} d\xi = (\mu_r^{(2)} - \mu_r^{(1)})\mu_0\vec{H}(\vec{r}) \times \vec{n} =: J_{ma}(\vec{r}) \quad (9)$$

In (9) the magnetic current density $\vec{J}_{ma}(\vec{r})$ at the interface between magnetic materials is introduced. As can be seen vividly from (9) the boundary current density $\vec{J}_{ma}(\vec{r})$ is tangential to the boundary. Making use of (9) the general solution of Poisson's Equation (8) for the magnetic vector potential in Coulomb gauging is given by:

$$\vec{A}(\vec{r}) = \frac{\mu_0}{4\pi}\int_{V'} \frac{\mu_r(\vec{r}')\vec{J}(\vec{r}')}{|\vec{r} - \vec{r}'|} dV' + \frac{\mu_0}{4\pi}\int_{a'} \frac{\vec{J}_{ma}(\vec{r}')}{|\vec{r} - \vec{r}'|} da' \quad (10)$$

In (10) integration is done over the volume V' of all conductive media and the overall boundary area a' between different media. We define the current density components $\vec{J}_k$ of circuit elements and $\vec{J}_{ma,l}$ of boundary elements in Cartesian coordinates (Fig. 4). For each boundary element exist two vectors $\vec{J}_{ma,l}$ representing the two Cartesian components of a boundary element (Fig. 4). Thus, each vector $\vec{J}_k$ and $\vec{J}_{ma,l}$ is parallel to a distinct Cartesian direction:

$$\vec{J}_k = J_k\vec{e}_i = \begin{cases} J_k\vec{e}_x: & x \text{ direction} \\ J_k\vec{e}_y: & y \text{ direction} \\ J_k\vec{e}_z: & z \text{ direction} \end{cases} \qquad \vec{J}_{ma,l} = J_{ma,l}\vec{e}_i = \begin{cases} J_{ma,l}\vec{e}_x: & x \text{ direction} \\ J_{ma,l}\vec{e}_y: & y \text{ direction} \\ J_{ma,l}\vec{e}_z: & z \text{ direction} \end{cases} \quad (11)$$

While the $\vec{J}_k$ belong to the circuit elements of the staggered grid and are connected by the current conservation law the $\vec{J}_{ma,l}$ are independent variables.

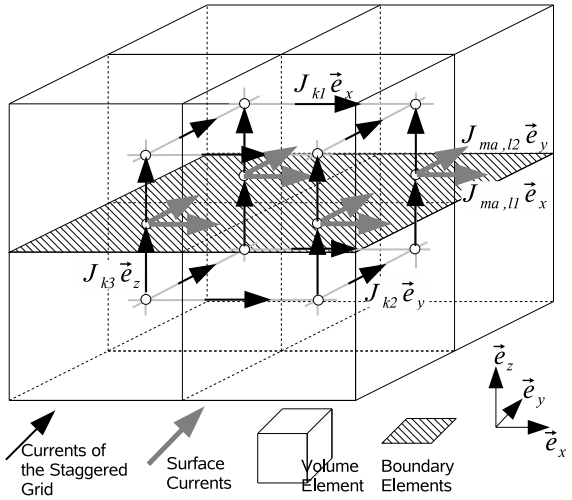

Figure 4: Currents of the staggered grid and surface currents of boundary elements between magnetic media.

When conducting media and boundaries are discretised into rectangular elements (10) can be written as sum of all volume elements k and all boundary elements l at the interface between media with different magnetic permeabilities. Since the theory deals with element-wise constant current

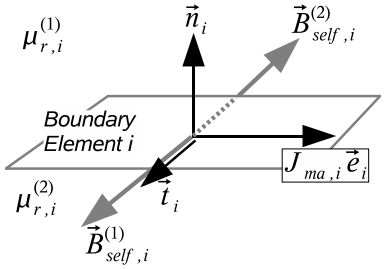

Figure 5: Magnetic flux components at the upper and lower side of the boundary element i created by the boundary current density $\vec{J}_{ma,i} = J_{ma,i}\vec{e}_i$ of the same element. The constant component $\vec{J}_{ma,i}$ of the rectangular boundary i element creates the flux $\vec{B}_{self,i}^{(1)} = +\frac{1}{2}\mu_0 J_{ma,i}\vec{e}_i \times \vec{n}_i$ above the boundary element and $\vec{B}_{self,i}^{(2)} = -\frac{1}{2}\mu_0 J_{ma,i}\vec{e}_i \times \vec{n}_i$ below with the well-known step $\mu_0 J_{ma,i}$.

densities the current densities of circuit and boundary elements are excluded from integration:

$$\vec{A}(\vec{r}_i) = \frac{\mu_0}{4\pi}\sum_k \mu_{r,k}\left[\int_{V_k}\frac{1}{|\vec{r}_i-\vec{r}_k|}dV_k\right]\vec{J}_k + \frac{\mu_0}{4\pi}\sum_l\left[\int_{a_l}\frac{1}{|\vec{r}_i-\vec{r}_l|}da_l\right]\vec{J}_{ma,l} \tag{12}$$

$$\vec{B}_i := \vec{B}(\vec{r}_i) = -\frac{\mu_0}{4\pi}\sum_k \mu_{r,k}\left[\int_{V_k}\frac{\vec{r}_i-\vec{r}_k}{|\vec{r}_i-\vec{r}_k|^3}dV_k\right]\times\vec{J}_k - \frac{\mu_0}{4\pi}\sum_l\left[\int_{a_l}\frac{\vec{r}_i-\vec{r}_l}{|\vec{r}_i-\vec{r}_l|^3}da_l\right]\times\vec{J}_{ma,l} \tag{13}$$

Equation (13) determines the flux density $\vec{B}$ at an arbitrary point $\vec{r}_i$ from (12) by the use of (6). Now $\vec{r}_i$ is the vector at the centre of the boundary element i with the area q_i. Furthermore, $\vec{t}_i$ is a unit tangential vector at the boundary element i and the currents I_k and $I_{ma,l}$ are used instead of the current densities J_k and $J_{ma,l}$. $\vec{B}_i \cdot \vec{t}_i$ is evaluated by the field coefficients $h_{V,ik}$ and $h_{a,il}$. The field coefficients include an averaging over the boundary element i (integration variable a_i):

$$\vec{B}_i \cdot \vec{t}_i = \mu_0\sum_k \mu_{r,k}h_{V,ik}I_k + \mu_0\sum_l h_{a,il}I_{ma,l} \quad \text{with } I_k = q_kJ_k, I_{ma,l} = b_lJ_{ma,l} \tag{14}$$

$$h_{V,ik} = -\left[\left(\frac{1}{4\pi q_i q_k}\int_{a_i}\int_{V_k}\frac{\vec{r}_i-\vec{r}_k}{|\vec{r}_i-\vec{r}_k|^3}dV_k da_i\right)\times\vec{e}_k\right]\cdot\vec{t}_i \tag{15}$$

$$h_{a,il} = -\left[\left(\frac{1}{4\pi q_i b_l}\int_{a_i}\int_{a_l}\frac{\vec{r}_i-\vec{r}_l}{|\vec{r}_i-\vec{r}_l|^3}da_l da_i\right)\times\vec{e}_l\right]\cdot\vec{t}_i \tag{16}$$

In (15) q_k is the cross of circuit element k perpendicular to the current direction. In (16) b_l is the width of boundary element l perpendicular to the direction of the boundary current. $\vec{B}_{self,i}$ is the flux density created by the boundary currents of the element i. $\vec{B}_{self,i}$ has a discontinuity across the boundary element which demands a distinction between the two sides of the boundary element (see Fig. 5):

$$\vec{B}_{self,i}\cdot\vec{t}_i = \begin{cases} +\frac{1}{2}\mu_0 J_{ma,i}\,(\vec{e}_i\times\vec{n}_i)\cdot\vec{t}_i: & \text{Medium 1 toward } \vec{n}_i, \vec{e}_i \perp \vec{t}_i \\ -\frac{1}{2}\mu_0 J_{ma,i}\,(\vec{e}_i\times\vec{n}_i)\cdot\vec{t}_i: & \text{Medium 2 against } \vec{n}_i, \vec{e}_i \perp \vec{t}_i \end{cases} \tag{17}$$

Thus a more precise definition of the field coefficients $h_{a,il}$ in (16) is given by the use of (17) when the destination $\vec{r}_i$ belongs to the boundary element a_l:

$$h_{a,il} = \begin{cases} \text{see (16)}: & \vec{r}_i \notin a_l \\ +2\pi\frac{I_{ma,l}}{b_l}\,(\vec{e}_l\times\vec{n}_i)\cdot\vec{t}_i: & \vec{r}_i \in a_l, \vec{r}_i \text{ toward } \vec{n}_i \\ -2\pi\frac{I_{ma,l}}{b_l}\,(\vec{e}_l\times\vec{n}_i)\cdot\vec{t}_i: & \vec{r}_i \in a_l, \vec{r}_i \text{ against } \vec{n}_i \end{cases} \tag{18}$$

The continuity of the tangential component of the magnetic field $\vec{H}$ at boundaries should be kept as a consequence of Maxwell's equation in the case of absent free surface currents:

$$\frac{1}{\mu_{r,i}^{(1)}\mu_0}\vec{B}_i^{(1)}\cdot\vec{t}_i = \frac{1}{\mu_{r,i}^{(2)}\mu_0}\vec{B}_i^{(2)}\cdot\vec{t}_i \tag{19}$$

Indices (1) and (2) denote the flux density above or below the boundary element i with respect to the normal direction $\vec{n}_i$ whereas $\mu_{r,i}^{(1)}$ and $\mu_{r,i}^{(2)}$ are the relative permeabilities at the sides of boundary element i. Equation (19) results by the help of (14) and (18) in the set of constraint equations for the magnetic surface currents $I_{ma,l}$ (Summation is taken over all volume elements k and all boundary elements l. Boundary currents of element i are excluded from summation):

$$\frac{1}{2}\left[\frac{1}{\mu_{r,i}^{(1)}}+\frac{1}{\mu_{r,i}^{(2)}}\right]I_{ma,i}+\left[\frac{1}{\mu_{r,i}^{(1)}}-\frac{1}{\mu_{r,i}^{(2)}}\right]\left[\sum_k \mu_{r,k}h_{V,ik}I_k+\sum_{l\neq i}h_{a,il}I_{ma,l}\right]=0 \tag{20}$$

Now Equation (1) is integrated over an arbitrary closed loop C_ν within conductive materials by the use of (10) and (4). The integration is taken over all circuit elements i of loop C_ν which is denoted by the summation index $i(C_\nu)$. Since we assume a constant current density of each circuit element i the integration can include the averaging over the cross section q_i perpendicular to the current direction:

$$\sum_{i(C_\nu)} s_{R,i}\frac{l_i}{\gamma_i q_i}q_i J_i(t)+\sum_{i(C_\nu)}\left[\frac{\mu_0}{4\pi}\sum_k \mu_{r,k}s_{ik}\left(\frac{1}{q_i}\int_{V_i}\int_{V_k}\frac{dV_i dV_k}{|\vec{r}_i-\vec{r}_k|}\right)\frac{\partial J_k(t)}{\partial t}\right]$$
$$+\sum_{i(C_\nu)}\left[\frac{\mu_0}{4\pi}\sum_l s_{il}\left(\frac{1}{q_i}\int_{V_i}\int_{a_l}\frac{dV_i da_l}{|\vec{r}_i-\vec{r}_l|}\right)\frac{\partial J_{ma,l}(t)}{\partial t}\right]=U_{q,\nu}(t) \tag{21}$$

In (21) the integration over the external electric field $\vec{E}_e(t)$ of the loop results in the voltage $U_{q,\nu}(t)$ of external sources. Summation $\sum_k$ is taken over all volume elements k and summation $\sum_l$ is taken over all boundary elements l. The direction of circuit elements and its currents is defined toward a positive Cartesian direction. Therefore the signs of the element-wise resistance s_{R_i} and the signs of element-wise inductance s_{ik} are defined in (21) with respect to the circulation of the loop C_ν:

$$s_{R,i}=\begin{cases}+1: & \text{Element i parallel to circulation of } C_\nu\\ -1: & \text{Element i anti-parallel to circulation of } C_\nu\end{cases} \tag{22}$$

$$s_{ik}=\begin{cases}0: & \text{Elements i and k with perpendicular currents}\\ +1: & \text{Element i parallel to circulation of } C_\nu\\ -1: & \text{Element i anti-parallel to circulation of } C_\nu\end{cases} \tag{23}$$

We introduce in (21) the resistances R_i, the self and mutual inductances $L_{V,ik}$ of volume elements and the mutual inductances $L_{a,il}$ between a volume element i and a boundary element k. Note that mutual inductances are defined only in the case of parallel current directions. The b_l is the width of the boundary element l with respect to its current direction:

$$R_i=\frac{l_i}{\gamma_i q_i}\qquad L_{V,ik}=\frac{\mu_0}{4\pi}\frac{1}{q_i q_k}\int_{V_i}\int_{V_k}\frac{dV_i dV_k}{|\vec{r}_i-\vec{r}_k|}\qquad L_{a,il}=\frac{\mu_0}{4\pi}\frac{1}{q_i b_l}\int_{V_i}\int_{a_l}\frac{dV_i da_l}{|\vec{r}_i-\vec{r}_l|} \tag{24}$$

In the harmonic case with angular frequency ω Equation (21) can be rewritten with the complex-valued currents $\underline{I}_k$ of volume elements and the complex-valued currents $\underline{I}_{ma,l}$ of boundary elements:

$$\sum_i s_{R,i}R_i\underline{I}_i+j\omega\sum_{i(C_\nu)}\sum_k s_{ik}\mu_{r,k}L_{V,ik}\underline{I}_k+j\omega\sum_{i(C_\nu)}\sum_l s_{il}L_{a,il}\underline{I}_{ma,l}=\underline{U}_q \tag{25}$$

Equations (20) and (25) provide a complete system of linear equations for the currents $\underline{I}_k$ and $\underline{I}_{ma,l}$. Replacing the currents $\underline{I}_k$ of volume elements k by appropriated mesh currents the linear system of equation can easily be solved by the mesh current method.

3. APPLICATION TO EDDY-CURRENT TESTING

An excitation coil carries a harmonic current with an amplitude $I_e = 1\,\mathrm{mA}$ at a frequency of 300 Hz or 700 Hz respectively (see Fig. 6). The primary excitation coil and the exploring coil have a

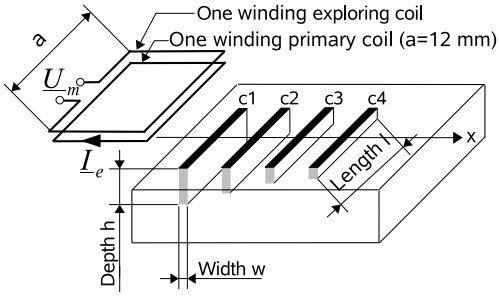

Figure 6: Geometry of the sample problem. The equidistant cracks have the same width, length and medium distance, by vary in height, see Table 1.

Table 1: Crack geometry of the ferromagnetic block, see Figure 6. Cracks are positioned at x and have the length l, the width w and the depths h.

Crack No. *(label)*	x [cm]	l [mm]	w [mm]	h [mm]
1 (c1)	0.0	12.6	0.28	1.2
2 (c2)	2.4	12.6	0.28	0.8
3 (c3)	3.6	12.6	0.28	0.4
4 (c4)	4.8	12.6	0.28	0.2

coincident quadratic shape with an edge length $a = 12\,\text{mm}$ and are positioned at a height of 2 mm above the ferromagnetic block. The crack geometry is given in Table 1. The medium distance between two cracks is 2.4 cm. The ferromagnetic block has a relative permeability of $\mu_r = 200$.

The aim of the simulation is the variation of the induced voltage in the exploring coil with the position of the coil center. The induced voltage $U_{m,wc}(x)$ is normalized to the voltage $U_{m,oc}$, which occurs at the absence of cracks:

$$\left|\frac{\Delta U_m(x)}{U_{m,oc}}\right| = \left|\frac{U_{m,wc}(x) - U_{m,oc}}{U_{m,oc}}\right| \tag{26}$$

A couple of simulation runs where performed to determine $U_{m,wc}(x)$ with varying coil center position x. The results are shown in Fig. 7. As expected, we obtain a maximum induced voltage when the coil center is situated above a crack. All cracks can be resolved at the proposed frequencies. The height of the maxima of the normalized measurement voltages increases with crack depth.

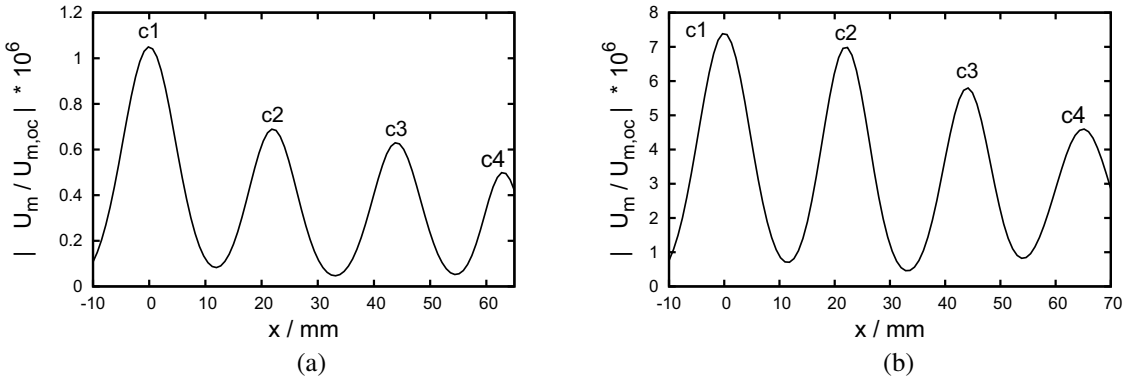

Figure 7: Variation of normalized measurement voltage given by Equation (26). The deepest crack is situated at $x = 0$, see Figure 6. (a) $\mu_r = 200$ and $f = 300\,\text{Hz}$, (b) $\mu_r = 200$ and $f = 700\,\text{Hz}$.

REFERENCES

1. Drechsler, S. and A. Farschtschi, "Dreidimensionale wirbelstromrechung mit der Finiten-Netzwerk-Methode (FNM)," it 40. IKW Imenau, Vol. 2, 180–185, 1995.

2. Drechsler, S., A. Farschtschi, J. Plontke, and H.-J. Roscher, "Berücksichtigung von ferromagnetischem material in der FNM durch einführung von magnetisierungsstromdichten," *Electrical Engineering*, Vol. 81, 56–68, Springer-Verlag, 1998.
3. Ruehli, A. E., "Inductance calculations in a complex integrated circuit environment," *IBM J. RES. DEVELOP.*, 470–481, Sept. 1972.
4. Heeb, H. and A. E. Ruehli, "Three-dimensional interconnect analysis using partial element equivalent circuits," *IEEE Trans. on Circuits and Systems*, Vol. 33, No. 11, 974–981, 1992.
5. Long, H., Z. Feng, H. Feng, A. Wang, and T. Ren, "magPEEC: Extended PEEC modeling for 3D arbitrary electro-magnetic devices with application for M-Cored inductors," *Proceedings of IEEE Radio Frequency Integrated Circuits Symposium 2003*, 251–254, 2003.

Calculation of Electromagnetic Field with Integral Equation Based on Clifford Algebra

A. Chantaveerod[1], **A. D. Seagar**[2], **and T. Angkaew**[1]

[1]Department of Electrical Engineering, Chulalongkorn University, Thailand
[2]Department of Telecommunication, Srivijaya University of Technology, Thailand

Abstract— Multidimensional Cauchy integrals are used to calculate numerically the electromagnetic field radiated internally and externally from surfaces on which the field is specified. The calculations are carried fully in the form of Clifford arithmetic and the results appear in the form of Clifford numbers, which are subsequently separated into electric and magnetic fields and compared directly with known analytical results.

1. INTRODUCTION

Maxwell's equations were first recast using vector calculus into the Helmholtz equation in about 1881. Since that time a variety of numerical methods have been developed to calculate the electromagnetic field using the Helmholtz equation either in differential form (such as the finite difference method (FDM) [1–4], the finite element method (FEM) [5–10] and the finite-difference time-domain method (FDTD) [11–13]) or in an integral form (such as the boundary element method (BEM) [14–22]). Characteristic of these methods is the separate treatment of the electric and magnetic fields because the Helmholtz equation is developed by eliminating one field or the other, and because a single three-dimensional vector cannot simultaneously represent both.

Somewhat earlier, around 1878, Maxwell's equations had been cast into the language of Clifford algebra, but this approach was less well known and was, for a long time, not taken seriously. More recently, applications of this algebra in mathematical physics, such as electromagnetism, gravitation and multi-particle quantum mechanics, have been studied by Lasenby, Doran and Arcaute [23]. In the Clifford approach the electric and magnetic fields are treated together, both encoded as a bivector into one part of a four-dimensional Clifford number [24, 25]. Maxwell's equations themselves are embedded into the Clifford algebra in the form of the k-Dirac equation [26], which in some senses behaves like the square root of the Helmholtz equation (see Section 2.2).

Conceptually, the method for solving Maxwell's equations using Clifford algebra is no different than for vector calculus. Using vector calculus an integral equation is constructed from the solution of the Helmholtz equation for a point source of radiation (i.e., the Green's function [11, 27]). The integral equation can be used to calculate the value of the field's potential on or off a closed surface if the potential on the surface is already known. This approach has been used widely for analysing electromagnetic field problems such as resonance [1, 2], waveguides [4, 5, 10], two-dimensional scattering [14, 19], three-dimensional scattering [20] and optical waveguides [3, 22].

Alternatively, using Clifford algebra, an integral equation is constructed from the solution of the k-Dirac equation for a point source of radiation. This integral equation can be used to calculate the value of the field (not the potential) on or off a closed surface if the field on the surface is already known. The key tools necessary to apply this approach, i.e., the fundamental solution for a point source [26], a discussion of boundary element methods for the k-Dirac equation [28, 29] and a method for treating interfaces between regions with different material properties [30] are already documented in the mathematical literature. However, it seems that they have not yet been applied.

The purpose of this article is to make the first step in developing a new numerical method for use in engineering problems, by applying Clifford algebra in an integral equation framework to the solution of Maxwell's equations, and to verify that the results are as expected. Section 2 reviews the fundamentals of applying Clifford algebra to Maxwell's equations, which are then used in Section 3 to introduce the key integral operators for solving electromagnetic field (*not* potential) problems. Section 4 compares for two simple test cases the fields calculated on and off a closed surface, with known analytical results. Concluding remarks are presented in Section 5.

2. BACKGROUND

2.1. Clifford Numbers and Arithmetic

A four-dimensional Clifford number $C_{(4)}$ is suitable for representing the electromagnetic field in either the time domain or in the frequency domain. Such a number has the general form

$$\begin{aligned} C_{(4)} \;=\; & a_0 + a_1e_1 + a_2e_2 + a_3e_1e_2 + a_4e_3 + a_5e_1e_3 + a_6e_2e_3 + a_7e_1e_2e_3 + a_8e_4 + a_9e_1e_4 \\ & + a_{10}e_2e_4 + a_{11}e_1e_2e_4 + a_{12}e_3e_4 + a_{13}e_1e_3e_4 + a_{14}e_2e_3e_4 + a_{15}e_1e_2e_3e_4 \end{aligned} \tag{1}$$

There are sixteen components, each of which contains two parts: one numeric and one symbolic. The numeric part a_i is complex number. The symbolic parts are divided into 5 grades containing respectively the symbols: 1 in grade 0; e_1, e_2, e_3 and e_4 in grade 1; e_1e_2, e_2e_3, e_3e_4, e_2e_3, e_2e_4 and e_3e_4 in grade 2; $e_1e_2e_3$, $e_1e_3e_4$ and $e_2e_3e_4$ in grade 3; and finally $e_1e_2e_3e_4$ in grade 4. Usually the symbol for grade zero is left unwritten, as in Eq. (1).

Two Clifford numbers can be added by bringing together all of the components containing the same symbolic parts and adding the corresponding numeric parts. Multiplication of two Clifford numbers can be performed by using the distributive law of multiplication over addition. The 256 components so produced can be reduced to the original sixteen by using two rules of multiplication which apply to the symbolic parts of Clifford numbers

$$e_ie_j \;=\; \begin{cases} -1 & \text{if} \quad i = j \\ -e_je_i & \text{if} \quad i \neq j \end{cases} \tag{2}$$

The same two rules can be used to reduce the squares of the original sixteen symbolic parts to either $+1$ or -1. Symbolic parts of Clifford numbers which reduce to plus or minus *unity* when squared, are called *units* of the Clifford number.

2.2. Maxwell-Dirac Equation

For the purposes of simplicity the discussion here is limited to electromagnetic fields which are time harmonic as $e^{i\omega t}$ with an angular frequency ω, in a source free region of space where the material properties are uniform, linear and isotropic. In this case Maxwell's equations can be written in vector notation as

$$\begin{cases} \nabla \cdot \overline{\mathbf{E}} \;=\; 0 \\ \nabla \times \overline{\mathbf{H}} - i\omega\epsilon\overline{\mathbf{E}} \;=\; 0 \\ \nabla \times \overline{\mathbf{E}} + i\omega\mu\overline{\mathbf{H}} \;=\; 0 \\ \nabla \cdot \overline{\mathbf{H}} \;=\; 0 \end{cases} \tag{3}$$

where $\overline{\mathbf{E}} = E_x\overline{\mathbf{a}}_x + E_y\overline{\mathbf{a}}_y + E_z\overline{\mathbf{a}}_z$ and $\overline{\mathbf{H}} = H_x\overline{\mathbf{a}}_x + H_y\overline{\mathbf{a}}_y + H_z\overline{\mathbf{a}}_z$ are the electric and magnetic fields respectively, and where ϵ and μ are the electric permittivity and magnetic permeability.

When embedded in Clifford algebra the same equations can be written as a single first order partial differential equation, the Maxwell-Dirac equation [26]

$$D_k u \;=\; 0 \tag{4}$$

where D_k is a differential operator, u is the electromagnetic field and $k = \omega/\sqrt{\mu\epsilon}$ is the wavenumber. The differential operator D_k, which can be written as the Clifford number

$$D_k \;=\; \frac{\partial}{\partial x}e_1 + \frac{\partial}{\partial y}e_2 + \frac{\partial}{\partial z}e_3 - ke_4 \tag{5}$$

is called either the Maxwell-Dirac operator or the k-Dirac operator. The Clifford unit e_4 plays the role of the time dimension. The Clifford units e_1, e_2 and e_3 similarly play the role of the Cartesian unit vectors $\overline{\mathbf{a}}_x$, $\overline{\mathbf{a}}_y$ and $\overline{\mathbf{a}}_z$ respectively. Simple algebra using the rules of Eq. (2) shows that $-D_k^2 = \frac{\partial^2}{\partial x^2} + \frac{\partial^2}{\partial y^2} + \frac{\partial^2}{\partial z^2} + k^2 = \nabla^2 + k^2 = H_k$, the Helmholtz operator.

The Clifford number u represents both the electric and magnetic fields in the form

$$u \;=\; \mu^{\frac{1}{2}}(H_xe_2e_3 - H_ye_1e_3 + H_ze_1e_2) \;+\; i\epsilon^{\frac{1}{2}}(E_xe_1 + E_ye_2 + E_ze_3)e_4 \tag{6}$$

The Maxwell-Dirac Eq. (4) can be expanded into components by using Eqs. (5) and (6), along with the rules of Eq. (2) for multiplication of Clifford units

$$D_k u \;=\; \left\{ \begin{array}{ll} -i\epsilon^{\frac{1}{2}}(\nabla\cdot\overline{\mathbf{E}})e_4 & \in T\Lambda^1 \\ +\mu^{\frac{1}{2}}[\nabla\times\overline{\mathbf{H}} - i\omega\epsilon\overline{\mathbf{E}}] & \in S\Lambda^1 \\ -i\epsilon^{\frac{1}{2}}[\nabla\times\overline{\mathbf{E}} + i\omega\mu\overline{\mathbf{H}}](e_1e_2e_3)e_4 & \in T\Lambda^3 \\ +\mu^{\frac{1}{2}}(\nabla\cdot\overline{\mathbf{H}})(e_1e_2e_3) & \in S\Lambda^3 \end{array} \right\} \;=\; 0 \tag{7}$$

The resulting Clifford number occupies time-like components T (containing the time unit e_4) and space-like components S (where the unit e_4 is missing) of both grade 1 (Λ^1) and grade 3 (Λ^3). These four components in the order listed represent respectively source free differential statements of Gausses' law, the Ampere-Maxwell law, Faraday's law, and a magnetic version of Gausses' law.

2.3. Fundamental Solution

The fundamental solution $B_k(r)$ for the potential associated with a point source of radiation satisfies the scalar-valued relationship $H_kB_k(r)=\delta(r)$, where H_k is the Helmholtz operator, r is radial distance, and $\delta(r)$ is a delta function at the origin $r=0$. The potential $B_k(r)$ is known as the Bessel potential.

In the case of the field, the fundamental solution $F_k(\overline{\mathbf{r}})$ satisfies the Clifford-valued relationship $D_kF_k(\overline{\mathbf{r}}) = \delta(|\overline{\mathbf{r}}|)$ where D_k is the k-Dirac operator, $\overline{\mathbf{r}} = xe_1 + ye_2 + ze_3$ is a Clifford number representing a point with Cartesian coordinates x, y, z and $\delta(|\overline{\mathbf{r}}|)$ is as before.

Putting $H_k=-D_k^2$ from Section 2.2 into the scalar-valued relationship and then inspecting the Clifford-valued one gives $F_k(\overline{\mathbf{r}})$ directly from the Bessel potential [26]

$$F_k(\overline{\mathbf{r}}) \;=\; -D_kB_k(|\overline{\mathbf{r}}|) \;=\; -D_k\left(-\frac{1}{4\pi|\overline{\mathbf{r}}|}e^{-ik|\overline{\mathbf{r}}|}\right) \;=\; \left\{-\frac{\overline{\mathbf{r}}}{|\overline{\mathbf{r}}|^2} + ik\left(ie_4 - \frac{\overline{\mathbf{r}}}{|\overline{\mathbf{r}}|}\right)\right\}\frac{e^{-ik|\overline{\mathbf{r}}|}}{4\pi|\overline{\mathbf{r}}|} \tag{8}$$

3. INTEGRAL EQUATIONS FOR FIELD

Construction of an integral equation for the potential is based on the fundamental solution of the Helmholtz operator together with Green's theorem. For the field, it is the fundamental solution of the k-Dirac operator and the boundary value theorem which are used instead [26]. The boundary value theorem can be written for two functions f and g

$$\int_\Sigma g(\overline{\mathbf{y}})n(\overline{\mathbf{y}})f(\overline{\mathbf{y}})\,d\sigma(\overline{\mathbf{y}}) \;=\; \int_{\Omega^+}\{(gD)(\overline{\mathbf{y}})f(\overline{\mathbf{y}}) + g(\overline{\mathbf{y}})Df(\overline{\mathbf{y}})\}\,d\overline{\mathbf{y}} \tag{9}$$

where $D=D_{k=0}$ is the Dirac (or Clifford) gradient, $\overline{\mathbf{y}}$ is a Clifford number representing a point on the boundary Σ or within its interior Ω^+, $n(\overline{\mathbf{y}})$ is a Clifford number representing the outward unit normal, and $d\sigma(\overline{\mathbf{y}})$ is the differential measure of area on the boundary.

The boundary theorem is more general than Green's theorem since the latter can be recovered from the former. This is achieved by first putting $g=0$, which gives both Stokes' theorem and the divergence theorem, and then by substituting into the divergence theorem as usual a vector field constructed from two scalar fields and their gradients. In the case of electromagnetic fields, it is more useful to put $g(\overline{\mathbf{y}})=E_k(\overline{\mathbf{y}}-\overline{\mathbf{x}})=-F_k(\overline{\mathbf{x}}-\overline{\mathbf{y}})$ the fundamental solution, and to put $f(\overline{\mathbf{y}})=u(\overline{\mathbf{y}})$ the field. The boundary value theorem then reduces to a different integral formulation [26]

$$u(\overline{\mathbf{x}}) \;=\; \int_\Sigma E_k(\overline{\mathbf{y}}-\overline{\mathbf{x}})n(\overline{\mathbf{y}})u(\overline{\mathbf{y}})\,d\sigma(\overline{\mathbf{y}}) \tag{10}$$

for the field u at one point $\overline{\mathbf{x}}$ inside the region Ω^+ from its value u at every point $\overline{\mathbf{y}}$ on the boundary Σ (see Figure 1). This result is in the form of a Cauchy integral with Clifford-valued functions in 4 dimensions [28] rather than the complex-valued functions in 2 dimensions [27] as is usually the case.

Eq. (10) is not the same style of integral as, for example, a Fredholm integral equation. There is no *equation* here to solve. Eq. (10) instead plays the role of a theorem that, for a function u which is monogenic (i.e., a solution to Eq. (4)) within some region Υ of space/time spanned by grade 1 of an n-dimensional Clifford algebra, states the following: "given any Cauchy surface Σ within Υ the trace of u on Σ can reproduce u in the sub-domain Ω^+ of Υ enclosed by Σ". In terms of applications

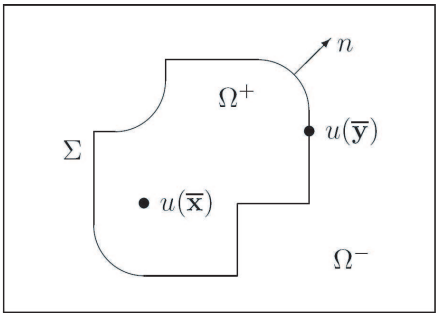

Figure 1: Calculation of field $u(\bar{\mathbf{x}})$ in region Ω^+ from its trace $u(\bar{\mathbf{y}})$ on the boundary Σ.

in electromagnetics this theorem may be restated as: "given the electromagnetic field on any closed surface in a region of space free of sources it is possible to reconstruct the field inside". However, Eq. (10) provides not only the assurance that reconstruction is possible but also provides the means (i.e., a formula) by which such a reconstruction may be achieved, as demonstrated in Section 4.

Since it is often of interest to obtain the field both inside and outside the boundary it is convenient to combine two copies of Eq. (10) into a single operator C, known as the Cauchy extension operator [26]

$$\begin{aligned}(Cu)(\overline{\mathbf{x}}) &= \int_\Sigma E_k(\overline{\mathbf{y}}-\overline{\mathbf{x}})n(\overline{\mathbf{y}})u(\overline{\mathbf{y}})\,d\sigma(\overline{\mathbf{y}}) \\ &= \begin{cases} u^+ & \overline{\mathbf{x}}\in\Omega^+ \\ -u^- & \overline{\mathbf{x}}\in\Omega^- \end{cases}\end{aligned} \tag{11}$$

where $u = u^+ + u^-$ and Ω^- is the region outside the boundary. The Cauchy extension operator can be used everywhere off the boundary.

For points on any smooth part of the boundary itself, the integral Eq. (10) returns only one half of the value of the field. To accommodate this case the operator C_Σ, known as the Cauchy integral operator [26]

$$(C_\Sigma u)(\overline{\mathbf{x}}) \;=\; 2\,\text{p.v.}\int_\Sigma E_k(\overline{\mathbf{y}}-\overline{\mathbf{x}})n(\overline{\mathbf{y}})u(\overline{\mathbf{y}})\,d\sigma(\overline{\mathbf{y}}) \tag{12}$$

should be used instead. The kernel of this integral is singular and must be evaluated in the sense of its principal value (p.v.).

Combining the Cauchy integral operator with other operators to link the fields on either side of the boundary provides a method for solving Maxwell's equations at the interface between two regions of different material properties. However, that is beyond the scope of the current work. See [26] and [30] for details.

4. NUMERICAL RESULTS

The Cauchy extension and Cauchy integral operators are applied here to calculate the electromagnetic field $u(\bar{\mathbf{x}})$ from its trace $u(\bar{\mathbf{y}})$ on the boundary Σ, for both the bounded region Ω^+ and the unbounded region Ω^-. For the bounded case the trace of the field is taken from an external (plane wave) source, and for the unbounded case the trace of the field is taken from an internal (short dipole) source. In both cases the boundary Σ takes the shape of a cube of $1\,\text{m}^3$ with its edges aligned to the axes of a Cartesian system of coordinates.

All of the calculations are carried using Clifford arithmetic, but the results are converted to vector form so they can be compared more easily with known solutions (*cf.* [31, 32]). Eq. (11) has been calculated using Gauss-Legendre integration [33]. Eq. (12), which contains a singularity, has been treated differently. Each side of the cube has been divided into square elements and rectangular integration used for all elements except the one containing the singularity. For that element, the integral equation has been recast in a local radial coordinate system. It is then possible to resolve the singular terms and to determine the value of the integral.

4.1. Bounded Region

A uniform plane wave travelling in the positive z direction written in terms of electric and magnetic fields as [31]

$$\begin{cases} \overline{\mathbf{E}}(x,y,z) &=& E_x\,\overline{\mathbf{a}}_x &=& E_0 e^{-j\beta z}\,\overline{\mathbf{a}}_x \\ \overline{\mathbf{H}}(x,y,z) &=& H_y\,\overline{\mathbf{a}}_y &=& H_0 e^{-j\beta z}\,\overline{\mathbf{a}}_y \end{cases} \tag{13}$$

was encoded into a Clifford number using Eq. (6) for points $\overline{\mathbf{y}}$ on the boundary Σ. Numerical values of $E_0 = 120\pi\,\mathrm{V/m}$ and $H_0 = 1\,\mathrm{A/m}$ were taken as the magnitudes of electric and magnetic fields respectively, and a numerical value of $\beta = 1\,\mathrm{r/s}$ was taken for the phase velocity. Values of the Clifford field u for points $\overline{\mathbf{x}}$ both on and off the boundary were calculated as described in Section 4, and then separated into electric and magnetic fields $\overline{\mathbf{E}}$ and $\overline{\mathbf{H}}$. The results are shown in Tables 1 to 4 and in Figures 2 to 5, along with fields calculated directly from Eq. (13) for comparison.

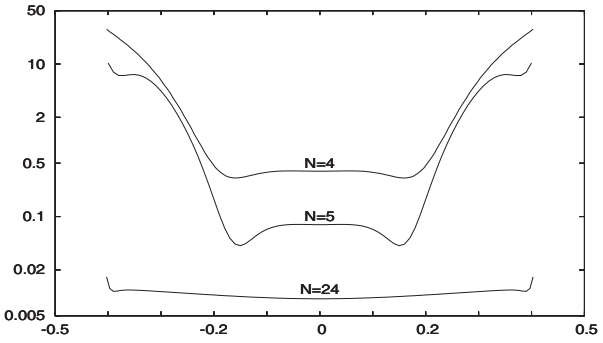

Figure 2: Error (%) in $\bar{\mathbf{E}}$ field along diagonal line in central plane.

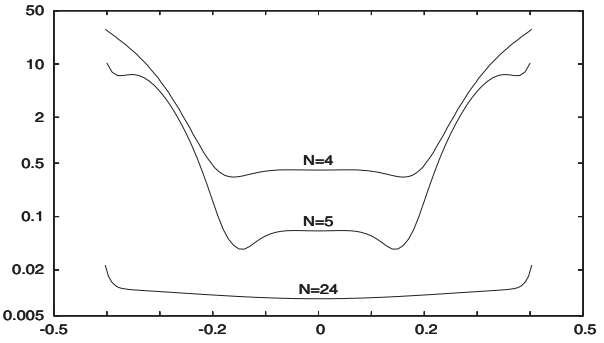

Figure 3: Error (%) in $\bar{\mathbf{H}}$ field along diagonal line in central plane.

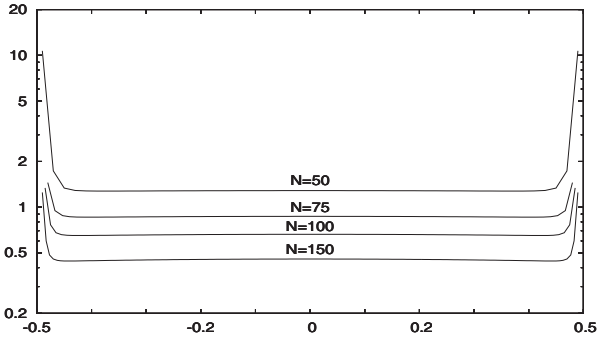

Figure 4: Error (%) in $\bar{\mathbf{E}}$ field along diagonal line on bottom face.

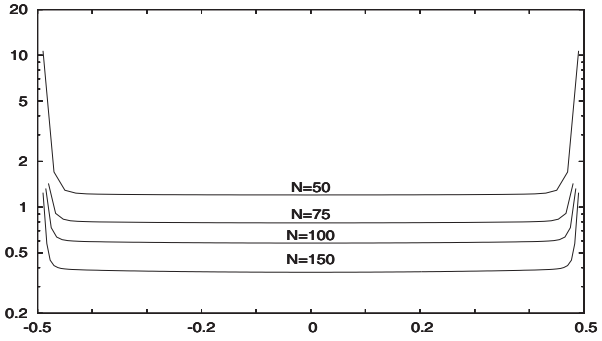

Figure 5: Error (%) in $\bar{\mathbf{H}}$ field along diagonal line on bottom face.

4.1.1. Cauchy Extension

Table 1 shows the fields at a point in the centre of the cube ($x = y = z = 0$) and Table 2 shows the fields at a point close to one corner of the cube ($x = y = z = 0.49$).

The error between the value delivered by the Cauchy extension and the known solution depends on both the location of the point $\overline{\mathbf{x}}$ at which the field is calculated and on the number N of points $\overline{\mathbf{y}}$ used as samples to represent the field on the boundary. For Tables 1 and 2 the number of samples N is fixed to a single value. As the point $\overline{\mathbf{x}}$ approaches the boundary the behaviour of the kernel of the Cauchy extension approaches that of a singular function. Unless special care is taken any fixed number of samples leads to higher error.

The error can be reduced if the number of samples is increased, as shown in Figures 2 and 3. These figures show the percentage error along a diagonal line from $x = y = -0.5$ to $x = y = 0.5$ in the central plane $z = 0$ for both electric and magnetic fields as the number of samples is increased from $N = 4$ to $N = 24$.

Table 1: Fields at centre of cube.

		Cauchy extension		exact	
		E V/m	**H** A/m	**E** V/m	**H** A/m
$\overline{a}_x$	$\Re$	377.0157	0.0	376.9911	0.0
	$\Im$	–0.0185	0.0	0.0	0.0
$\overline{a}_y$	$\Re$	0.0	0.999930	0.0	1.0
	$\Im$	0.0	0.000492	0.0	0.0
$\overline{a}_z$	$\Re$	0.0	0.0	0.0	0.0
	$\Im$	0.0	0.0	0.0	0.0

Table 2: Fields near corner of cube.

		Cauchy extension		exact	
		E V/m	**H** A/m	**E** V/m	**H** A/m
$\overline{a}_x$	$\Re$	327.9228	0.0	332.6316	0.0
	$\Im$	–174.8668	0.0	–177.4217	0.0
$\overline{a}_y$	$\Re$	0.0	0.870444	0.0	0.882943
	$\Im$	0.0	–0.463881	0.0	–0.470951
$\overline{a}_z$	$\Re$	–0.0135	0.000916	0.0	0.0
	$\Im$	0.0345	0.000358	0.0	0.0

4.1.2. Cauchy Integral

Table 3 shows the fields at a point in the centre of the bottom face of the cube ($x=y=0, z=-0.5$) and Table 4 shows the fields at a point on the same face close to one corner of the cube ($x=y=0.49, z=-0.5$).

The singularity on the bottom face itself is accounted for in the calculation. However, as the point $\overline{\mathbf{x}}$ approaches any adjacent face the behaviour of the kernel again approaches that of a singular function. For Tables 3 and 4 the number of samples is fixed to a single value. In this case a higher error at the corner is to be expected.

Table 3: Fields at centre of bottom face.

		Cauchy integral		exact	
		E V/m	**H** A/m	**E** V/m	**H** A/m
$\overline{a}_x$	$\Re$	331.3588	0.0	330.8408	0.0
	$\Im$	179.7766	0.0	180.7391	0.0
$\overline{a}_y$	$\Re$	0.0	0.878589	0.0	0.877582
	$\Im$	0.0	0.477618	0.0	0.479425
$\overline{a}_z$	$\Re$	0.0001	9×10^{-8}	0.0	0.0
	$\Im$	0.0012	0.000003	0.0	0.0

Table 4: Fields near corner of bottom face.

		Cauchy integral		exact	
		E V/m	**H** A/m	**E** V/m	**H** A/m
$\overline{a}_x$	$\Re$	331.3701	0.0	330.8408	0.0
	$\Im$	180.1692	0.0	180.7391	0.0
$\overline{a}_y$	$\Re$	0.0	0.878829	0.0	0.877582
	$\Im$	0.0	0.478334	0.0	0.479425
$\overline{a}_z$	$\Re$	0.6793	0.001782	0.0	0.0
	$\Im$	0.3224	0.001102	0.0	0.0

The error can be reduced if the number of samples is increased, as shown in Figures 4 and 5. These figures show the percentage error along a diagonal line from $x=y=-0.5$ to $x=y=0.5$ in the bottom face $z=-0.5$ for both electric and magnetic fields as the number of samples is increased from $N=50$ to $N=150$.

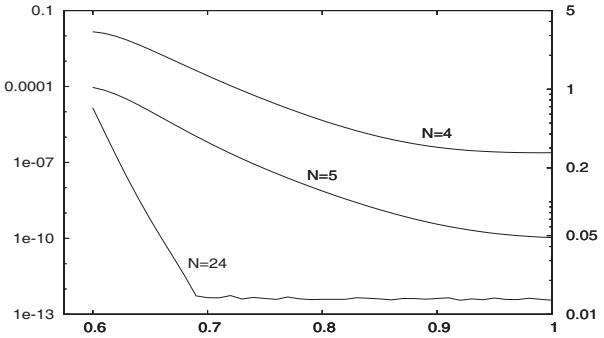

Figure 6: Error (%) in $\bar{\mathbf{E}}$ field along vertical line above centre of top face. $N = 4, 5$ on right scale, $N = 24$ on left scale.

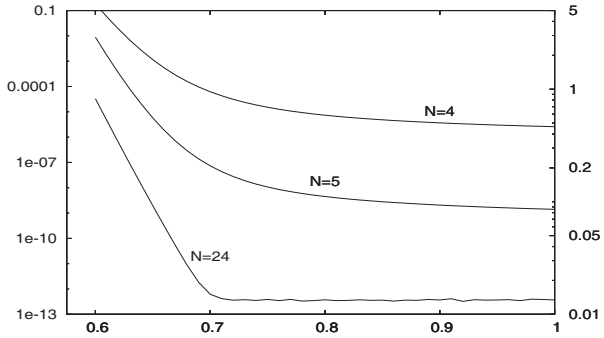

Figure 7: Error (%) in $\bar{\mathbf{H}}$ field along vertical line above centre of top face. $N = 4, 5$ on right scale, $N = 24$ on left scale.

4.2. Unbounded Region

The wave emanating from a short (Hertzian) dipole oriented along the positive z direction written in terms of electric and magnetic fields as [32]

$$\begin{cases} \overline{\mathbf{E}}(x,y,z) = E_r\,\overline{\mathbf{a}}_r + E_\theta\,\overline{\mathbf{a}}_\theta = \frac{I_0\ell}{4\pi}e^{-j\beta r}\left[\left(\frac{2\eta}{r^2}+\frac{2}{j\omega\epsilon r^3}\right)\cos\theta\,\overline{\mathbf{a}}_r + \left(\frac{j\omega\mu}{r}+\frac{1}{j\omega\epsilon r^3}+\frac{\eta}{r^2}\right)\sin\theta\,\overline{\mathbf{a}}_\theta\right] \\ \overline{\mathbf{H}}(x,y,z) = H_\phi\overline{\mathbf{a}}_\phi \qquad\qquad = \frac{I_0\ell}{4\pi}e^{-j\beta r}\left(\frac{j\beta}{r}+\frac{1}{r^2}\right)\sin\theta\,\overline{\mathbf{a}}_\phi \end{cases} \tag{14}$$

was converted to Cartesian coordinates and encoded into a Clifford number using Eq. (6) for points $\overline{\mathbf{y}}$ on the boundary Σ. Numerical values of $I_0 = 1\,\mathrm{A}$ and $\ell = 0.04\,\mathrm{m}$ were taken as the magnitude of the current and the length of the dipole respectively, and a numerical value of $\beta = 1\,\mathrm{r/s}$ was taken for the phase velocity. Free space values were taken for the electric permittivity ϵ, magnetic permeability μ and intrinsic impedance $\eta = \sqrt{\mu/\epsilon}$. Values of the Clifford field u for points $\overline{\mathbf{x}}$ both on and off the boundary were calculated as described in Section 4, and then separated into electric and magnetic fields $\overline{\mathbf{E}}$ and $\overline{\mathbf{H}}$. The results are shown in Tables 5 to 8 and in Figures 6 to 9, along with fields calculated directly from Eq. (14) (converted to Cartesian coordinates) for comparison.

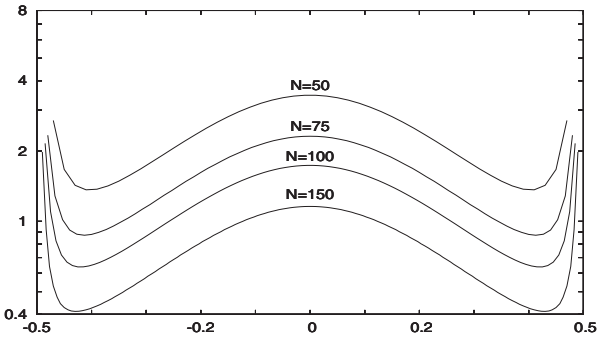

Figure 8: Error (%) in $\bar{\mathbf{E}}$ field along diagonal line on bottom face.

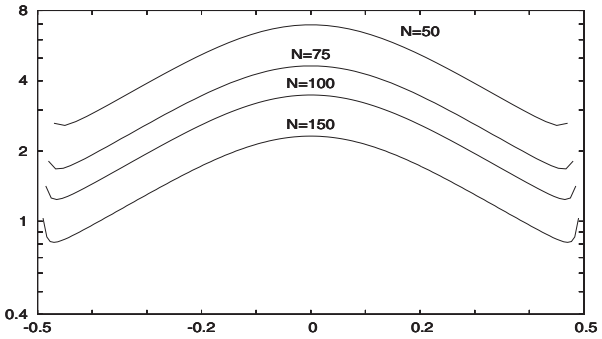

Figure 9: Error (%) in $\bar{\mathbf{H}}$ field along diagonal line on bottom face.

4.2.1. Cauchy Extension

Table 5 shows the fields at a point vertically above the centre of the top face of the cube ($x = y = 0, z = 1$) and Table 6 shows the fields at the same height but closer to one corner of the cube ($x = y = 0.49, z = 1$). In both cases the vertical distance to the top face is the same as the distance between the top face and the centre of the cube. The error in these two cases is not significantly different, because the shortest distance to the surface is the same.

Table 5: Fields above centre of top face.

		Cauchy extension		exact	
		E V/m	**H** A/m	**E** V/m	**H** A/m
$\overline{a}_x$	$\Re$	0.0	0.0	0.0	0.0
	$\Im$	0.0	0.0	0.0	0.0
$\overline{a}_y$	$\Re$	0.0	0.0	0.0	0.0
	$\Im$	0.0	0.0	0.0	0.0
$\overline{a}_z$	$\Re$	–0.722302	0.0	–0.722304	0.0
	$\Im$	–3.313951	0.0	–3.313962	0.0

Table 6: Fields above corner of top face.

		Cauchy extension		exact	
		E V/m	**H** 10^{-3}A/m	**E** V/m	**H** 10^{-3}A/m
$\overline{a}_x$	$\Re$	–0.003519	–1.2869	–0.003519	–1.2869
	$\Im$	–0.870808	0.4469	–0.870809	0.4469
$\overline{a}_y$	$\Re$	–0.003519	–1.2869	–0.003519	–1.2869
	$\Im$	–0.870808	0.4469	–0.870809	0.4469
$\overline{a}_z$	$\Re$	–0.652704	0.0	–0.652705	0.0
	$\Im$	–1.128192	0.0	–1.128193	0.0

Figures 6 and 7 show the percentage error along a line vertically above the centre of the top face of the cube from $x = y = 0, z = 0.6$ to $x = y = 0, z = 1$. The error is seen to decrease with distance from the surface and to decrease as the number of samples is increased from $N = 4$ to $N = 24$.

4.2.2. Cauchy Integral

Table 7 shows the fields at a point in the centre of the bottom face of the cube ($x = y = 0, z = -0.5$) and Table 8 shows the fields at point on the same face close to one corner of the cube ($x = y = 0.49, z = -0.5$). The error is higher near the corner for exactly the same reasons as described in Section 4.1.2.

The error can be reduced if the number of samples is increased, as shown in Figures 8 and 9. These figures show the percentage error along a diagonal line from $x = y = -0.5$ to $x = y = 0.5$ in the bottom face $z = -0.5$ for both electric and magnetic fields as the number of samples is increased from $N = 50$ to $N = 150$.

Table 7: Fields at centre of bottom face.

	Cauchy integral		exact	
	E 10^{-4}V/m	**H** 10^{-4}A/m	**E** 10^{-4}V/m	**H** 10^{-4}A/m
$\overline{a}_x$ $\Re$	3.9262	2.8200	3.9588	2.8419
$\Im$	5.9984	–0.10344	5.9668	–0.10647
$\overline{a}_y$ $\Re$	3.9262	2.8200	3.9588	2.8419
$\Im$	5.9984	–0.10344	5.9668	–0.10647
$\overline{a}_z$ $\Re$	–7796.0	0.0	–7795.5	0.0
$\Im$	–2138.9	0.0	–2130.6	0.0

Table 8: Fields near corner of bottom face.

	Cauchy integral		exact	
	E 10^{-6}V/m	**H** 10^{-6}A/m	**E** 10^{-6}V/m	**H** 10^{-6}A/m
$\overline{a}_x$ $\Re$	–6.5618	–3.6356	–6.5695	–3.6458
$\Im$	5.3140	0.54108	5.5302	0.54135
$\overline{a}_y$ $\Re$	–6.5618	–3.6356	–6.5695	–3.6458
$\Im$	5.3140	0.54108	5.5302	0.54135
$\overline{a}_z$ $\Re$	2.0307	0.0	2.0047	0.0
$\Im$	–2.1005	0.0	–2.1012	0.0

5. CONCLUSION

The algebra developed by Clifford [34] offers a boundary integral method for the solution of Maxwell's equations based on fields, complementary to the more traditional method based on potentials and Green's functions. From a theoretical viewpoint, both methods are similar — involving integrals which in some cases contain integrable singularities and in other cases are non-singular.

From a practical viewpoint the methods to deal with singularities (or near singularities) for both methods are the same. The behaviour of a straightforward numerical implementation is similar — with errors increasing when approaching any piece of boundary for which singular or near-singular behaviour has not been explicitly taken into account.

The usual method of increasing the number of points used to represent (sample) the field on the boundary shows (as expected) a reduction in the error. For the simple rectangular method of integration used with the Cauchy integral (Eq. (12)) an error of around 1% can be achieved with 100 samples, and this error can be reduced if the number of samples is increased. For the more sophisticated integration used with the Cauchy extension (Eq. (11)) the same levels of error can be achieved with fewer samples. It seems preferable to use the more sophisticated techniques, certainly for the Cauchy extension and probably also for the Cauchy integral provided that they can be modified so as to properly account for the singularity therein. A full error analysis has not been attempted here. For a detailed theoretical mathematical error analysis the work of Mitrea and Mitrea [35] should be consulted.

The examples presented here serve as a simple test to determine whether the Cauchy integrals based on Clifford algebra, which from a theoretical standpoint are unassailable, contain hidden any behaviour which is either totally unexpected or significantly more detrimental for a numerical solution than alternative methods. The results do not show any such behaviour. From both a theoretical and numerical viewpoint it therefore makes good sense to include the Clifford-valued Cauchy integrals along with the complex-valued Cauchy integral and all of the other techniques in the armamentarium of methods for solving Maxwell's equations.

ACKNOWLEDGMENT

Two of the authors wish to acknowledge partial support in funding from the Cooperation Project between the Department of Electrical Engineering and Private Sector for Research and Development at Chulalongkorn University.

REFERENCES

1. Fernandes, P. and R. Parodi, "Computation of electromagnetic fields in multicell resonant structures for particle acceleration," *IEEE Trans. on Magnetics*, Vol. MAG-19, No. 6, 2421–2424, 1983.
2. Fernandes, P. and R. Parodi, "Computation of electromagnetic fields in TE and TM resonators and in waveguides," *IEEE Trans. on Magnetics*, Vol. MAG-21, No. 6, 2246–2249, 1985.
3. Michae, S., "Review of numerical methods for the analysis of arbitrarily shaped microwave and optical dielectric waveguides," *IEEE Trans. on Microwave Theory and Techniques*, Vol. MTT-33, No. 10, 894–899, 1985.
4. Dong, H., A. Chronopoulos, J. Zou, and A. Gopinath, "Vectorial integrated finite difference analysis of dielectric waveguides," *Jnl. of Lightwave Technol.*, Vol. 11, No. 10, 1559–1564, 1993.
5. Koshiba, M., K. Hayata, and M. Suzuki, "Finite element formulation in terms of the electric field vector for electromagnetic waveguide problems," *IEEE Trans. on Microwave Theory and Techniques*, Vol. MTT-33, No. 10, 900–905, 1985.

6. Moyer, E. T. Jr. and E. Schroeder, "Finite element formulations of Maxwell's equations — Advantages and comparisons between available approaches," *IEEE Trans. on Magnetics*, Vol. MAG-27, No. 5, 4217–4220, 1991.
7. Paulsen, K. D., W. E. Boyse, and D. R. Lynch, "Continuous potential Maxwell solution on nodal based finite elements," *IEEE Trans. on Antennas and Propagation*, Vol. 40, 1192–1200, 1992.
8. Boyse, W. E., D. R. Lynch, K. D. Paulsen, and G. N. Minerbo, "Applications of potentials to finite element modeling of Maxwell's equations," *IEEE Trans. on Magnetics*, Vol. 29, 1333–1336, 1993.
9. Clegg, S. T., K. A. Murphy, W. T. Joines, G. Rine, and T. V. Samulski, "Finite element computation of electromagnetic fields," *IEEE Trans. on Microwave Theory and Techniques*, Vol. 42, No. 10, 1984–1991, 1994.
10. Li, D. and H. Chang, "An efficient full-vectorial finite element modal analysis of dielectric waveguides incorporating inhomogeneous elements across dielectric discontinuities," *IEEE Jnl. on Quantum Electrics*, Vol. 36, No. 11, 1251–1261, 2000.
11. Holtzman, R. and R. Kastner, "The time domain discrete Green's function method (GFM) characterizing the FDTD grid boundary," *IEEE Trans. on Antennas and Propagation*, Vol. 49, 1079–1093, 2001.
12. Cottee, A., W. Ma, M. Rayner, and C. G. Parini, "Application of the DGF-FDTD technique to log periodic antennas," *In Proc. Twelfth International Conference on Antennas and Propagation (ICAP'03)*, Vol. 2, 553–556, 2003.
13. Ma, W., M. Rayner, and C. G. Parini, "Discrete Green's function formulation of the FDTD method and its application in antenna modeling," *IEEE Trans. on Antennas and Propagation*, Vol. 53, 339–346, 2005.
14. Mei, K. and J. V. Bladel, "Scattering by perfectly conducting rectangular cylinders," *IEEE Trans. on Antennas and Propagation*, Vol. 11, 185–192, 1963.
15. Wang, T. N. C., "A set of integral equations for electromagnetic wave radiation from an arbitrary source in a linear, lossy, inhomogeneous, cold magnetic medium," *Proceedings of the IEEE*, Vol. 59, 1724–1725, 1971.
16. Lean, M. H. and A. Wexler, "Accurate field calculation with the boundary element method," *IEEE Trans. on Magnetics*, Vol. 18, No. 2, 331–335, 1982.
17. Kagami, S. and I. Fukai, "Application of boundary element method to electromagnetic field problems," *IEEE Trans. on Microwave Theory and Techniques*, Vol. 32, No. 4, 455–461, 1984.
18. Lean, M. H., "Application of boundary integral equation methods to electromagnetics," *IEEE Trans. on Magnetics*, Vol. MAG-21, No. 5, 1823–1828, 1985.
19. Toyoda, I., M. Matsuhara, and N. Kumakai, "Extended integral equation formulation for scattering problems from a cylindrical scatterer," *IEEE Trans. on Antennas and Propagation*, Vol. 36, No. 11, 1580–1586, 1988.
20. Rucker, W., E. Schlemmer, and K. R. Richter, "The solution of 3D multiple scattering problems using the boundary element method," *IEEE Trans. on Magnetics*, Vol. 30, No. 5, 3132–3135, 1994.
21. Cecchini, P., F. Bardati, and R. Ravanelli, "A general approach to edge singularity extraction near composed wedges in boundary element method," *IEEE Trans. on Microwave Theory and Techniques*, Vol. 49, No. 4, 730–733, 2001.
22. Lu, T. and D. Yevick, "A vectorial boundary element method analysis of integrated optical waveguides," *Jnl. of Lightwave Technol.*, Vol. 21, No. 8, 1793–1807, 2003.
23. Lasenby, A., C. Doran, and E. Arcaute, "Applications of geometric algebra in electromagnetism, quantum theory and gravity," In R. Ablamowicz, editor, *Proc. Sixth International Conference on Clifford Algebras and Their Application*, 467, 2003.
24. McIntosh, A. and M. Mitrea, "Clifford algebras and Maxwell's equations in Lipschitz domains," *Math. Meth. Appl. Sci.*, Vol. 22, 1599–1620, 1999.
25. Hestenes, D., "Oersted medal lecture 2002: Reforming the mathematical language of physics," *American Jnl. of Physics*, Vol. 71, No. 2, 101–121, 2003.
26. Axelsson, A., R. Grognard, J. Hogan, and A. McIntosh, "Harmonic analysis of Dirac operators on Lipschitz domains," *Clifford Analysis and Its Applications*, No. 25; *NATO Sci. Ser. II Math. Phys. Chem.*, 231–246, Dordrecht, 2001; Kluwer, Prague, 2000.
27. Morse, P. M. and H. Feshbach, *Methods of Theoretical Physics*, McGraw-Hill, New York, 1953.

28. McIntosh, A., "Clifford algebras and the higher dimensional Cauchy integral," *Approximation Theory and Function Spaces*, No. 22, 253–267, Banach Center Publications, 1989.
29. McIntosh, A., "Clifford algebras, Fourier theory, singular integrals and harmonic functions on Lipschitz domains," In John Ryan, editor, *Clifford Algebras in Analysis and Related Topics, Studies in Advanced Mathematics*, 33–87, CRC press, Boca Raton, 1996.
30. Axelsson, A., "Transmission problem for Dirac's and Maxwell's equations with Lipschitz interfaces," PhD thesis, Australian National University, Canberra, Australia, November 2002.
31. Balanis, C. A., *Advanced Engineering Electromagnetics*, Wiley, New York, 1989.
32. Balanis, C. A., *Antenna Theory Analysis and Design*, Wiley, New York, 1997.
33. Press, W. H., S. A. Teukolsky, W. T. Vetterling, and B. P. Flannery, *Numerical Recipes in C++ — The Art of Scientific Computing*, Cambridge University Press, 2 edition, 2002.
34. Clifford, W. K., "Applications of Grassmann's extensive algebra," In R. Tucker, editor, *Mathematical Papers by William Kingdon Clifford*, 265–276, Chelsea, 1968.
35. Mitrea, D. and M. Mitrea, "Finite energy solutions of Maxwell's equations and constructive Hodge decompositions on nonsmooth Riemannian manifolds," *Jnl. of Functional Analysis*, Vol. 190, No. 2, 339–417, 2002.

Wiener-Hopf Analysis of the Diffraction by a Terminated, Semi-infinite Parallel-plate Waveguide with Four-layer Material Loading

E. H. Shang and K. Kobayashi
Department of Electrical, Electronic, and Communication Engineering, Chuo University
1-13-27 Kasuga, Bunkyo-ku, Tokyo 112-8551, Japan

Abstract— We shall consider a four-layer-loaded cavity formed by a semi-infinite parallel-plate waveguide with an interior planar termination, and analyze the plane wave diffraction rigorously for E polarization by means of the Wiener-Hopf technique. Introducing the Fourier transform for the scattered field and applying boundary conditions in the transform domain, the problem is formulated in terms of the simultaneous Wiener-Hopf equations satisfied by the unknown spectral functions. The Wiener-Hopf equations are solved via the factorization and decomposition procedure leading to the exact solution. The scattered field in the real space is evaluated by taking the inverse Fourier transform and applying the saddle point method.

1. INTRODUCTION

Analysis of the scattering from open-ended metallic waveguide cavities has received much attention recently in connection with the prediction and reduction of the radar cross section (RCS) of a target [1]. A number of two- and three-dimensional (2-D and 3-D) cavity diffraction problems have been analyzed thus far by means of high-frequency ray techniques and numerical methods, but it appears that the solutions obtained by these approaches are not uniformly valid for arbitrary cavity dimensions.

In the previous papers [2, 3], we have carried out a rigorous RCS analysis of canonical 2-D cavities with and without material loading, formed by a finite parallel-plate waveguide, using the Wiener-Hopf technique. We have also considered a terminated, semi-infinite parallel-plate waveguide with three-layer material loading as a related cavity geometry, and carried out the Wiener-Hopf analysis of the plane wave diffraction [4, 5]. As an important generalization to the geometry in [4, 5], we shall consider, in this paper, a terminated, semi-infinite parallel-plate waveguide with four-layer material loading, and analyze the E-polarized plane wave diffraction by means of the Wiener-Hopf technique. Our final solution is shown to be valid for arbitrary cavity dimensions. Main results of this paper are already presented elsewhere [6].

The time factor is assumed to be $e^{-i\omega t}$, and suppressed throughout this paper.

2. FORMULATION OF THE PROBLEM

We consider the diffraction of an E-polarized plane wave by a terminated, semi-infinite parallel-plate waveguide with four-layer material loading, as shown in Fig. 1, where the waveguide plates are infinitely thin, perfectly conducting, and uniform in the y-direction. The material layers I $(-d_1 < z < -d_2)$, II $(-d_2 < z < -d_3)$, III$(-d_3 < z < -d_4)$, and IV $(-d_4 < z < -d_5)$ are characterized by the relative permittivity/permeability $(\varepsilon_{rm},\ \mu_{rm})$ for $m = 1, 2, 3$, and 4, respectively.

Let the total electric field $\phi^t(x, z)$ $\left[\equiv E_y^t(x, z)\right]$ be

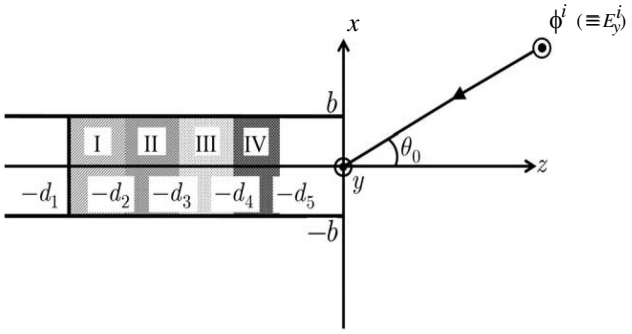

Figure 1: Geometry of the problem.

$$\phi^t(x, z) = \phi^i(x, z) + \phi(x, z), \tag{1}$$

where $\phi^i(x,z)$ is the incident field of E polarization defined by

$$\phi^i(x,z) = e^{-ik(x\sin\theta_0 + z\cos\theta_0)} \tag{2}$$

for $0 < \theta_0 < \pi/2$ with $k[\equiv \omega(\mu_0\varepsilon_0)^{1/2}]$ being the free-space wavenumber. We shall assume that the vacuum is slightly lossy as in $k = k_1 + ik_2$ with $0 < k_2 \ll k_1$, and take the limit $k_2 \to +0$ at the end of analysis. The total field $\phi^t(x,z)$ satisfies the 2-D Helmholtz equation

$$\left[\partial^2/\partial x^2 + \partial^2/\partial z^2 + \mu(x,z)\varepsilon(x,z)k^2\right]\phi^t(x,z) = 0, \tag{3}$$

where

$$\mu(x,z) = \begin{cases} \mu_{r1}\,(\text{layer I}), \\ \mu_{r2}\,(\text{layer II}), \\ \mu_{r3}\,(\text{layer III}), \\ \mu_{r4}\,(\text{layer IV}), \\ 1\,(\text{otherwise}), \end{cases} \qquad \varepsilon(x,z) = \begin{cases} \varepsilon_{r1}\,(\text{layer I}), \\ \varepsilon_{r2}\,(\text{layer II}), \\ \varepsilon_{r3}\,(\text{layer III}), \\ \varepsilon_{r4}\,(\text{layer IV}), \\ 1\,(\text{otherwise}). \end{cases} \tag{4}$$

Nonzero components of the total electromagnetic fields are derived from

$$\left(E_y^t, H_x^t, H_z^t\right) = \left[\phi^t, \frac{i}{\omega\mu_0\mu(x,z)}\frac{\partial\phi^t}{\partial z}, \frac{i}{\omega\mu_0\mu(x,z)}\frac{\partial\phi^t}{\partial x}\right]. \tag{5}$$

It follows from the radiation condition that

$$\phi\,(x,z) = \begin{cases} O\left(e^{k_2 z\cos\theta_0}\right) & \text{as } z \to -\infty, \\ O\left(e^{-k_2 z}\right) & \text{as } z \to \infty. \end{cases} \tag{6}$$

We now define the Fourier transform of the scattered field as

$$\Phi(x,\alpha) = (2\pi)^{-1/2}\int_{-\infty}^{\infty}\phi(x,z)e^{i\alpha z}dz, \quad \alpha = \mathrm{Re}\alpha + i\mathrm{Im}\alpha(\equiv \sigma + i\tau). \tag{7}$$

In the view of the radiation condition, it is found that $\Phi(x,\alpha)$ is regular in the strip $-k_2 < \tau < k_2\cos\theta_0$ of the complex α-plane. Introducing the Fourier integrals as

$$\Phi_+(x,\alpha) = (2\pi)^{-1/2}\int_0^{\infty}\phi(x,z)e^{i\alpha z}dz, \tag{8}$$

$$\Phi_-(x,\alpha) = (2\pi)^{-1/2}\int_{-\infty}^{0}\phi(x,z)e^{i\alpha z}dz, \tag{9}$$

$$\Phi_1^{(m)}(x,\alpha) = (2\pi)^{-1/2}\int_{-d_m}^{-d_{m+1}}\phi^t(x,z)e^{i\alpha z}dz, \quad m = 1,2,3,4, \tag{10}$$

$$\Phi_1^{(5)}(x,\alpha) = (2\pi)^{-1/2}\int_{-d_5}^{0}\phi^t(x,z)e^{i\alpha z}dz, \tag{11}$$

it is found that $\Phi_+(x,\alpha)$ and $\Phi_-(x,\alpha)$ are regular in $\tau > -k_2$ and $\tau < k_2\cos\theta_0$, respectively, whereas $\Phi_1^m(x,\alpha)$ for $m = 1,2,3,4$, and 5 are entire functions.

Taking the Fourier transform and the Fourier integration of (3) with the aid of (7)–(11) and using boundary conditions, we can derive the transformed wave equations. For the region $|x| < b$, the transformed wave equations involve unknown inhomogeneous terms due to the medium discontinuities, which we denote by $f_+(x)$ and $f_m(x)$, $g_m(x)$ for $m = 1,2,3,4$. We expand these inhomogeneous terms into the Fourier sine series as follows:

$$f_+(x) = \frac{1}{b}\sum_{n=1}^{\infty} f_n^+ \sin\frac{n\pi}{2b}(x+b), \tag{12}$$

$$\left.\begin{matrix} f_m(x) \\ g_m(x) \end{matrix}\right\} = \frac{1}{b}\sum_{n=1}^{\infty}\left\{\begin{matrix} f_{mn} \\ g_{mn} \end{matrix}\right\}\sin\frac{n\pi}{2b}(x+b). \tag{13}$$

Solving the transformed wave equations with the aid of (12) and (13) and carrying out some manipulations, we derive a scattered field representation in the Fourier transform domain as in

$$\begin{aligned}\Phi(x,\alpha) &= \Psi_{(+)}(\pm b,\alpha)e^{\mp\gamma(x\mp b)} \quad \text{for } x \gtrless \pm b,\\ &= \Psi_{(+)}(b,\alpha)\frac{\cosh\gamma(x+b)}{\sinh 2\gamma b} - \Psi_{(+)}(-b,\alpha)\frac{\sinh\gamma(x-b)}{\sinh 2\gamma b}\\ &\quad -\frac{1}{b}\sum_{n=1}^{\infty}\frac{c_{5n}(\alpha)}{\alpha^2+\gamma_n^2}\sin\frac{n\pi}{2b}(x+b)\\ &\quad -\frac{1}{b}\sum_{m=1}^{4}\sum_{n=1}^{\infty}\frac{c_{mn}(\alpha)}{\alpha^2+\Gamma_{mn}^2}\sin\frac{n\pi}{2b}(x+b) \quad \text{for } |x|<b, \end{aligned} \tag{14}$$

where $\gamma=(\alpha^2-k^2)^{1/2}$ with $\mathrm{Re}\,\gamma>0$, and

$$\Psi_{(+)}(\pm b,\alpha) = (1/2)[U_{(+)}(\alpha)\pm V_{(+)}(\alpha)], \tag{15}$$
$$\gamma_n = [(n\pi/2b)^2-k^2]^{1/2}, \tag{16}$$
$$\Gamma_{mn} = [(n\pi/2b)^2-k_{rm}^2]^{1/2}, \quad k_{rm}=(\mu_m\varepsilon_m)^{1/2}k, \quad m=1,2,3,4, \tag{17}$$
$$c_{5n}(\alpha) = e^{-i\alpha d_5}c_{5n}^{+}(\alpha), \tag{18}$$
$$c_{mn}(\alpha) = e^{-i\alpha d_m}c_{mn}^{+}(\alpha) - e^{-i\alpha d_{m+1}}c_{(m+1)n}^{-}(\alpha), \quad m=1,2,3,4. \tag{19}$$

In (15), $U_{(+)}(\alpha)$ and $V_{(+)}(\alpha)$ are unknown functions, which will be determined later by solving the Wiener-Hopf equations. The coefficients $c_{mn}^{\pm}(\alpha)$ in (18) and (19) are defined by using the Fourier coefficients f_+, f_{mn}, and g_{mn} as in

$$c_{1n}^{+}(\alpha) = f_n^{+}, \qquad c_{2n}^{-}(\alpha) = f_{1n}-i\alpha g_{1n}, \tag{20}$$
$$c_{2n}^{+}(\alpha) = \mu_{r2}/\mu_{r1}f_{1n}-i\alpha g_{1n}, \quad c_{3n}^{-}(\alpha) = f_{2n}-i\alpha g_{2n}, \tag{21}$$
$$c_{3n}^{+}(\alpha) = \mu_{r3}/\mu_{r2}f_{2n}-i\alpha g_{2n}, \quad c_{4n}^{-}(\alpha) = f_{3n}-i\alpha g_{3n}, \tag{22}$$
$$c_{4n}^{+}(\alpha) = \mu_{r4}/\mu_{r3}f_{3n}-i\alpha g_{3n}, \quad c_{5n}^{-}(\alpha) = f_{4n}-i\alpha g_{4n}. \tag{23}$$

We differentiate (14) with respect to x and set $x=b\pm 0,-b\pm 0$ in the results. Carrying out some manipulations by using boundary conditions, we find that $U_{(+)}(\alpha)$ and $V_{(+)}(\alpha)$ in (15) satisfy the Wiener-Hopf equations

$$J_1^d(\alpha) = -\frac{U_{(+)}(\alpha)}{M(\alpha)} - \sum_{n=1,\mathrm{odd}}^{\infty}\frac{n\pi}{b^2}\left[\frac{c_{5n}(\alpha)}{\alpha^2+\gamma_n^2}+\sum_{m=1}^{4}\frac{c_{mn}(\alpha)}{\alpha^2+\Gamma_{mn}^2}\right], \tag{24}$$

$$J_1^s(\alpha) = -\frac{V_{(+)}(\alpha)}{N(\alpha)} + \sum_{n=2,\mathrm{even}}^{\infty}\frac{n\pi}{b^2}\left[\frac{c_{5n}(\alpha)}{\alpha^2+\gamma_n^2}+\sum_{m=1}^{4}\frac{c_{mn}(\alpha)}{\alpha^2+\Gamma_{mn}^2}\right], \tag{25}$$

where $J_1^{d,s}(\alpha)$ are unknown functions, and $M(\alpha)$ and $N(\alpha)$ are kernel functions defined by

$$M(\alpha)=\frac{e^{-\gamma b}\cosh\gamma b}{\gamma}, \quad N(\alpha)=\frac{e^{-\gamma b}\sinh\gamma b}{\gamma}. \tag{26}$$

3. SOLUTION OF THE WIENER-HOPF EQUATIONS

The kernel functions $M(\alpha)$ and $N(\alpha)$ are factorized as [4]

$$M(\alpha)=M_+(\alpha)M_-(\alpha), \quad N(\alpha)=N_+(\alpha)N_-(\alpha), \tag{27}$$

where

$$\begin{aligned} M_+(\alpha)\,[&= M_-(-\alpha)] \\ &= (\cos kb)^{1/2} e^{i\pi/4} (k+\alpha)^{-1/2} \exp\{(i\gamma b/\pi)\ln[(\alpha-\gamma)/k]\} \\ &\quad \cdot \exp\{(i\alpha b/\pi)[1-C+\ln(\pi/2kb)+i\pi/2]\} \\ &\quad \cdot \prod_{n=1,\text{odd}}^{\infty} (1+\alpha/i\gamma_n) e^{2i\alpha b/n\pi}, \end{aligned} \tag{28}$$

$$\begin{aligned} N_+(\alpha)\,[&= N_-(-\alpha)] \\ &= (\sin kb/k)^{1/2} \exp\{(i\gamma b/k)\ln[(\alpha-\gamma)/k]\} \\ &\quad \cdot \exp\{(i\alpha b/\pi)[1-C+\ln(2\pi/kb)+i\pi/2]\} \\ &\quad \cdot \prod_{n=2,\text{even}}^{\infty} (1+\alpha/i\gamma_n) e^{2i\alpha b/n\pi} \end{aligned} \tag{29}$$

with $C(=0.57721566\cdots)$ being Euler's constant.

Decomposing (24) and (25) with the aid of (27), we obtain, after some manipulations, that

$$\frac{U_{(+)}(\alpha)}{b} = \frac{M_+(\alpha)}{b^{1/2}} \left[-\frac{A}{b(\alpha - k\cos\theta_0)} + \sum_{n=1}^{\infty} \frac{\delta_{2n-1} a_n p_n U_{(+)}(i\gamma_{2n-1})}{b^2(\alpha + i\gamma_{2n-1})} \right], \tag{30}$$

$$\frac{V_{(+)}(\alpha)}{b} = \frac{N_+(\alpha)}{b^{1/2}} \left[\frac{B}{b(\alpha - k\cos\theta_0)} + \sum_{n=1}^{\infty} \frac{\delta_{2n} b_n q_n V_{(+)}(i\gamma_{2n})}{b^2(\alpha + i\gamma_{2n})} \right], \tag{31}$$

where the definition of several quantities is omitted due to space limitations [6]. Equations (30) and (31) are the exact solutions to the Wiener-Hopf equations (24) and (25), respectively.

4. SCATTERED FIELD

The scattered field in the real space can be derived by taking the inverse Fourier transform of (14) according to the formula

$$\phi(x,z) = (2\pi)^{-1/2} \int_{-\infty+ic}^{\infty+ic} \Phi(x,\alpha) e^{-i\alpha z} d\alpha, \quad -k_2 < c < k_2 \cos\theta_0. \tag{32}$$

Substituting (14) into (32) and evaluating the resultant integral for $|x| < b$ with the aid of (30) and (31), an explicit expression for the scattered field inside the waveguide is derived as

$$\begin{aligned} \phi(x,z) &= -\phi^i(x,z) + \sum_{n=1}^{\infty} T_{1n} \sinh\Gamma_{1n}(z+d_1) \sin\frac{n\pi}{2b}(x+b) \\ &\qquad \text{for } -d_1 < z < -d_2, \\ &= -\phi^i(x,z) + \sum_{n=1}^{\infty} \left[T^-_{mn} e^{\Gamma_{mn}(z+d_{m+1})} - T^+_{mn} e^{-\Gamma_{mn}(z+d_m)} \right] \sin\frac{n\pi}{2b}(x+b) \\ &\qquad \text{for } -d_m < z < -d_{m+1}\,(m=2,3,4), \\ &= -\phi^i(x,z) + \sum_{n=1}^{\infty} \left[T^-_n e^{\gamma_n(z+d_5)} - T^+_n e^{-\gamma_n(z+d_5)} \right] \sin\frac{n\pi}{2b}(x+b) \\ &\qquad \text{for } -d_5 < z < 0, \end{aligned} \tag{33}$$

where the definition of the coefficients T_{1n}, $T^{\pm}_{mn}$, and $T^{\pm}_n$ is given in [6].

Next we shall consider the field outside the waveguide and derive a scattered far field. The region outside the waveguide consists of region $|x| < b$ with $z > 0$ and region $|x| > b$. However the contribution from region $|x| < b$ outside the waveguide is negligibly small at large distances from the origin. Therefore, the derivation of the scattered far field for $|x| < b$ will not be discussed in

the following. In view of (14) and (32), the integral representation of the scattered field for $x \gtrless \pm b$ is given by

$$\phi(x,z) = (2\pi)^{-1/2} \int_{-\infty+ic}^{\infty+ic} \Psi_{(+)}(\pm b, \alpha) e^{\mp\gamma(x\mp b)-i\alpha z} d\alpha. \tag{34}$$

It is noted from (15), (30), and (31) that $\Psi_{(+)}(\pm b, \alpha)$ have a simple pole at $\alpha = k\cos\theta_0$. To evaluate (34), we express $\phi(x,z)$ as in

$$\phi(x,z) = \phi_1(x,z) + \phi_2(x,z), \tag{35}$$

where

$$\phi_1(x,z) = (2\pi)^{-1/2} \int_{-\infty+ic}^{\infty+ic} \left[\Psi_{(+)}(\pm b, \alpha) - \tilde{\Phi}(\pm b, \alpha)\right] e^{\mp\gamma(x\mp b)-i\alpha z} d\alpha, \tag{36}$$

$$\phi_2(x,z) = (2\pi)^{-1/2} \int_{-\infty+ic}^{\infty+ic} \tilde{\Phi}(\pm b, \alpha) e^{\mp\gamma(x\mp b)-i\alpha z} d\alpha \tag{37}$$

for $x \gtrless \pm b$ with

$$\tilde{\Phi}(\pm b, \alpha) = \frac{e^{\mp ikb\sin\theta_0} i(k + k\cos\theta_0)^{1/2}}{(2\pi)^{1/2}(\alpha + k)^{1/2}(\alpha - k\cos\theta_0)}. \tag{38}$$

It can be verified by (15), (30), and (31) that the residue of $\Psi_{(+)}(\pm b, \alpha)$ at $\alpha = k\cos\theta_0$ is

$$\mathrm{Res}\Psi_{(+)}(\pm b, k\cos\theta_0) = \frac{ie^{\mp kb\sin\theta_0}}{(2\pi)^{1/2}}, \tag{39}$$

which implies that the integrand of (36) is regular in the neighborhood of $\alpha = k\cos\theta_0$. Let us introduce the cylindrical coordinates $(\rho_{1,2}, \theta_{1,2})$ centered at the waveguide edges $(x,z) = (\pm b, 0)$ as follows:

$$x - b = \rho_1 \sin\theta_1 \quad z = \rho_1\cos\theta_1 \quad \text{for } 0 < \theta_1 < \pi, \tag{40}$$

$$x + b = \rho_2 \sin\theta_2 \quad z = \rho_2\cos\theta_2 \quad \text{for } -\pi < \theta_2 < 0. \tag{41}$$

Applying the saddle point method, $\phi_1(x,z)$ defined by (36) can be expanded asymptotically with the result that

$$\phi_1(\rho_{1,2}, \theta_{1,2}) \sim \pm\left[\Psi_{(+)}(\pm b, -k\cos\theta_{1,2}) - \tilde{\Phi}(\pm b, -k\cos\theta_{1,2})\right] \cdot k\sin\theta_{1,2} \frac{e^{i(k\rho_{1,2}-\pi/4)}}{(k\rho_{1,2})^{1/2}} \tag{42}$$

for $x \gtrless \pm b$ as $k\rho_{1,2} \to \infty$. The term $\phi_2(x,z)$ given by (37) is evaluated exactly as in

$$\begin{aligned}\phi_2(\rho_{1,2}, \theta_{1,2}) = & -e^{\mp ikb\sin\theta_0}\Big(e^{-ik\rho_{1,2}\cos(\theta_{1,2}-\theta_0)} F\Big\{(2k\rho_{1,2})^{1/2}\cos[(\theta_{1,2}-\theta_0)/2]\Big\} \\ & + e^{-ik\rho_{1,2}\cos(\theta_{1,2}+\theta_0)} F\Big\{(2k\rho_{1,2})^{1/2}\cos[(\theta_{1,2}+\theta_0)/2]\Big\}\Big)\end{aligned} \tag{43}$$

for $x \gtrless \pm b$, where $F(\cdot)$ is the Fresnel integral defined by

$$F(w) = \frac{e^{-i\pi/4}}{\pi^{1/2}} \int_w^\infty e^{it^2} dt. \tag{44}$$

Therefore, substituting (42) and (43) into (35) leads to

$$\begin{aligned}\phi_(\rho_{1,2}, \theta_{1,2}) \sim & \pm\left[\Psi_{(+)}(\pm b, -k\cos\theta_{1,2}) - \tilde{\Phi}(\pm b, -k\cos\theta_{1,2})\right] k\sin\theta_{1,2} \frac{e^{i(k\rho_{1,2}-\pi/4)}}{(k\rho_{1,2})^{1/2}} \\ & - e^{\mp ikb\sin\theta_0}\Big(e^{-ik\rho_{1,2}\cos(\theta_{1,2}-\theta_0)} F\Big\{(2k\rho_{1,2})^{1/2}\cos[(\theta_{1,2}-\theta_0)/2]\Big\} \\ & + e^{-ik\rho_{1,2}\cos(\theta_{1,2}+\theta_0)} F\Big\{(2k\rho_{1,2})^{1/2}\cos[(\theta_{1,2}+\theta_0)/2]\Big\}\Big)\end{aligned} \tag{45}$$

for $x \gtrless \pm b$, which gives a scattered far field expression uniformly valid in observation angles $\theta_{1,2}$.

5. CONCLUSIONS

In this paper, we have rigorously analyzed the E-polarized plane wave diffraction by a terminated, semi-infinite parallel-plate waveguide with four-layer material loading using the Wiener-Hopf technique. The scattered field inside and outside the waveguide has been explicitly evaluated. It is to be noted that the results presented in this paper are uniformly valid for arbitrary cavity dimensions.

ACKNOWLEDGMENT

This work was supported in part by the Institute of Science and Engineering, Chuo University.

REFERENCES

1. Lee, S.-W. and H. Ling, "Data book for cavity RCS: Version 1," *Tech. Rep.*, No. SWL 89-1, Univ. Illinois, Urbana, 1989.
2. Kobayashi, K. and A. Sawai, "Plane wave diffraction by an open-ended parallel plate waveguide cavity," *J. Electromagn. Waves Appl.*, Vol. 6, 475–512, 1992.
3. Koshikawa, S., T. Momose, and K. Kobayashi, "RCS of a parallel-plate waveguide cavity with three-layer material loading," *IEICE Trans. Electron.*, Vol. E77-C, 1514–1521, 1994.
4. Koshikawa, S. and K. Kobayashi, "Diffraction by a terminated, semi-infinite parallel-plate waveguide with three-layer material loading," *IEEE Trans. Antennas Propagat.*, Vol. 45, 949–959, 1997.
5. Koshikawa, S. and K. Kobayashi, "Diffraction by a terminated, semi-infinite parallel-plate waveguide with three-layer material loading: the case of H polarization," *Electromagnetic Waves & Electronic Systems*, Vol. 5, 13–23, 2000.
6. Shang, E. H. and K. Kobayashi, "Diffraction by a terminated, semi-infinite parallel-plate waveguide with four-layer material loading," *IEEJ Technical Report*, No. EMT-07-38, May 2007.

Combined Perturbation and Wiener-Hopf Analysis of the Diffraction by Two Parallel, Corrugated Half-planes

J. P. Zheng and K. Kobayashi
Department of Electrical, Electronic, and Communication Engineering, Chuo University
1-13-27 Kasuga, Bunkyo-ku, Tokyo 112-8551, Japan

Abstract— The plane wave diffraction by two parallel half-planes with sinusoidal corrugation is analyzed using the Wiener-Hopf technique together with the perturbation scheme. Introducing the Fourier transform for the unknown scattered field and applying approximate boundary conditions, the problem is formulated in terms of the simultaneous Wiener-Hopf equations. By employing the factorization and decomposition procedure together with a perturbation series expansion, the zero- and first-order solutions of the Wiener-Hopf equations are derived. The scattered field in the real space is evaluated by taking the inverse Fourier transform and applying the saddle point method.

1. INTRODUCTION

The analysis of wave scattering by gratings and waveguides with periodic structures is important in electromagnetic theory and optics. Various analytical and numerical methods have been developed so far and the diffraction phenomena have been investigated for many kinds of periodic structures. However, there are only a few treatments of the diffraction by periodic structures using rigorous function-theoretic methods. The Wiener-Hopf technique [1] is known as a powerful tool for analyzing electromagnetic wave problems rigorously, and can be applied efficiently to the diffraction by specific grating geometries. However, most of the analyses are restricted to periodic structures of infinite extent and plane boundaries. Therefore, it is important to investigate scattering problems involving periodic structures without these restrictions.

As an example of infinite periodic structures with non-plane boundaries, Das Gupta [2] analyzed the plane wave diffraction by a half-plane with sinusoidal corrugation by means of the Wiener-Hopf technique together with the perturbation method. The results presented in [2] have been generalized thereafter by Chakrabarti and Dowerah [3] for the analysis of diffraction by two parallel sinusoidal half-planes using the Wiener-Hopf technique. We have also considered a finite sinusoidal grating as another important generalization and analyzed the plane wave diffraction by means of the Wiener-Hopf technique [4].

In this paper, we shall reconsider, from a mathematical point of view, the problem solved by Chakrabarti and Dowerah [3] for the H-polarized plane wave incidence, and analyze the E-polarized plane wave diffraction by two parallel, corrugated half-planes using the Wiener-Hopf technique. Assuming that the corrugation amplitude is small compared with the wavelength, we replace the original problem by the problem of diffraction by two parallel half-planes with impedance-type boundary conditions. Taking the Fourier transform of the wave equation and applying approximate boundary conditions in the transform domain, the problem is formulated in terms of the simultaneous Wiener-Hopf equations. The Wiener-Hopf equations are then solved approximately via the factorization and decomposition procedure together with the perturbation scheme leading to the efficient zero- and first-order solutions. Taking the Fourier inverse of the solution in the transform domain and applying the saddle point method, the scattered far field in the real space is evaluated asymptotically.

The time factor is assumed to be $e^{-i\omega t}$, and suppressed throughout this paper.

2. FORMULATION OF THE PROBLEM

Let us consider the diffraction of an E-polarized plane wave by two parallel half-planes with sinusoidal corrugation as shown in Fig. 1. The surface of the two half-planes is assumed to be infinitely thin, perfectly conducting, and uniform in the y-direction, and defined by

$$x = \pm b + h \sin mz, \quad z < 0, \tag{1}$$

where m and h are positive constants. We define the total electric field $\phi^t(x,z)[\equiv E_y^t(x,z)]$ by

$$\phi^t(x,z) = \phi^i(x,z) + \phi(x,z), \tag{2}$$

where $\phi^i(x,z)$ is the incident field given by

$$\phi^i(x,z) = e^{-ik(x\sin\theta_0 + z\cos\theta_0)}, \quad 0 < \theta_0 < \pi/2 \tag{3}$$

with $k[\equiv \omega(\mu_0\varepsilon_0)^{1/2}]$ being the free-space wavenumber. Nonzero components of the scattered electromagnetic fields are derived from

$$(E_y, H_x, H_z) = \left[\phi, \frac{i}{\omega\mu_0\mu(x,z)}\frac{\partial\phi}{\partial z}, \frac{i}{\omega\mu_0\mu(x,z)}\frac{\partial\phi}{\partial x}\right]. \tag{4}$$

Assuming that the amplitude of sinusoidal corrugation $2h$ is small compared with the wavelength, we approximate the boundary condition on the corrugated half-planes by ignoring the $O(h^2)$ terms with the aid of Taylor's theorem. Then we deduce that

$$\phi^t(\pm b, z) + h\sin mz\frac{\partial\phi^t(\pm b, z)}{\partial x} + O(h^2) = 0, \quad z < 0. \tag{5}$$

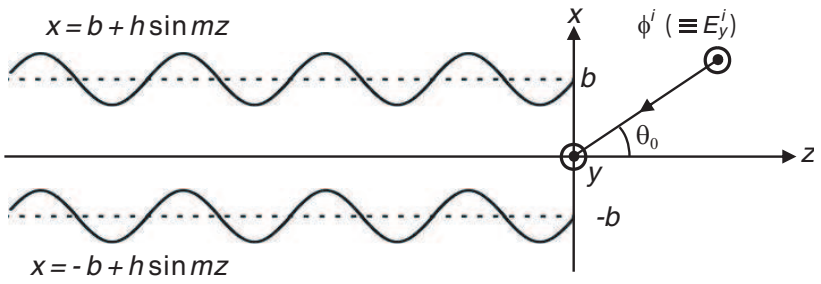

Figure 1: Geometry of the problem.

We introduce the Fourier transform of the scattered field as in

$$\Phi(x,\alpha) = (2\pi)^{-1/2}\int_{-\infty}^{\infty}\phi(x,z)e^{i\alpha z}dz, \quad \alpha = \mathrm{Re}\,\alpha + i\mathrm{Im}\,\alpha(\equiv \sigma + i\tau). \tag{6}$$

In view of the radiation condition, it is found that $\Phi(x,\alpha)$ is regular in the strip $-k_2 < \tau < k_2\cos\theta_0$ of the complex α-plane. Taking the Fourier transform of the two-dimensional Helmholtz equation and solving the resulting equation, it is found that the scattered field is expressed as

$$\begin{aligned}\Phi(x,\alpha) &= A(\alpha)e^{-\gamma(\alpha)x}, \quad x > b,\\ &= B(\alpha)e^{-\gamma(\alpha)x} + C(\alpha)e^{\gamma(\alpha)x}, \quad |x| < b,\\ &= D(\alpha)e^{\gamma(\alpha)x}, \quad x < -b\end{aligned} \tag{7}$$

in the Fourier transform domain, where $\gamma(\alpha) = (\alpha^2 - k^2)^{1/2}$ with $\mathrm{Re}[\gamma(\alpha)] > 0$, and

$$\begin{aligned}\left.\begin{matrix}A(\alpha)\\ D(\alpha)\end{matrix}\right\} &= -\frac{e^{\pm\gamma(\alpha)b}}{2}\left\{\frac{M_-(\alpha)}{\gamma(\alpha)} - \frac{ih}{2}\left[M_-(\alpha\pm m) - M_-(\alpha\mp m)\right]\right\}\\ &\quad -\frac{e^{\mp\gamma(\alpha)b}}{2}\left\{\frac{N_-(\alpha)}{\gamma(\alpha)} - \frac{ih}{2}\left[N_-(\alpha\pm m) - N_-(\alpha\mp m)\right]\right\},\end{aligned} \tag{8}$$

$$B(\alpha) = -\frac{e^{-\gamma(\alpha)b}}{2}\left\{\frac{N_-(\alpha)}{\gamma(\alpha)} - \frac{ih}{2}\left[N_-(\alpha+m) - N_-(\alpha-m)\right]\right\}, \tag{9}$$

$$C(\alpha) = -\frac{e^{-\gamma(\alpha)b}}{2}\left\{\frac{M_-(\alpha)}{\gamma(\alpha)} - \frac{ih}{2}\left[M_-(\alpha-m) - M_-(\alpha+m)\right]\right\}, \tag{10}$$

$$\left.\begin{matrix}M_-(\alpha)\\ N_-(\alpha)\end{matrix}\right\} = \int_{-\infty}^{0}\left[\frac{\partial\phi(\pm b+0,z)}{\partial x} - \frac{\partial\phi(\pm b-0,z)}{\partial x}\right]e^{i\alpha z}dz. \tag{11}$$

Using the boundary conditions and carrying out some manipulations, we derive that

$$\begin{aligned} S_+(\alpha)+G_1(\alpha) &= -K(\alpha)U_-(\alpha)+(ih/4)\left\{V_-(\alpha-m)\left[e^{-2\gamma(\alpha)b}-e^{-2\gamma(\alpha-m)b}\right]\right. \\ &\quad \left.+V_-(\alpha+m)\left[e^{-2\gamma(\alpha+m)b}-e^{-2\gamma(\alpha)b}\right]\right\}, \qquad (12) \\ D_+(\alpha)+G_2(\alpha) &= -L(\alpha)V_-(\alpha)+(ih/4)\left\{U_-(\alpha+m)\left[e^{-2\gamma(\alpha)b}-e^{-2\gamma(\alpha+m)b}\right]\right. \\ &\quad \left.+U_-(\alpha-m)\left[e^{-2\gamma(\alpha-m)b}-e^{-2\gamma(\alpha)b}\right]\right\}, \qquad (13) \end{aligned}$$

where

$$\begin{aligned} \left.\begin{matrix} S_+(\alpha) \\ D_+(\alpha) \end{matrix}\right\} &= P_+(\alpha)\pm Q_+(\alpha), \qquad \left.\begin{matrix} U_-(\alpha) \\ V_-(\alpha) \end{matrix}\right\} = M_-(\alpha)\pm N_-(\alpha), \qquad (14) \\ \left.\begin{matrix} P_+(\alpha) \\ Q_+(\alpha) \end{matrix}\right\} &= \int_{-\infty}^{0}\left[\phi(\pm b\pm 0,z)+h\sin mz\frac{\partial\phi(\pm b\pm 0,z)}{\partial x}\right]e^{i\alpha z}dz, \qquad (15) \\ G_{1,2}(\alpha) &= 2\left\{\begin{matrix} i\cos(kb\sin\theta_0) \\ \sin(kb\sin\theta_0) \end{matrix}\right\}\left[\frac{1}{\alpha-k\cos\theta_0}-\frac{kh\sin\theta_0}{m^2-(\alpha-k\cos\theta_0)^2}\right], \qquad (16) \\ K(\alpha) &= e^{-\gamma(\alpha)b}\frac{\cosh[\gamma(\alpha)b]}{\gamma(\alpha)}, \quad L(\alpha)=e^{-\gamma(\alpha)b}\frac{\sinh[\gamma(\alpha)b]}{\gamma(\alpha)}. \qquad (17) \end{aligned}$$

Equations (12) and (13) are the simultaneous Wiener-Hopf equations satisfied by $S_+(\alpha)$, $D_+(\alpha)$, $U_-(\alpha)$, and $V_-(\alpha)$. It is to be noted that, setting $h\to 0$, (12) and (13) are reduced to the Wiener-Hopf equations arising in the problem of diffraction by a semi-infinite parallel-plate waveguide [1].

3. PERTURBATION SERIES SOLUTION OF THE WIENER-HOPF EQUATIONS

We express the unknown functions occurring in the simultaneous Wiener-Hopf equations (12) and (13) in terms of a perturbation series expansion in h as

$$\begin{aligned} \left.\begin{matrix} S_+(\alpha) \\ D_+(\alpha) \end{matrix}\right\} &= \left\{\begin{matrix} S_+^0(\alpha) \\ D_+^0(\alpha) \end{matrix}\right\}+h\left\{\begin{matrix} S_+^1(\alpha) \\ D_+^1(\alpha) \end{matrix}\right\}+O(h^2), \qquad (18) \\ \left.\begin{matrix} U_-(\alpha) \\ V_-(\alpha) \end{matrix}\right\} &= \left\{\begin{matrix} U_-^0(\alpha) \\ V_-^0(\alpha) \end{matrix}\right\}+h\left\{\begin{matrix} U_-^1(\alpha) \\ V_-^1(\alpha) \end{matrix}\right\}+O(h^2). \qquad (19) \end{aligned}$$

Substituting (18) and (19) into (12) and (13), the original Wiener-Hopf equations can be separated into the zero-order equations

$$S_+^0(\alpha)=-e^{-\gamma(\alpha)b}\frac{\cosh[\gamma(\alpha)b]}{\gamma(\alpha)}U_-^0(\alpha)-\frac{2i\cos(kb\sin\theta_0)}{\alpha-k\cos\theta_0}, \qquad (20)$$

$$D_+^0(\alpha)=-e^{-\gamma(\alpha)b}\frac{\sinh[\gamma(\alpha)b]}{\gamma(\alpha)}V_-^0(\alpha)-\frac{2\sin(kb\sin\theta_0)}{\alpha-k\cos\theta_0} \qquad (21)$$

and the first-order equations

$$\begin{aligned} S_+^1(\alpha) &= -e^{-\gamma(\alpha)b}\frac{\cosh[\gamma(\alpha)b]}{\gamma(\alpha)}U_-^1(\alpha)+\frac{i}{4}\left[e^{-2\gamma(\alpha)b}-e^{-2\gamma(\alpha-m)b}\right]V_-^0(\alpha-m) \\ &\quad +\frac{i}{4}\left[e^{-2\gamma(\alpha+m)b}-e^{-2\gamma(\alpha)b}\right]V_-^0(\alpha+m)+\frac{2ik\sin\theta_0\cos(kb\sin\theta_0)}{m^2-(\alpha-k\cos\theta_0)^2}, \qquad (22) \\ D_+^1(\alpha) &= -e^{-\gamma(\alpha)b}\frac{\sinh[\gamma(\alpha)b]}{\gamma(\alpha)}V_-^1(\alpha)+\frac{i}{4}\left[e^{-2\gamma(\alpha-m)b}-e^{-2\gamma(\alpha)b}\right]U_-^0(\alpha-m) \\ &\quad +\frac{i}{4}\left[e^{-2\gamma(\alpha)b}-e^{-2\gamma(\alpha+m)b}\right]U_-^0(\alpha+m)+\frac{2k\sin\theta_0\sin(kb\sin\theta_0)}{m^2-(\alpha-k\cos\theta_0)^2}. \qquad (23) \end{aligned}$$

Equations (20) and (21) are the Wiener-Hopf equations of the diffraction problem for a semi-infinite parallel-plate waveguide, and has the exact solution [1]

$$U_-^0(\alpha) = \frac{2i\cos(kb\sin\theta_0)}{K_+(k\cos\theta_0)(\alpha - k\cos\theta_0)K_-(\alpha)}, \tag{24}$$

$$V_-^0(\alpha) = -\frac{2\sin(kb\sin\theta_0)}{L_+(k\cos\theta_0)(\alpha - k\cos\theta_0)L_-(\alpha)}, \tag{25}$$

where $K_\pm(\alpha)$ and $L_\pm(\alpha)$ are the split functions of the Wiener-Hopf kernels $K(\alpha)$ and $L(\alpha)$, respectively, which are defined by

$$\begin{aligned} K_\pm(\alpha) &= (\cos kb)^{-1/2}\exp(i\pi/4)\,(k\pm\alpha)^{-1/2} \\ &\quad\cdot\exp\{(\pm i\alpha b/\pi)[1 - C + \ln(2\pi/kb) + i\pi/2]\} \\ &\quad\cdot\exp\left([ib\gamma(\alpha)/\pi]\ln\{[\pm\alpha - \gamma(\alpha)]/k\}\right) \\ &\quad\cdot\prod_{n=1,\text{odd}}^{\infty}(1\pm\alpha/i\gamma_n)\exp(\pm 2i\alpha b/n\pi), \end{aligned} \tag{26}$$

$$\begin{aligned} L_\pm(\alpha) &= (\sin kb/k)^{-1/2}\exp\{(\pm i\alpha b/\pi)\,[1 - C + \ln(2\pi/kb) + i\pi/2]\} \\ &\quad\cdot\exp\left([ib\gamma(\alpha)/\pi]\ln\{[\pm\alpha - \gamma(\alpha)]/k\}\right) \\ &\quad\cdot\prod_{n=2,\text{even}}^{\infty}(1\pm\alpha/i\gamma_n)\exp(\pm 2i\alpha b/n\pi) \end{aligned} \tag{27}$$

with $C = 0.57721566\cdots$ being Euler's constant and $\gamma_n = -i[k^2 - (n\pi/2b)^2]^{1/2}$.

Equations (22) and (23) are solved exactly by the factorization and decomposition procedure leading to

$$U_-^1(\alpha) = \frac{1}{K_-(\alpha)}\left[\frac{A_1}{(\alpha - k\cos\theta_1)} + \frac{A_2}{(\alpha - k\cos\theta_2)} + H_1(\alpha) + H_2(\alpha)\right], \tag{28}$$

$$V_-^1(\alpha) = -\frac{1}{L_-(\alpha)}\left[\frac{D_2}{(\alpha - k\cos\theta_2)} - \frac{D_1}{(\alpha - k\cos\theta_1)} + J_1(\alpha) + J_2(\alpha)\right], \tag{29}$$

where $\cos\theta_{1,2} = \cos\theta_0 \pm m/k$, and

$$A_{1,2} = \frac{k\sin\theta_0\cos(kb\sin\theta_0)}{mK_+(k\cos\theta_{1,2})}, \quad D_{1,2} = \frac{k\sin\theta_0\sin(kb\sin\theta_0)}{mL_+(k\cos\theta_{1,2})}, \tag{30}$$

$$H_{1,2}(\alpha) = \pm\frac{1}{8\pi}\int_{-\infty+id}^{\infty+id}\frac{V_-^0(u\pm m)\left[e^{-2\gamma(u)b} - e^{-2\gamma(u\pm m)b}\right]}{K_+(u)(u-\alpha)}du, \tag{31}$$

$$J_{1,2}(\alpha) = \pm\frac{1}{8\pi}\int_{-\infty+id}^{\infty+id}\frac{U_-^0(u\pm m)\left[e^{-2\gamma(u)b} - e^{-2\gamma(u\pm m)b}\right]}{L_+(u)(u-\alpha)}du \tag{32}$$

with d being chosen as $-k_2 < \tau < d < k_2\cos\theta_0$. Equations (31) and (32) are evaluated in closed form as

$$\begin{aligned} H_{1,2}(\alpha) &= \mp\frac{i\sin(kb\sin\theta_0)}{2L_+(k\cos\theta_0)}\sum_{j=1}^{\infty}\left[\frac{e^{-2\gamma(x)b} - e^{-2\gamma(x-m)b}}{(x\pm k\cos\theta_{1,2})K_\mp(x)(x\pm\alpha)}\right]_{x=\mp i\beta_j+m} \\ &\quad\cdot\frac{(\sin kb/k)^{-1/2}\,i\beta_j\exp\{(ib\gamma(\alpha)/\pi)\ln[(-i\beta_j - \gamma(\alpha))/k]\}}{\exp\{(\beta_j b/\pi)[1 - C + \ln(2\pi/kb) + i\pi/2]\}\exp(2\beta_j b/j\pi)} \\ &\quad\cdot\prod_{n=2,\text{even},n\neq j}^{\infty}\frac{\beta_n\exp(-2\beta_n b/n\pi)}{\beta_n - \beta_j}, \end{aligned} \tag{33}$$

$$J_{1,2}(\alpha) = \mp\frac{\cos(kb\sin\theta_0)}{2K_+(k\cos\theta_0)}\sum_{j=1}^{\infty}\left[\frac{e^{-2\gamma(x)b}-e^{-2\gamma(x-m)b}}{(x\pm k\cos\theta_{1,2})L_\mp(x)(x\pm\alpha)}\right]_{x=\mp i\gamma_j+m}$$
$$\cdot\frac{i\gamma_j(\cos kb)^{-1/2}\,(k-i\gamma_j)^{1/2}\exp\{(ib\gamma(\alpha)/\pi)}{\exp(i\pi/4)\exp\{(\gamma_j b/\pi)[1-C+\ln(2\pi/kb)+i\pi/2]\}}\frac{\ln[(-i\gamma_j-\gamma(\alpha))/k]\}}{\exp(2\gamma_j b/j\pi)}$$
$$\cdot\prod_{n=1,\text{odd},n\neq j}^{\infty}\frac{\gamma_n\exp(-2\gamma_j b/n\pi)}{\gamma_n-\gamma_j}, \tag{34}$$

where $\beta_n=[(n\pi/2b)^2-k^2]^{1/2}$.

4. SCATTERED FIELD

In this section, we shall take the inverse Fourier transform of the results obtained in the previous sections to derive the scattered far field by employing the saddle point method.

The scattered field $\phi(x,z)$ in the real space is obtained by taking the inverse Fourier transform according to the following formula:

$$\phi(x,z)=(2\pi)^{-1/2}\int_{-\infty+ic}^{\infty+ic}\Phi(x,\alpha)e^{-i\alpha z}d\alpha,\quad -k_2<c<k_2\cos\theta_0. \tag{35}$$

Substituting (7) into (35) and using (8) and (14), the scattered field is expressed as

$$\phi(x,z) = (2\pi)^{-1/2}\int_{-\infty+ic}^{\infty+ic}\left(\left\{\pm\frac{hi}{4}\left[\frac{U_-(\alpha+m)\mp V_-(\alpha+m)}{2}\right.\right.\right.$$
$$\left.-\frac{U_-(\alpha-m)\mp V_-(\alpha-m)}{2}\right]-\frac{U_-(\alpha)\mp V_-(\alpha)}{2}\Bigg\}e^{-\gamma(\alpha)b}$$
$$\pm\left\{\frac{hi}{4}\left[\frac{U_-(\alpha+m)\pm V_-(\alpha+m)}{2}-\frac{U_-(\alpha-m)\pm V_-(\alpha-m)}{2}\right]\right.$$
$$\left.\left.-\frac{U_-(\alpha)\pm V_-(\alpha)}{2}\right\}e^{\gamma(\alpha)b}\right)e^{-\gamma(\alpha)|x|-i\alpha z}d\alpha \tag{36}$$

for $x\gtrless\pm b$, where $-k_2<c<k_2\cos\theta_0$.

Let us introduce the cylindrical coordinate centered at the origin as

$$x=\rho\sin\theta,\ z=\rho\cos\theta\quad\text{for } 0<\theta<\pi. \tag{37}$$

Applying the saddle point method, (36) can be evaluated asymptotically for $k\rho\to\infty$ as

$$\phi(\rho,\theta)\sim\sum_{j=0}^{2}R_j\left(\theta_0,\theta_j\right)H\left(\theta_j+\theta-\pi\right)\exp\left[-ik\rho\cos\left(|\theta|+\theta_j\right)\right]$$
$$+\sum_{j=0}^{2}D_j\left(\theta,\theta_0,\theta_j\right)\frac{\exp[i(k\rho-\pi/4)]}{(k\rho)^{1/2}}, \tag{38}$$

where

$$H(x) = 0,\quad x<0,$$
$$= 1/2,\quad x=0,$$
$$= 1,\quad x>0, \tag{39}$$
$$R_0\left(\theta_0,\theta_0\right) = -1, \tag{40}$$

$$R_1(\theta_0,\theta_1) = ikh\sin\theta_0\left[\frac{i\cos(kb\sin\theta_0)\cosh(ikb\sin\theta_1)}{1+\exp(-2ikb\sin\theta_0)} + \frac{i\sin(kb\sin\theta_0)\sinh(ikb\sin\theta_1)}{1-\exp(-2ikb\sin\theta_0)}\right] + \frac{kh\sin\theta_0}{m}\exp\left[ikb(\sin\theta_1-\sin\theta_0)\right], \quad (41)$$

$$R_2(\theta_0,\theta_2) = -ikh\sin\theta_0\left[\frac{i\cos(kb\sin\theta_0)\cosh(ikb\sin\theta_2)}{1+\exp(-2ikb\sin\theta_0)} + \frac{i\sin(kb\sin\theta_0)\sinh(ikb\sin\theta_2)}{1-\exp(-2ikb\sin\theta_0)}\right] + \frac{kh\sin\theta_0}{m}\exp\left[ikb(\sin\theta_2+\sin\theta_0)\right], \quad (42)$$

$$\begin{aligned} D_0(\theta,\theta_0,\theta_0) = &-\frac{1}{ik(\cos\theta+\cos\theta_0)}\left[\frac{i\cos(kb\sin\theta_0)\cos(kb\sin\theta)}{K_+(k\cos\theta_0)K_+(k\cos\theta)}\right. \\ &\left.+\frac{\sin(kb\sin\theta_0)\sin(kb\sin\theta)}{L_+(k\cos\theta_0)L_+(k\cos\theta)}\right] - \frac{h}{8i}\left(\frac{i\cos(kb\sin\theta)}{K_+(k\cos\theta)}\sum_{q=2}^{\infty}\left\{\frac{i\beta_q}{(\sin kb/k)^{1/2}\exp(2\beta_q b/q\pi)}\right.\right. \\ &\cdot\frac{1}{\exp\{(\beta_q b/\pi)[1-C+\ln(2\pi/kb)+i\pi/2]\}\exp\{(-kb\sin\theta/\pi)\ln[(-i\beta_q-\gamma)/k]\}} \\ &\left.\cdot\prod_{n=2,\text{even},n\neq q}^{\infty}\frac{\beta_n\exp(-2\beta_q b/n\pi)}{\beta_n-\beta_q}\right\}\left\{\sum_{p=2}^{\infty}\frac{\exp[-2\gamma(-i\beta_p+m)]-\exp[-2\gamma(-i\beta_p)b]}{(k\cos\theta_0-i\beta_p)K_-(m-i\beta_p)(m-i\beta_p-k\cos\theta)}\right. \\ &\left.+\sum_{p=2}^{\infty}\frac{\exp[-2\gamma(i\beta_p)b]-\exp[-2\gamma(i\beta_p+m)]}{(i\beta_p-k\cos\theta_0)K_+(i\beta_p+m)(k\cos\theta+m+i\beta_p)}\right\} \\ &+\frac{i\sin(kb\sin\theta)}{L_+(k\cos\theta)}\sum_{q=1}^{\infty}\left\{\frac{i\gamma_q(k-i\gamma_q)^{1/2}}{(\cos kb)^{1/2}\exp(i\pi/4)\exp(2\gamma_q b/q\pi)}\right. \\ &\cdot\frac{1}{\exp\{(\gamma_q b/\pi)[1-C+\ln(2\pi/kb)+i\pi/2]\}\exp\{(-kb\sin\theta/\pi)\ln[(-i\gamma_q-\gamma)/k]\}} \\ &\left.\cdot\prod_{n=1,\text{odd},n\neq q}^{\infty}\frac{\gamma_n\exp(-2\gamma_q b/n\pi)}{\gamma_n-\gamma_q}\right\}\left\{\sum_{p=1}^{\infty}\frac{\exp[-2\gamma(-i\gamma_p+m)]-\exp[-2\gamma(-i\gamma_p)b]}{(k\cos\theta_0-i\gamma_p)L_-(m-i\gamma_p)(m-i\gamma_p-k\cos\theta)}\right. \\ &\left.\left.+\sum_{p=1}^{\infty}\frac{\exp[-2\gamma(i\gamma_p)b]-\exp[-2\gamma(i\gamma_p+m)b]}{(i\gamma_p-k\cos\theta_0)L_+(i\gamma_p+m)(k\cos\theta+m+i\gamma_p)}\right\}\right), \end{aligned} \quad (43)$$

$$\begin{aligned} D_1(\theta,\theta_0,\theta_1) = &\frac{ih\sin\theta}{2^{3/2}\pi^{1/2}(\cos\theta+\cos\theta_1)}\left[\frac{i\cos(kb\sin\theta_0)\cos(kb\sin\theta)}{K_+(k\cos\theta_0)K_+(k\cos\theta-m)}\right. \\ &\left.+\frac{i\sin(kb\sin\theta_0)\sin(kb\sin\theta)}{L_+(k\cos\theta_0)L_+(k\cos\theta-m)}\right] \\ &+\frac{h\sin\theta_0}{2^{3/2}\pi^{1/2}mi(\cos\theta+\cos\theta_1)}\left[\frac{i\cos(kb\sin\theta_0)\cos(kb\sin\theta)}{K_+(k\cos\theta_1)K_+(k\cos\theta)}\right. \\ &\left.+\frac{i\sin(kb\sin\theta_0)\sin(kb\sin\theta)}{L_+(k\cos\theta_1)L_+(k\cos\theta)}\right], \end{aligned} \quad (44)$$

$$\begin{aligned} D_2(\theta,\theta_0,\theta_2) = &-\frac{ih\sin\theta}{2^{3/2}\pi^{1/2}(\cos\theta+\cos\theta_2)}\left[\frac{i\cos(kb\sin\theta_0)\cos(kb\sin\theta)}{K_+(k\cos\theta_0)K_+(k\cos\theta+m)}\right. \\ &\left.+\frac{\sin(kb\sin\theta_0)\sin(kb\sin\theta)}{L_+(k\cos\theta_0)L_+(k\cos\theta+m)}\right] \\ &+\frac{h\sin\theta_0}{2^{3/2}\pi^{1/2}mi(\cos\theta+\cos\theta_2)}\left[\frac{i\cos(kb\sin\theta_0)\cos(kb\sin\theta)}{K_+(k\cos\theta_2)K_+(k\cos\theta)}\right. \\ &\left.-\frac{i\sin(kb\sin\theta_0)\sin(kb\sin\theta)}{L_+(k\cos\theta_2)L_+(k\cos\theta)}\right]. \end{aligned} \quad (45)$$

Equation (38) gives the scattered far field expression for $0 < \theta < \pi$. The results for $-\pi < \theta < 0$ can be derived by the same procedure and omitted here.

5. CONCLUSIONS

In this paper, we have analyzed the diffraction by two parallel half-planes with sinusoidal corrugation using the Wiener-Hopf technique combined with the perturbation scheme. The results obtained in this paper are valid for the case where the corrugation amplitude is small compared with the wavelength. Taking the inverse Fourier transform and applying the saddle point method, we have derived a scattered far field expression explicitly.

ACKNOWLEDGMENT

This work was supported in part by the Institute of Science and Engineering, Chuo University.

REFERENCES

1. Noble, B., *Methods Based on the Wiener-Hopf Technique for the Solution of Partial Differential Equations*, Pergamon, London, 1958.
2. Das Gupta, S. P., "Diffraction by a corrugated half-plane," *Proc. Vib. Prob.*, Vol. 3, 413–424, 1970.
3. Chakrabarti, A. and S. Dowerah, "Traveling wave in a parallel plate waveguide with periodic wall perturbations," *Can. J. Phys.*, Vol. 62, 271–284, 1984.
4. Kobayashi, K. and T. Eizawa, "Plane wave diffraction by a finite sinusoidal grating," *IEICE Trans.*, Vol. E74, 2815–2826, 1991.

Polarization Evolution in Weakly Anisotropic Media: Quasi-Isotropic Approximation (QIA) of Geometrical Optics Method and Its Recent Generalizations

Yu. A. Kravtsov[1,2], **P. Berczynski**[3], **B. Bieg**[2], **K. Yu. Bliokh**[4,5], **and Z. H. Czyz**[6]

[1]Space Research Institute, Profsoyuznaya St. 82/34, Moscow 117997, Russia
[2]Institute of Physics, Maritime University of Szczecin
1-2 Waly Chrobrego St., Szczecin 70500, Poland
[3]Institute of Physics, Szczecin University of Technology, Szczecin 70-310, Poland
[4]Institute of Radio Astronomy, 4 Krasnoznamyonnaya St., Kharkov 61002, Ukraine
[5]A. Ya. Usikov Institute of Radiophysics and Electronics, Kharkov 61085, Ukraine
[6]Telecommunications Research Institute, Warsaw 04051, Poland

Abstract— Quasi-isotropic approximation (QIA) of geometrical optics method is presented, which describes evolution of electromagnetic waves in weakly anisotropic media. This method was generalized recently in different directions. At first, it was shown that in combination with paraxial complex geometrical optics, which describes diffraction of the Gaussian beams in inhomogeneous media, QIA is able to embrace both polarization and diffraction changes of the electromagnetic waves in weakly anisotropic media. At second, QIA equations are presented in a compact form by involving the complex polarization angle (CPA). Relations between CPA and traditional parameters of polarization ellipse are established. Equations for CPA evolution are derived for inhomogeneous magnetized plasma accounting both Faraday effect and Cotton-Mouton phenomenon. At third, equations for Stokes vector evolution, which are widely used in plasma polarimetry, are derived directly from QIA, what demonstrates deep unity of two seemingly different approaches to the solution of polarimetric problems.

1. INTRODUCTION

There exist two main approaches for description of electromagnetic wave propagation and polarization in weakly anisotropic media. The first of them is Budden's method [1, 2], which deals with coupled wave equations for the components of the electromagnetic wave field. Coupled wave equations for weakly anisotropic media were suggested in [3] in the form of quasi-isotropic approximation (QIA) of the geometrical optics method. QIA was developed in depth in subsequent publications [4, 5] and briefly outlined in the books [6, 7].

Alternative approach — "Stokes vector formalism", have been developing by Segre for the purposes of plasma polarimetry [8–11]. Comparative analysis of two approaches mentioned was performed by Serge in [12]. Segre has analyzed advantages and shortcomings of each technique, omitting yet their deep unity, if not equivalence. It was shown recently [13] that equation for Stokes vector evolution can be derived in a consequent way from the Maxwell equations on the basis of the quantum-mechanical diagonalization procedure, which generalizes QIA approach.

This paper intends to present in brief the basic equations of QIA and to outline its recent generalizations, in particular, to derive equations for the Stokes vector directly from QIA equations and thereby to reveal a practical equivalence of two techniques under discussion.

2. QUASI-ISOTROPIC APPROXIMATION (QIA)

Quasi-isotropic approximation (QIA) of the geometrical optics method [3–7] describes propagation of electromagnetic waves in weakly anisotropic media. In similar media all the components of the anisotropy tensor $\nu_{mn} = \varepsilon_{mn} - \varepsilon_0\delta_{mn}$ are small as compared with ε_0, where ε_0 is an electric permittivity of the isotropic background medium, ε_{mn} is the full tensor of electrical permittivity and δ_{mn} is a unit tensor. Besides traditional "geometrical" small parameter

$$\mu_{GO} = 1/k_0 L << 1 \tag{1}$$

(here k_0 is a wave number and L is a characteristic scale of the medium inhomogeneity) QIA involves additional small parameter

$$\mu_A = \max|\nu_{mn}|/\varepsilon_0 << 1, \tag{2}$$

which characterizes weakness of the medium anisotropy.

According to [3–7], asymptotic solution of the Maxwell equations in the lowest approximation in small parameters μ_{GO} and μ_A can be presented as

$$\mathbf{E} = A\mathbf{\Gamma}\exp(ik\Psi), \tag{3}$$

where A and Ψ are correspondingly amplitude and eikonal of the electromagnetic wave in isotropic medium and $\mathbf{\Gamma}$ is a polarization vector, which is orthogonal to the reference ray, like in an isotropic medium. Let the unit vectors $\mathbf{e}_1$ and $\mathbf{e}_2$ together with the tangent unit vector $\mathbf{l}$ form a basis for the Popov's orthogonal coordinate system (ξ_1, ξ_2, σ), associated with a selected (reference) ray [14] (see also Ch. 9 in the book [15] as well as Ch. 4 in the book [16]; in the latter one Popov's system appears as "ray centered coordinate system"). Unit vectors $\mathbf{e}_1$ and $\mathbf{e}_2$ of the Popov's orthogonal system obey the equations

$$\frac{d\mathbf{e}_i}{d\sigma} = -\frac{1}{2}\left(\mathbf{e}_i \cdot \nabla \ln \varepsilon_0\right)\mathbf{l}, \quad i = 1, 2. \tag{4}$$

The most important feature of these vectors is their ability to describe parallel transport of the electrical vector $\mathbf{E}$ along the reference ray in an isotropic medium.

In the Popov's orthogonal coordinate system the polarization vector $\mathbf{\Gamma}$ can be presented as

$$\mathbf{\Gamma} = \Gamma_1\mathbf{e}_1 + \Gamma_2\mathbf{e}_2. \tag{5}$$

The components Γ_1 and Γ_2 of polarization vector obey the QIA equations

$$\begin{aligned} \frac{d\Gamma_1}{d\sigma} &= \tfrac{1}{2}ik_0\varepsilon_0^{-1/2}(\nu_{11}\Gamma_1 + \nu_{12}\Gamma_2), \\ \frac{d\Gamma_2}{d\sigma} &= \tfrac{1}{2}ik_0\varepsilon_0^{-1/2}(\nu_{21}\Gamma_1 + \nu_{22}\Gamma_2), \end{aligned} \tag{6}$$

where σ is an arc length along the reference ray. In distinction to the original form of the QIA equations, written in frame of natural trihedral coordinate system [3–7], Equations (6) do not contain torsion of the ray, because the Popov's orthogonal system provides parallel, i.e., torsionless transport of the electrical intensity vector along the ray.

3. COMBINATION OF QIA WITH COMPLEX GEOMETRICAL OPTICS (CGO)

In frame of CGO eikonal Ψ and amplitude A become complex valued and thereby allow describing diffraction of the Gaussian beams. In the case of paraxial CGO [17, 18] eikonal Ψ can be presented as a quadratic form $\Psi = \Psi_c + \frac{1}{2}B_{ij}\xi_i\xi_j$, where Ψ_c is an eikonal along the central ray and ξ_i are deviations from central ray. Matrix elements B_{ij} becomes complex valued in frame of CGO and satisfy nonlinear matrix Ricatti equation

$$\frac{dB_{ij}}{d\tau} + B_{ik}B_{kj} = \alpha_{ij}, \tag{7}$$

where parameters

$$\alpha_{ij}(\tau) = \frac{1}{2}\frac{\partial^2 n_c^2}{\partial\xi_i\partial\xi_j} - \frac{3}{4n_c^2}\frac{\partial n_c^2}{\partial\xi_i}\frac{\partial n_c^2}{\partial\xi_j} \tag{8}$$

are the derivatives of the dielectric permittivity transverse the ray [17, 18]. The real parts $\mathrm{Re}B_{ij}$ of parameters B_{ij} describe the curved phase front of the beam, whereas imaginary parts $\mathrm{Im}(B_{ij})$ corresponds to Gaussian profile of the electromagnetic beam and describe its diffraction in inhomogeneous plasma. The amplitude A of the wave field (3) might be determined from the transport equation, it satisfies the energy flow conservation law in a beam cross-section [17, 18]. Thus, being combined with QIA, CGO allows to describe simultaneously both polarization and diffraction phenomena.

4. COMPLEX POLARIZATION ANGLE (CPA)

Tangent of CPA is involved as a ratio of complex amplitudes [3–7, 19]: $\tan\gamma = \Gamma_2/\Gamma_1$. The components of CPA $\gamma = \gamma' + i\gamma''$ characterize the angular parameters ψ, χ of the polarization ellipse: real part γ' defines polarization angle, $\gamma' = \psi$ and imaginary part — its ellipticity: $\tanh\gamma'' = \tan\chi = e$.

QIA Equations (6) lead to the following equation for complex polarization angle γ in magnetized plasma:

$$\dot{\gamma} = \tfrac{1}{2}k_0 V u^{1/2}\cos\alpha_{||} - \tfrac{1}{4}ik_0 V u \sin^2\alpha_{||}\sin(2\gamma - 2\alpha_\perp). \tag{9}$$

Here $\dot{\gamma} = d\gamma/d\sigma$ is a derivative along the ray, $v = \omega_p^2/\omega^2$ and $u = \omega_c^2/\omega^2$ are standard plasma parameters [2], ω_p and ω_c are plasma frequency and electron cyclotron frequency correspondingly and parameter V is defined as $V = v/(1-u)$.

This equation can be presented also as [19]

$$\dot{\gamma} = \tfrac{1}{2}\Omega_3 - \tfrac{1}{2}i\Omega_1\sin 2\gamma + \tfrac{1}{2}i\Omega_2\cos 2\gamma = \tfrac{1}{2}\Omega_3 - \tfrac{1}{2}i\Omega_\perp\sin(2\gamma - 2\alpha_\perp), \tag{10}$$

where

$$\Omega_1 = \tfrac{1}{2}k_0 V u\sin^2\alpha_{||}\cos 2\alpha_\perp, \quad \Omega_2 = \tfrac{1}{2}k_0 V u\sin^2\alpha_{||}\sin 2\alpha_\perp, \quad \Omega_3 = k_0 V u^{1/2}\cos\alpha_{||} \tag{11}$$

are parameters, frequently used in plasma polarimetry [8–13], and $\Omega_\perp = \sqrt{\Omega_1^2 + \Omega_2^2}$. Angles $\alpha_\perp$ and $\alpha_{||}$ characterize orientation of the basis $\mathbf{e}_1$, $\mathbf{e}_2$, $\mathbf{l}$ relative the static magnetic vector $\mathbf{B}_0$, Fig. 1.

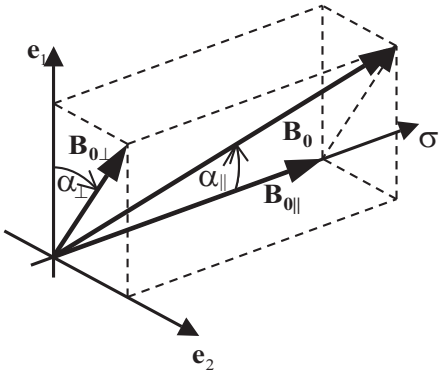

Figure 1: Orthogonal basis $\mathbf{e}_1$, $\mathbf{e}_2$ presented together with the static magnetic vector $\mathbf{B}_0$.

The term Ω_3 in Equation (10) corresponds to the Faraday effect, and the term $\Omega_\perp$ describes Cotton-Mouton phenomenon. Equations. (9) and (10) for CPA have proved to be very helpful for solution of problems in plasma polarimetry.

5. EQUATION FOR STOKES VECTOR EVOLUTION DERIVED FROM QIA

For monochromatic wave field the components of the full (four components) Stokes vector $\mathbf{S} = (s_0,\, s_1,\, s_2,\, s_3)$ are connected with the components of the polarization vector by relations:

$$\begin{cases} s_0 = |\Gamma_1|^2 + |\Gamma_2|^2, & s_2 = \Gamma_1\Gamma_2^* + \Gamma_1^*\Gamma_2, \\ s_1 = |\Gamma_1|^2 - |\Gamma_2|^2, & s_3 = i\left(\Gamma_1^*\Gamma_2 - \Gamma_1\Gamma_2^*\right). \end{cases} \tag{12}$$

Making use of QIA Equations (6), one can show that evolution equation for Stokes vector $\mathbf{S} = (s_0,\, s_1,\, s_2,\, s_3)$ acquires a compact vector form:

$$\dot{\mathbf{S}} = \hat{\mathbf{M}}\mathbf{S}. \tag{13}$$

Here $\hat{\mathbf{M}}$ is a general form of differential Mueller 4×4 matrix for weakly anisotropic media:

$$\hat{\mathbf{M}} = \frac{k_0}{2\sqrt{\varepsilon_0'}}\begin{Bmatrix} i\left(\nu_{11}^a + \nu_{22}^a\right) & i\left(\nu_{11}^a - \nu_{22}^a\right) & i\left(\nu_{12}^a + \nu_{21}^a\right) & \left(\nu_{12}^a - \nu_{21}^a\right) \\ i\left(\nu_{11}^a - \nu_{22}^a\right) & i\left(\nu_{11}^a + \nu_{22}^a\right) & -i\left(\nu_{21}^h - \nu_{12}^h\right) & \left(\nu_{12}^h + \nu_{21}^h\right) \\ i\left(\nu_{12}^a + \nu_{21}^a\right) & i\left(\nu_{21}^h - \nu_{12}^h\right) & i\left(\nu_{11}^a + \nu_{22}^a\right) & -\left(\nu_{11}^h - \nu_{22}^h\right) \\ \left(\nu_{12}^a - \nu_{21}^a\right) & -\left(\nu_{12}^h + \nu_{21}^h\right) & \left(\nu_{11}^h - \nu_{22}^h\right) & i\left(\nu_{11}^a + \nu_{22}^a\right) \end{Bmatrix} \tag{14}$$

and ν_{ij}^h, ν_{ij}^a are Hermitian and anti-Hermitian parts of the anisotropy tensor ν_{ij}. Evolution Equation (14) happens to be in general agreement with the Segre's results for magnetized plasma, obtained for simplified plasma model [8–13].

In the case of collisionless plasma one deals with a reduced (three component) Stokes vector $\mathbf{s} = (s_1,\, s_2,\, s_3)$ with $s_1 = \cos 2\chi\cos 2\psi$, $s_2 = \cos 2\chi\sin 2\psi$, $s_3 = \sin 2\chi$. In this case Equation (14) takes a form

$$\dot{\mathbf{s}} = \boldsymbol{\Omega}\times\mathbf{s}, \tag{15}$$

with parameters $\boldsymbol{\Omega} = [\Omega_1,\, \Omega_2,\, \Omega_3]$, mentioned above.

6. EVOLUTION EQUATIONS FOR TRADITIONAL ANGULAR POLARIZATION PARAMETERS

It follows from Sec. 4 that $\dot{\gamma}' = \dot{\psi}$, $\dot{\gamma}'' = \dot{\chi}/\cos 2\chi$, $\tanh 2\gamma'' = \sin 2\chi$, $\sinh 2\gamma'' = \tan 2\chi$ and $\cosh 2\gamma'' = 1/\cos 2\chi$. Substituting these relations into Equations (10) one can obtain the following system of equations for the traditional angular polarization parameters (ψ, χ):

$$\begin{aligned} \dot{\psi} &= \frac{\Omega_3}{2} + \frac{\Omega_\perp}{2}\cos(2\psi - 2\alpha_\perp)\tan 2\chi, \\ \dot{\chi} &= -\frac{\Omega_\perp}{2}\sin(2\psi - 2\alpha_\perp). \end{aligned} \tag{16}$$

Solutions of these equations allow finding the components $s_1 = \cos 2\chi \cos 2\psi$, $s_2 = \cos 2\chi \sin 2\psi$, $s_3 = \sin 2\chi$ of the reduced Stokes vector $\mathbf{s} = (s_1, s_2, s_3)$. In fact, Equation (16) is equivalent both to the Equation (15) for the Stokes vector evolution and to Equations (9, 10) for complex polarization angle $\gamma = \gamma' + i\gamma''$.

7. COMPARISON OF QIA EQUATIONS WITH EQUATIONS FOR STOKES VECTOR EVOLUTION

The equations for Stokes vector, derived from quasi-isotropic approximation of geometrical optics, are very close in form to the equations, obtained in [8–13] on the basis of quite simple if not primitive electrodynamical model, dealing with independent normal modes in locally homogeneous anisotropic medium.

In contrast to Segre's simplified approach, QIA stems from Maxwell equations in a consequent way, using an asymptotic expansion of the wave field in small parameters μ_A and μ_{GO} Equations (1) and (2).

Equations of QIA determine evolution of polarization vector along the rays, experiencing curvature and torsion and are able to describe mode conversion due to medium inhomogeneity [3–5]. Therefore equations for the Stokes vector evolution obtained from quasi-isotropic approximation of geometrical optics, acquire all the merits of QIA, in particular, they describe effects of the ray curvature and torsion. It is quasi-isotropic approximation of geometrical optics method, which justifies the equations like (14) and (15), because in fact the papers [8–13] assume the medium to be weakly anisotropic one.

In spite of high degree of similarity, QIA Equations (5) and Equations (14, 15) for Stokes vector evolution, in fact, can not be considered as completely identical ones because of phase distinctions. To illustrate this, let us present polarization vector

$$\mathbf{\Gamma} = (\Gamma_1, \Gamma_2) = (|\Gamma_1|e^{i\delta_1}, |\Gamma_2|e^{i\delta_2}) \tag{17}$$

as

$$\mathbf{\Gamma} = e^{i(\delta_1+\delta_2)/2}(|\Gamma_1|e^{i(\delta_1-\delta_2)/2}, |\Gamma_2|e^{i(-\delta_1+\delta_2)/2}) \tag{18}$$

and express four field parameters (two modules $|\Gamma_1|$, $|\Gamma_2|$ and two phases δ_1, δ_2) through the components s_0, s_1, s_2, s_3 of the Stokes vector $\mathbf{S}$. It follows from Equations (12) that

$$|\Gamma_1|^2 = \frac{1}{2}(s_0 + s_1), \quad |\Gamma_2|^2 = \frac{1}{2}(s_0 - s_1), \quad \tan(\delta_1 - \delta_2) = -\frac{s_3}{s_2}. \tag{19}$$

Only three parameters: two modules $|\Gamma_1|$, $|\Gamma_2|$ and phases difference $(\delta_1 - \delta_2)$, can be found from Equations (13) for Stokes vector. It means that four Equations (13) are not completely equivalent to the QIA Equations (5): the phase half sum $(\delta_1 + \delta_2)/2$ principally can not be extracted from Stokes vector. The reason is that the components s_0, s_1, s_2 and s_3 of the Stokes vector are connected by a relation $s_0^2 = s_1^2 + s_2^2 + s_3^2$, so that each of Equations (12) is dependent on three others.

Though the phase $(\delta_1 + \delta_2)/2$ does not influence on the shape of polarization ellipse, it might be important for forming interference pattern, created by two or more polarized wave fields.

8. CONCLUSIONS

Evolution of the polarization vector in inhomogeneous plasma is described on the basis of quasi-isotropic approximation of the geometrical optics method. QIA equations take into account: i) curvature and torsion of the ray; ii) longitudinal and lateral inhomogeneity of plasma; iii) torsion

of the static magnetic field; iv) weak absorption and dichroism. QIA equations are the basis for consequent derivation of the equation for the complex polarization angle, which promises to become an effective instrument for plasma polarimetry. Besides, QIA equations are favorable basis for substantiation of the equation for the Stokes vector evolution. The results under consideration might be quite helpful for solution of the inverse problems of plasma diagnostics.

ACKNOWLEDGMENT

This work was supported in part by Association Euratom-IPPLM and Polish Ministry of Science and Higher Education in frame of the project P-12.

REFERENCES

1. Budden, K. G., *Radio Waves in the Ionosphere*, Cambridge Univ. Press, Cambridge, UK, 1961.
2. Ginzburg, V. I., *Propagation of Electromagnetic Waves in Plasma*, Gordon and Breach, New York, 1970.
3. Kravtsov, Y. A., "Quasi-isotropic geometrical optics approximation," *Sov. Phys. — Doklady*, Vol. 13, No. 11, 1125–1127, 1969.
4. Kravtsov, Y. A., O. N. Naida, and A. A. Fuki, "Waves in weakly anisotropic inhomogeneous media: quasi-isotropic approximation of geometrical optics," *Physics-Uspekhi*, Vol. 39, No. 2, 129–134, 1996.
5. Fuki, A. A., Y. A. Kravtsov, and O. N. Naida, *Geometrical Optics of Weakly Anisotropic Media*, Gordon & Breach, Lond., N.Y., 1997.
6. Kravtsov, Y. A. and Y. I. Orlov, *Geometrical Optics of Inhomogeneous Media*, Springer Verlag, Berlin, Heidelberg, 1990.
7. Kravtsov, Y. A., *Geometrical Optics in Engineering Physics*, Alpha Science, London, 2005.
8. Segre, S. E., "A review of plasma polarimetry-theory and methods," *Plasma Phys. Control. Fusion*, Vol. 41, R57–R100, 1999.
9. Segre, S. E., "New formalism for the analysis of polarization evolution for radiation in a weakly nonuniform, fully anisotropic medium: a magnetized plasma," *J. Opt. Soc. Am. A*, Vol. 18, No. 10, 2601–2606, 2001.
10. Segre, S. E., "Polarization evolution of radiation propagating in weakly non-uniform magnetized plasma with dissipation," *J. Phys. D: Appl. Phys.*, Vol. 36, 2806–2810, 2003.
11. Segre, S. E. and V. Zanza, "Derivation of the pure faraday and cotton-mouton effects when polarimetric effects in a tokamak are large," *Plasma Phys. Controlled Fusion*, Vol. 48, 339–351, 2006.
12. Segre, S. E., "Comparison between two alternative approaches for the analysis of polarization evolution of EM waves in a nonuniform, fully anisotropic medium: magnetized plasma," Preprint RT/ERG/FUS/2001/13, ENEA, Frascati, Italy, 2001.
13. Bliokh, K. Y., D. Y. Frolov, and Y. A. Kravtsov, "Non-abelian evolution of electromagnetic waves in a weakly anisotropic inhomogeneous medium," accepted for publication in *Phys. Rev. E*, 2007.
14. Popov, M. M., "Eigen-oscillations of multi-mirrors resonators," Vestnik Leningradskogo Universiteta (Bulletin of the Leningrad University), N 22, 44–54, 1969 (in Russian) (Popov's orthogonal coordinate system is described also in [15] and in [16]).
15. Babich, V. M. and V. S. Buldyrev, *Short-wavelength Diffraction Theory: Asymptotic Methods*, Springer Verlag, Berlin, 1990.
16. Červený, V., *Seismic Ray Theory*, Cambridge University Press, Cambridge, UK, 2001.
17. Berczynski, P., K. Y. Bliokh, Y. A. Kravtsov, and A. Stateczny, "Diffraction of Gaussian beam in 3D smoothly inhomogeneous media: eikonal-based complex geometrical optics approach," *J. Opt. Soc. Amer. A*, Vol. 23, No. 6, 1442–1451, 2006.
18. Kravtsov, Y. A. and P. Berczynski, "Gaussian beams in inhomogeneous media: a review," *Stud. Geophys. Geod.*, Vol. 51, 1–36, 2007.
19. Czyz, Z. H., B. Bieg, and Y. A. Kravtsov, "Complex polarization angle: relation to traditional polarization parameters and application to microwave plasma polarimetry," Accepted for publication in *Phys. Lett. A*, March 2007.

Field Propagation in Nanoporous Metal Waveguides

A. J. Viitanen[1], **I. S. Nefedov**[2], **and S. A. Tretyakov**[2]

[1]Electromagnetics Laboratory, TKK Helsinki University of Technology, Finland
[2]Radio Laboratory/SMARAD Center of Excellence, TKK Helsinki University of Technology, Finland

Abstract— In this paper propagation of electromagnetic fields in a structure with regular arrays of pores in metal is considered. This structuce is analyzed in a similar way as the arrays of dipoles. Now in this case, the surrounding medium is metal while the inclusions are empty spheres. The inclusions resonate at the certain frequency making the interaction between the inclusions very strong. The linear chain of such resonating particles forms a waveguide. Although the field is decaying outside the pores, these inclusions are so close to each other that there is interaction with the neighbouring pores. Near the resonance this interaction is strong enough that there exist guided wave modes along the array. Properties of these modes are investigated. The allowed frequency range where the guided modes exist depend on the geometry, i.e., how close the pores are and what is the size of pores. There exist two propagating modes, transversal and axial polarizations. The transversally polarized field propagates as a forward wave and the axially polarized field as a backward wave.

1. INTRODUCTION

In recent years a lot of attention is paid for metal nanoscale structures because of new phenomena and potential applications for waveguide and antenna techniques. Especially in optical region new effects arise based on plasmon resonances. Optical properties of metals with nanopores are now of particular current interest [1–3]. Remarkable optical effects caused by excitation of plasmons in nanoporous metals such as extraordinary transmission [4] and total absorption of light [5] have been predicted theoretically. In [1] strong resonant dips in the reflectivity spectra of light were observed from nanoporous metal surfaces formed by periodic arrangements of close-packed spherical voids. In a recent paper [5] it was theoretically shown that this effect is caused by excitation of plasmons in voids (void plasmons). Arrays of regular resonant inclusions are theoretically studied in [6, 7].

In this paper we consider propagation characteristics in a wave guide structure which consists of regular linear array of pores in plasma. An analogous structure has been considered in optics by Weber and Ford [8] where a chain of silver nanospheres are operating at frequencies near the plasmon resonance of an individual sphere. If the spheres are polarized transversally with respect to the chain axis, and the chain is dense, there appears a frequency band in which each frequency corresponds to two modes: the forward mode and the backward mode. At the upper edge of this frequency band both these solutions join one another that correspond to zero group velocity but nonzero phase velocity. In the vicinity of this frequency the dispersion curve is almost flat that makes this structure suitable for a subwavelength imaging. In [9] similar dispersion was found in two coupled chains of silver spheres and it was proposed to use this effect for obtaining subwavelength images.

We expect that localized void plasmons in a thin layer of nanopore metal, interacting with surface plasmons, can be used instead the chain of metal spheres. In this paper we study wave propagation in the chain of spherical holes in a bulk metal using approximation of point-like dipoles as in [8, 9]. Actually the studied case is a dual problem to the chain of metal spheres in air and we compare features of spectra of modes for these two cases.

2. FIELD EXPRESSIONS

We consider metal structure with regular arrays of pores. The geometry is illustrated in Figure 1. This structuce can be analyzed in a similar way as the arrays of dipoles. Now in this case, the surrounding medium is metal while the inclusions are spherical holes. Making a linear chain of such particles we have a waveguide. In optical region metals behave almost as a lossless plasma. In the beginning we model the spheres as dipoles with the polarizability α. In the expression of the polarizability it is seen that the inclusions resonate at the frequency where the relative permittivity of the surrounding medium is $\epsilon_r = -\frac{1}{2}$.

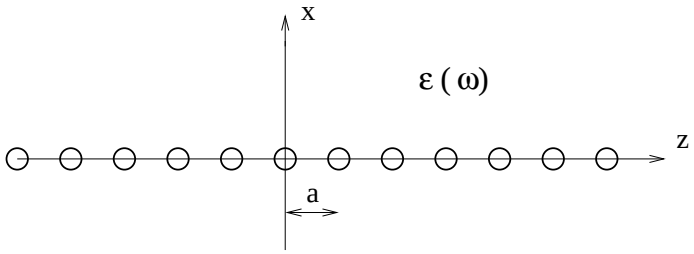

Figure 1: Geometry.

We consider spherical empty cavities in isotropic plasma. The polarizability of the sphere in plasma is

$$\alpha = \frac{3\epsilon_h(\epsilon_s - \epsilon_h)}{\epsilon_s + 2\epsilon_h} V \tag{1}$$

where the host medium is plasma $\epsilon_h = \epsilon_o \epsilon_r$

$$\epsilon_r = 1 - \frac{\omega_p^2}{\omega^2} \tag{2}$$

and the permittivity inside the sphere is $\epsilon_s = \epsilon_o$. The volume of the sphere is $V = 4\pi r_o^3/3$. We are looking for propagating fields in a region where the permittivity of the host medium is negative which is the case below the plasma frequency. In the frequency range below the plasma frequency after inserting the permittivities into the expression for the polarizability we can write the inverse of the polarizability in the following form

$$\frac{1}{\alpha} = \frac{1}{4\pi\epsilon_o r_o^3} \frac{2|\epsilon_r| - 1}{|\epsilon_r|(1 + |\epsilon_r|)} \tag{3}$$

The dipole moment of the pore is

$$\overline{p} = \alpha \overline{E} \tag{4}$$

where $\overline{E}$ is the local field. In a chain of dipoles the local field is obtained from the field expression for dipoles

$$\overline{E} = \frac{1}{4\pi\epsilon} \left[k^2 (\overline{u} \times \overline{p}) \times \overline{u} \frac{e^{-jkr}}{r} + [3\overline{u}(\overline{u} \cdot \overline{p}) - \overline{p}] \left(\frac{1}{r^3} + \frac{jk}{r^2} \right) e^{-jkr} \right] \tag{5}$$

where $\overline{u}$ is the unit vector indicating the direction from source dipole to the reference point.

In a chain the fields are decomposed into transversal and axial components. From the above field expression we can identify the interaction components for transversal and axial polarizations. The interaction dyadic is

$$\overline{\overline{\beta}} = \beta_\perp \overline{\overline{I}}_t + \beta_\parallel \overline{u}_z \overline{u}_z \tag{6}$$

where the interaction coefficients are

$$\beta_\perp = \frac{1}{4\pi\epsilon} \left[\frac{k^2}{|z - z'|} - \frac{1}{|z - z'|^3} - \frac{jk}{(z - z')^2} \right] e^{-jk|z - z'|} \tag{7}$$

$$\beta_\parallel = \frac{1}{2\pi\epsilon} \left[\frac{1}{|z - z'|^3} + \frac{jk}{(z - z')^2} \right] e^{-jk|z - z'|} \tag{8}$$

Taking the reference dipole at $z' = 0$ and $x' = 0$, and because the structure is periodic in z direction ($z = na$), the dipole moments of each dipole can be written according to the Floquet theorem

$$\overline{p}(n) = \overline{p}(0) e^{-jqna} \tag{9}$$

The local field at the reference point is caused by all the dipoles in the array

$$\overline{E} = \sum_n \overline{\overline{\beta}} \cdot \overline{p}(n) \tag{10}$$

In the summation the reference point, $n = 0$ is omitted.

In the frequency range below the plasma frequency the permittivity is negative and the wave number is imaginary $k = -j|k|$. This means that the fields are decaying and only the neighbouring spheres interact. This effect is seen in the expressions of the interaction coefficients which are exponentially decaying functions. The total interaction coefficients for the two eigenpolarizations are

$$C_\perp = \frac{1}{2\pi\epsilon_o a^3|\epsilon_r|}\sum_{n=1}^{\infty}\left(\frac{k^2a^2}{n}+\frac{1}{n^3}+\frac{|k|a}{n^2}\right)e^{-|k|na}\cos qna \tag{11}$$

$$C_\parallel = -\frac{1}{\pi\epsilon_o a^3|\epsilon_r|}\sum_{n=1}^{\infty}\left(\frac{1}{n^3}+\frac{|k|a}{n^2}\right)e^{-|k|na}\cos qna \tag{12}$$

3. DISPERSION RELATIONS

The eigenvalue equation for solving the propagation factor q along the array is obtained combining Equations (4), (9) and (10) which leads to two equations of the corresponding polarizations

$$C_\perp = \frac{1}{\alpha}, \qquad C_\parallel = \frac{1}{\alpha} \tag{13}$$

Because the components in the summation of the interaction coefficients are fast decaying functions we can approximate the infinite summation by taking only the first term. This approximation gives us an analytic solution which is quite close to exact one

$$\cos q_\perp a \approx \frac{\left(\frac{a}{r_o}\right)^3\left(1-\frac{3}{2}\frac{\omega^2}{\omega_p^2}\right)e^{|k|a}}{1+|k|a+|k|^2a^2} \tag{14}$$

and

$$\cos q_\parallel a \approx \frac{\left(\frac{a}{r_o}\right)^3\left(\frac{3}{2}\frac{\omega^2}{\omega_p^2}-1\right)e^{|k|a}}{2(1+|k|a)} \tag{15}$$

In these results we can conclude that there exist guided waves in the frequencies close to $\sqrt{\frac{2}{3}}\omega_p$. In this special frequency the inclusions resonate, and it corresponds to the special permittivity value, $\epsilon_r = -\frac{1}{2}$ of the medium. The other observation is that because the right-hand side of the above equations are of opposite sign, one of these eigenwaves is a forward wave and the other one is a backward wave. In Figure 2 are illustrasted the dispersion curves for transversally and axially polarized fields. These solutions are calculated using exact expressions of interaction coefficients.

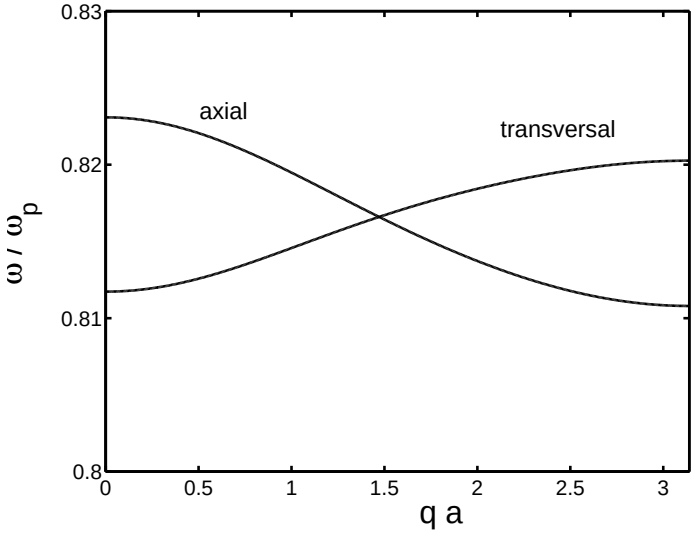

Figure 2: Dispersion curves calculated for spheres $a/r_o = 3$.

It is seen that the transversally polarized field is the forward wave and the axially polarized field is the backward wave. These results can be compared to the results of the dual problem, regular array of plasma spheres in free space. In [8, 9] it is shown that in the line of metal spheres the axially polarized field is a forward wave and the transversely polarized field has a backward wave component. Also the resonance frequencies are different, in our case $\omega_r = \sqrt{\frac{2}{3}}\omega_p$ and in [9] $\omega_r = \omega_p/\sqrt{3}$

In Figure 3 the effect of geometry for the band width is illustrated. The dispersion curves are calculated for fixed period with different pore radius. For larger relative radius of pores the allowed frequency range for guided waves is larger than for small radius values.

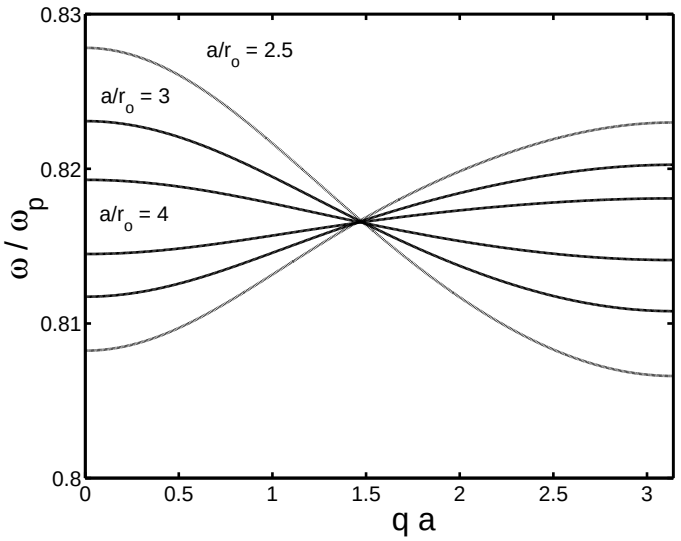

Figure 3: Dispersion curves, calculated for different ratios $a/r_o = 4$, $a/r_o = 3$ and $a/r_o = 2.5$.

4. CONCLUSION

The dispersion characteristics of regular arrays of pores in plasma are considered. The structure is analyzed in a similar way as arrays of dipoles, now the surrounding medium is plasma and the inclusions are empty spheres. The inclusions resonate at the frequency where the relative permittivity of the plasma is $-1/2$. Although the field is decaying outside the pores, these pores are so close to each other that there exists interaction with the neighbouring pores, which is strong enough near the resonance that there are propagating guided modes along the array. The linear array of such inclusions forms a waveguide whose dispersion relation is calculated. It is found that the transversely polarized field propagates as a forward wave and the axially polarized field as a backward wave. The effects of geometry for dispersion characteristics of propagating waves are also studied. The band width is broader when the inclusions are closer to each other and the interaction is stronger.

ACKNOWLEDGMENT

This research is partially supported by the Academy of Finland (Grant No. 118509) and the Russian Foundation for Basic Research.

REFERENCES

1. Coyle, S., M. C. Netti, J. J. Baumberg, M. A. Ghanem, P. R. Birkin, P. N. Bartlett, and D. M. Whittaker, "Confined plasmons in metallic nanocavities," *Phys. Rev. Lett.*, Vol. 87, No. 17, 176801(1–4), 2001.
2. Velev, O. D., P. M. Tessier, A. M. Lenhoff, and E. W. Kaler, "A class of porous metallic nanostructures," *Nature*, Vol. 401, 548, 1999.
3. Wijnhoven, J. E. G. J., S. J. M. Zevenhuizen, M. A. Hendriks, D. Vanmaekelbergh, J. J. Kelly, and W. L. Vos, "Electrochemical assembly of ordered macropores in gold," *Advanced Materials*, Vol. 12, No. 12, 888–890, 2000.

4. Stefanou, N., A. Modinos, and V. Yannopapas, "Optical transparency of mesoporous metals," *Solid State Commun.*, Vol. 118, No. 2, 69–73, 2001.
5. Teperik, T. V., V. V. Popov, and F. J. Garcia de Abajo, "Void plasmons and total absorption of light in nanoporous metallic films," *Physical Review B*, Vol. 71, 085408(1–9), 2005.
6. Tretyakov, S. A. and A. J. Viitanen, "Line of periodically arranged passive dipole scatterers," *Electrical Engineering, Archiv für Elektrotechnik,* Vol. 82, No. 6, 353-361, 2000.
7. Viitanen, A. J. and S. A. Tretyakov, "Metawaveguides formed by arrays of small resonant particles over a ground plane," *Journal of Optics A: Pure and Applied Optics,* Vol. 7, No. 2, S133-S140, 2005.
8. Weber, W. H. and G. M. Ford, "Propagation of optical excitations by dipolar interactions in metal nanoparticle chains," *Physical Review B*, Vol. 70, 125429(1–8), 2004.
9. Simovski, C. R., A. J. Viitanen, and S. A. Tretyakov, "Resonator mode in chains of silver spheres and its possible application," *Physical Review E,* Vol. 72, 066606(1-10), 2005.

Metamaterial Comprising Plasmonic Nanolasers

Andrey K. Sarychev, **Alexander A. Pukhov**, **and Gennady Tartakovsky**

Institute of Theoretical and Applied Electrodynamics RAS, Izhorskaya 13, Moscow 125412, Russia

Abstract— We consider plasmonic nanoantennas immersed in active host medium. Specifically shaped metal nanoantennas can exhibit strong magnetic properties in the optical spectral range due to the excitation of magnetic plasmon resonance. We propose plasmonic nanolaser, where the metal nanoantenna operates like a resonator. The size of the proposed plasmonic laser is much smaller than the wavelength. Therefore, it can serve as a very effective source of EM radiation.

1. INTRODUCTION

Extending the range of electromagnetic properties of naturally occurring materials motivates the development of artificial metamaterials. For example, it has been demonstrated recently that metamaterials may exhibit such exotic properties as artificial magnetism [1, 2], negative dielectric permittivity (see, for example [1–3]), negative magnetic permeability [4, 5], and even both [6–8]. The double-negative case of $\mathrm{Re}\varepsilon < 0$ and $\mathrm{Re}\mu < 0$ is often referred as a lefthanded material (LHM) because the electric and magnetic fields and the wavevector are left system in a plane wave propagating in material as it was first found by Veselago [6]. Situations when a negative refractive index can be realized in practice are particularly interesting because of "perfect" lens with subwavelength resolution [8]. Negative refraction and subwavelength imaging has been demonstrated in the microwave range [7, 9–11]. For microwave LHMs, artificial magnetic elements providing $\mathrm{Re}\mu < 0$ are the resonators of the split ring type [7, 11, 12].

For the optical range, LHM with a negative refractive index were first demonstrated in [13] and [14–16]. The authors of [14–16] observed the negative real part of the refractive index at the telecommunication wavelength of 1550 nm. In [14–16] the authors experimentally verified their earlier theoretical prediction of negative refraction in the array of parallel metal nanorods [17–19]. The first experimental observations of negative n in the optical range were followed by another successful experiment [20]. Very recently a macroscopic, far field image of the subwavelength object was obtained from cylindrical superlens [21]. Note that the losses become progressively important with decreasing the wavelength towards the optical range [22]. Moreover, finite losses inside the LHM superlens could dramatically reduce the resolution of such lens [23] and made a dream of a full-scale superlens unattainable.

To reduce the loss we suggest filling the metal horseshoe resonator, shown in Fig. 1, with an active medium. We consider the interaction of such nanoantenna with *a two-level amplifying system* (TLS), which can be represented by quantum dot in the semiconductor host, quantum well, dye molecules, or another high gain medium. Horseshoe-shaped subwavelength nanoantennas were first suggested in [24, 25]. These structures support strong magnetic moments at frequencies higher than microwave-mid-IR range for which traditional split ring resonators (see [4, 5, 12, 26–28] for details) were sufficient.

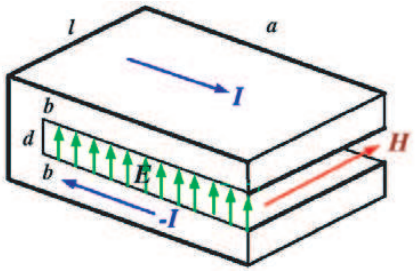

Figure 1: Horseshoe optical nanoantenna is excited by magnetic field **H**; arm length a, arm thickness b, lateral size l, gap width d; electric current flows in metal arms; displacement currents in the gap short the circuit; magnetic moment of the current is either parallel ($\mu > 0$) or antiparallel ($\mu < 0$) to **H**.

2. L-C-R MODEL OF HORSESHOE RESONATOR FILLED WITH ACTIVE MEDIUM

The main features of horseshoe electrodynamics can be understood in terms of a simple equivalent L-C-R model shown in Fig. 2 [29, 30]. We consider the metal horseshoe nanoantenna, which is excited by the magnetic component H of the impingent electromagnetic field. The length a, width l and the thickness b of the metal arms as well as the gap d between the arms are supposed to be much smaller than the wavelength. The electric current $I = \dot{q}$, flowing in the metal arms of the antenna, is shorted by the displacement currents in the gap.

The metal part of the nanoantenna can be presented as an inductance L. The gap between two arms is modeled as capacitance C. Thus the horseshoe antenna can be presented as L-R-C circuit, shown in Fig. 2. The inductance $L = 8\pi a/(k^2|\varepsilon_m|bl)$, where waevector $k = \omega/c$, simulate the metal since metal's permittivity is typically negative in the optics and IR range and it is proportional to ω^{-2}. The resistance R equals to $R = R_1 + R_2$, where $R_1 > 0$ presents the losses in the metal, and R_2 stands for the losses in the dielectric, which fills the space between the two arms of the nanoantenna. For the ordinary dielectric material $R_1 > R_2 > 0$. EMF "generator" $V = V_0 \cos(\omega t)$ presents the electromotive force induced by the external magnetic field H according to Faraday law $V \sim -c^{-1}ad(\partial H/\partial t)$.

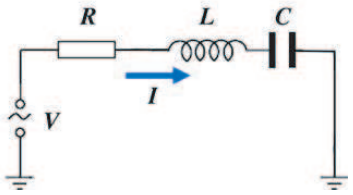

Figure 2: Equivalent L-C-R circuit of the horseshoe nanoantenna.

For the equivalent circuit we obtain the following Kirchhoff's equation, which we write in terms of the electric charge q of the metal arms

$$c^{-2}L\ddot{q} + U + R\dot{q} = V, \tag{1}$$

where $U = Ed = 4\pi d(q/S - P_1 - P_2)$ is the potential drop in horseshoe gap, $S = la$ is the gap area, $P_1 = \chi_1 E$ and P_2 are the regular and resonance (gain) polarization of the medium in the horseshoe (we use CGS units throughout the notes.) We introduce the real capacitance $C = \varepsilon_d S/(4\pi d)$, $(\varepsilon_d = 1 + 4\pi\chi_1)$; then the potential drop equals to $U = q/C - SNp/C$, where N and p is the density and dipole moment of TLS (e.g., quantum dots) placed inside the gap. Substituting U in Eq. (1), we obtain

$$c^{-2}L\ddot{q} + (q - SNp)/C + R\dot{q} = V. \tag{2}$$

It is the closed equation for the charge (current) oscillation in the horseshoe resonator in the presence of gain medium. Note that the TLS dipole moment p in Eq. (2) is the quantum operator, which works as a driving force for the self-oscillation of the horseshoe resonator.

3. INTERACTION OF NANOANTENNAS WITH GAIN MEDIUM AND PLASMONIC LASER

In order to understand the origin of the lasing in the gain medium we will consider a microscopic model following the consideration [29, 30]. We use the quantum-mechanical derivation of the equations of motion for the system shown in Figs. 1 and 2, but will neglect quantum correlations and fluctuations in our analysis. The Hamiltonian of the nanoantenna interacting with a TLS is given by the expression:

$$H = H_0 + H_{TLS} + V_{\text{int}} + \Gamma, \tag{3}$$

where H_0 and H_{TLS} describe respectively the horseshoe nanoantenna and TLS. The operator $V_{\text{int}} = -pE$ gives the interaction between the TLS and the nanoantenna, where E is the electric field in the horseshoe. The term Γ describes dissipation and pump effects.

Electrons in the horseshoe nanoantenna couple to the local electric field and oscillate with the frequency ω, close to the plasmon resonance frequency $\omega_r = c/\sqrt{LC}$. Thus, such oscillation presents the surface plasmon in nanoantenna. We will treat the electric charge $q(t) = q_1(t)\exp(-i\omega t) + q_1^*(t)\exp(i\omega t)$ as classical object. Let us introduce the "slow" operator $b(t) = \eta(t)\exp(i\omega t)$ that

corresponds to the transition operator $\eta(t)$ between the excited $|e\rangle$ and ground $|g\rangle$ state of the TLS, i.e., $|g\rangle = \eta|e\rangle$ and $\eta|g\rangle = 0$. Then the operator of the dipole moment in Eq. (3) can be represented as

$$p = \Pi b \exp(-i\omega t) + \Pi^* b^+ \exp(i\omega t), \tag{4}$$

where $\Pi = \langle g|re|e\rangle$ is the dipole matrix element. We will also introduce the population inversion operator

$$D(t) = n_g(t) - n_e(t), \tag{5}$$

where $n_e(t) = b^+ b$ and $n_g(t) = bb^+$ are the populations of the excited and ground states of the TLS. We assume that the TLS oscillates between the upper and lower level with the frequency ω close to frequency ω_2, where $\hbar\omega_2$ is the energy distance between the levels in the TLS. Neglecting the fast oscillating terms, $\sim \exp(\pm 2i\omega t)$ we can express the Hamiltonian (3) in terms of the following operators:

$$H_{TLS} = \hbar\omega_2 n_e, \tag{6}$$

$$V_{\text{int}} = -pE = -(Cd)^{-1}\left(\Pi^* q_1 b^+ + \Pi q_1^* b\right) + |\Pi|^2 SN, \tag{7}$$

where the electric field E in the gap of the horseshoe estimates as $E = U/d$. The last term in r.h.s. of Eq. (7) is a constant and, therefore, does not influence the dynamic of the system.

By using the well-known commutation rules for the operators b, b^+ and $n_{e,g}$, we derive the equations of motion for the operators: $i\hbar\dot{b} = [b, H]$ and $i\hbar\dot{D} = [D, H]$. We first consider the lasing as a natural oscillation of the electric charge in the horseshoe resonator in the absence of external field ($V = 0$ in Eq. (2).) For simplicity we neglect the loss in the dielectric, i.e., $R_2 = 0$ in Eq. (2). We suppose that the amplitudes of the resonator oscillation do not change ($\dot{q}_1 = \dot{b} = \dot{D} = 0$) so the resonator moves over its limit cycle. Thus, the lasing is the auto-oscillating in the system of nanoantenna+gain medium. Then Eq. (2) and equations for b and D can be rewritten the following form

$$(i\delta + \gamma)q_2 - ib = 0,\ (i\Delta + \Gamma)\, b - iADq_2 = 0,\ (D - D_0)/\tau - 2iA\left(q_2^* b - q_2 b^+\right) = 0, \tag{8}$$

where $q_2 = q_1/(SN\Pi)$, $\delta = 1 - (\omega/\omega_r)^2$, $\gamma = (\varepsilon_m''/|\varepsilon_m'|)\,(\omega/\omega_r)^2 \simeq \varepsilon_m''/|\varepsilon_m'|$, $\Delta = (\omega_2 - \omega)/\omega_r$ [29, 30]; the terms involving Γ and τ account for the relaxation and pump processes in TLS correspondingly. D_0 would be the stationary value of the TLS population if it were not interacted with the horseshoe. We assume $D_0 < 0$ because the pumping process provides the initial population inversion in the TLS. By neglecting quantum fluctuations and correlation, D and b can be treated as complex variables with operators b, and b^+ being replaced by complex variables b and b^* respectively. The dimensionless constant A equals to $A = 4\pi N|\Pi|^2/(\omega_r \hbar n^2) > 0$, where $n = \sqrt{\varepsilon_d}$ is the regular, i.e., nonresonant refractive index of the medium inside the horseshoe. Eqs. (8) define the lasing condition in the horseshoe plasmonic resonator, namely, they have nonzero solution when

$$\Delta/\Gamma = -\delta/\gamma, \quad (\delta/\gamma)^2 + 1 + AD_0/(\Gamma\gamma) = 0. \tag{9}$$

First condition (9) gives the lasing frequency $\omega_L = \omega_r + \gamma(\omega_2 - \omega_r)/(\gamma + 2\Gamma)$, which is always in-between the magnetic plasmon resonance frequency ω_r and TLS resonance frequency ω_2. All terms are positive but the population D_0 in the second lasing condition (9). Therefore, this condition holds only in the inverted medium $n_e > n_g$ when $D_0 < 0$. The population D_0 cannot be smaller than -1, which corresponds to the case when all TLSs are excited. Thus we obtain the lasing condition for the horseshoe nanolaser $A/(\Gamma\gamma) > 1$. As soon as this condition is fulfilled the interaction between TLS and the plasmonic nanoantenna leads to the coherent oscillations of electric charge and the magnetic moment of the horseshoe, even in the absence of the external electromagnetic field.

The same lasing condition can be expressed in terms of the gain G in the active medium inside of the horseshoe [29, 30]

$$G\lambda/(2\pi n\gamma) > 1, \tag{10}$$

where $\gamma = \varepsilon_m'/|\varepsilon_m''| \ll 1$ is the metal loss factor and the refractive index $n \sim 1$. Note that the lasing condition depends on the gain in the active medium and the loss in the metal only. We assume that Eq. (10) holds for any geometry of the subwavelength sized plasmonic laser. For instance, the silver horseshoe shaped nanolaser would lase at wavelength 1.5 μm if the gain medium can maintain optical gain larger than the critical gain $G_c \approx 3 \cdot 10^3\,\text{cm}^{-1}$. Such gain is typical for "good" quantum

well medium (see, e.g., [31, 32] and references therein). In the recent study very high material gain $G \simeq 2 \cdot 10^5\,\mathrm{cm}^{-1}$, was obtained for $InAs$ quantum dot laser created inside the photonic crystal [33]. Less than five quantum dots were enough to get lasing.

Consider now the pumping of the nanolaser, which is excited by the magnetic component H of the impingent electromagnetic wave with frequency ω. The high frequency magnetic field excites currents in the horseshoe and operates as a driving force. Without the driving force the plasmonic nanolaser, which is a nonlinear oscillator, makes auto-oscillations and moves over its limit cycle given by Eq. (8) with lasing frequency ω_L (see Eq. (9)). When the driving force is applied the plasmonic nanolaser still moves over the limit cycle but with frequency ω of the driving force. The well-known synchronization takes place: the nanolaser generates with the frequency ω of the driving force (see e.g., [34].) The impingent em wave retunes the nanolaser. Therefore, the metamaterial comprised by plasmonic nanolasers operates as material with zero or negative loss. Moreover, the nanolaser metamaterial can change the frequency and direction of the emitted coherent light under the action of external light beam. As result we obtain not only the plasmonic nanolaser but also metamaterial for the macroscopic superlens with unlimited resolution since the loss is compensated by the gain. Authors acknowledge stimulating discussions with A. N. Lagarkov and V. G. Veselago.

REFERENCES

1. Lagarkov, A. N., et al., *J. Elect. W. Appl.*, Vol. 6, 1159, 1992.
2. Lagarkov, A. N. and A. K. Sarychev, *Phys. Rev. B*, Vol. 53, 6318, 1996.
3. Pendry, J. B., A. J. Holden, W. J. Stewart, and I. Youngs, *Phys. Rev. Lett.*, Vol. 76, 4773, 1996.
4. Pendry, J. B., et al., *IEEE Microwave Th.*, Vol. 47, 2075, 1999.
5. Wiltshire, M. C. K., et al., *Optic Express*, Vol. 11, 709, 2003.
6. Veselago, V. G., *Soviet Physics Uspekhi*, Vol. 10, 509, 1968.
7. Smith, D. R., W. J. Padilla, D. C. Vier, S. C. Nemat-Nasser, and S. Schultz, *Phys. Rev. Lett.*, Vol. 84, 4184, 2000.
8. Pendry, J. B., *Phys. Rev. Lett.*, Vol. 85, 3966, 2000.
9. Houck, A. A., J. B. Brock, and I. L. Chuang, *Phys. Rev. Lett.*, Vol. 90, 137401, 2003.
10. Parazzoli, C. G., R. B. Greegor, K. Li, B. E. C. Koltenbah, and M. Tanielian, *Phys. Rev. Lett.*, Vol. 90, 107401, 2003.
11. Lagarkov, A. N. and V. N. Kissel, *Phys. Rev. Lett.*, Vol. 92, 077401, 2004.
12. Lagarkov, A. N., V. N. Semenenko, V. A. Chistyaev, D. E. Ryabov, and S. A. Tretyakov, *Electromagnetics*, Vol. 17, 213, 1997.
13. Zhang, S., W. Fan, N. C. Panoiu, K. J. Malloy, R. M. Osgood, and S. R. J. Brueck, *Phys. Rev. Lett.*, Vol. 95, 137404, 2005.
14. Shalaev, V. M., et al., arXiv: *Physics*/0504091, 2005;
15. Shalaev, V. M., et al., *Laser Phys. Lett.*, Vol. 3, 49, 2006.
16. Shalaev, V. M., et al., *Opt. Lett.*, Vol. 30, 3356, 2005.
17. Sarychev, A. K., et. al., *SPIE Proceedings*, Vol. 5219, 92, San Diego, 2003.
18. Podolskiy, V. A., A. K. Sarychev, and V. M. Shalaev, *J. Nonlin. Opt. Phys. Mat.*, Vol. 11, 65, 2002.
19. Podolskiy, V. A., A. K. Sarychev, and V. M. Shalaev, *Optics Express*, Vol. 11, 735, 2003.
20. Grigorenko, A. N., et al., *Nature*, Vol. 438, 335, 2005.
21. Liu, Z., H. Lee, Y. Xiong, C. Sun, and X. Zhang, *Science*, Vol. 315, 1686, 2007.
22. Dimmock, J. O., *Optics Express*, Vol. 11, 2397, 2003.
23. Podolskiy, V. A. and E. E. Narimanov, *Opt. Lett.*, Vol. 30, 75, 2005.
24. Sarychev, A. K. and V. M. Shalaev, *Complex Mediums V, Proc. SPIE*, Vol. 5508, 128, 2004.
25. Sarychev, A. K., G. Shvets, and V. M. Shalaev, *Phys. Rev. E*, Vol. 73, 036609, 2006.
26. Linden, S., et al., *Science*, Vol. 306, 1351, 2004.
27. Katsarakis, N., et al., *Appl. Phys. Lett.*, Vol. 84, 2943, 2004.
28. Zhou, J., et al., *Phys. Rev. Lett.*, Vol. 95, 223902, 2005.
29. Sarychev, A. K. and G. Tartakovsky, *Proc. SPIE*, Vol. 6320, 0A, 2006.
30. Sarychev, A. K. and G. Tartakovsky, *Phys. Rev. B*, Vol. 75, 085436, 2007.
31. Carrère, H., et al., *Appl. Phys. Lett.*, Vol. 89, 181115, 2006.
32. Carrère, H., et al., *Appl. Phys. Lett.*, Vol. 86, 071116, 2005.
33. Strauf, S., et al., *Phys. Rev. Lett.*, Vol. 96, 127404, 2006.
34. Kuznetsov, A. P., et al., *Nonlinear Oscillations*, 292, Science Publishing, Moscow, 2002.

Wave Interaction with Double-negative and Double-positive Plates

F. Urbani[1], **C. Sabah**[2], **and S. Uckun**[2]

[1]Department of Engineering, University of Texas at Brownsville
80 Fort Brown, Brownsville TX 78520, USA
[2]Electrical and Electronics Engineering Department, University of Gaziantep
27310, Gaziantep, Turkey

Abstract— In this study, wave interaction with double-negative (DNG) and double-positive (DPS) plates is presented. Theoretically, the structure is composed by DNG and DPS plates with different material properties and thicknesses forming an N-tier structure. The DNG plates are described by using the Lorentz and Drude media parameters while the DPS plates are defined by known dielectric materials. The incident electric field is assumed to be a monochromatic plane wave with any arbitrary polarization. After obtaining the electric and magnetic fields both inside and outside the plates and imposing the boundary conditions, the reflected and transmitted powers are calculated using the transfer matrix method in order to observe their behaviors. In this paper, the frequency response of the DNG and DPS plates is deeply analyzed both analytically and numerically. Finally, the computations of reflected and transmitted powers are analyzed numerically with the purpose of designing efficient filters at the microwave, millimeter wave, and optical frequency regions.

1. INTRODUCTION

Nowadays, it is well known that the concept of double-negative (DNG) materials plays important role in science, and technology for its broad usage in industry [1–9]. The DNG materials are artificial structures with electromagnetic properties different from the conventional materials. In this paper wave interaction with double-negative (DNG) and double-positive (DPS) plates is presented. The structure is formed by DNG and DPS plates with different material properties and thicknesses. The DNG plates are described by using the Lorentz and Drude media parameters while the DPS plates are defined by known dielectric materials. Transfer matrix method is used in the analysis. Finally, the reflected and transmitted powers are analyzed numerically to show the use of the structure as filters at the microwave, millimeter wave, and optical frequency regions.

2. THEORY

In the analysis, we consider an electric field with any arbitrary polarization coming from free space and propagating through N-tier structure which has different material properties and thicknesses d shown in Figure 1.

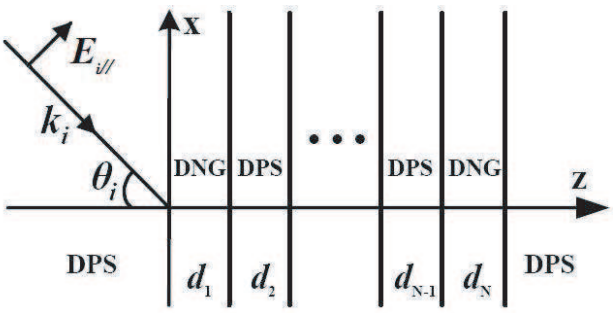

Figure 1: The geometry of N-tier DNG and DPS plates.

In the theory, $\exp(i\omega t)$ time dependence is assumed and suppressed. The incident electric filed is expressed as:

$$\boldsymbol{E}_i = [E_{i//}(\cos\theta_i \boldsymbol{a}_x + \sin\theta_i \boldsymbol{a}_z) + E_{i\perp}\boldsymbol{a}_y] \cdot \exp[-i(-k_{ix}x + k_{iz}Z)] \tag{1}$$

where θ_i is the angle of the incidence, $k_{ix}(= k_i \sin\theta_i)$ and $k_{iz}(= k_i \cos\theta_i)$ are the x- and z-components of the wave number $k_i(= \omega\sqrt{\mu_i\varepsilon_i})$ respectively. Note that, the subscripts // and $\perp$ refer to the

parallel and perpendicular components (relative to the plane of incidence) of the electric field vector, in that order. The other electric and magnetic fields inside and outside the structure can easily be found using the Maxwell's equations.

The permittivity and permeability of the DNG plates are defined using Lorentz [7] and Drude [8, 9] media which have simultaneously negative permittivity and permeability in a certain frequency band. The permittivity and permeability of Lorentz medium are given as:

$$\varepsilon(\omega) = \varepsilon_o \left(1 - \frac{f_{ep}^2 - f_{eo}^2}{f^2 - f_{eo}^2 + j\Gamma_e \omega}\right), \tag{2}$$

$$\mu(\omega) = \mu_o \left(1 - \frac{f_{mp}^2 - f_{mo}^2}{f^2 - f_{mo}^2 + j\Gamma_m \omega}\right), \tag{3}$$

where f_{eo} is the electronic resonance frequency, f_{ep} is the electronic plasma frequency, Γ_e is the electronic damping frequency, f_{mo} is the magnetic resonance frequency, f_{mp} is the magnetic plasma frequency, and Γ_m is the magnetic damping frequency. Furthermore, the permittivity and permeability of Drude medium are given as:

$$\varepsilon(\omega) = \varepsilon_o \left(1 - \frac{f_{ep}^2}{f^2 + j\Gamma_e \omega}\right), \tag{4}$$

$$\mu(\omega) = \mu_o \left(1 - \frac{f_{mp}^2}{f^2 + j\Gamma_m \omega}\right). \tag{5}$$

Now, imposing the boundary conditions at the interfaces the relationships among the fields in all regions can be obtained in a similar way as in [1] and [10] by the transfer matrix $[U]$ as follows:

$$\begin{bmatrix} E_{i\perp} \\ E_{r\perp} \\ E_{i//} \\ E_{r//} \end{bmatrix} = [U] \begin{bmatrix} E_{t\perp} \\ E_{t//} \end{bmatrix} = \begin{bmatrix} u_{11} & u_{12} \\ u_{21} & u_{22} \\ u_{31} & u_{32} \\ u_{41} & u_{42} \end{bmatrix} \begin{bmatrix} E_{t\perp} \\ E_{t//} \end{bmatrix}. \tag{6}$$

Note that, $[U]$ is a 4×2 matrix and the elements of it are expressed as a function of the incidence angle, structure parameters, thickness of each DNG and DPS plates, and frequency.

3. NUMERICAL RESULTS

In this section, the computations for the reflected and transmitted powers are presented to analyze their characteristics when the incident power is normalized to unity at normal incidence ($\theta_i = 0$). The incident electric field is assumed to be plane weave with parallel polarization ($E_{i\perp} = 0$). In addition, five layered structure considered as DNG-DPS-DNG-DPS-DNG ($N = 5$). The first and the last media are assumed to be free space and glass. The DPS plates are selected to become cryolite (Na_3AlF_6) with refractive index of $n = 1.35$. In the first example, DNG plates are realized using Lorentz medium parameters given in Eqs. 2 and 3. In the calculations, the following parameters are used: $f_{mp} = 8.50\,\text{GHz}$, $f_{mo} = 12.05\,\text{GHz}$, $f_{ep} = 12.80\,\text{GHz}$, and $f_{eo} = 10.30\,\text{GHz}$. The electronic and magnetic damping frequencies are selected to be equal each other and zero ($\Gamma_e = \Gamma_m = \Gamma = 0$). The optical lengths ($\text{OL} = n \times d$) of the plates are selected to be multiple of wavelength in free space at operation frequency of 11.2 GHz. Figure 2 shows the reflected and transmitted powers as a function of frequency. From this figure, when $\text{OL}_{\text{DNG}} = \text{OL}_{\text{DPS}} = \lambda_0/4$, the bandwidth extends from 10.5 GHz to 11.5 GHz and there is a sharp peak for the transmitted power at 10.9 GHz. At this frequency, the structure can be utilized as a transmission filter in which the transmitted power becomes unity and the reflected power becomes zero. Also, it can be used as a reflection filter except the range between 10.5 GHz and 11.5 GHz in which the reflected power becomes unity and the transmitted power becomes zero. When $\text{OL}_{\text{DNG}} = \lambda_0/2$ and $\text{OL}_{\text{DPS}} = \lambda_0/4$, it is seen from solid line, the structure behaves like an all pass filter in a wide range of frequency since the transmitted power is dominant and around one.

In the second example, DNG plates are realized using Drude medium parameters given in Eqs. 4 and 5. In the calculations, the following parameters are used: $f_{mp} = 10.95\,\text{GHz}$, and $f_{ep} = 14.50\,\text{GHz}$. The electronic and magnetic damping frequencies are again zero. The operation

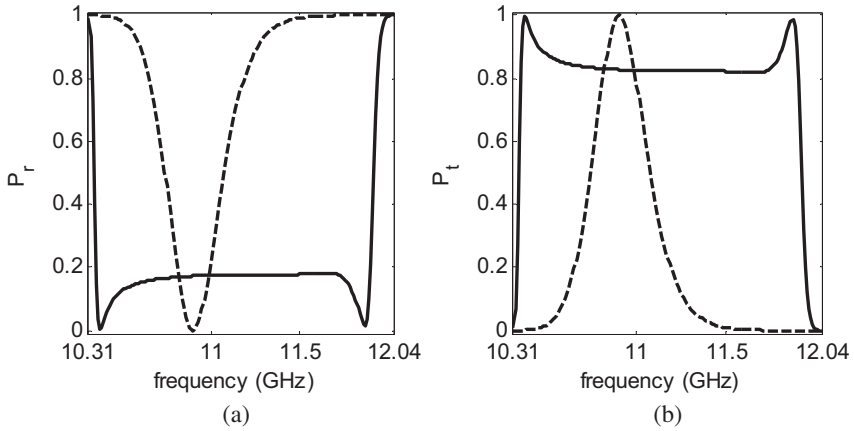

Figure 2: Reflected (a) and transmitted (b) powers as a function of frequency for Lorentz DNZ plates. Broken lines correspond to $\mathrm{OL_{DNG}} = \mathrm{OL_{DPS}} = \lambda_0/4$ and solid lines to $\mathrm{OL_{DNG}} = \lambda_0/2,\ \mathrm{OL_{DPS}} = \lambda_0/4$.

frequency is selected to be 4.0 GHz. The other parameters are the same with the first example. Note that, here the frequency range is wider than the range of Lorentz medium; hence, the simultaneously negative permittivity and permeability can be obtained in a wider frequency band for Drude medium more easily than Lorentz medium. Figure 3 illustrates the reflected and transmitted powers versus frequency. From this plot, the reflected and transmitted powers make oscillation with different periods in different ranges. As it is seen from dashed ($\mathrm{OL_{DNG}} = \mathrm{OL_{DPS}} = \lambda_0/4$) and solid ($\mathrm{OL_{DNG}} = \lambda_0/2,\ \mathrm{OL_{DPS}} = \lambda_0/4$) lines, the transmitted power is dominant and varies between the values of 0.8 and 1.0. Thus it can be said that the structure can be used as an oscillatory transmission filter for the transmitted wave.

Note that, similar numerical results can be obtained for the incident wave with the perpendicular polarization.

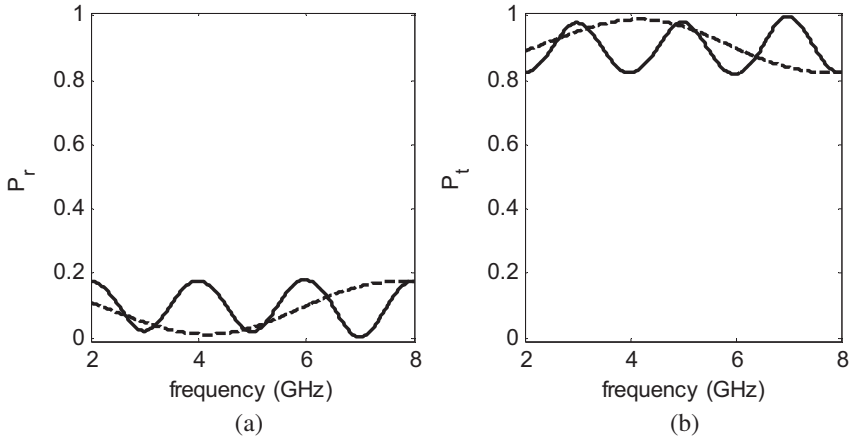

Figure 3: Reflected (a) and transmitted (b) powers versus frequency for Drude DNG plates. Broken lines stand for $\mathrm{OL_{DNG}} = \mathrm{OL_{DPS}} = \lambda_0/4$ and solid lines for $\mathrm{OL_{DNG}} = \lambda_0/2,\ \mathrm{OL_{DPS}} = \lambda_0/4$.

4. CONCLUSION

In this study, wave interaction with the structure formed by DNG and DPS plates are investigated for the incident electric field with any arbitrary polarization. DNG plates are realized by using Lorentz and Drude media parameters. The transfer matrix method is used in the theory. At last, the reflected and transmitted powers are computed numerically to show the frequency response of the structure. As it is seen from the numerical results, the structure can be used as a reflection and transmission filter at some frequency band. As a result, design of some efficient filters at the microwave, millimeter wave, and optical frequency regions can be achieved by arranging the structure parameters, layer numbers, and optical length.

REFERENCES

1. Sabah, C., G. Ögücü, and S. Uckun, "Reflected and transmitted powers of electromagnetic wave through a double-negative slab," *Journal of Optoelectronics and Advanced Materials (JOAM)*, Vol. 8, No. 5, 1925–1930, 2006.
2. Gerardin, J. and A. Lakhtakia, "Negative index of refraction and distributed Bragg reflectors," *Microwave and Optical Technology Letters*, Vol. 34, No. 6, 409–411, 2002.
3. Guven, K., D. Caliskan, and E. Ozbay, "Experimental observation of left-handed transmission in a bilayer metamaterial under normal-to-plane propagation," *Optics Express*, Vol. 14, No. 19, 8685–8693, 2006.
4. Wu, D., N. Fang, C. Sun, X. Zhang, W. J. Padilla, D. N. Basov, D. R. Smith, and S. Schultz, "Terahertz plasmonic high pass filter," *Applied Physics Letters*, Vol. 83, No. 1, 201–203, 2003.
5. Ramakrishna, S. A. and J. B. Pendry, "Removal of absorption and increase in resolution in a near-field lens via optical gain," *Physical Review B*, Vol. 67, 201101-1–201101-4, 2003.
6. Ziolkowski, R. W., "Design, fabrication, and testing of double negative metamaterials," *IEEE Transactions on Antennas and Propagation*, Vol. 51, No. 7, 1516–1529, 2003.
7. Shelby, R. A., D. R. Smith, and S. Schultz, "Experimental verification of a negative index of refraction," *Science*, Vol. 292, 77–79, 2001.
8. Smith, D. R., D. C. Vier, N. Kroll, and S. Schultz, "Direct calculation of permeability and permittivity for a left-handed metamaterial," *Applied Physics Letters*, Vol. 77, No. 14, 2246–2248, 2000.
9. Pendry, J. B., "Negative refraction makes a perfect lens," *Physical Review Letters*, Vol. 85, No. 18, 3966–3969, 2000.
10. Sabah, C. and S. Uckun, "Reflection and transmission coefficients of multiple chiral layers," *Science in China Series E: Technological Sciences*, Vol. 49, No. 4, 457–467, 2006.

Mutual Coupling Effects on the Mean Capacity of MIMO Antenna Systems

Andrea Farkasvolgyi and Lajos Nagy
Department of Broadband Infocommunications and Electromagnetic Theory
Budapest University of Technology and Economics
H-1111 Budapest, Goldmann sq 3, Hungary

Abstract— We would like to show in this article the effect of the antenna position changing on the capacity of the multiple-input — multiple-output (MIMO) system considering effect of the mutual coupling. In the course of the simulation we analyzed a 3×3 MIMO antenna system.

1. INTRODUCTION

We chose low elements-number-antenna-system because this system is the most suitable design on the end-user-market. We are supposing this antenna buildup (three elements on both receiver and transmitter) issues in the simplest structure with the highest mean capacity. With other antenna-number-reduction capacity of so-called multiple antenna system would have a beyond measure low level. Goal of this simulation is the capacity maximization by changing antennas' positions and observe the effects of mutual coupling for mean channel capacity. Orthogonal parallel transmission links can be found by eigenvectors of the channel matrix. The parallel transmission links coexist in the frequency band named eigenchannels. The capacity of a multiple antenna system depends on the number of eigenchannels. The MIMO channel is similar to a low correlation diversity channel. MIMO systems generally operate in an indoor rich scattering environment and takes advantage of uncorrelated electric and magnetic fields. In the paper we present that the channel capacity is affected by the antenna structures and the mutual coupling.

2. THE MIMO ANTENNA SYSTEM AND CAPACITY

The channel capacity fundamentally depends on the number of the antenna-elements at the transmitter and the receiver side. However it is being supposed that the channel capacity is affected by the structure of the antennas, and by this method we can maximize the efficiency of transmission. We make an effort to show the changing of channel capacity according to the variation of angles between the antenna elements. For the optimizations we take the three dimension (3-D) double bouncing (DB) stochastic scattering model with wide angular spread as a basis at both ends. We want to make these optimizations for an unmitigated indoor environment. The antenna system is situated in a 3-D scattering environment indoor channel. Waves of arbitrary polarizations are incident on the antenna structure from all possible directions. The transmission matrix (**H**) which connects the receiver and transmitter antennas is filled by assuming DB scattering.[1, 2]

Our multiple antenna system is composed of $M_t = 3$ and $N_r = 3$ electric dipoles at both the transmitter and the receiver units. The radiated electric field of each dipole is applied for the calculation of the transmission matrix. The current distribution for each electric dipole is sinusoidal, which is often supposed for finite length dipoles. H matrix of the DB model, which is in this case the transmission matrix of the antenna system, consists of three sub-matrixes. We chose the number of scattering points on the reflection surface for hundred. The complete MIMO transmission matrix, H is of size $N_r \times M_t$ (in this case the element number of H is 9) with entries H[n,m] which describe the path from nth receiver to mth transmitter. The received incident electric field at the elements of the first reflection surface (at the first scattering points) around the transmitter unit has ϑ and φ direction components. The transmission matrix, H, is computed from the induced voltage on the receiving antenna elements. If there are W multipath incident on the receiving antenna, the induced voltage from the direction ϑ and φ are given as $V_{i,\vartheta} = \sum_{w=1}^{W} E_{r,\vartheta,w} \cdot h_{eff,\vartheta,w}$, and $V_{i,\varphi} = \sum_{w=1}^{W} E_{r,\varphi,w} \cdot h_{eff,\varphi,w}$,where h_{eff} is the vector effective length of the dipole which is given as $h_{eff} = (E_{rad}/j\beta I_{in}\eta) \cdot 4\pi r e^{j\beta r}$. Here I_{in} is the excitation electric currents and, respectively, $\eta = 120\pi$ [Ω] is the free space intrinsic impedance, $\beta = 2^*\pi/\lambda$. The total received voltage on the Ith antenna output is given from the subcomponents of V (direction $V_{i,\varphi}$ and $V_{i,\vartheta}$) $V_{0,i} = V_{i,\vartheta} + V_{i,\varphi}$. [3–5] For this MIMO radio channel the capacity was calculated with

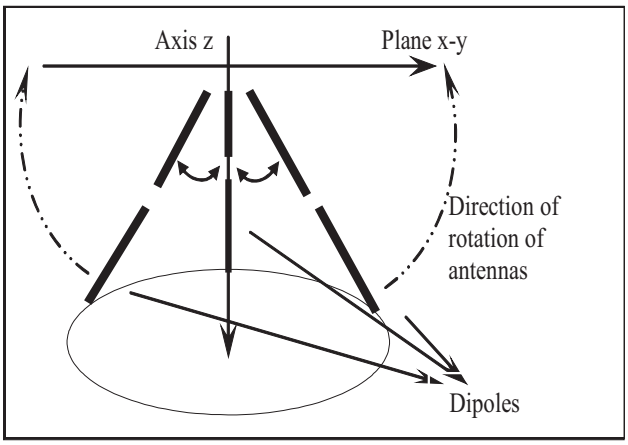

Figure 1: 3×3 MIMO antenna structure for maximize the mean capacity by rotation of the antennas, parallel at the transmitter and the receiver units, from the axis Z toward X-Y plane (it is opened like an umbrella).

this well known function $C = \sum_{i=1}^{r'} \log_2(1 + \lambda_i SNR_i)$ where λ are the eigen-values of the channel by SVD, $SNR_i = P_t/\sigma^2$ is the individual SNR of the eigenmodes after waterfilling and r' denotes the number of useful eigenmodes with positive power allocation. [6, 7] At the examination of the effect of mutual coupling we have to use the modified channel matrix H_{mut}. It is given by $H_{mut} = (C_{tr\_mut}{}^* H^* C_{re\_mut})/C_{re}{}^* C_{tr}$, where $C_{re} = Z_{11\_re}/2\Re e\{Z_{11\_re}\}$ and $C_{tr} = Z_{11\_tr}/2\Re e\{Z_{11\_tr}\}$ are normalizing factors for C_{tr_mut} and C_{re_mut}. The mutual coupling matrixes on the receiver and transmitter sides are given $C_{re\_mut} = Z_{load}/(Z_{re} + Z_{load})$ and $C_{tr\_mut} = Z_{tr}/(Z_{tr} + Z_{source})$, where Z_{tr} and Z_{re} are 3×3 mutual impedance matrixes and Z_{load} and Z_{source} are diagonal matrixes. In the case of conjugate matching we calculated with $Z_{load}(n, n) = Z^*re(n, n)$ and $Z_{source}(n, n) = Z^*tr(n, n)$, and at non conjugate matching case, when we tried to simulate a true-measurement-system $Z_{load}(n, n) = 50\,\Omega$ and $Z_{source}(n, n) = 50\,\Omega$. [2, 8]

3. RESULTS OF SIMULATION

In this simulation the scatterers were on a ball-shape surface around the both units and the number of them was 100. In the course of the simulation we examined the effect of the mutual coupling for the mean channel capacity and we examined that the shape of the characteristics are changed by the effect of mutual coupling. Fig. 1 shows the method of rotating of antenna system.

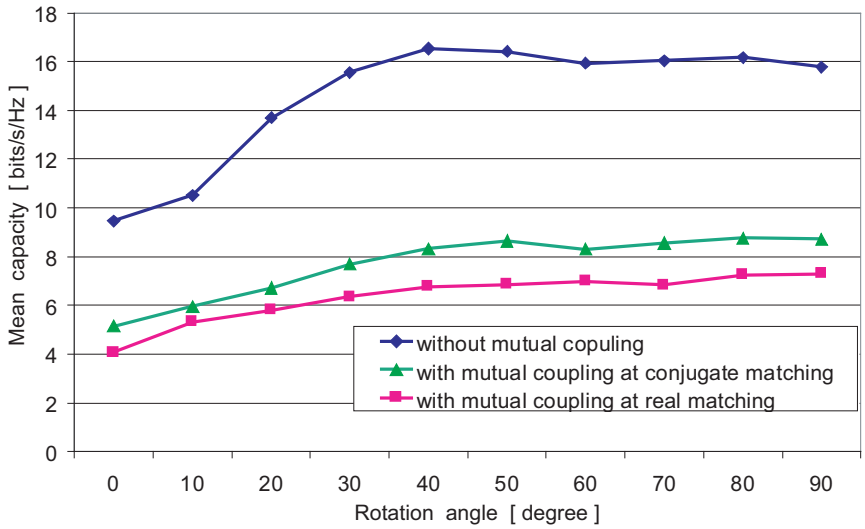

Figure 2: The effect of mutual coupling for the mean channel capacity in a 3×3 MIMO antenna system ($1/\lambda = 0.25$), versus angle of rotation. $SNR = 20\,\mathrm{dB}$.

At first the antennas are parallel with the axis Z. In the midst of the simulation the antennas opened in the space like an umbrella. In the end of the simulation the antennas reached the X-Y plane. The phases between the projections of the antennas (for the X-Y plane) were constant 120°. In this case the antennas are on the farthest position, the phase (γ) between the antenna and the axis Z was changed from 0° to 90°. The Fig. 2 shows the result of the simulation for $1/\lambda = 0.25$ and $SNR = 20\,\mathrm{dB}$. The upper curve is the normal mean capacity; the highest value is 16.8 bits/s/Hz at about $\gamma \sim 45°$. The mean capacity is reduced by the mutual coupling. The middle curve shows the effect of mutual coupling for the channel capacity at conjugate matching. The lower curve is the channel capacity with non conjugate matching. In this case we tried near to the real load impedance ($Z_{load} = 50\,\Omega$ and $Z_{source} = 50\,\Omega$). We found that the conjugate matching cause higher mean capacity or lower negative effect for the mean capacity than the true load, 50 ohm.

We simulated the effect of the mutual coupling for the different antenna length. We studied the 0.25, 0.2, 0.15 and 0.1 antenna length to wavelength ratio, so the optimal dipole length $(1/\lambda = 0.25)$

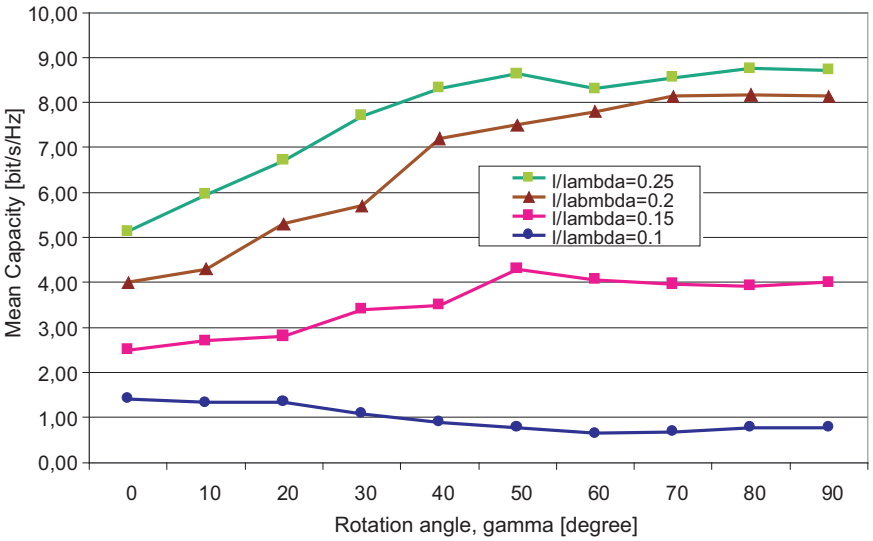

Figure 3: The effects of mutual coupling for mean capacity in a 3×3 MIMO antenna system versus angle of rotation and versus $1/\lambda$, case of conjugate matching, $SNR = 20\,\mathrm{dB}$.

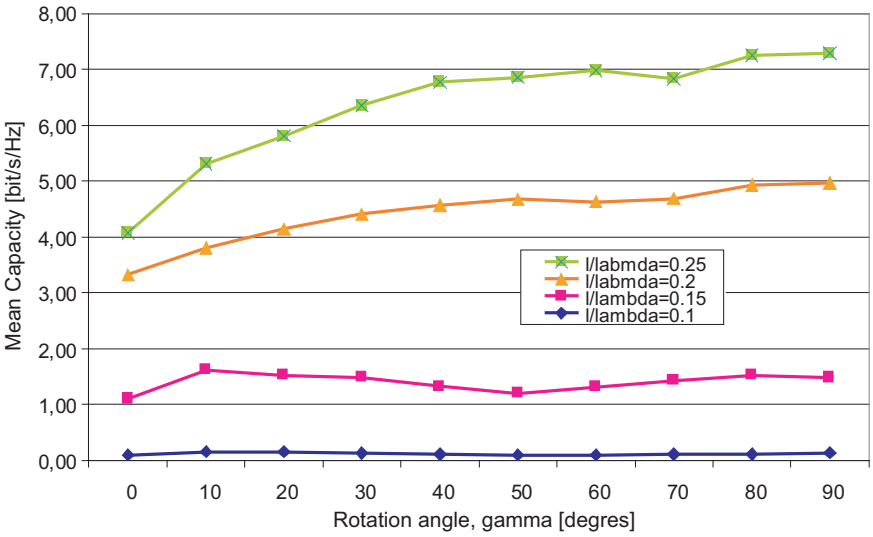

Figure 4: The effects of mutual coupling for mean capacity in a 3×3 MIMO antenna system versus angle of rotation and versus $1/\lambda$, at case of non conjugate matching, $SNR = 20\,\mathrm{dB}$.

and for smaller antennas. We found that in case of conjugate matching the mean channel capacity

is higher than non conjugate matching case. According to our expectation the effect of the mutual coupling is stronger if the antenna-length is reduced. Interest result that the effect of the mutual coupling does not change the character of curves at $1/\lambda > 0.2$, and in this case the highest capacity is at $\lambda \sim 45°$. However at small antenna length $1/\lambda < 0.1$ the character of capacity curve is changing and the top of the curve will be at $\lambda \sim 20°$. The results of simulation are on Fig. 3. and Fig. 4.

4. CONCLUSION

We found in this simulation that the capacity of a MIMO system depends not only on the number of elements of the receiver and transmitter side but the position of the antennas. We could describe the normal indoor environment with 3-D DB model. We found that the effect of the mutual coupling is stronger by non conjugate matching. We studied the cause of mutual coupling for different antenna length. We think that the negative effect of the mutual coupling predominates least of all if the antenna length is 0.25 in wavelength and in case of conjugate matching.

ACKNOWLEDGMENT

This work was carried out in the framework of Mobile Innovation Center, Hungary (Mobil Innovációs Központ).

REFERENCES

1. Getu, B. N. and J. B. Andersen, "The MIMO cube-A compact MIMO antenna," *IEEE Trans. Wireless Commun.*, Vol. 4, No. 3, 1136–1141, May 2005.
2. Getu, B. N. and R. Janaswamy, "The effect of mutual coupling on the capacity of the MIMO cube," *IEEE Wireless Propagation Letters*, Vol. 4, 240–244, 2005.
3. Zombory., L. and M. Koltai, "Elektromagneses terek gepianalizise," *Muszaki Konyvkiado*, in Hungarian, 1979.
4. Gustafsson, M. and S. Nordebo, "Characterization of MIMO antennas using spherical vector waves," *IEEE Transactions on Antennas and Propagation*, Vol. 54, No. 9, Sep. 2006.
5. http://www.mathworks.com/matlabcentral/fileexchange/loadFile.do?objectId=12491&objectType=file
6. Vucetic, B. and J. H. Yuan, *Space-Time Coding*, Wiley, England, 2004.
7. Chiu, C. Y. and R. D. Murch, "Experimental Results for a MIMO Cube," *IEEE Transactions on Antennas and Propagation*.
8. Janaswamy, R., "Effect of element mutual coupling on the capacity of fixed length linear arrays," *IEEE Antennas Wireless Propagat. Lett.*, Vol. 1, 157–160, 2002.

Ultrashort Electromagnetic Pulse Dynamics in the Singular and Weak Dispersion Limits

K. E. Oughstun and N. A. Cartwright

College of Engineering & Mathematical Sciences, University of Vermont, USA

Abstract— The asymptotic description of the dynamical evolution of an ultrashort electromagnetic pulse in a dispersive medium has shown that the temporal pulse structure evolves into a set of so-called precursor fields that are characteristic of the dispersive medium. Of particular interest is the evolution of the Brillouin precursor whose peak amplitude experiences zero exponential decay with propagation distance $z > 0$, decreasing algebraically as $z^{-1/2}$ in a dispersive, absorptive medium. The limiting behavior of this algebraic peak amplitude decay in both the zero damping (or singular dispersion) limit as well as the zero density (or weak dispersion) limit is investigated here for a single resonance Lorentz model dielectric in order to establish whether or not this rather unique behavior persists in these two different limits.

1. INTRODUCTION

The asymptotic theory of dispersive pulse propagation in a Lorentz model dielectric has its origin in the now classic research by A. Sommerfeld [1] and L. Brillouin [2, 3] which established the physical phenomena of the forerunners, or precursor fields as they were later named [4], that are associated with the evolution of a step-function modulated signal. This asymptotic description is derived from the exact Fourier-Laplace integral representation of the propagated plane wave field, given by [5]

$$A(z,t) = \frac{1}{2\pi}\int_C \tilde{f}(\omega)e^{(z/c)\phi(\omega,\theta)}d\omega, \tag{1}$$

for $z \geq 0$, where

$$\tilde{f}(\omega) = \int_{-\infty}^{\infty} f(t)e^{i\omega t}dt \tag{2}$$

is the temporal Fourier transform of the initial plane wave pulse $A(0,t) = f(t)$. Here $A(z,t)$ represents any scalar component of the plane wave electric or magnetic field vector whose spectral amplitude $\tilde{A}(z,\omega)$ satisfies the Helmholtz equation

$$\left(\nabla^2 + \tilde{k}^2(\omega)\right)\tilde{A}(z,\omega) = 0, \tag{3}$$

with complex wave number $\tilde{k}(\omega) = (\omega/c)n(\omega)$ in the temporally dispersive medium with complex index of refraction $n(\omega) = n_r(\omega) + in_i(\omega)$. In addition,

$$\phi(\omega,\theta) \equiv i\frac{c}{z}\left[\tilde{k}(\omega) - \omega t\right] \tag{4}$$

$$= i\omega\left[n(\omega) - \theta\right] \tag{5}$$

is the complex phase function, where $\theta \equiv ct/z$ is a non-dimensional space-time parameter. Based upon this integral representation, the modern asymptotic theory [5] provides a complete, uniform asymptotic description of the associated dispersive pulse dynamics in a Lorentz model dielectric for a variety of canonical pulse shapes and signals, showing that the observed pulse distortion is primarily due to the precursor fields. In particular, the peak amplitude point of the second forerunner or Brillouin precursor was shown to experience zero exponential decay with propagation distance $z > 0$, decreasing algebraically as $z^{-1/2}$ in a dispersive, absorptive medium. This rather unique phenomena renders the Brillouin precursor as a powerful tool for imaging through a given obscuring, dispersive medium.

The complex index of refraction of a single resonance Lorentz model dielectric is given by

$$n(\omega) = \left(1 - \frac{\omega_p^2}{\omega^2 - \omega_0^2 + 2i\delta\omega}\right)^{1/2}, \tag{6}$$

where ω_0 is the undamped angular resonance frequency, $\delta > 0$ the phenomenological damping constant, and $\omega_p^2 = Nq_e^2/(m_e\epsilon_0)$ is the square of the plasma frequency with N denoting the number density of Lorentz oscillators in the medium. The material absorption then decreases when either $\delta \to 0$ or when $N \to 0$. In the first limiting case, the material dispersion becomes increasingly localized about the resonance frequency as $\delta \to 0$ and so is referred to here as the *singular dispersion limit*. In the second limiting case, the material absorption vanishes while the material dispersion approaches unity at all frequencies as $N \to 0$ and so is referred to here as the *weak dispersion limit*. These two limiting cases are fundamentally different in their effects upon ultrashort pulse propagation and are thus treated separately in the following two sections.

2. ULTRASHORT PULSE DYNAMIICS IN THE SINGULAR DISPERSION LIMIT

The asymptotic theory [2, 3, 5] shows that the two first-order near saddle points $\omega_{SP_N}^{\pm}(\theta)$ of the complex phase function $\phi(\omega, \theta)$ for a single resonance Lorentz model dielectric coalesce into a single second-order saddle point at

$$\omega_{SP_N}^{\pm}(\theta_1) \cong -\frac{2\delta}{3\alpha}i, \tag{7}$$

where [5]

$$\theta_1 \approx \theta_0 + \frac{2\delta^2\omega_p^2}{3\alpha\theta_0\omega_0^4}, \tag{8}$$

with $\theta_0 = n(0)$ and $\alpha \approx 1$. At the space-time point $\theta = \theta_0$, the dominant near saddle point $\omega_{SP_N}^{+}(\theta)$ crosses the origin $[\omega_{SP_N}^{+}(\theta_0) = 0]$ so that its contribution to the asymptotic behavior of the propagated wave-field experiences zero exponential attenuation, viz.

$$\phi(\omega_{SP_N}^{+}(\theta_0), \theta_0) = 0, \tag{9}$$

the peak amplitude point decaying only as $z^{-1/2}$ as $z \to \infty$, while at the space-time point $\theta = \theta_1$ this contribution to the asymptotic wave field experiences a small (but nonzero) amount of exponential attenuation as well as a $z^{-1/3}$ algebraic decay as $z \to \infty$, provided that $\delta > 0$.

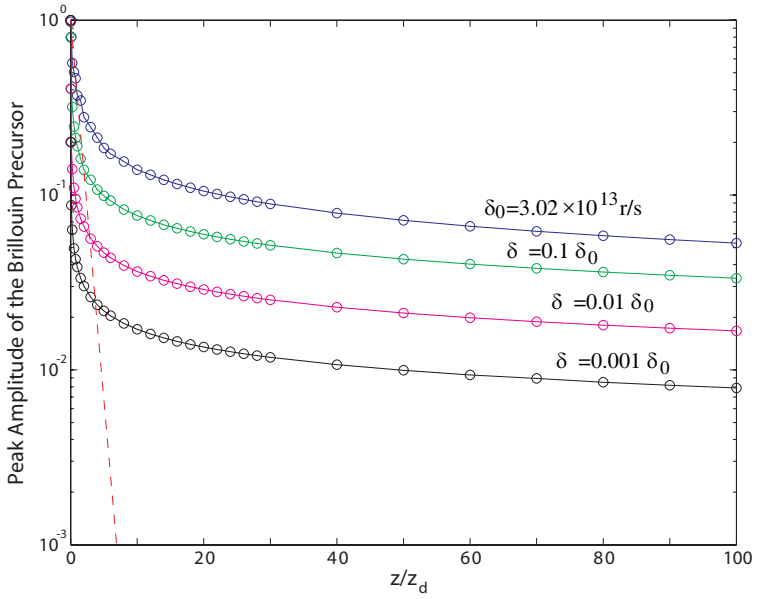

Figure 1: Numerically determined peak amplitude decay due to an input unit step function modulated signal with below resonance carrier frequency $\omega_c = 3.0 \times 10^{14}$ r/s in a single resonance Lorentz model dielectric with angular resonance frequency $\omega_0 = 3.9 \times 10^{14}$ r/s and plasma frequency $\omega_p = \sqrt{9.29} \times 10^{14}$ r/s as a function of the relative propagation distance z/z_d for decreasing values of the phenomenological damping constant δ.

In the singular dispersion limit as $\delta \to 0$, however, the two near saddle points $\omega_{SP_N}^{\pm}(\theta)$ coalesce into a single second-order saddle point at the origin, resulting in an asymptotic behavior whose

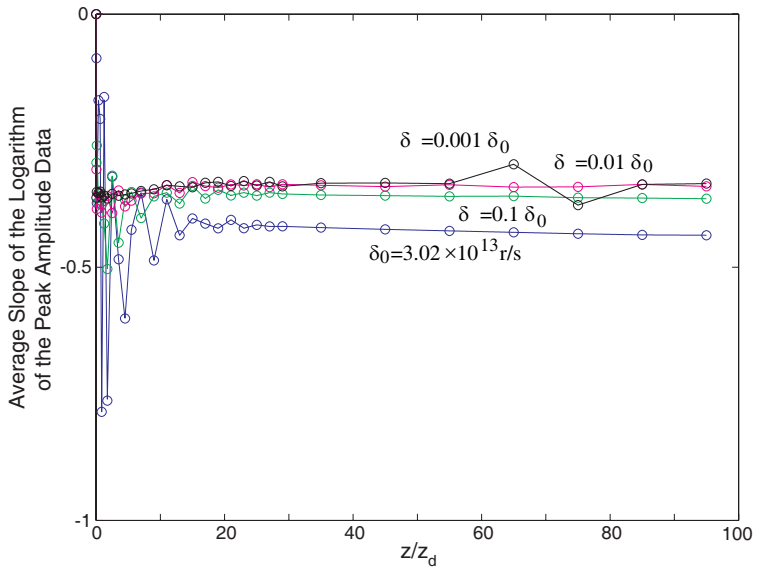

Figure 2: Average slope of the base ten logarithm of the numerical data presented in Fig. 1.

peak amplitude experiences zero attenuation, the amplitude now decaying only as $z^{-1/3}$. Notice that this limiting behavior is entirely consistent with the modern asymptotic theory [5].

The numerically determined peak amplitude decay with relative propagation distance z/z_d is presented in Fig. 1 for an input Heaviside unit step function modulated signal

$$A(0,t) = f(t) = U(t)\sin(\omega_c t), \tag{10}$$

with below resonance carrier frequency $\omega_c = 3.0 \times 10^{14}\,\mathrm{r/s}$ in a single resonance Lorentz model dielectric with angular resonance frequency $\omega_0 = 3.9 \times 10^{14}\,\mathrm{r/s}$ and plasma frequency $\omega_p = \sqrt{9.29} \times 10^{14}\,\mathrm{r/s}$ for several decreasing values of the phenomenological damping constant δ. Here $z_d \equiv \alpha^{-1}(\omega_c)$ denotes the e^{-1} amplitude penetration depth in the dispersive dielectric at the angular frequency ω_c, where $\alpha(\omega) \equiv \Im\left\{\tilde{k}(\omega)\right\}$ is the attenuation coefficient. The dashed line in the figure describes the pure exponential attenuation described by the function e^{-z/z_d}. The peak amplitude used here is given by the measured amplitude of the first maximum in the temporal evolution of the propagated pulse at a fixed observation distance $z \geq 0$. Notice that this "leading-edge" peak amplitude point initially attenuates more rapidly than that of the signal at $\omega = \omega_c$, but that as the mature dispersion regime is reached and the Brillouin precursor emerges, a transition is made from exponential attenuation to algebraic decay. Notice further that this transition occurs at a larger relative propagation distance z/z_d as the phenomenological damping constant δ decreases and the medium dispersion becomes increasingly localized about the medium resonance frequency ω_0, and hence, more singular. Finally, as the material dispersion becomes more singular (i.e., as δ decreases), the number of sample points required to accurately model the material dispersion and resultant propagated field structure increases. At the smallest value of δ considered here, a 2^{23} point FFT was required.

The algebraic power associated with the measured peak amplitude decay presented in Fig. 1 may be accurately determined [6] by plotting the base ten logarithm of the peak amplitude data versus the base ten logarithm of the relative propagation distance z/z_d. If the algebraic relationship between these two quantities is of the form $A_{peak} = B(z/z_d)^p$ where B is a constant,then the value of the power p is given by the slope of the relation $\log(A_{peak}) = \log(B) + p\log(z/z_d)$. The numerically determined average slope of the base ten logarithm of the data presented in Fig. 1 is given in Fig. 2 for each value of δ considered. These numerical results show that the power p increases from a value approaching $-1/2$ as $z \to \infty$ to a value approaching $-1/3$ as $z \to \infty$ when δ is decreased such that $\delta/\omega_0 \ll 1$, in complete agreement with the asymptotic theory.

An example of the numerically computed dynamical field evolution in the singular dispersion limit is presented in Fig. 3. The initial wave field at $z = 0$ is a Heaviside unit step function signal with below resonance angular carrier frequency $\omega_c = 3.0 \times 10^{14}\,\mathrm{r/s}$. The propagated wave field illustrated here was calculated at ten absorption depths into a single resonance Lorentz model

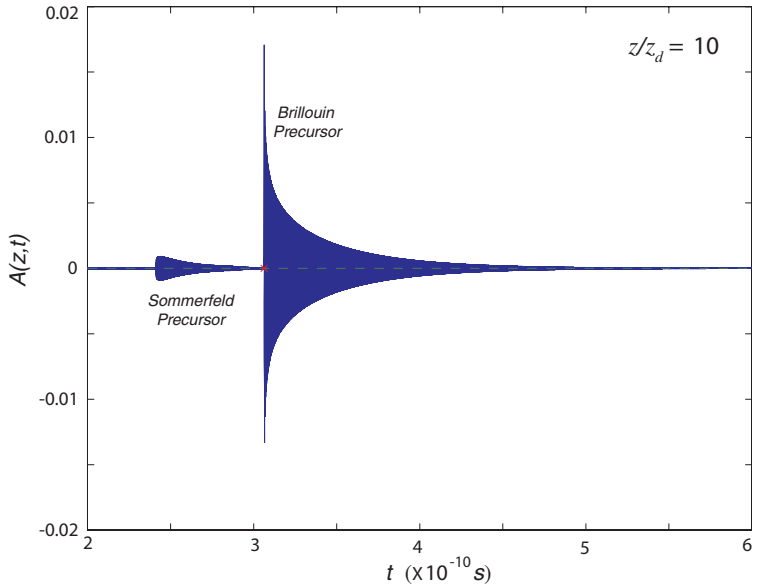

Figure 3: Propagated wave field at ten absorption depths ($z = 10z_d$) due to an input unit step function modulated signal with below resonance angular carrier frequency $\omega_c = 3.0 \times 10^{14}\,\mathrm{r/s}$ in a single resonance Lorentz model dielectric with resonance frequency $\omega_0 = 3.9 \times 10^{14}\,\mathrm{r/s}$, plasma frequency $\omega_p = \sqrt{9.29} \times 10^{14}\,\mathrm{r/s}$, and phenomenological damping constant $\delta = 3.02 \times 10^{10}\,\mathrm{r/s}$.

dielectric with resonance frequency $\omega_0 = 3.9 \times 10^{14}\,\mathrm{r/s}$, plasma frequency $\omega_p = \sqrt{9.29} \times 10^{14}\,\mathrm{r/s}$, and phenomenological damping constant $\delta = 3.02 \times 10^{10}\,\mathrm{r/s}$. Since $\delta/\omega_0 = 7.74 \times 10^{-5}$, this case is well within the singular dispersion regime.

3. ULTRASHORT PULSE DYNAMIICS IN THE WEAK DISPERSION LIMIT

In the weak dispersion limit as $N \to 0$, the material dispersion approaches that for vacuum at all frequencies, i.e., $n(\omega) \to 1$. This then introduces a rather curious difficulty into the numerical FFT simulation of pulse propagation in this weak dispersion limit as the number of sample points required to accurately model the propagated pulse behavior rapidly increases as the number density N decreases to zero. In order to circumvent this problem, an approximate equivalence relation has been developed that allows one to compute the propagated field behavior in an equivalent dispersive medium that is strongly dispersive. This approximate equivalence relation, which becomes exact in the limit as $N \to 0$, follows from the integral representation of the propagated wave field given in Eq. (1) as follows.

Two different propagation problems for the same input pulse $A(0,t) = f(t)$ are identical provided that the relation

$$\tilde{k}_1(\omega)z_1 - \omega t_1 = \tilde{k}_2(\omega)z_2 - \omega t_2 \tag{11}$$

is satisfied for all ω. Upon equating real and imaginary parts, there results the pair of relations

$$\beta_1(\omega)z_1 - \omega t_1 = \beta_2(\omega)z_2 - \omega t_2, \tag{12}$$

$$\alpha_1(\omega)z_1 = \alpha_2(\omega)z_2, \tag{13}$$

both of which must be satisfied for all ω, where $\beta(\omega) \equiv \Re\left\{\tilde{k}(\omega)\right\}$ and $\alpha(\omega) \equiv \Im\left\{\tilde{k}(\omega)\right\}$. For the absorptive part, one obtains the equivalence relation

$$z_2 = \frac{\alpha_1(\omega)}{\alpha_2(\omega)}z_1, \quad \forall\ \omega. \tag{14}$$

If the two media differ only through their densities, then because $\alpha(\omega) = (\omega/c)n_i(\omega)$ for real ω and $n(\omega) = \sqrt{1 + Ng(\omega)} \to 1 + \frac{1}{2}Ng(\omega)$ as $N \to 0$, so that $n_i(\omega) \approx \frac{1}{2}Ng(\omega)$, the above equivalence relation becomes

$$z_2 \approx \frac{N_1}{N_2}z_1. \tag{15}$$

The corresponding equivalence relation for the phase part then becomes

$$\begin{aligned}\frac{\omega}{c}\left(1+\frac{1}{2}N_1 g(\omega)\right)z_1-\omega t_1 &\approx \frac{\omega}{c}\left(1+\frac{1}{2}N_2 g(\omega)\right)z_2-\omega t_2\\ &\approx \frac{\omega}{c}\left(1+\frac{1}{2}N_2 g(\omega)\right)\frac{N_1}{N_2}z_1-\omega t_2,\end{aligned} \tag{16}$$

so that

$$t_2 \approx t_1+\left(\frac{N_1}{N_2}-1\right)\frac{z_1}{c}, \tag{17}$$

which is the second part of the desired equivalence relation. For example, if $N_1/N_2 = 1\times 10^{-2}$, then $z_2 = z_1\times 10^{-2}$ and $t_2 \approx t_1 - (0.33\times 10^{-8}\,\mathrm{s/m})z_1$. In that case, the propagated wave field structure illustrated in Fig. 3 also applies to the case when the plasma frequency ω_p is reduced by the factor 10 and the propagation distance z is increased by the factor 100 provided that the time scale is adjusted according to Eq. (16).

4. CONCLUSION

The results presented here have defined the singular and weak dispersion limits for ultrawideband pulse propagation. Most importantly, these results have shown that the Brillouin precursor persists in both of these limiting cases, dominating the propagated field structure as $z\to\infty$.

ACKNOWLEDGMENT

The research presented in this paper was supported in part by the United States Air Force Office of Scientific Research under Grants F49620-01-306 and FA9550-07-1-0112.

REFERENCES

1. Sommerfeld, A., "Über die fortpflanzung des lichtes in disperienden medien," *Ann. Phys. (Leipzig)*, Vol. 44, No. 4, 177–202, 1914.
2. Brillouin, L., "Über die fortpflanzung des licht in disperienden medien," *Ann. Phys. (Leipzig)*, Vol. 44, No. 4, 203–240, 1914.
3. Brillouin, L., *Wave Propagation and Group Velocity*, Academic Press, New York, 1960.
4. Stratton, J. A., *Electromagnetic Theory*, McGraw-Hill, New York, 1941.
5. Oughstun, K. E. and G. C. Sherman, *Electromagnetic Pulse Propagation in Causal Dielectrics*, Springer-Verlag, Berlin-Heidelberg, 1994.
6. Oughstun, K. E., "Dynamical evolution of the Brillouin precursor in Rocard-Powles-Debye model dielectrics," *IEEE Trans. Antennas & Prop.*, Vol. 53, No. 5, 1582–1590, 2005.

Optimizing of System Partition and Software Architecture of Distributed Control Computer of Power Electronics Facility

J. Zdenek

Faculty of Electrical Engineering, Czech Technical University in Prague
Technicka 2, 166 27 Prague 6, Czech Republic

Abstract— The principles and methodology of system and software architecture design of the distributed network control computer (DNCC) of a mid-range complexity power electronics facility are presented. The system design is based on such criteria as functionality, reliability and maintainability. To reach these properties special emphasis is placed on correct and optimal system functions partition among distributed computer nodes to be minimized the overall communication overhead and on minimizing the hardware parts of the system by moving maximum of facility user and system functions into the software. As an examples of such design task the DNCC structure of two implemented power systems is introduced. These are the scientific high temperature material processing equipment for research in space orbital station and the electric locomotive.

1. INTRODUCTION

The software architecture of computer controlled systems has many modifications and depends on the application size, required speed, available design time, budget size, experience of software designer, tight cooperation with hardware designer and many other factors. In a simple drive systems with sufficient number of the hardware interrupt resources the interrupt-background system is often used [1]. In more complex systems the selected architecture may depend on the number of application tasks required. If the number of tasks is from tenths to hundreds preemptive Real Time Operating System (RTOS) [2, 3] may be used as a reliable basic layer to schedule and execute application tasks and to support inter-task and/or inter-node communication [4, 5]. As the number of tasks increases an RTOS overhead increases rapidly and total throughput and time response of an RTOS can be unsatisfactory. In such design cases using of the co-routines may be a good solution [6, 7] with low overhead even if we use excessive amount of the application tasks [8, 9]. On the other hand such solution requires higher user programming discipline i.e., short action tasks only for CPU have to be shared voluntarily. The system integrity may be more easily disturbed by incorrect programmer action in comparison with RTOS.

2. CORRECT SYSTEM PARTITION

The design keystone is correct distributed system functional partition to set up no node processor throughput or communication bottleneck. First of all it is necessary to collect all system functional requirements (this task is typically very difficult) and to analyze them very carefully. To define control computer system partition we can use sequence of steps defined by formulae (1)–(9) using properly defined criterial (threshold) functions.

Let us define following symbols:
$ThFR_i$—task function requirement threshold function,
$ThFT_i$—system fault tolerant threshold function,
$ThUT_i$—user task selection threshold function,
$utgXX_i$—user task group selected by XX criterion,
$pjrq_i$—project function requirements,
$pjSW$—project software,
$ThCM_i$—inter-task communication threshold function,
$ThTP_i$—CPU throughput threshold function,
$pjSW_k$—unassigned software after step k,
ss_i—system software support, RTOS etc.,
ut_i—user task,
utg_i—user task group,
$hwNode_i$—hardware network node with CPU.

Now we define a pool of user tasks ut_j with help of a set of application selection threshold functions $ThUT_j$ from set of project functions $pjrq_i$ (1) and we get unassigned software tasks $pjSW$ (2)

$$ut_j = ThUT_j\left(\sum_i pjrq_i\right) \tag{1}$$

$$pjSW = \sum_i ut_i + \sum_j ss_j \tag{2}$$

Then we define groups of user tasks $utgXX_j$ by criterial functions $ThXX_j$ relating to application function requirements (3), inter-tasks data flow rate (4), required CPU throughput (5) and fault

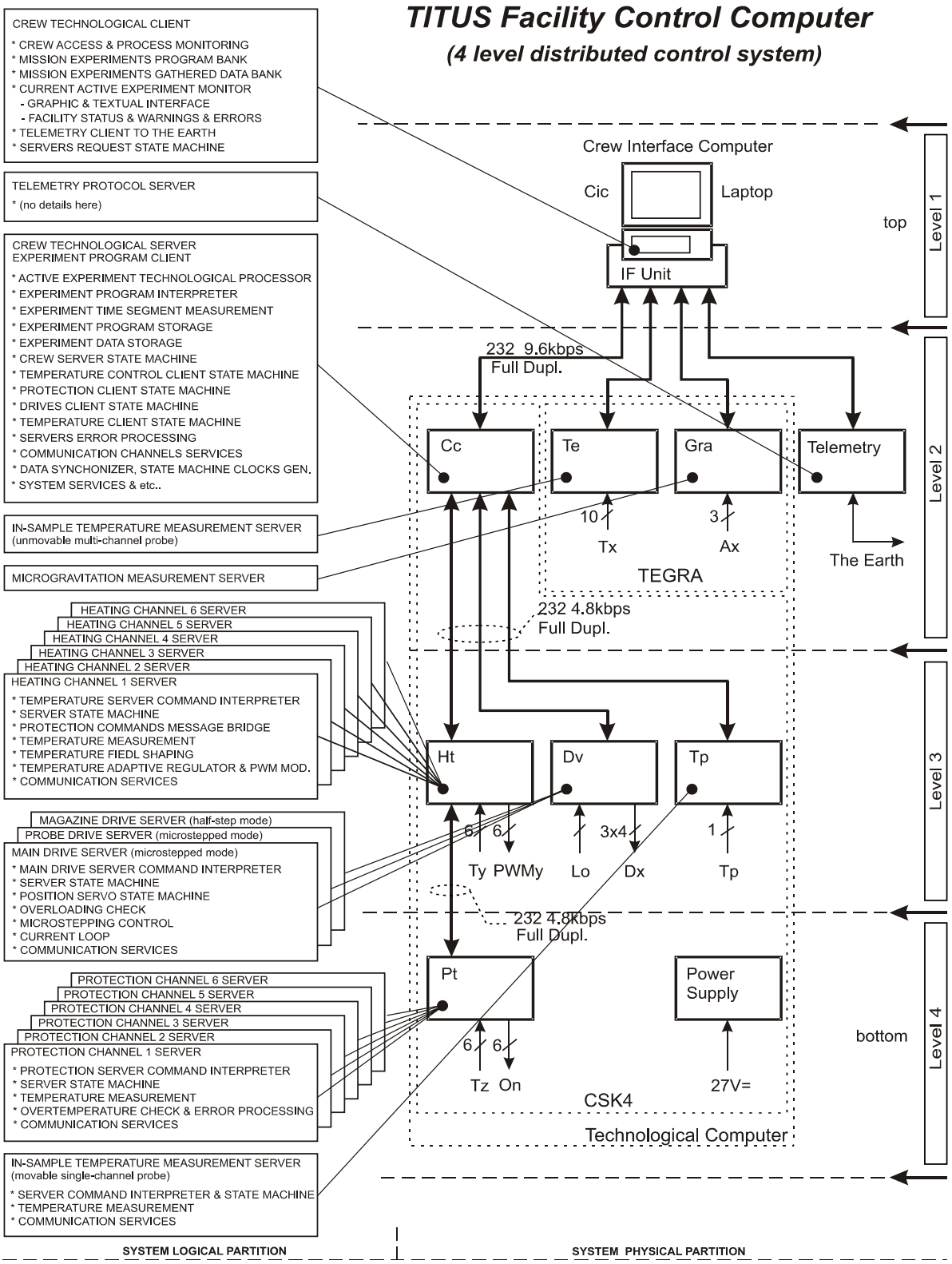

Figure 1: Scientific space research facility distributed network control computer (DNCC) — structural view.

tolerance design (6)

$$utgFR_j = \sum_i ThFR_j\left(ut_i\right) \tag{3}$$

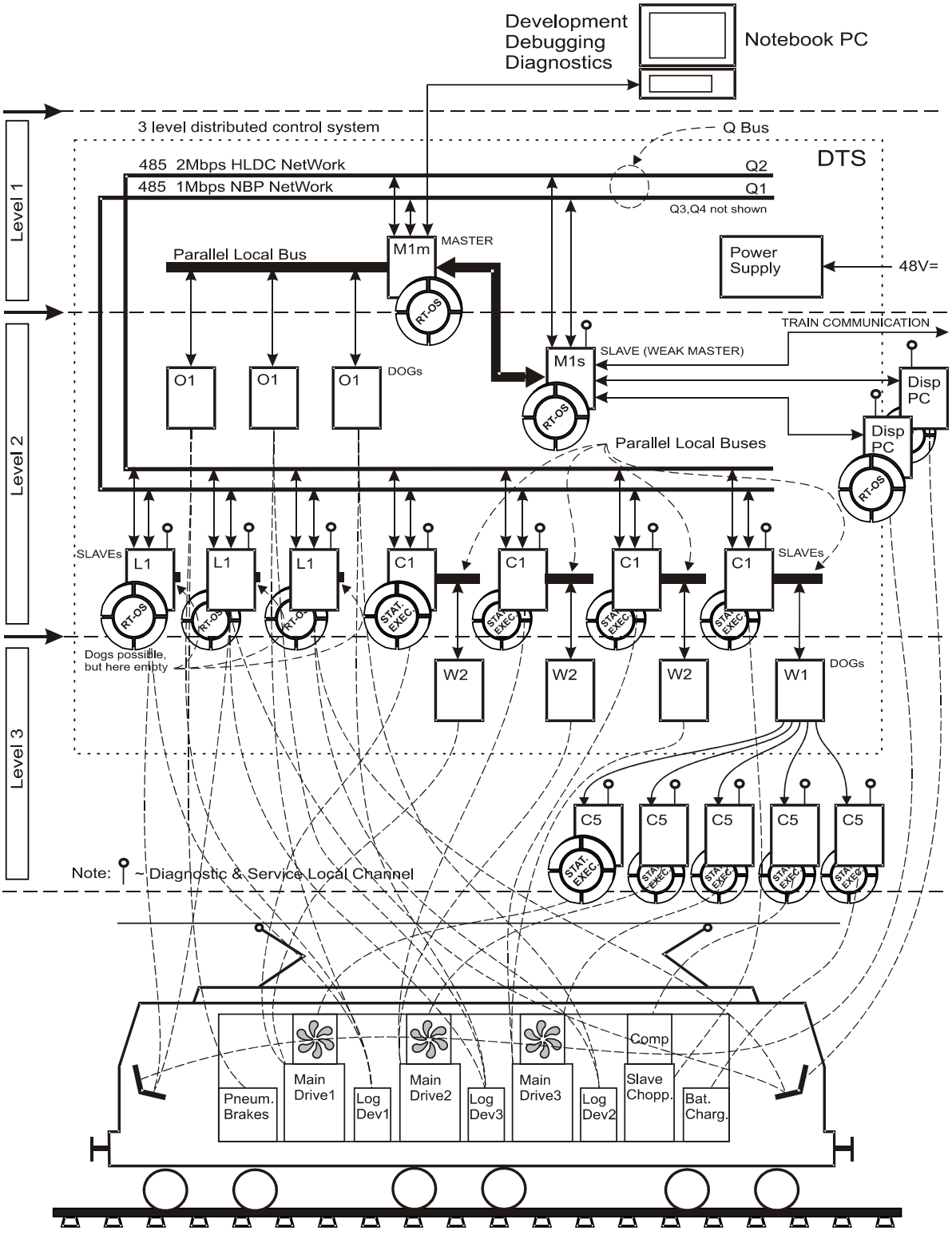

Figure 2: Traction vehicle distributed network control computer (DNCC) — structural view.

$$utgCM_j = \sum_i ThCM_j\left(ut_i\right) \tag{4}$$

$$utgTP_j = \sum_i ThTP_j\left(ut_i\right) \tag{5}$$

$$utgFT_j = \sum_i ThFT_j\left(ut_i\right) \tag{6}$$

Finally we get group of tasks utg_j (7) to that it will be designed (assigned) proper hardware $hwNode_j$ (8)

$$utg_j = utgFR_j \cap utgCM_j \cap utgTP_j \cap utgFT_j \tag{7}$$

$$hwNode_j \leftarrow utg_j \tag{8}$$

Unassigned software $pjSW_k$ (9) have to be solved in the next iterations until $pjSW_k$ set is not empty.

$$pjSW_k = \sum_i ut_i - \sum_k utg_k + \sum_m ss_m \tag{9}$$

When all groups of user tasks utg_j are assigned to hardware, type of system software (RTOS, static executive timing requirement, number of tasks inside group, interrupt latency, data flow rate, communication channels capacity and latency, real time debugging tools, real time monitor features, etc.) has to be selected.

3. USING CO-ROUTINES AND POINT-TO-POINT CHANNELS

The DNCC structure of the scientific space research facility for high-temperature material processing in zero gravity environment designed by presented methodology is in Fig. 1, details see [6, 8, 9]. In this application thousands of user task have to be used but especially in higher DNCC hierarchical levels time response requirements are only medium. The final solution (Fig. 1.) is four level star-like DNCC structure with serial communication point-to-point channels and table driven scheduler with uniform coroutine processing in all DNCC hierarchical levels. This structure has among others advantage to be easily debugged separately.

4. USING RTOS AND BUS STRUCTURE

The DNCC structure of the traction vehicle designed by presented methodology is in Fig. 2, details see [5, 10]. In this application number of user tasks is not so high (15–20) but time response requirements are high especially in lower DNCC hierarchical levels. The final solution (Fig. 2) is the three level DNCC structure with serial bus-like communication channels, highly scalable RTOS with dynamic scheduler-dispatcher inside higher level and static executive in other DNCC levels and with uniform RTOS communication services used in all DNCC nodes.

5. CONCLUSION

Both presented DNCC structures of power system facilities proved itself to be fully feasible. They are in standard operation with stable and correct behavior with no known essential problems.

ACKNOWLEDGMENT

The research was partly supported by the research program No. MSM6840770015 of the CTU in Prague sponsored by the MEYS of the Czech Republic.

REFERENCES

1. Lettl, J. and S. Fligl, "Matrix converter control system," *Proceedings of International Symposium PIERS2005*, 395–398, Hangzou, China, August 2005.
2. Cheng, A. M. K., *Real-Time Systems: Scheduling, Analysis and Verification*, ISBN-0471184063, John Wiley, 2002.
3. Kopetz, H., *Real Time Systems: Scheduling, Design Principles for Distributed Embedded Applications*, ISBN-07923989947, Kluwer, 2003.
4. Zdenek, J., "Efficient DMA based local computer network communication services for traction vehicle," *Proceedings of International Conference SPRTS2005*, 44–51, Bologna, Italy, October 2005.

5. Zdenek, J., "Maximization throughput of the distributed control computer of power system using DMA and optimal partition," *WSEAS Transactions on Power Systems*, Vol. 1, No. 5, 947–952, 2006.
6. Zdenek, J., "Control electronics of scientific space technological facility," *Proceedings of 11th International Conference EPE-PEMC2004*, CD ROM, Riga, Latvia, September 2004.
7. Zdenek, J., "Efficient scheduler-dispatcher software architecture of the space power facility distributed control computer," *Proceeding of International Conference EPE2007*, Aalborg, Denmark, September 2007, in print.
8. Zdenek, J., L. Koucky, P. Mnuk, "Node for drive control of scientific equipment for high temperature material processing in space station," *Proceedings of International Conference EDPE2003*, 201–206, High Tatras, Slovak Repuplic, September 2003.
9. Zdenek, J., L. Koucky, P. Mnuk, "Network node for temperature control of scientific equipment for high temperature material processing in space station," *Proceedings of IFAC International Workshop PDS2003*, 291–294, Ostrava, Czech Republic, January 2003.
10. Zdenek, J., "System design and software architecture of traction vehicle control computer," *Proceedings of 12th International Conference EPE-PEMC2006*, 1205–1210, Portoroz, Slovenia, Aug. 2006.

EMI in Induction Motor Drive Fed from IGCT Voltage Source Inverter

S. Bartoš[1], **V. Jehlička**[1], **J. Škramlík**[1], **and V. Valouch**[2]

[1]Institute of Thermomechanics, Department of Electrical Machines, Drives, and Power Electronics
Academy of Sciences of the Czech Republic, Prague, Czech Republic
[2]Department of Electrical Drives and Traction, Faculty of Electrical Engineering
CTU Prague, Czech Republic

Abstract— The paper summarizes the experience acquired during laboratory experimental operation of an IGCT inverter feeding a 3-phase induction machine (IM) as well as practical knowledge gained from the employment of the IGCT switching devices in vehicles of city mass transportation. Among others, overvoltage phenomena occurring between the inverter and the IM, the influence of the feeding cables, and the causes of electromagnetic interference (EMI) were traced.

1. INTRODUCTION

The problem of EMI has become severe with the advent of fast switching devices, such as the IGBTs or IGCTs. The increase in EMI is due to very steep edges in current and voltage waveforms and can be considered as a tax paid for the device fast switching ability. As a matter of fact, power switching devices feature permanent improvement which can be demonstrated e.g., by the successive development of GTOs into IGCTs, and now, most recently, into the mighty devices called ETOs. In general, the objective has been an increase in the device ratings, especially in terms of the repetitive peak blocking voltage (nowadays up to $V_{\mathrm{DRM}} = 4500\,\mathrm{V}$), the maximum controllable turn-off current (nowadays up to $I_{\mathrm{TGQM}} = 4000\,\mathrm{A}$) and the device switching frequency. Both the IGCT as well as the ETO are based on the same operation principle, i.e., on the hard-driven turn-off process, which is known also as unity-gain turn-off. This makes us believe that our conclusions and experience with IGCT inverters will be transferable to future ETO converters, too. It has been our effort to provide in the present paper an objective description and results of measurements that we carried out on IGCT and IGBT converters.

2. VOLTAGE FRONT EDGES

For an objective evaluation of the electromagnetic compatibility (EMC), the performed measurements had to be analyzed very carefully. Simultaneously with the voltage front edge, the respective current was measured, too. For current measurements, the Rogowski current waveform transducer was used. The probes were located very close to the inverter at one end of the cables, and also very close to the motor terminals at the other end.

Figure 1 compares the voltage front edges produced by an IGCT inverter to voltage front edges produced by an usual IGBT inverter. For this comparison, however, inverters with the same dc supply voltage were not at our disposal. The IGBT inverter was made up of a MITSUBISHI module and the provided dc feeding voltage was 310 V. The IGCT inverter, on the other hand, was supplied by 550 V.

- IGCT inverter

  a) separate phase cables, point of measurement 1 m distant from the inverter,

- IGBT inverter, 3-phase cable employed. The values were measured

  b) very close to the inverter,

  c) on the motor terminals

We see that the voltage front edges at both the IGBT and IGCT inverters have similar steep slopes and, although the switching times at the IGCT-based inverters are longer than those at the IGBT inverters, it may be expected that these inverters will produce also similar voltage waves traveling along the cables connecting the inverters and ac motors and resulting phenomena.

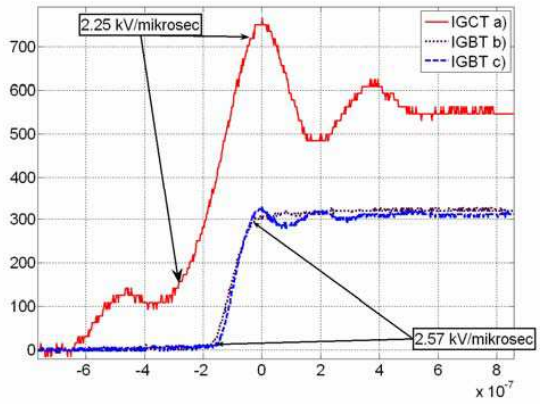

Figure 1: Comparison of voltage front edges, the voltage across the minus dc input terminal and any of ac outputs, cable length 3 m.

3. MODELS OF CABLES

Two notes first: i) By "separate phase cables" three cables lying free are meant, with the distance of some 10 centimetres between each other. ii) The hf voltage and current waveforms pursued in the following figures are responses just to one change in the state of the converter switches, e.g., to the turn-on of one device in the inverter.

The frequency of the generated waves is of the order of units of MHz. For such frequencies, the impedance of the induction machine (IM) is too large and has practically no influence on the pursued waveforms. Therefore, the IM is not involved in the equivalent diagram in Fig. 2, the current/voltage responses being determined, next to the switching speed, by the cable parameters only.

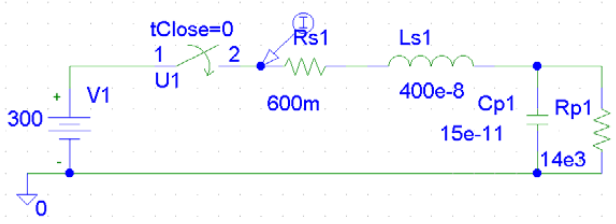

Figure 2: Simple equivalent diagram for a three-phase cable 3 m long.

Figure 2 depicts a simple equivalent diagram for one phase of a three-phase cable, 3 m long. The aim was the determination of resonance frequencies of the circuits. The equivalent diagram in Fig. 2 corresponds, in fact, to a loop created by one cable at the output of the inverter and all the inverter conductors connected galvanic to the minus dc supply terminal of the inverter. The particular values of the circuit elements Rs, Ls, Cp, and Rp in the equivalent diagram were measured on a real cable 4×1.5 PVC. In the same way, a 10 m long cable was modeled.

In the following Fig. 3, (corresponding to Fig. 2) the obtained waveforms and the results of their harmonic analysis are depicted. The knowledge of resonance frequencies is essential for correct evaluation of the current and voltage waveforms measured by the analyzer. One can't dispense with the mentioned modeling when identifying particular sources of EMI noise in the examined room, such as a trolleybus, a streetcar or a car on the metro. In real environment, the scanning antenna picks up namely interferences also from sources different from the electric drive itself. Such significant foreign sources are e.g., current collectors, auxiliary power supplies, other converters, etc..

4. MEASURED WAVEFORMS

The influence of the cables connecting the induction machine to the inverter can be appreciated with the help of Fig. 4. Two plots of voltage are shown: one measured at a point close to the

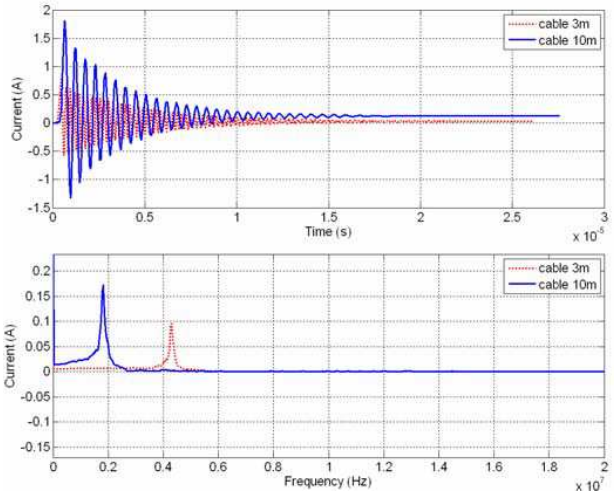

Figure 3: The dc input currents into the inverter versus time and their Fourier transformation, three-phase cables, 3 m and 10 m long, at the inverter output.

inverter, the other close to the motor. The same is valid for the current plots in the lower part of Fig. 4. To eliminate solitary, accidental, and abnormal waveforms, two characteristic waveforms (samples) measured very close to the inverter and two characteristic samples measured very close to the motor were selected for the harmonic analysis.

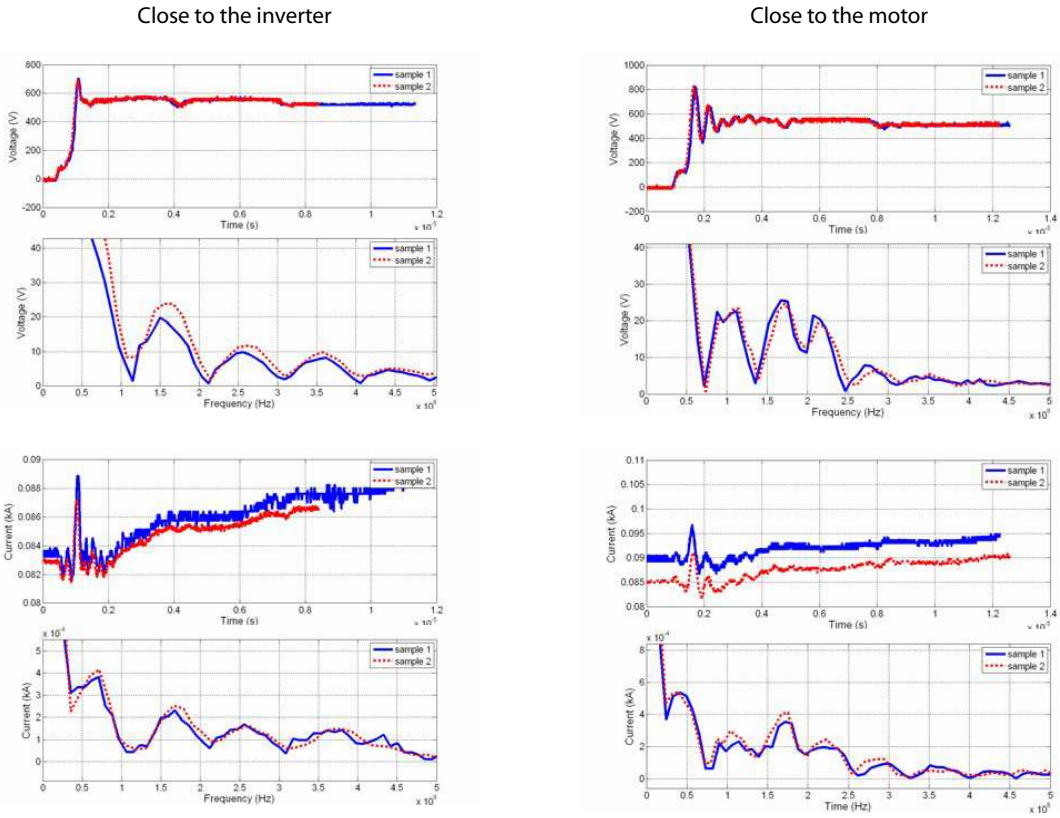

Figure 4: Voltage-time, voltage-frequency, current-time, and current-frequency relationships, measured at two mentioned different positions. IGCT inverter, 3 separate phase cables 10 m long.

The IGCT inverter is made up of three blocks PSC 6051, one block implementing one inverter leg. Each block consists of two IGCT devices TC 918-800-25 (produced by the Czech company Polovodiče, Inc.). The supplied motor was an IM of the type TB 702 with rated values 85 kW, 75 Hz, 2214 rpm, 133.8 A.

5. ELECTROMAGNETIC INTERFERENCE (EMI)

For EMI measurements, the EMC ANALYZER E7401A with circular antenna 11966A was used. Before starting the work, the EMI background had to be measured. In the measured frequency ranges (given by respective standards) also foreign sources of EMI occur that must be eliminated. Fig. 5 shows the measured levels of EMI in the city transport enterprises in Czech towns Hradec Králové and Plzeň, respectively. It is important to note that at Hradec Králové a trolleybus with a dc chopper with IGCT devices was pursued. The EMI background there was influenced by other trolleybuses equipped also with IGCT choppers, which were operating at the same time. In the other place, in Plzeň, the EMI of a streetcar equipped with IGBT inverters was measured. The streetcar was a prototype under test operation and no other similar streetcars were connected to the overhead contact system. This is evident from the measured EMI background, too. To increase the objectivity, many measurements at various localities were carried out. Therefore, the results summarized in Fig. 5 can be helpful when suggesting measures aimed at the reduction or elimination of EMI. The present paper is a continuation of former works [1–4] dealing with mathematical modeling of EMI.

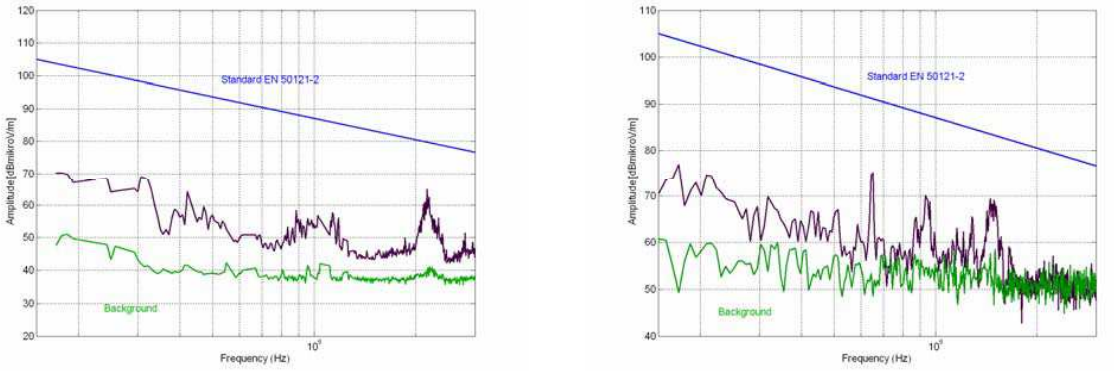

Figure 5: Values of EMI obtained from the analyzer E7401A at Hradec Králové and at Plzeň. The measurements were performed in accordance with the demands (distance of the antenna, etc.) of the Standard EN 50121-2.

6. CONCLUSION

Situation in the system consisting of a PWM inverter, feeding cable and induction motor (IM) is characterised by circulation of the high-frequency parasitic common and differential mode currents. Analysis of the complete set of the indicated phenomena is extremely difficult and requires correct mathematical models of all parts of the system. Besides that, the problems connected with the interferences and related effects in real applications have to be analysed and assessed by using appropriated experimental instruments, sophisticated procedures and experience as well.

The paper summarizes the experience acquired during laboratory experimental operation of an IGCT inverter feeding a 3-phase induction machine (IM) as well as practical knowledge gained from the employment of the IGCT switching devices in vehicles of city mass transportation.

ACKNOWLEDGMENT

The financial supports of the Grant Agency of the Czech Republic (project No. 102/06/0112), the Academy of Sciences of the Czech Republic (Institutional Research Plan Z20570509 of the Institute of Thermomechanics), and of the Ministry of Education, Youth and Sports (Research Plan MSM 6840770017 of the Czech Technical University) are highly acknowledged.

REFERENCES

1. Valouch, V., J. Šramlík, and I. Doležel, "Voltage and current conditions when feeding an induction motor from a transistor PWM inverter (in Czech)," *National Conf. Elec. Drives and Power Electronics, EPVE 95*, 7–15, FEL VUT Brno, Czech Republic, 1995.
2. Valouch, V., J. Šramlík, and I. Doležel, "Transient electromagnetic effects in the system PWM

inverter-long cable-induction motor," *Proc. of the Conf. EPNC (Electromagnetic Phenomena in Nonlinear Circuits)*, 267–272, Poznaň, Poland, May 1996.

3. Valouch, V., J. Šramlík, and I. Doležel, "Inverter-fed induction motor drive model for determining the stray current disturbances," *EMC 98 Roma*, 63–68, Roma, Italy, Sept. 14–18, 1998.
4. Valouch, V., J. Šramlík, and I. Doležel, "High-frequency intereferences produced in systems consisting of PWM inverter, long cable and induction motor," *AUTOMATIKA 42 (2001)*, 1–2, 45–51, Croatia, 2001.

PWM Strategy Applied to Realized Matrix Converter System

J. Lettl and S. Fligl

Department of Electric Drives and Traction, Faculty of Electrical Engineering
Czech Technical University in Prague, Czech Republic

Abstract— The presented paper deals with the realized matrix converter induction motor drive with emphasis on the PWM strategy design. Sophisticated pulse width modulation strategies in terms of various optimization criteria are known in case of indirect frequency converters, whereas both the inverter and the rectifier can be operated with pulse width modulation. The instantaneous states of both the output and the input converter waveforms depend at any time on the switch state of the converter power switches. Suitable switch states sequence of the nine matrix converter switches can be indirectly derived from the given switch states sequence of the twelve switchers of the indirect frequency converter. However, the main goal is to achieve the maximal possible output voltage by overmodulation employment. The special digital control system consisting of two personal computers was designed. The first PC serves for monitoring purposes only, the second one is equipped with a common interface card and works in real time.

1. INTRODUCTION

The matrix converter [1] received its name because its switches can be formed into a two dimensional matrix topology consisting of nine bidirectional switches. Generally, when talking about the transfer functions of matrix converters, it is silently assumed that ideal voltage sources and ideal current sources are attached to the input and output, respectively. Each current source is to be connected to a single voltage source. In other words a voltage source might be left unconnected and hence must not be connected to any other voltage source. Since the mains behaves typically as an ideal voltage source with an inductor and a resistor serially connected together, it is necessary to plug capacitors, in a star or delta arrangement, to the mains. However, by adding these capacitors an oscillating circuit is created with a natural frequency of oscillations that depends on mains inductance. This is why it is justifiable to put a whole 3 phase LC-input filter in front of a matrix converter. Naturally, the inductance of the inductor in the input filter has to be significantly larger than the mains inductance in order to keep its natural frequency under control. On the load side, there is normally no additional circuit required. Common representatives of load, an asynchronous or synchronous motor, fulfil the asked condition thanks to their leakage inductance (see Fig. 1). The employed control system [4–6] is based on two common personal computers. The first one

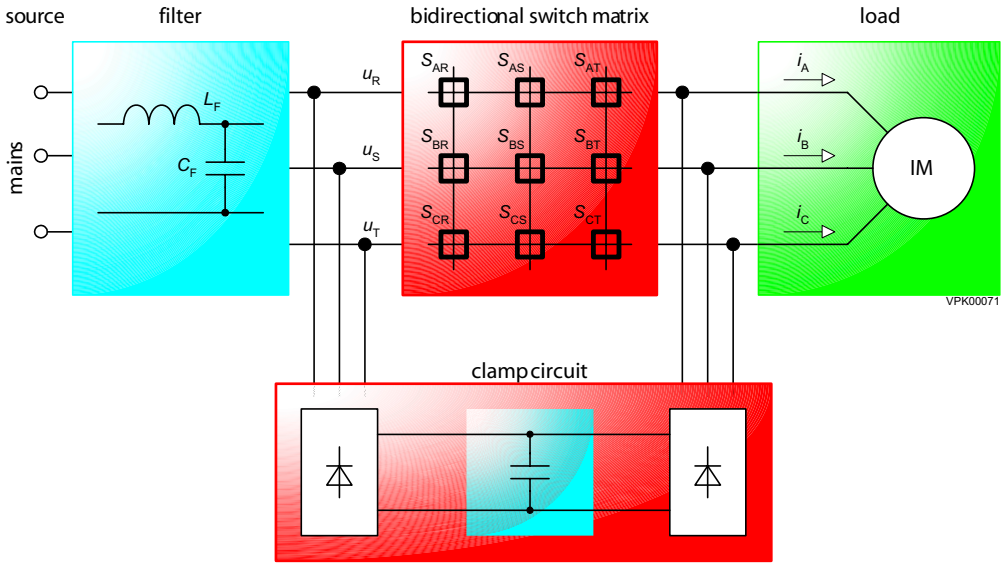

Figure 1: Basic power circuit of matrix converter induction motor drive.

(Host PC) is equipped with any multitasking operating system as is usual nowadays. It serves for compilation of the target real-time applications and for monitoring purposes only. The latter PC is equipped with a multi I/O PCI card Meilhaus ME-2600i containing 16 A/D and 4 D/A converters and a 32 bit bidirectional digital I/O port. This card is connected with an external rack that deals first of all with signal adjusting, pulse generation, and error signal management.

2. INDIRECT SPACE VECTOR MODULATION

This method strives to generate a desired output voltage vector (in a harmonic steady state with a constant amplitude $|\underline{u}_{\text{out}}|$ rotating with a constant angular speed ω_{out}) and simultaneously to take from the mains current a space vector that keeps a constant angle φ_{in} towards the rotating filter output voltage space vector at $\omega_{\text{in}} = \omega_{\text{mains}}$ (i.e., a constant input displacement factor of $\cos\varphi_{\text{in}}$). The situation is depicted in Fig. 2.

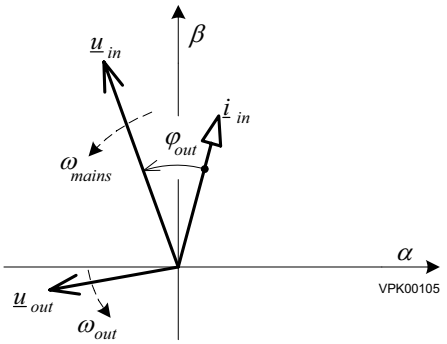

Figure 2: The indirect space vector modulation formulation.

The indirect space vector modulation is based on the idea of the virtual dc-link. The converter can be seen as a combination of a rectifier and inverter part [2, 3]. The space vector theory applied to the rectifier leads to the well known formulas that determine necessary switching times

$$\begin{pmatrix} d_{\underline{\gamma}} \\ d_{\underline{\delta}} \end{pmatrix} = \sqrt{6}/3 \frac{|\underline{i}_{in}|}{i_{P\alpha}} \begin{pmatrix} \sin(\pi/3 - \theta_{S-I}) \\ \sin(\theta_{S-I}) \end{pmatrix} \tag{1}$$

Similarly, we obtain for a given voltage vector

$$\begin{pmatrix} d_{\underline{\alpha}} \\ d_{\underline{\beta}} \end{pmatrix} = \sqrt{2} \frac{|\underline{u}_{out}|}{(u_{P\alpha - u_{N\beta}})} \begin{pmatrix} \sin\left(\frac{\pi}{3} - \theta_{S-U}\right) \\ \sin\theta_{S-U} \end{pmatrix} \tag{2}$$

The current modulation index

$$m_{C\alpha} = \frac{|\underline{i}_{in}|}{i_{p\alpha}} \tag{3}$$

is proposed to be kept constant by most authors. The output voltage can be then adjusted by means of d_α and d_β. But, the current modulation index influences the virtual DC-link voltage and subsequently the output voltage also

$$u_{P\alpha} - u_{N\beta} = |\underline{u}_{in}| \cdot \frac{|\underline{i}_{in}|}{i_{P\alpha}} \cdot \cos\varphi_{in} \tag{4}$$

Irrespective from the particular voltage adjustment method, the maximum available voltage transfer ratio seems to be 0,866.

3. OVERMODULATION

However, it is known from the area of indirect converters that a motor can be fed from a non-sinusoidal voltage source. The decisive parameter to the motor is then the first harmonic component of the delivered voltage. In the next considerations we assume the input displacement factor to be equal to one. Then when indirect space vector modulation is employed, the voltage in the virtual DC-link is constant and can be regulated from zero to 0.866 of the input voltage maximum value.

The amplitude of the output line-voltage can be regulated from zero up to the voltage value in the virtual DC-link. In an indirect converter with the included energy storage of huge capacity and with a diode rectifier on the input side, the DC-link voltage can be very close to the input line-voltage amplitude. However, it would be connected with a very deformed input current waveform. In other cases the DC-link will be slightly smaller

$$A_{u\,\max,IC\,\sin} \to 1 \tag{5}$$

So, such a converter can produce a sinusoidal output line voltage with amplitude nearly equal to the mains voltage. In the worst case if the rectifier diodes should carry the current all the time, the DC-link voltage would be given by the average value of the waveform covering absolute values of the input line-voltages

$$A_{u\,\max,IC\,\sin} \geq \frac{3}{\pi} \cong 0.955 \tag{6}$$

As mentioned above the voltage transfer ratio for the matrix converter is

$$A_{u\,\max,MC\,\sin} = \frac{\sqrt{3}}{2} \cong 0.866 \tag{7}$$

From the theory of inverters it is known that the maximum output voltage can be achieved when a square waveform is employed. The amplitude of the first harmonic component can be determined by means of Fourier transformation which from an algebraic point of view is simply scalar multiplication of the analyzed function with the basis component divided by scalar multiplication of the basis component with itself. From

$$\frac{\mathrm{u_{SQI}}}{\mathrm{u_{SQ}}} = \frac{\int\limits_{\pi/6}^{5\pi/6} 1 \cdot \sin\vartheta \cdot d\vartheta}{\int\limits_{0}^{\pi} \sin^2\vartheta \cdot d\vartheta} = \frac{2 \cdot \sqrt{3}}{\pi} \cong 1.103 \tag{8}$$

we can express

$$A_{u\,\max,MC\mathrm{square}} = \frac{3}{\pi} \cong 0.95 \tag{9}$$

Such modulation can be easily achieved by a modification of the indirect space vector modulation. If in each step we compare $d_{\underline{\alpha}}$ with $d_{\underline{\beta}}$ and set the larger one to unity and the smaller one to zero, the output voltage vector will move with steps of 60° which correspond to generating a square wave form output voltage.

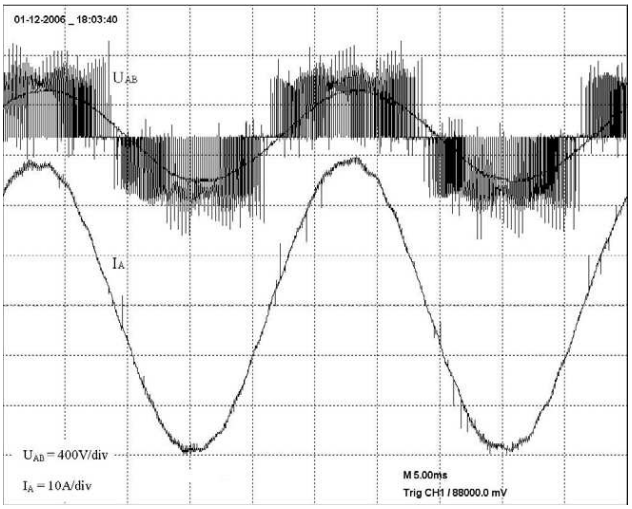

Figure 3: Measured output voltage and current waveforms for $U_{\mathrm{out}} = 430\,\mathrm{V}$, $f_{\mathrm{out}} = 40\,\mathrm{Hz}$, $M_{\mathrm{load}} = 48\,\mathrm{Nm}$.

4. MEASURED RESULTS

The converter was supplied from $3 \times 400\,\mathrm{V}$ mains. The power analyzers NORMA D500 were joined to the input side of the matrix converter as well as to the output side, where the digital oscilloscope TEKTRONIX was employed, too. An induction motor of 5 kW was coupled on and a DC dynamometer was used as a load. As an example in Fig. 3 the waveforms taken by means of the oscilloscope are shown. Fig. 4 and Fig. 5 then prove the very good harmonic composition of the waveforms.

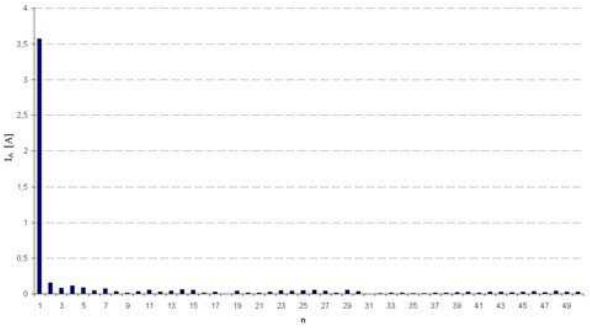

Figure 4: Measured output current harmonics.

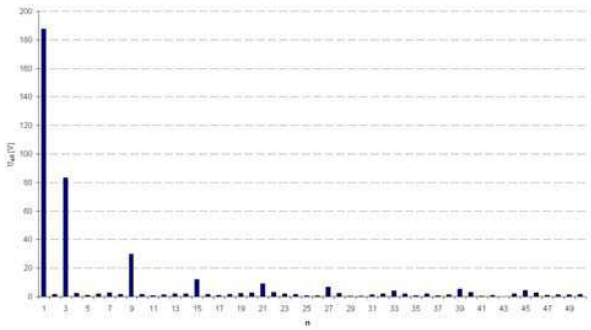

Figure 5: Measured output voltage harmonics.

5. CONCLUSION

The results obtained on the built-up experimental test bed have proved validity of the designed pulse width modulation strategy and matrix converter control system conception, proper function of the developed control hardware and software, and high level of the matrix converter energy conversion electromagnetic compatibility as concerns both the input phase displacement and the current and voltage harmonic content.

ACKNOWLEDGMENT

The research was partly supported by the research program No. MSM 6840770017 of the CTU in Prague sponsored by the MEYS of the Czech Republic.

REFERENCES

1. Gyugyi, L. and B. R. Pelly, *Static Power Frequency Changers*, Wiley, New York, 1976.
2. Alesina, A. and M. Venturini, "Analysis and design of optimum amplitude nine-switch AC-AC converters," *IEEE Transactions on Power Electronics*, Vol. 4, No. 1, 101–112, 1989.
3. Lettl, J. and S. Fligl, "Matrix converter control system," *Proceedings of International Symposium PIERS 2005*, 395–398, Hangzhou, China, August 2005.
4. Lettl, J., "Matrix converter hybrid drive system," *WSEAS Transactions on Power Systems*, Vol. 1, Issue 7, 1217–1222, July 2006.
5. Lettl, J., "Matrix converter induction motor drive," *Proceedings of International Conference EPE-PEMC 2006*, 787–792, Portoroz, Slovenia, August–September 2006.
6. Lettl, J. and S. Fligl, "Electromagnetic compatibility of matrix converter system," *Radioengineering*, Vol. 15, No. 4, 58–64, December 2006.
7. Dolecek, R. and O. Cerny, "Analysis of 25 kV, 50 Hz traction supply system at czech railways," *WSEAS Transactions on Power Systems*, Vol. 1, Issue 7, 1259–1266, July 2006.
8. Zdenek, J., "System design and software architecture of traction vehicle control computer," *Proceedings of International Conference EPE-PEMC 2006*, 1205–1210, Portoroz, Slovenia, August–September 2006.
9. Dolecek, R. and K. Hlava, "Transient effects at power-supply system of czech railways from EMC viewpoint," *Radioengineering*, Vol. 16, No. 1, April 2007.

Technological Aspects of Noise-suppressing Filter Design

K. Künzel and V. Papež
Czech Technical University in Prague, Czech Republic

Abstract— The noise suppression is up to date problem of power electronic devices like power sources, power converters etc. Paper deals with suppression of conducted disturbances. Main topic is filter design and it's assembling from real devices with theirs real characteristics. Filter topology and device wiring are very important too. Paper calls attention to selected questions and proposes their solution.

1. INTRODUCTION

The disturbance is one of the most serious problems of electronic equipment design. Conventional linear power sources containing transformer and rectifier working on power line frequency are replaced by switching mode power sources with modulation frequency tens or hundreds kilohertz. The power converters became common part of all kind of electrical drives. The switching speed of switching devices goes up as well as working (modulating) frequency. The emission level of produced disturbance signals increases for all these reasons. Technical standards try to restrict electromagnetic emissions by given emission limits radiated and conducted as well as restrict the sensitivity of electrical equipments working in given environment. The suppression of disturbance signal incoming from environment to equipment or originated in equipment and propagated to environment is necessary. The usual way is to use noise-suppressing filters and shielding.

2. FILTER CONSTRUCTION

The noise-suppressing filter is designed usually like a low pass filter with as possible minimum attenuation for effective signal — transmitted power — on low frequency range and as possible maximum attenuation for disturbance (on high frequency range). The reactance filters with coils and capacitors are commonly used. Such solution is theoretically executed very well, but the practical implementation is associated with many difficulties. The parasitic characteristic of used devices, nonlinearities, parasitic couplings and transmissions caused by bad mechanic design or assembly and bad impedance matching to connected input and output circuit cause frequently poor results. The fundamental noise-suppression filter characteristic is its transfer function in dependence on frequency e.g., amplitude characteristic. The measurement on high frequencies (noise-suppression range) is performed usually in accordance with Fig. 1. The measuring circuit consists from source of signal, filter and power indicator. The impedances of source output and indicator input are selected identically $50\,\Omega$ real. The filter transfer is defined as a ratio between power indicated in the measurement circuit with filter and without filter, e.g., with direct connection between source and indicator. From practical point of view it represents only approximation of real conditions. The used impedance is the same as impedance of line impedance stabilization network used for measurements of conducted emissions during test of electromagnetic compatibility, but it can be quite different from actual impedance of connected arrangement on the filter working place. This unmatched impedance can cause parasitic resonances with intensive influence on the amplitude characteristic.

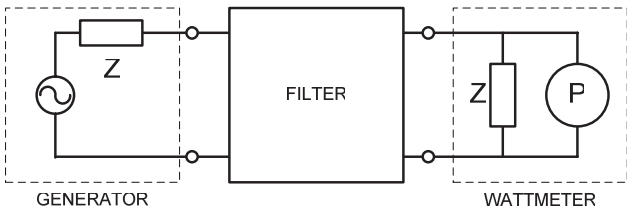

Figure 1: Filter characteristic measurement.

The maximum current is the most important parameter in the bandwidth for the useful signal. It depends on the power transmitted by filter. Similar characteristic is a serial impedance of filter.

These two characteristics define the voltage drop on the filter. These values are limited by inductor nonlinearities and ohmic losses in all loaded wires.

It is possible to find the value of components in many circuit synthesis handbooks for standard filter topologies [1], if the filter is assembled from discrete components including idealized amplitude characteristic. The actual characteristics of filter designed by this way can be quite different. Fig. 2 shows theoretical amplitude characteristic with comparison to characteristic of actual filter. Large differences are especially out off pass band, especially on high frequencies. The main reason is in parasitic characteristics of used components, e.g., parasitic inductance of capacitors and parasitic capacitance of inductors. These parasitic characteristics cause component self-resonances. The phase inverts and above resonance frequency capacitor turn into inductor and inductor turn into capacitor. Above maximum resonance frequency of all used components the filter changes its structure and the filter works as high pass filter. The increasing frequency dependence is evident on high frequencies.

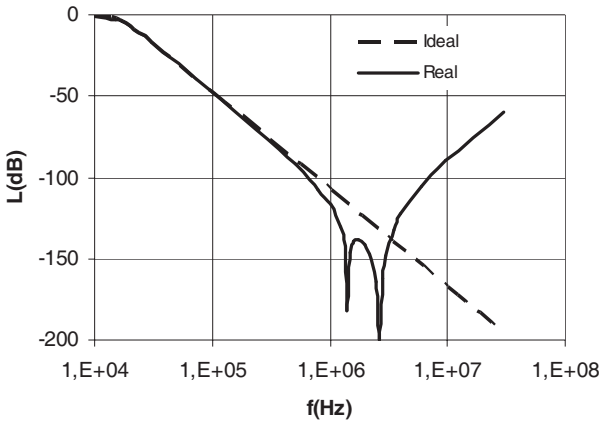

Figure 2: Filter characteristic: ideal vs. real.

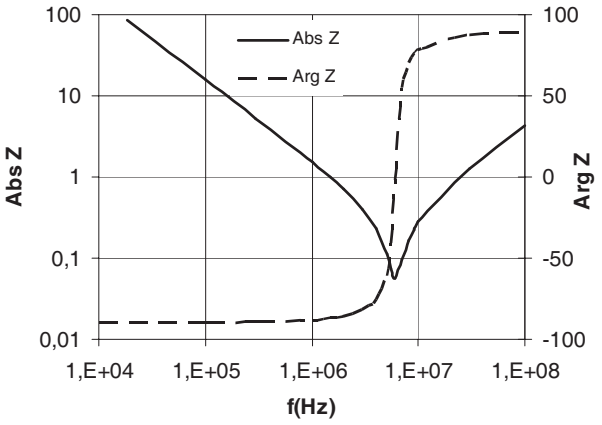

Figure 3: Capacitor impedance characteristics.

3. FILTER COMPONENTS

The components characteristics can be monitored on the base of their complex impedance. Typical characteristics of an actual capacitor are shown in Fig. 3. The amplitude and phase characteristics are presented. The characteristic be getting near ideal on low frequencies. The amplitude is inversely proportional to frequency and the phase is near $-90°$. Fictive capacitance and loss angle increase with increased frequency. The impedance of capacitor is purely real on the resonance frequency. The impedance characteristics above change to characteristics of loss inductor. On highest frequencies the characteristics be getting close to ideal inductor characteristics and the amplitude is proportional to frequency, the phase is close to $90°$. Equivalent scheme of capacitor is shown in Fig. 4.

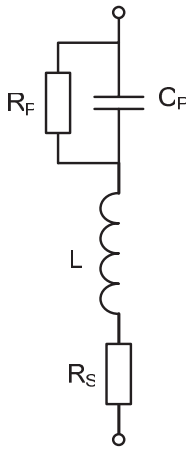

Figure 4: Capacitor.

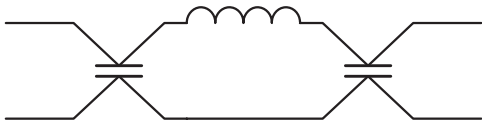

Figure 5: Capacitor wiring.

C_0 ... equivalent capacitance of capacitor

L ... inductance of leads and capacitor system

R_S ... serial ohmic resistance of leads and capacitor system

R_P ... resistance representing dielectric losses

The serial inductance L of capacitors used in filter has to be as low as possible in wide frequency range. It ensures high resonance frequency and low impedance. Capacitors with minimal inductance can be ceramic (plate or tubular) or non-inductive roll. The same attention has to be focused on capacitor leads. The best solution is to connect the capacitor with other filter components directly on capacitor electrodes — see Fig. 5. It is also suitable to use the feed-trough capacitors designed for such purposes. The caution should be focused on eventual parallel coupling of several capacitors. When two capacitors with nonzero inductance (internal or external) are coupled their resonance frequency can be different. In frequency bandwidth between resonances one capacitor has capacity reactance and the other has inductive reactance. The parallel resonance that event is illustrated on Fig. 6. Two 0.1 µF capacitors are coupled with unequal leading wires 2.5 cm and 0 cm. The parallel resonance can be observed around frequency 3.7 MHz as an impedance increase.

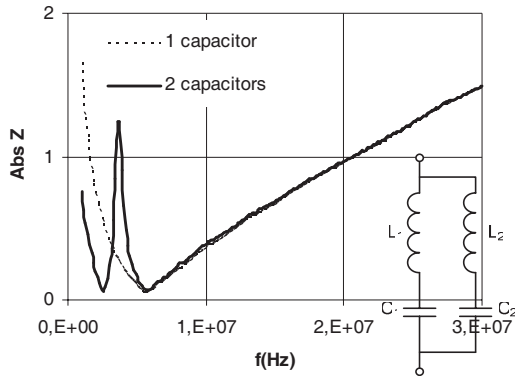

Figure 6: Two parallel capacitors.

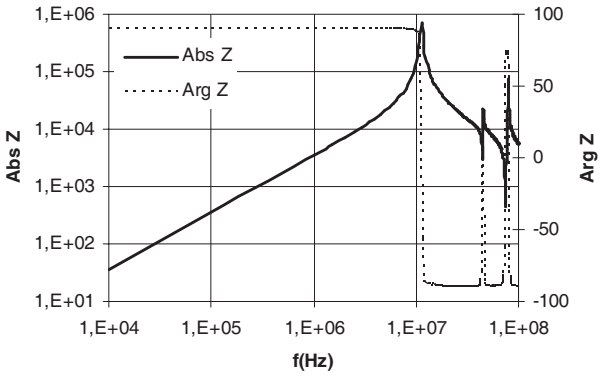

Figure 7: Inductor impedance characteristics.

Typical amplitude and phase characteristic of complex impedance of real inductor is shown in Fig. 7. Characteristics are close to ideal inductor in low frequency range when the amplitude is proportional to frequency and the phase is near to 90°. Fictive inductance and loss angle increase with increasing frequency. On resonance frequency the impedance of inductor is maximum and purely real. Above resonance frequency the impedance characteristics change to characteristics of loss capacitor. The characteristics be getting close to ideal capacitor on highest frequencies, the amplitude is inversely proportional to frequency and the phase is close to −90°. Equivalent scheme of inductor is shown in Fig. 8.

L_0 ... equivalent inductance of inductor

C ... capacitance of inductor and leads

R_S ... serial ohmic resistance of leads and winding

R_P ... resistance representing core losses

The capacitance C has to be as low as possible for getting resonance frequency as high as possible and maximum impedance in wide frequency range. The winding design and technology should be conforming to these demands. The coil core should be made from non-conducting material or should be well grounded. Optimum winding technology is single layer cylindrical space wound winding or winding into chambers. The length of winding conductor is limited by one half of wavelength corresponding to maximum working frequency propagated trough transmission line realized by inductor winding. The inductor with longer conductor has non-matched transmission line characteristics, impedance has maxima and minima on quarter-wave and half-wave resonances of working frequency range. The magnetic induction excited in core by passing current should be taken in account too. The ferrite core should work at magnetic field strength 100 A/m, powdered-iron core at one or two order higher strength. In case of higher magnetic field strength the core should be designed with air gap. Another way is to use current compensated coil. Several winding are arranged so as they compensate excited magnetic field in the core. That coil is inconvenient for symmetrical signals. In this case the filter characteristics go off rapidly.

4. FILTER DESIGN

The filter design starts usually from demanded amplitude characteristics. It is defined by comparison of disturbance signal level inside the equipment and allowed signal level on the device terminals. The standard approximation without nulls in suppressed band type Butterworth or Chebyshev is used. The amplitude characteristic has four critical points with regard to conventional characteristics of monitored functions.

- working frequency — with minimal attenuation for transmitted power
- frequency 150 kHz — minimum frequency limit, given by technical standards
- frequency 30 MHz — maximum frequency limit, given by technical standards (probably minimum attenuation of filter on high frequencies)
- frequency with maximum disturbance signal (or frequencies)

The cutoff frequency of low pass filter f_m is usually selected within the range from 10 kHz to 30 kHz. Filter capacitors within the range from 0.1 µF to 0.5 µF and filter inductors within the range from 200 µH to 2000 µH correspond to considered input and output impedance 50 Ω. The filter order n is essentially independent on used approximation and for demanded filter attenuation $L_{0,15}$ for frequency $f_{\min} = 150\,\text{kHz}$.

$$n > L_{0,15}/20 \lg \frac{f_{\min}}{f_m} \tag{1}$$

The amplitude characteristic distortion is defined in high frequency range (see Fig. 2) by parasitic characteristic of devices used for filter realization. It can be approach according to average resonance frequency of filter f_r. This frequency is average of minimum and maximum resonance frequencies of all capacitors and inductors of filter and it corresponds to fictive crossing point decreasing and increasing part of real amplitude characteristic. The filter attenuation above frequency f_r may be evaluated by next formula.

$$L_s = 20n\,(1 \lg f_r - \lg f_m - \lg f_s) \tag{2}$$

The approximation is not efficient in range of devices resonance frequencies. But the filter attenuation on these frequencies is high, so it is sufficient. Formula (2) is suitable for verification of demanded attenuation on the maximum frequency $f_{\max} = 30\,\text{MHz}$ ($f_s = f_{\max}$) and on the frequency with maximum disturbance signal, in case that this frequency f_s is higher then frequency f_r.

In case that $f_s < f_r$, the attenuation does not depend on frequency f_r and it can be determined by formula (2) with condition $f_s = f_r$.

If the attenuation on high frequencies (above f_r) is not sufficient, it is usually impossible to improve the characteristic by decreasing cutoff frequency f_m or by increasing nominal values of capacitors and inductors. The resonance frequency f_r decreases at the same time. The improvement of filter order is only possible solution of this problem. The easiest way is to use in addition to filter

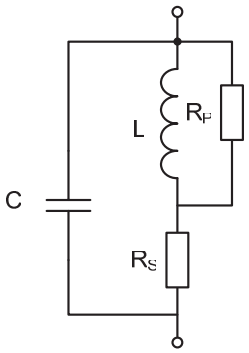

Figure 8: Inductor.

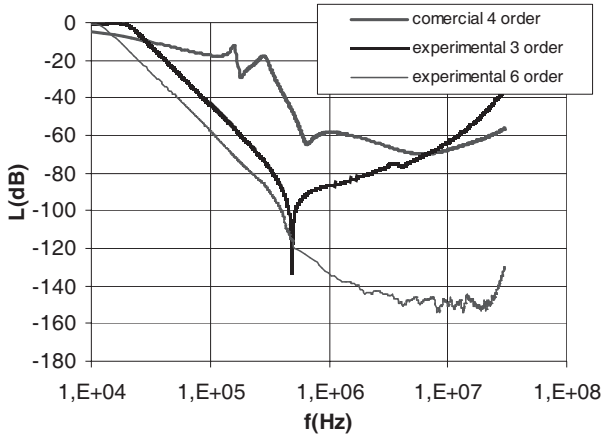

Figure 9: Filter characteristic.

with low cutoff frequency additional filter with higher cutoff frequency in the same range where the first filter has its resonance frequency. The resonance frequency of additional filter will be out of monitored range. Additional filter easily ensures demanded attenuation on high frequencies. The low values of capacitance and inductance are needed, so this filter is easy to realize and it represents low cost solution.

5. CONCLUSIONS

It is very useful to verificate the design verification by computer simulation of proposed circuit. Simulation has to include parasitic parameters of components. The last step is the validation of demanded characteristics on filter prototype and comparison with designed and simulated parameters. Resulting parameters of filter depend significantly on mounting into fixed installation especially for filter attenuation more than 60 dB.

The examples of characteristic of simple filters are in the Fig. 9

ACKNOWLEDGMENT

This paper was supported by research project of Ministry of Education, Youth and Sports of Czech Republic No. MSM 6840770017.

REFERENCES

1. Hájek, K. and J. Sedláček, Frequency Filter, BEN, Prague, 2002.
2. Künzel, K., V. Papež, and J. Žáček, "Design of electromagnetically compatible power electrical systems," In *Proceedings of Advanced Engineering Design AED 2006*, Prague, Czech Republic, [CD-ROM].
3. Küzel, K., V. Papež, and J. Žáček, "The problems of RF conducted emissions measurement," In *Proceedings of COMITE 2003*, 121–124, Prague, Czech Republic.

Testing of Robust Control Characteristics for Traction PMSM

O. Černý, J. Šimánek, R. Doleček, and J. Novák

University of Pardubice, The Czech Republic

Abstract— The paper deals with our research in the field of control of drive with permanent magnet synchronous motor (PMSM), particularly verification of control characteristics. We focus to development the robust control algorithm for direct drive PMSM. We have designed and simulated an algorithm of phase current control.

1. INTRODUCTION

Our field of research is aimed at traction drive with permanent magnet synchronous motor (PMSM) for application of rail transport and city local transport in particular. Advantages of PMSM are known well. The torque moment from point of view of dimension and weigh of drive is greatest advantage. This characteristic makes possible realization so-called direct drive (i.e., drive of axle or wheels without use of any gears) from electric traction point of view. Direct drives with other motors (e.g., asynchronous motors) are not possible to make in practice because they have big dimensions. Application of simple direct wheel drive enables simply realization of low-floor vehicle.

Our goal of research is made robust control algorithm for this traction drive. Calculation sophistication of algorithm is also followed, so that it will be possible to use a control algorithm into microprocessor control unit. Of course, every drive is necessary to feed from own inverter in case of individual drive of wheel by PMSM.

Research is proceeding in two levels. At the first level of the research, we concern with the simulation of this drive inclusive of its control. Comparison of characteristics of various control algorithms is purpose of simulations. At the second level of the research, algorithms are tested by testing stand with direct drive of tram wheel. This testing stand was lent from Research institution rail vehicles to laboratories of Jan Perner Transport Faculty.

2. TESTING STAND WITH PMSM

A testing stand of direct drive PMSM was lent to Jan Perner Transport Faculty. It was made by VÚKV (Research Institute of Rail Vehicles Prague). The testing stand consists of traction PMSM, tram wheel and "rotating rail" (second wheel).

PMSM is placed on silent blocks in frame of stand. Silent blocks allow swing of motor in vertical axis. Motor drives tram wheel by shaft without any gearing. Tram wheel is placed on a swinging arm in bearings. Cardan joint of driving shaft is placed inside of tram wheel. Tram wheel is pneumatically pressed to the "rotating rail". Pressure is variable from 4 kN to 50 kN.

PMSM is a prototype of traction motor for low-floor trams. It was made by VÚES Brno (Research Institute of electric machines Brno). The motor has inner rotor and its stator is cooled by liquid. Table 1 shows several characteristics of motor.

Asynchronous engine will be used for loading testing stand. The engine has similar parameters like PMSM used in testing stand. Engine has these parameters: nominal power 55 kW, nominal

Table 1: Motor characteristics.

Nominal power	58 kW
Nominal torque	852 Nm
Nominal speed	650 rpm
Nominal current	122 A
Maximal torque	2000 Nm
Maximal speed	1000 rpm
Maximal current	368 A
Number of poles	44

voltage 380 V and nominal speed 589 rpm. Loading engine will be fed by converter. DC-bus of converter will be also used for feeding PMSM inverter. Due this situation, the operation of whole workplace will be effective. Loses of drive will be covered by mains (3×400 V, 50 Hz). Break chopper will be also connected to the DC-bus. Break chopper will be important during failure of converter or inverter.

Figure 1: Testing workplace.

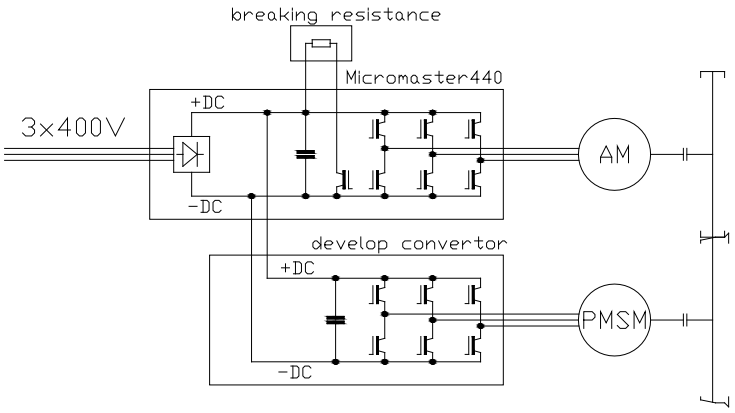

Figure 2: Electronic structure of testing workplace.

3. CONTROL ALGORITHM

The phase current control algorithm is based on control of actual phase currents. Setpoints of phase currents are sinusoidal. Phase displacement between setpoints is 120°. Magnitudes of current setpoints are proportional to a torque setpoint. Phases of current setpoints are derived from actual value of rotor angular position. Current space vector is controlled to be concentric with induced voltage. It means that actual value of phase current is maximal at the moment when rotor flux vector is orthogonal to profile of this stator winding. This control needs no coordinate conversions which have high requirements to computing power of controller. Block diagram of phase current control algorithm is shown in Figure 3. Current setpoints for phases A and B are calculated from actual angular position and current magnitude setpoint (proportional to torque setpoint). Control deviations are calculated from setpoints and actual currents in subtraction elements. Control deviations are sent to PI controllers. Two-state controllers are also applicable. However we do not suppose that for traction application due to EMC. Setpoint values have harmonic course (frequency from 0 to hundreds of Hz) thus the PI controllers have to have very fast response. An adaptation of

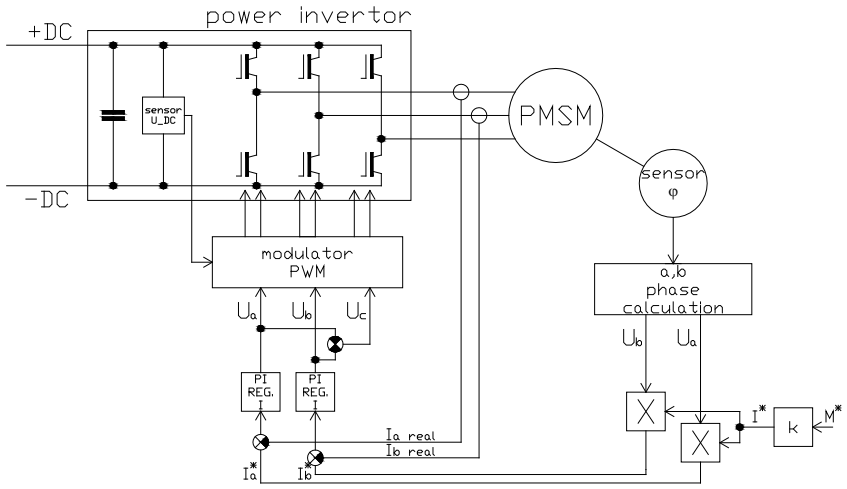

Figure 3: Block diagram of phase current control.

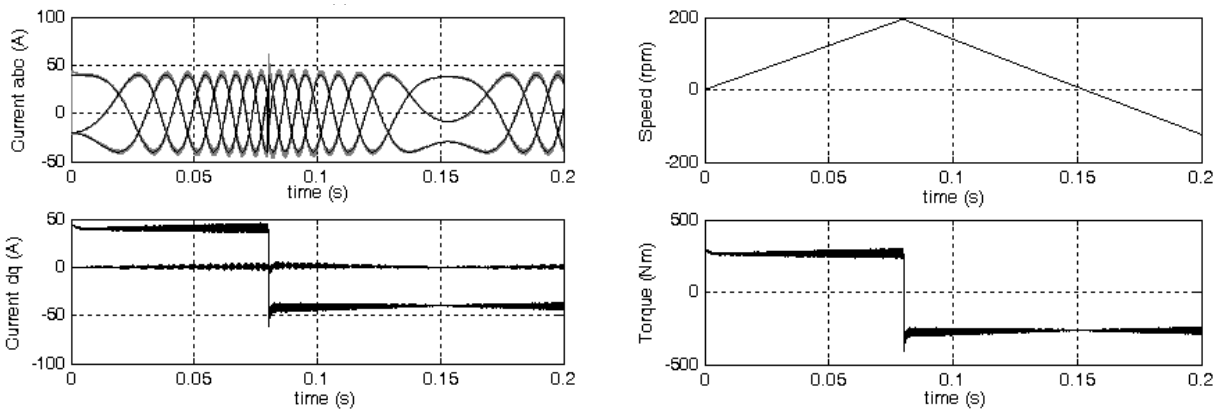

Figure 4: Simulating sequence of phase current control algorithm.

constants of PI controllers is suitable for optimal PI controller settings within the whole frequency range. Constants are adapted by speed. Actual induced voltage is added to PI controller output to reach better behavior of whole control algorithm. The induced voltage is calculated from actual speed, motor voltage parameter and actual rotor angular displacement.

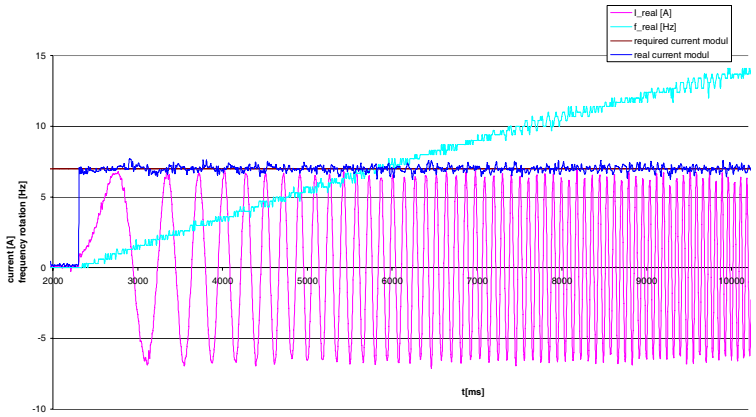

Figure 5: Motor starting by $I_{MAX} = 7A$.

4. SIMULATIONS OF CONTROL ALGORITHM

The application MATLAB Simulink was used for simulations of control algorithm and PMSM drive. Inertia torque of PMSM was simulated lower to reach faster simulations in Figures 5 which shows time behavior of speed, torque, phase currents and current components. There is simulated starting of PMSM to 200 rpm, subsequently electrodynamic brake and changeover of rotation direction. Sequence was simulated for DC-bus voltage 200 V and PWM frequency 5 kHz. The figures demonstrate simulation of both algorithms. The algorithms have similar behavior.

5. VERIFICATION OF CONTROL CHARACTERISTICS

Figures 5 and 6 are presented control characteristics' results. Characteristics verification are tested without load. Motor was loaded only by inertia moment and mechanical losses. Feeding voltage of converter was 560 V. Algorithm was done in DSP processor 320C240 by Texas Instrument. Sample period of control algorithm calculation is 200 µs and PWM frequency 5 kHz. Tests were done up to 100 Hz.

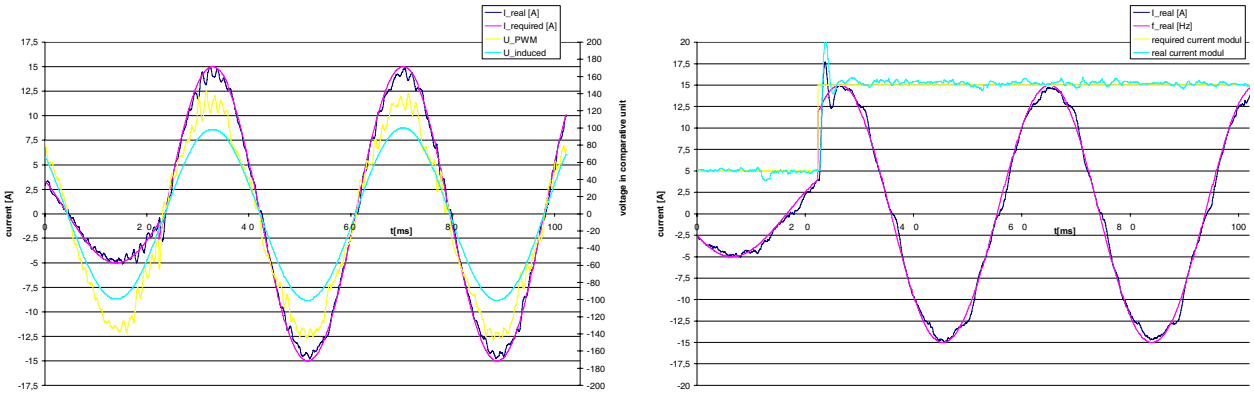

Figure 6: Response of current control from 5A to 15A.

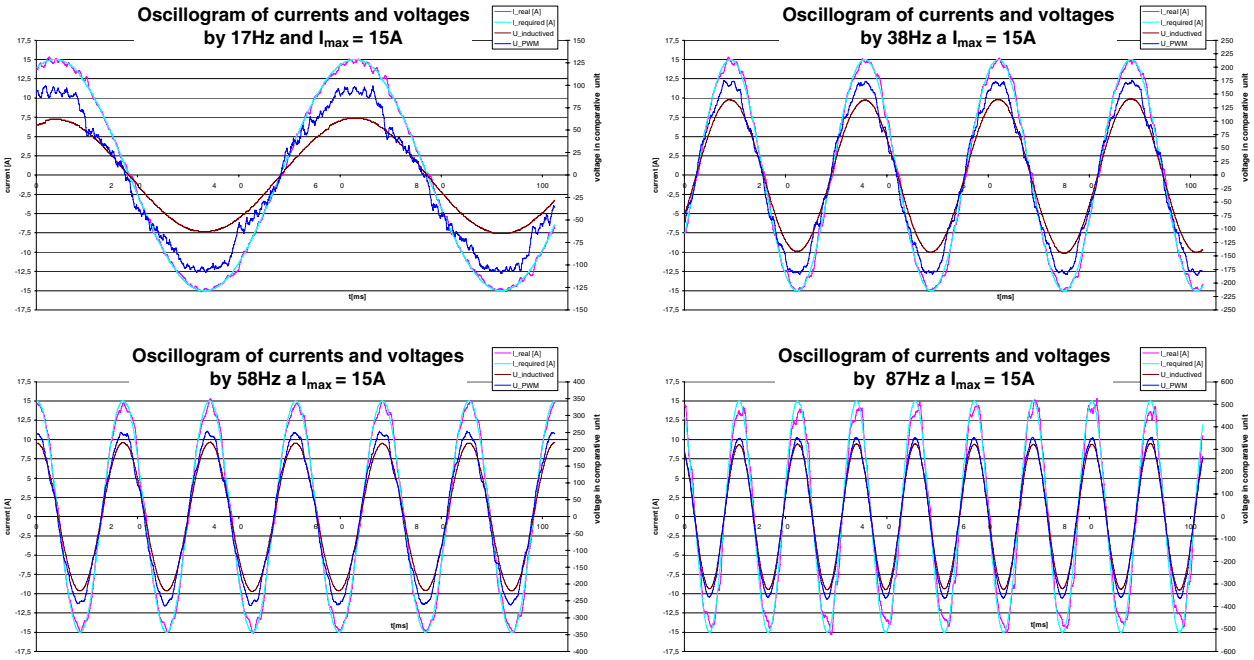

Figure 7: Control quality.

6. CONCLUSION

The paper deals with our research in the field of control of drive with PMSM. We focus to development the robust control algorithm for direct drive PMSM. We have designed a control algorithm. The phase current control algorithm is based on sinus commutation algorithm of brushless DC motor. This algorithm was simulated and verified in laboratory. We have adapted this algorithm to improve its behavior during generating of higher frequency. The improvement is caused by induced voltage compensation and adaptation of PI constants of controllers.

REFERENCES

1. Lettl, J. and S. Fligl,, "Electromagnetic compatibility of matrix converter system," *Radioengineering*, Vol. 15, No. 4, 2006.
2. Dolecek, R. and O. Cerný, "Short-circuits simulation at 25 kV, 50 Hz contact line system," *Proceedings of International Conference ICREPQ 07*, 322–327, Sevilla, Spain, March 2007.
3. Simon, E., "Implementation of a speed field oriented control of 3-phase PMSM motor using TMS320F240," Texas Instruments Aplication Report, September 1999.

Automated Passive Ground Remote Surveillance of Critical Oil & Gas Transport Infrastructures

F. Kaspareck and E. Poggiagliolmi
Entec Integrated Tech., UK

Abstract— Gas transport presents less risk to disruption when compared to oil transport. In case of accident, oil flow can be restored quickly and represents a limited loss, unlike gas that is normally linked to contracted quantities. Any gas interruption affects downstream and consumer supply, whereas any incident on a crude or product line carries a high environmental risk and associated remedial costs.

Pipelines are more vulnerable than what assessed and perceived at present. This is confirmed by the extremely high number of IT attacks on pipeline operating systems, but also by recent accidents caused by assaults in remote areas. Threats mostly affect operational systems but in other cases they imply physical and mechanical damage to the pipeline. Most hydrocarbon transport infrastructures are not equipped with physical perimeter security because threats are not apparent and there are opex and construction capex limitations with respect to available technology. Automated perimeter surveillance, when in place, is carried out by satellite with limitations of resolution and logistics, besides involving high costs for image processing and interpretation.

This paper introduces a new, reliable, fully automated and cost effective pipeline passive surveillance system that, when installed and interfaced with the pipeline operational system, can virtually eliminate the risk of physical perimeter intrusions. Intrusion detection is achieved by means of a large number of sensors deployed on or below the ground surface. The transmitted sensors signals are analyzed in pseudo real time by means of neural nets and pattern recognition algorithms. Adaptable beam forming transforms are utilized in real time processing and analysis to output type of intrusion, position, azimuth and approaching speed with reference to the infrastructure. The results can be automatically correlated to a signature database for automated alarm triggering decision and, or displayed on monitor screens. In case of noisy background, pattern recognition techniques are also employed to isolate the signal. The system works in hibernation mode until it detects a meaningful signal. The system can be ported also to offshore and sub sea application and it is virtually effective on any type of terrain.

Other advantages of this method are that surveillance is carried out without high profile protections such as barbed wire and fences, the system is entirely unmanned, it is not visible from the air or from land, it is instrumentally undetectable and it draws electric power from photovoltaic solar panels.

1. INTRODUCTION

Gas transport presents less risk to disruption when compared to oil transport. In case of accident, oil flow can be restored quickly and represents a limited loss, unlike gas that is normally linked to contracted quantities. Any gas interruption affects downstream and consumer supply, whereas any incident on a crude or product line carries a high environmental risk and associated remedial costs.

Pipelines are more vulnerable than what assessed and perceived at present. This is confirmed by the extremely high number of IT attacks on pipeline operating systems, but also by recent accidents caused by assaults in remote areas. Threats mostly affect operational systems but in other cases they imply physical and mechanical damage to the pipeline. Most hydrocarbon transport infrastructures are not equipped with physical perimeter security because threats are not apparent and there are opex and construction capex limitations with respect to available technology. Automated perimeter surveillance, when in place, is carried out by satellite with limitations of resolution and logistics, besides involving high costs for image processing and interpretation.

This paper introduces a new, reliable, fully automated and cost effective pipeline passive ground surveillance system that, when installed and interfaced with the pipeline operational system, can virtually eliminate the risk of physical perimeter intrusions. Intrusion detection is achieved by means of a large number of sensors deployed on or below the ground surface. The transmitted sensors signals are analyzed in pseudo real time by means of neural nets and pattern recognition algorithms. Adaptable beam forming transforms are utilized in real time processing and analysis

to output type of intrusion, position, azimuth and approaching speed with reference to the infrastructure. The results can be automatically correlated to a signature database for automated alarm triggering decision and, or displayed on monitor screens. In case of noisy background, pattern recognition techniques are also employed to isolate the signal. The system works in hibernation mode until it detects a meaningful signal. The system can be ported also to offshore and sub sea application and it is virtually effective on any type of terrain.

Other advantages of this method are that surveillance is carried out without high profile protections such as barbed wire and fences or superstructures, the system is entirely unmanned, it is not visible from the air or from land, it is instrumentally undetectable and it draws electric power from photovoltaic solar panels.

2. SYSTEM DESCRIPTION

The ground detection system consists of an array of sensors. Its configuration depends on the type of terrain, the nature of expected intrusion and size/dimensions of the installation to be protected. Miniature surface sensors are encapsulated in a water and shock resistant plastic container. All surface sensors are equipped with radio transceivers and a microprocessor to provide a number of control functions including hibernation/wake-up states.

Signals generated by a moving body across or in the vicinity (ground and air) of the array, together with sensor coordinates, are transmitted to a central monitoring control unit. The received signals and sensor coordinates are analyzed in pseudo real time by means of neural nets and pattern recognition algorithms implemented with hybrid firm-and-soft-ware. The outcome of the analysis is displayed on screen in an interpretable format to derive type of intrusion and position.

Detection time ranges between tens of milliseconds to few seconds.

The system can be deployed in a variety of ways: it can be launched from a land vehicle or from the air by means of airplane or helicopter, and it can be deployed in a matter of hours from a distance behind obstacles by launching devices. Alternatively, passive sensors can be buried few tens centimetres below the earth surface and connected to a monitoring station by means of buried electrical cables. The deployment of a buried passive detector-cable system is a cost effective alternative to the surface system. Apart from the additional work required for the burial of the hardware, this system configuration is less expensive than the surface version since it requires no sensor based electronics. It also has the added advantage that the coordinates of each sensor are fixed during deployment and remain invariant. On the other hand, it does not have the flexibility, the ease of deployment and the electronic intruder detection sophistication of surface sensors.

3. BACKGROUND THEORY

Any activity occurring on the earth surface, such as moving vehicles, walking animals or humans produce distinct vibrational patterns traveling below and along the earth surface. In particular direct waves travel along a half space with complex interactions depending on the type of terrain and subsurface weathering. Direct wave patterns follow normally a straight line time distance function that can be assimilated to a spherical front.

The next figure shows some of the critical modes along with their ray path characteristics. Modes development is a function of transmission coefficients. The two main interfaces for transmission are vacuum-solid and solid-solid. Interface waves will have mainly elliptical and hyperbolical wave fronts. This ground roll is easily detected by the sensors and will reach the sensors before or after other converted modes according to critical angle, wave type velocity and medium transmission properties. Velocities can range between 100 and over 1500 m/s with average bandwidth 2–60 Hz.

The deeper interface wave has an annular wave front but its contribution cannot be recorded by the sensors. Shear direct and converted modes will travel along the wave path but can be isolated from compressional modes by pattern recognition. Hyperbolical fronts of reflections are easily recognisee by travel time and front shape. Only in the near field primary and shear reflections will dominate at certain subsurface conditions.

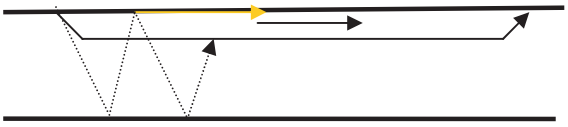

The following modes are taken into consideration by the system for real time analysis: I, PI,

IPI, $SI\ P$, S, IP^iI, P^i, P^r, S^r, S^i, PS^i, where I is the interface wave or ground roll, P and S compression and shear, and the suffix indicates reflection or refraction.

The first five modes of propagation follow in a homogenous medium a straight line along a half space time axis.

Seismic field contributions generated by moving objects within the array range along the deployment ground (vertical line in the figure below), which could conform to the side of a perimeter or to a pipeline, can be detected and recorded.

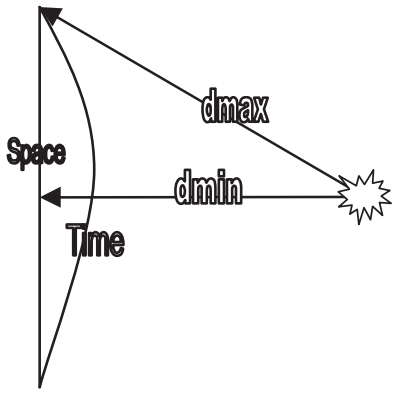

In the imaginary array above Dmin and Dmax represent the minimum and maximum distance travel path for a source at a certain distance with travel times source-target within a few seconds range for average ground roll velocities. Travel time represented over a defined segment is parabolic with the apex intersecting Dmin. Since the system starts recording when sensors are approached vibrations generated firsts will be usually recorded later. An approaching object is equivalent to a dipolar source.

The signal received by the sensors is characterized by certain frequencies, amplitudes and wave numbers, which are the object characteristics (clutters). Data alignment, association and cross-correlation will provide different sets conditions, which are in turn compared to predetermined field tested sets to ascertain 'false' objects. 'True' objects can then be aligned, correlated in space and frequency, back transformed and integrated to derive differential velocities, thus speed gradients and azimuths, which are then input for real time multiple tracking.

4. SYSTEM OPERATIONS AND INTRUSION DETECTION

Under normal conditions, i.e., in the absence of an intrusion or attack, each sensor package is in a dormant (hibernating) state. In this state, the system is instrumentally undetectable since it is totally passive.

Upon an intrusion event the system wakes up and the signature of the intruder is transmitted to a monitoring station where it will be processed and cross-analyzed.

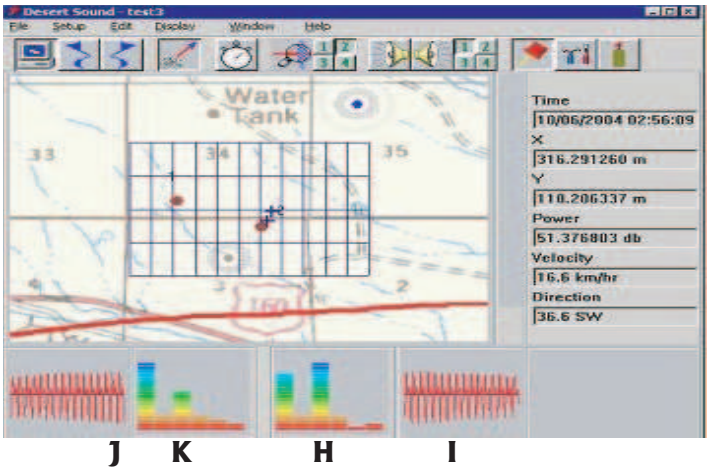

A typical screenshot is shown below for a car slowly approaching a target. J I signals from left

and right detectors, H and K Frequency amplitude spectra. The main parameters identified upon detection of disturbance are as follows:

- Number of objects;
- Location and coordinates;
- Speeds and azimuths (likely target);
- Distances and time to target;
- Signatures of intruders.

5. SYSTEM APPLICATIONS AND MARKET BASE

This system is particularly cost effective for land pipelines, it requires minimum manning, is very precise, and it is highly flexible, i.e., it can be installed while pipes are laid or after. The system is available as a high end and low end system with similar operating characteristics, but different deployment strategies. It can be easily part of a multilayer system and can be patched into the existing system or Scada.

The overall market base comprehends among the others operators and services, institutions and governments, city and regional bodies involved with running or responsible for infrastructures, refineries, fields, buildings.

6. CONCLUSIONS

Third party theft and attacks together with accidental involuntary interference with land lines represent by far the main cause of spillage (close to 50% over the past twenty years). Pipelines are more vulnerable than what assessed and perceived at present. Threats are changing but in 90% of cases imply presence in pipeline vicinity. Existing security products do not address physical perimeter effectively or efficiently. The overall result is increase cost of shipping, environmental harm and lower supply security.

The system described offers an invisible protection of critical fixed infrastructures at low capex and opex. The system incorporates false alarms technology, its reliability is high, close to 100% and its deployment may save costly interventions, thus opex, extend the infrastructure life, avoid costly environmental remediation jobs and product losses.

Comparative Analysis of WLAN, WiMAX and UMTS Technologies

Aktül Kavas

Department of Electronics & Communication Engineering
Electrical and Electronics Faculty, Yıldız Technical University
Beşiktaş 34349, Istanbul, Turkey

Abstract— Today wireless communication systems can be classified in two groups. The first group technology provides low data rate and mobility while the other one procures high data rate and bandwidth with small coverage. Cellular systems and Broadband Wireless Access technologies can be given as proper examples respectively. In this study WLAN, WiMAX and UMTS technologies are introduced and comparative analysis in terms of peak data rate, bandwidth, multiple access techniques, mobility, coverage, standardization, and market penetration is presented.

1. INTRODUCTION

Wireless broadband technologies promise to make all kinds of information available anywhere, anytime, at a low cost, to a large portion of population. From the end user perspective the new technologies provide the necessary means to make life more convenient by creating differentiated and personalized services. In the last decade we were primarily used to accessing people via voice, but there are of course other forms of communication like gestures, facial expressions, images and even moving pictures. Today we increasingly need user devices wireless for mobility and flexibility with total coverage on small light and affordable terminals then ever.

Evolving of circuit switched networks towards packet switched technology high data rates is acquired and this evolution has opened new opportunities. 2.5 and 3 G networks provide high mobility for the packet domain users. The commercial UMTS networks defined by 3GPP are launched by major telecom operators. Communication over UMTS networks provides broadband voice, data and video traffic to mobile users.

On the other hand the development of the technology has opened new era like WLAN, WiMAX and HSDPA communication. Therefore the merging IP based services provide broadband data access in fixed, mobile and nomadic environments supporting voice, video and data traffic with high speed, high capacity and low cost per bit.

At the moment the main question would be to find out whether these new emerging technologies are competitive or complementary technologies to UMTS.

In this paper WLAN, 3G technologies (UMTS, HSDPA) and Broadband Wireless Access Technologies (WiMAX, WiBro) introduced in Sections 2, 3 and 4 respectively. In Section 5, a comparative analysis is done. Finally Section 6 concludes the findings of the paper.

2. WLAN (WIRELESS LOCAL AREA NETWORK)

The Institute of Electrical and Electronics Engineers (IEEE) ratified the original 802.11 specifications in 1997 as the standard for Wireless LANs. WLANs provide all the features and benefits of traditional LAN technologies without the limitations of wires and cables.

Today 802.11 standards can be used for both indoor peer to peer networks as well as for outdoor point to point and point to multipoint applications.

WLAN operates on the unlicensed 2.4 GHz and 5 GHz frequency bands achieving 54 Mbps theoretical data rates range about 30 meters.

802.11a uses unlicensed 5 GHz frequency band with physical layer implementation based to OFDM (Orthogonal Frequency Division Multiplexing) providing 52 sub carriers, where 48 of them used for traffic. In 802.11a standard each sub carrier provides 6, 9, 12, 18, 24, 36, 48 or 54 Mbps digital bandwidth. Theoretical data rates decrease with the distance more quickly than 802.11b.

802.11b uses 2.4 GHz frequency band achieving 11 Mbps theoretical data rates range of 100 m to a maximum of a few hundred meters, with physical layer implementation based on DSSS (Direct Sequence Spread Spectrum). 802.11b channels 1 to 13 with 5 MHz spacing are used in Europe, Middle East and Asia each channel provides 1, 2, 5.5 or 11 Mbps bandwidth depending on channel quality.

IEEE 802.11 Standards:

802.11a	54 Mbps standard, 5 GHz signalling
802.11b	11 Mbps standard, 2.4 GHz signaling
802.11c	operation of bridge connections (moved to 802.1)
802.11d	worldwide compliance with regulations for use of wireless signal spectrum
802.11e	Quality of Service (QoS) support
802.11f	Inter-Access Point Protocol (to support roaming clients), IAPP
802.11g	54 Mbps standard, 2.4 GHz signalling
802.11h	enhanced version of 802.11a to Support European regulatory requirements
802.11i	security improvements for the 802.11 family
802.11j	enhancements to 5 GHz signalling to support Japan regulatory requirements
802.11k	WLAN system management (in progress)
802.11l	skipped to avoid confusion with 802.11i
802.11m	maintenance of 802.11 family documentation
802.11n	100+Mbps standard

802.11g uses 2.4 GHz frequency achieving 54Mbps range of hundred meters with physical layer implementation based on OFDM [1].

WLAN cell size is restricted to few tens of meters in efficient usage, the hundred meters limit is difficult to reach due to signal weakness at the edge of the cell.

3. 3G TECHNOLOGIES

IMT-2000 technologies, known popularly as 3 G, are also starting to grow broadband subscribers achieving high data rates. The most of the popular 3G technologies are WCDMA, the migration path for GSM networks and the family of CDMA technologies including CDMA20001x and CDMA 1xEV-DO.

3.1. UMTS (Universal Mobile Telecommunications System)

Standing for "Universal Mobile Telecommunications System", UMTS represents an evolution in terms of capacity, data speeds and new service capabilities from second generation mobile networks.

3G/UMTS employs a 5 MHz channel carrier width to deliver significantly higher data rates and increased capacity compared with second generation networks with 1900–1980 MHz, 2010–2025 MHz, 2110–2170 MHz operating frequencies [2].

3G/UMTS in its initial phase offers theoretical bit rates of up to 384 kbps in high mobility situations such as urban and suburban areas, 144 kbps in rural areas and 2 Mbps in stationary/nomadic user environments for short range applications. Symmetry between uplink and downlink data rates when using paired (FDD) spectrum also means that 3G/UMTS is ideally suited for applications such as real-time video telephony — in contrast with other technologies such as ADSL where there is a pronounced asymmetry between uplink and downlink throughput rates.

3.2. HDSPA (High Speed Packet Access)

High Speed Packet Access (HSPA) is a generic term adopted by the UMTS Forum to refer to improvements in the UMTS Radio Interface in the Releases 5 and 6 of the 3rd Generation Partnership Project (3GPP) standards.

HSPA refers to both the improvements made in the UMTS downlink, often referred to as High Speed Downlink Packet Access (HSDPA) and the improvements made in the uplink, often referred to as High Speed Uplink Packet Access (HSUPA) but also referred to as Enhanced Dedicated Channel (E-DCH).

HSDPA enables data transmission speeds of up to 14.4 Mbit/s per user. Both HSDPA and HSUPA can be implemented in the standard 5 MHz carrier of UMTS networks and can co-exist with the first generation of UMTS networks based on the 3GPP Release 99 (R99) standard [3].

The key benefits of HSPA can be categorized in 3 ways;

- Improved speed for end user applications

- Improved interactivity for end user applications,
- Improved network capacity for the operator.

4. BROADBAND WIRELESS ACCESS TECHNOLOGIES

4.1. WIMAX (Worldwide Interoperability For Microwave Access)

Wimax is the name of a mark intended for labeling compatible equipment with IEEE 802.16 (Broadband Wireless Access) and European ETSI HiperMAN standard. It mainly does not act to allow the direct access but rather to interconnect the various access points on a city scale for today.

WiMAX operates at the bandwidth between 10 to 66 GHz ratified in April 2002 by IEEE. Its theoretical data rate is 70 Mbps with a range of up to 50 km. In January 2003 IEEE approved the 802.11a standard which covers frequency band between 2 GHz and 11 GHz. These sub 11 GHz frequency ranges enable a non-line of sight performance, where obstacles like trees and buildings are often present and where base stations may need to be unobtrusively mounted on the roofs of homes or buildings rather than towers on mountains.

WiMAX systems promise to be very high capacity (up to 134.4 Mbps in a 28 MHz channel), travel long distances 50 km or more, not require line of sight and to be work at vehicular speeds under 802.16e extension. [4]

WiMAX systems persue a goal for the provision of broadband internet services especially in remote areas and especially when fully ubiquitous access is needed.

IEEE 802.16 Standards:

802.16a	works in 2–11 GHz range and supports mesh deployments.
802.16b	Increase the amount of spectrum that can be used in 5 and 6 GHz range. Provides Quality of Service guarantees.
802.16c	works in higher frequency range of 10 to 66 GHz.
802.16d	Improvements to 802.16a. Deals specifically with wireless connectivity between fixed devices.
802.16e	Supports mobile devices such as laptops, personal digital assistants and mobile phones.
802.16f	works on incorporating mesh networking capabilities.

4.2. WIBRO (Wireless Broadband)

Companies from Korea Republic have developed a WiMAX styled technology called WiBro (Wireless Broadband). WiBro is designed for 2.3 GHz and offers 512–1024 kbps per user and allows users to travel at near vehicular speeds (around 60 km/h).

The European Telecommunications Standards Institute ETSI has also developed broadband metropolitan area network standards under the name HiperMAN. Like WiBro and other related technologies, these systems allow for long distances (10's of kilometers) and high bandwidth (up to 280 Mbps per base station).

The WiMAX forum has been working with the HiperMAN, WiBro and 802.16 standards to ensure interoperability amongst these various systems.

5. ANALYSIS

In this study comparative analysis of WLAN, WiMAX,, WiBro UMTS and HSPA is done according to market penetration, vendor difficulties, power of buyers, threat of new entrants and threat of new substitutes.

Comparisons of aforementioned systems are given in Tables 1 and 2.

5.1. Market Penetration

UMTS provides users wide range of cellular services. UMTS infrastructure is available at big cities because of investment costs. Generally GSM operators are also UMTS operators. UMTS operators have large GSM customer basis and established organization to serve users. Operators have also working profitable business model and longer term experience about cellular communication business.

Table 1: BWA technology comparison.

	WLAN	**WiMAX**	**WiBro**
Peak Data Rate	802.11a,g=54 Mbps	DL:70 Mbps	DL:18.4 Mbps
	802.11b=11 Mbps	UL:70 Mbps	UL:6.1 Mbps
Bandwidth	20 MHz	5–6 GHz	9 MHz
Multiple Access	CSMA/CA	OFDM/OFDMA	OFDMA
Duplex	TDD	TDD	TDD
Mobility	Low	Low	Mid
Coverage	Small	Mid	Mid
Standardization	IEEE802.11x	802.16	TTA&802.16e
Target Market	Home/ Enterprise	Home/ Enterprise	Home/ Enterprise

Table 2: 3G technology comparison.

	UMTS	**EV-DO**	**HSDPA**
Peak Data Rate	DL:2 Mbps	DL:3.1 Mbps	DL:14 Mbps
	UL:2 Mbps	UL:1.2 Mbps	UL:2 Mbps
Bandwidth	5 MHz	1.25 MHz	5 MHz
Multiple Access	CDMA	CDMA	TDMA,CDMA
Duplex	FDD	FDD	FDD
Mobility	High	High	High
Coverage	Large	Large	Large
Standardization	3GPP	3GPP	3GPP
Target Market	Public	Public	Public

5.2. Vendor Difficulties

The infrastructure investment for existing and developing technologies causes financially hard times for operators and cause vendor difficulties. From this point of view vendors are willing to grow the market worldwide with interoperable technologies.

5.3. Power of Buyers

Ordinary users do not very interested using new technologies and high data rates. Also the users do not yet have understandings how to measure the price of the technology that they are using.

5.4. Threat of New Entrants

UMTS has advantage in cities by established infrastructure and customer basis. WiMAX is now a wireless cable replacement technology and does not compete with UMTS.WLAN is the technology with limited coverage.

5.5. Threat of New Substitutes

There are no direct substitutes for UMTS in density traffic areas especially in big city centers for today. WiMAX competes with wired operators. WLAN competes in hotspots providing internet access and VOIP calls with high data rates in unlicensed spectrum.

6. CONCLUSION

At the moment WiMAX and WiBro does not yet support mobility of terminal therefore WiMAX can be categorized more likely as cable replacement technology than real competitor of UMTS.

WLAN is a hotspot technology with very limited coverage providing more capacity to small area than UMTS with high bandwidth. WLAN is more complementary technology for UMTS in hotspots.

On the other hand HSPA refers to improvements in both the downlink and uplink of the radio access network, known as HSDPA and HSUPA respectively. The first terminals for HSDPA will be category 6 terminals, capable of supporting up to 3.6 Mbit/s. Therefore HSPA technology will thus offer cost effective wide-area broadband mobility and play a significant role in stimulating the demand for data services, whether they be consumer multimedia and gaming or corporate email and mobile access by using existing UMTS networks..

REFERENCES

1. Cisco WLAN course, 2004, Ankara, 20.02, 2005.
2. Walke, B., *Mobile Radio Networks*, 327–339, Wiley, 2003(1).
3. Batil, B., et al., *IP in Wireless Networks*, 216, Prentice Hall, 2003(1).
4. WiMAX Forum, Business Case Models for Fixed Broadband Wireless Access based on WiMAX Technology and the 802.16 Standard, 2004(2), Available at: http://www.wimaxforum.org/news/downloads/WiMAX-The_Business_Case-Rev3.pdf

Research on Asymmetric Characteristics of Mobile Communications System Based on Electromagnetic Radiation

Weidong Wang, Yinghai Zhang, Kaijie Zhou, and Heng Zhang

Information & Electronics Technology Lab, Beijing University of Posts and Telecommunications
P. O. Box 116, Beijing 100876, China

Abstract— It's well known that data traffic brings asymmetry which is called Service Asymmetry (SA) to mobile communications system. This paper discusses asymmetry between uplink and downlink in mobile communications system in a new aspect — in view of the effects of electromagnetic radiation to human body, which is termed as Electromagnetic Asymmetry (EA). It's stated that both EA and SA should be taken into account, but EA has higher priority to SA. By calculating, it's concluded that under the restriction of electromagnetic radiation, the downlink data rate should be much higher than that of uplink. It is demonstrated that to adapt to EA and SA, the equivalent bandwidth of uplink should be narrower than that of downlink in view of duplex techniques including FDD and TDD.

1. INTRODUCTION

In the future, most mobile communications services will be asymmetric, such as high multimedia [1, 3]. The downlink of service requirement is much greater than the uplink both in transmission total amount and transmission rate. So this asymmetric transmission characteristic is caused by traffic demand [2–4]. We call it as Service Asymmetry (SA) between uplink and downlink.

Nowadays, only SA is considered as the effect of asymmetric characteristic. In this paper, we also consider the asymmetric characteristic of uplink and downlink caused by electromagnetic radiation, which is termed as Electromagnetic Asymmetry (EA) between uplink and downlink. The influence on surrounding environment caused by electromagnetic radiation is always a controversial problem. With the large-scale application of mobile communications, the total amount of electromagnetic radiation will increase and people will have to re-evaluate the social effect of mobile communications [5]. The influence of electromagnetic radiation will be one of the most important elements which should be considered in research and design of mobile communications system.

This paper analyzes the asymmetric characteristics of mobile communications system influenced by electromagnetic radiation. The structure of this paper is as follows: Section 2 analyses the characteristics of asymmetric transmission caused by electromagnetic radiation influence, Section 3 studies the methods to adapt to EA in view of duplex technique, and Section 4 is the conclusion.

2. THE ASYMMETRIC TRANSMISSION CHARACTERISTICS OF MOBILE COMMUNICATIONS CAUSED BY ELECTROMAGNETIC RADIATION

It is notable that the mobile terminal is very close to human body, which is a small transceiver. The distance from mobile terminal to human body ranges from several centimeters to dozens of centimeters. In contrast to that, the distance from base station to human body is much longer, which ranges from dozens of meters to several kilometers. So the electromagnetic radiation impact on human body caused by mobile terminal is much more intense than that caused by base station.

Then, we will respectively calculate the radiation power to human body caused by base station and mobile terminal.

1. Radiation power of base station absorbed by human body

As there is a long distance from base station to human body, under the presupposition of ideal LOS propagation environment, we can use the Free Space Propagation Model. The power received by human body is

$$P_r = \frac{A_e G_t P_t}{4\pi d^2} \tag{1}$$

where d is the distance from base station to human body, A_e is the effective surface area, G_t is the gain of antenna, and P_t is the transmission power of base station.

2. Radiation power of mobile absorbed by human body

The mobile terminal is close to human body and the radiation field is inductive, so the free space propagation model above is not suitable. Here we introduce the concept of antenna propagation efficiency [6, 7].

To ignore the heat loss of mobile terminal itself, the total emission power of the antenna is

$$P_t = P_a + P_r \tag{2}$$

P_a is the power transmitted to faraway place, and P_r is the power absorbed by human body.

The Definition of antenna transmission efficiency η is

$$\eta = \frac{P_a}{P_t} \times 100\% \tag{3}$$

According to (2) and (3), we can conclude that radiation power of a mobile terminal received by human body is

$$P_r = P_t \times (1 - \eta) \tag{4}$$

There are many indexes used to evaluate the electromagnetic radiation influence upon human body. Among these, Specific Absorption Rate (SAR) is fundamental and widely used for analysis of electromagnetic radiation. The SAR means the power absorbed by unit weight of organism exposed to the electromagnetic fields. So the SAR can be calculated by the expressions as follows:

$$SAR = \frac{P_r}{M} \tag{5}$$

where P_r is the power absorbed by human body, and M is the weight of the absorbing radiation part of human body.

Then, we will respectively calculate the SAR to human body caused by base station and mobile terminal.

1. SAR to human body caused by base station

As there is a long distance from base station to human body, the radiation distribution on each part of human body can be considered even. So the SAR of human body could be calculated by the expressions as follows:

$$SAR_{b,h} = \frac{P_{b,h}}{M_b} \tag{6}$$

$P_{b,h}$ is the radiation power of base station absorbed by human body, the expression of $P_{b,h}$ is (1); M_b is the weight of whole human body absorbing radiation. Then

$$SAR_{\max} = SAR_{b,h} = \frac{P_{b,h}}{M_b} = \frac{A_e G_t P_t}{4\pi d^2 M_b} \tag{7}$$

The transmission power of base station P_t : $P_t = E_b^d \times R_0^d$. R_0^d is the maximum transmission rate of downlink. E_b^d is the transmission energy of one bit. Then

$$SAR_{\max} = SAR_{b,h} = \frac{P_{b,h}}{M_b} = \frac{A_e G_t P_t}{4\pi d^2 M_b} = \frac{A_e G_t \times E_b^d \times R_0^d}{4\pi d^2 M_b} \tag{8}$$

2. SAR to human body caused by mobile terminal

The radiation of mobile to human body differs from that base station to human body. It is inductive close field radiation and its intensity decreases rapidly when the distance increases. The influences of electromagnetic radiation on human body mainly focus on human parts close to mobile terminal. In this paper, two using mobile modes are considered:

A. Mobile near the ear. This is a common mode of calling, the radiation on human body mostly focuses on head.

B. Mobile terminal is in the same height with person's eyes and the distance between them is about 50 cm. This mode corresponds to high downlink services such as video on demand or online game. In this mode, the radiation mostly focuses on head and parts of chest.

For simplicity, we also assume that the radiation distribution on the absorbing radiation part of human body is even. So the SAR threshold of human body caused by mobile terminal is:

$$SAR_{m,h} = \frac{P_{m,h}}{M_h} \tag{9}$$

$P_{m,h}$ is radiation power of a mobile terminal received by human body, the expression of $P_{m,h}$ is (4), M_h is the weight of partial human body which absorbs radiation, mainly the head and chest. Then

$$SAR_{\max} = SAR_{m,h} = \frac{P_{m,h}}{M_h} = \frac{P_t \times (1-\eta)}{M_h} \tag{10}$$

The transmission power of mobile P_t can be expressed as: $P_t = E_b^u \times R_0^u$. R_0^u is the maximum transmission rate of uplink under the restriction of electromagnetic radiation. E_b^u is the transmission energy of one bit. Then

$$SAR_{\max} = SAR_{m,h} = \frac{P_{m,h}}{M_h} = \frac{P_t \times (1-\eta)}{M_h} = \frac{E_b^u \times R_0^u \times (1-\eta)}{M_h} \tag{11}$$

So, combined with Equations (8) and (11), we can get the ratio of maximum uplink rate to maximum downlink rate:

$$\frac{R_0^d}{R_0^u} = \frac{4\pi d^2 \times M_b \times E_b^u \times (1-\eta)}{A_e G_t \times E_b^d \times M_h} \tag{12}$$

Now we will analyze that the maximum transmission rate of downlink is much higher than that of uplink under the restriction of electromagnetic radiation.

Here is an example which demonstrates the asymmetric characteristics of uplink rate to downlink rate.

Parameters in the Equation (12) are assumed as follows: the effective surface area of human body A_e is about $0.6\,\mathrm{m}^2$, the gain of transmitting antenna G_t is 1, and the distance from base station to human body is 50 meters. For simplicity, supposed $E_b^u = E_b^d$.

When MS is used in the mode A (near ear), the transmission efficiency of antenna η is about 57% [7], the weight of the head M_h is about 8% of the whole body weight. The ratio of maximum uplink rate to maximum downlink rate:

$$R_0^d / R_0^u = 2.8 \times 10^5$$

When MS is used in the mode B, the transmission efficiency of antenna η is about 85% [7], the weight including chest and head M_h is about 15% of the whole body weight. The ratio of maximum uplink rate to maximum downlink rate:

$$R_0^d / R_0^u = 5.2 \times 10^4$$

As the distance from base station to human body increases, the ratio of downlink rate to uplink rate (R_o^d / R_o^u) becomes much higher. This is shown in Figure 1. And the R_o^d / R_o^u in mode A is much higher than in mode B. Because in mode A, the mobile is much closer to human body, the uplink is much easier to be restricted with the mobile's electromagnetic radiation. Furthermore, in mode A, when it is 50 meters from base station to human body, the R_o^d / R_o^u is about 55 dB, and when distance form base station to human body reaches 300 meters, the R_o^d / R_o^u is even to 70 dB.

Under the constraint of electromagnetic radiation, we can find that the downlink transmission rate is much higher than that of uplink in mobile telecommunication system. In mode A, the ratio of maximum rate of downlink and uplink is more than 10^5 times, which shows the asymmetric transmission characteristic of uplink and downlink. The uplink is much easier to reach transmission capacity saturation for one user, while there is much transmission rate and transmission power margin in downlink. So we call it Electromagnetic Asymmetry (EA) between uplink and downlink.

3. METHODS TO ADAPT EA IN THE FUTURE COMMUNICATIONS SYSTEM

According to the analysis above, a new and comprehensive understanding about mobile communications system should be built. The transmission rate of future mobile communications system will increase greatly, and it is important to take the EA into account, when we design the system.

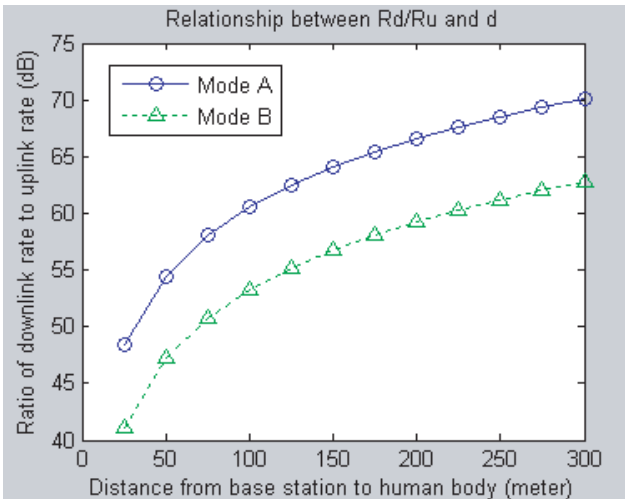

Figure 1: The relationship between ratio of downlink rate to uplink rate (dB) and distance form base station to human body (meter).

As mentioned above, the asymmetric characteristic caused by service will also be remarkable in the future communications system. So both SA and EA should be taken into account in the future mobile communication system. However, EA is different from SA. The ratio of downlink to uplink bandwidth caused by EA is 10^5, while the ratio caused by SA is less than 10^2. Meanwhile, EA corresponds with human safety tightly. So, in a word, the EA should have the higher priority to SA in the design of future mobile communications system, the asymmetric characteristic of uplink and downlink mainly depends on EA. According to Shannon theory: $C = B \times \log_2(1 + \frac{S}{N})$, suppose the $\frac{S}{N}$ of uplink and downlink are probably the same.

For SA: The ratio of uplink rate to downlink rate: $R_0^d/R_o^u \approx 10^2$, so the ratio of uplink bandwidth to downlink bandwidth: $B^d/B^u \approx 10^2$.

For EA: The ratio of uplink rate to downlink rate: $R_0^d/R_0^u \approx 10^2$, so the ratio of uplink bandwidth to downlink bandwidth: $B^d/B^u \approx 10^5$.

The equations above demonstrate that uplink bandwidth should be narrower than down bandwidth and EA will play an more important part in future communications system as the asymmetric characteristic between uplink and downlink is more obvious in EA than SA.

To protect people from electromagnetic radiation, the resource allocated to uplink must be restricted. According to Shannon Theory, the equivalent bandwidth of uplink should be narrower than that of downlink. In view of duplex technique, it means the uplink bandwidth should be narrower than that of downlink in FDD system and the number of uplink time slot should be less than that of downlink in TDD system.

But the traditional duplex technique can't support the asymmetric characteristic of uplink and downlink efficiently. FDD allocates the same spectrum resource for uplink and downlink, so it can't meet asymmetric transmission. TDD can transmit the traffic asymmetrically by dynamic uplink and downlink timeslot distribution, but because of the interference at crossed time slot and synchronization problem, TDD allocate the same time slot numbers for uplink and downlink in practical use. So, to adapt the asymmetric transmission in future, one way is to develop methods to allocate uplink and downlink bandwidth asymmetrically for FDD, another way is to find methods to eliminate the interference at crossed time slot in TDD.

Therefore, for the application of duplex techniques including FDD and TDD, to adapt the asymmetric transmission both on SA and EA in future, the equivalent bandwidth of uplink should be narrower than that of downlink.

4. CONCLUSION

This paper discusses the asymmetric transmission characteristic of mobile communications system from the point of the influence of electromagnetic radiation to human body. It demonstrates that under the restriction of electromagnetic radiation, the uplink is more easily to reach transmission capacity saturation for users, while there is much transmission rate margin and transmission power

margin in the downlink. The effects of electromagnetic radiation in mobile communications system will be one of the important elements that restrict the growth of uplink-transmission capacity. It is termed Electromagnetic Asymmetry (EA) between uplink and downlink. Meanwhile, the asymmetric characteristic is also caused by SA. Both SA and EA should be paid much attention in the research, design and application of mobile communications system, but EA has higher priority to SA. In view of duplex techniques including FDD and TDD, to adapt the asymmetric transmission both on SA and EA in future, the equivalent bandwidth of uplink should be narrower than that of downlink.

ACKNOWLEDGMENT

This study is supported by National Natural Science Foundation of China (60572123).

REFERENCES

1. Holma, H. and A. Toskala, *WCDMA for UMTS-Radio Access for Third Generation Mobile Communications*, John Wiley & Sons, Ltd., 2000.
2. Povey, G. J. R., "A review of time division duplex-CDMA techniques [C]," *1998 IEEE 5th International Symposium on Spread Spectrum Techniques and Applications*, 1998.
3. Stevens, P., "Operator design and planning issues for UMTS networks," *UMTS — The R&D Challenges (Ref. No. 1998/496), IEE Colloquium*, 3/1–3/5, 23 Nov., 1998.
4. Esmailzadeh, R. and M. Nkagawa, *TDD-CDMA for Wireless Communications*, Artech House, 2002.
5. Liu, Y., *Electromagnetic Biology Effect*, Beijing University of Posts and Telecommunications, Jan. 2002.
6. Sun, Z., P. Liu, and Z. Qing, "FDTD analysis on influence of electromagnetic radiation of mobile communication terminal to human body," Shantou University bulletin.
7. Kang, G., X. Zhu, and C. Wang, "Electromagnetic dose analysis of monopole mobile phone acting on human body," Beijing University bulletin.